

# **An Engineering Methodology for Kite Design**

Copyright © 2010 by J. Breukels  
Printed by: Proefschriftmaken.nl || Printyourthesis.com  
Published by: Uitgeverij BOXPress, Oisterwijk

All rights reserved. No part of the material protected by this copyright notice may be reproduced or utilized in any form or by any means, electronic or mechanical, including photocopying, recording or by any information storage and retrieval system, without the prior permission of the author.

ISBN 978-90-8891-230-6

Typeset by the author with the L<sup>A</sup>T<sub>E</sub>X documentation system.

Cover design composition made by the author.

Author email: [jeroenbreukels@hotmail.com](mailto:jeroenbreukels@hotmail.com)



# An Engineering Methodology for Kite Design

PROEFSCHRIFT

ter verkrijging van de graad van doctor  
aan de Technische Universiteit Delft,  
op gezag van de Rector Magnificus Prof. ir. K.Ch.A.M. Luyben,  
voorzitter van het College voor Promoties,  
in het openbaar te verdedigen op vrijdag 21 januari 2011 om 10.00 uur  
door

Jeroen BREUKELS

Ingenieur Luchtvaart en Ruimtevaart  
geboren te Elst.

Dit proefschrift is goedgekeurd door de promotoren:

Prof. dr. W.J. Ockels

Prof. dr. ir. J.A. Mulder

Samenstelling promotiecommissie:

Rector Magnificus	voorzitter
Prof. dr. W.J. Ockels	Technische Universiteit Delft, promotor
Prof. dr. ir. J.A. Mulder	Technische Universiteit Delft, promotor
Prof. dr. ir. J.C. Brezet	Technische Universiteit Delft
Prof. dr. D.J. Rixen	Technische Universiteit Delft
Prof. M. Milanese	Politecnico di Torino
Dr. R. Schmehl	Technische Universiteit Delft
Dr. H. Rebbeck	Mutiny kites

De volgende bedrijven en instellingen hebben in belangrijke mate financieel bijgedragen aan de totstandkoming van dit proefschrift.

The Rotterdam Climate Initiative, Stichting Shell Research, E-on, Provincie Groningen, Energy Delta Institute, Gasunie, Fugro, Rijksuniversiteit Groningen, Gemeente Delft, Gemeente Groningen, Energy Valley, Prolyte Products.

*For my parents Henk en Ineke and my girlfriend Judith*



# De vlieger

Mijn vlieger gaat naar boven,  
Wat heeft de wind veel kracht!

Wie zou het ooit gelooven,  
Ik trok, met al mijn magt;  
'k Heb zoo veel touw gekregen  
En 't is er aan besteed;  
Hij is zoo hoog gestegen,  
Dat ik hem naauwlijks weet.

Ik moet mijn' vlieger binden,  
Want anders reis ik meê;  
Waar zal men mij dan vinden,  
Hij trok mij wis in zee! -  
'k Zal op mijn' vader wachten,  
Dat die hem naar zich trekt;  
Ik heb mijn kleine krachten  
Niet vruchteloos ontdekt. -

De wind heeft veel vermogen,  
Wie kan hem tegen gaan? -  
Wij zien hier, met onze oogen,  
Toch niets van zijn bestaan! -  
Dit is nooit aangewezen;  
God geeft die kennis niet,  
Wiens almacht elk moet vreezen,  
Die ook den wind gebiedt. -

*Johannes Hazeu Cornelisz*

”Kinderspelen, in leerzame gedichtjes”  
Ten Brink en De Vries, Amsterdam z.j.  
2<sup>e</sup> druk, 1837.



---

## Preface

---

When I first heard of energy generation using large controlled kites that go up thousands of feet, I was struck by a feeling of disbelief. It is simply hard to imagine what such a system would entail. The mental picture I had of a kite was that of a small, square shaped toy which was fragile and crashed every time the wind changed. During the course of my master thesis and later, the work presented in this dissertation, I came to realize the real potential of kites. If anything, my hopes are to communicate this realization to the reader as much as I can.

The odd thing is that no one bats an eyelash at the large commercial aircraft that land at Schiphol airport every three minutes with pinpoint precision. We have become both accustomed and dependent to this sight that even a brief period of stagnation in air transport seems to throw the whole world into disarray. It is a testament to the phenomenal achievements of the aviation industry that we have become so blase about our dependence on those planes landing every three minutes. We simply assume they will. We can, because they always do!

But when you are at the beach, flying a kite with airplane controls, it doesn't take long for a crowd to gather and to look on in amazement. My personal experiences at conferences were much the same. The concept of a kite hanging in the sky while you steer it from left to right using a flightstick is something most people have never seen. This very fact shows, with undeniable clarity, the difference in public awareness with regard to airplanes and kites. I myself was a victim of that discrepancy in awareness as well until I started to look at kites as an engineer with an open mind.

During my work, I have found no reason why controlled kites should be so rare. From an engineering point of view, a kite is a tethered airplane which adheres to the same laws of physics as airplanes do. The applications for controlled kites are abundantly clear and very diverse. As a result of my publications and videos on the internet I have received a great deal of interest from not just kite companies, but also other large companies who often inquired about the use of kites for a particular application which I myself had never thought of. The potential for kites is now more obvious to me than ever.

As far as scientific research goes, kites have seen very little so far. This makes the subject of this thesis somewhat of an odd duck. This has its advantages and disadvantages. An advantage is that no matter what you do, it is almost always new. Kites present a largely unexplored field with a lot of potential for researchers. The disadvantage is that, during my work, almost no one was doing similar work which creates an atmosphere of isolation. It makes it more difficult to be accepted to conferences and to get papers published. It seemed that with every presentation, I had to tell the story of the potential of kites all over again in order to convince my audience. However, in all honesty I have to say that I have greatly enjoyed doing so.

I am most grateful to my promotor, Prof. Dr. Wubbo J. Ockels, for the opportunity to pursue this research project. His vision is what has made this work possible in the first place and his input during the course of my PhD track has been most valuable. I also would like to thank Dr. Roland Schmehl for his patience in proof reading all that I wrote and his great insight which has helped me a great deal. I am also most grateful to Prof. Dr. Ir. Bob Mulder for believing in this, and I quote: "exotic project" enough to be involved in such an intense manner. His input has had a significant impact on this work. Lastly, without the support and organizational skills of Nana Saaneh, management assistant at ASSET, none of us at ASSET would be able to do what we do.

Much of this work has been made possible by the sponsorship of The Rotterdam Climate Initiative, the University of Groningen, the Town of Delft, Gasunie, E-on, Fugro, Energy Delta Institute, Stichting Shell Research, Prolyte products, the Town and Province of Groningen and Energy Valley. Without their support, the Laddermill project would not even exist. I owe them my gratitude.

For providing support for MSC ADAMS, I am most thankful for Ir. Chris Verheul of Sayfield International. I have thoroughly enjoyed working together with Chris and I would like to thank him for all his effort. I am also thankful for the help provided by Ir. Arend Schwab and Ir. Edwin de Vries on the multi-body simulations. Furthermore, I am most appreciative for the excellent discussions I have had with Peter Lynn of Peter Lynn Kites, Armin Harich from Flysurfer and Dr. Henry Rebbeck of mutiny kites (formerly of FlexiFoil) for sharing their knowledge and experience in the kite industry. Their insights have been most helpful. I also owe a debt of gratitude to Mike Lam and Corneilla Lam of Lam Sails in Hong Kong for producing some of the kite designs that were devised. I would also like to thank Dr. Keith Alexander of the Canterbury University in Christchurch, New Zealand for his hospitality and for sharing his insights with me.

During my work I have had the good fortune to work together with a large number of students. I have found the cooperation with students to be both inspiring and enjoyable. I am especially grateful to the master students I was given the opportunity to supervise. Edwin Terink, Stefan de Groot, Aart de Wachter, John van den Heuvel, Joep Breuer and Gert-Jan Spierenburg have all made valuable contributions to this thesis. I am also grateful for the cooperation with Lillian



van Emden, Alberto Saez, Jan Muijt, Thomas Frenkel and Rene Oudeman for all their work during their graduation projects. Lastly I want to especially mention Roland Verheul and express my gratitude for all his support during the course of my thesis work.

I would like to thank both my parents Henk en Ineke Breukels for all their incredible support during my time in Delft. Without them, everything would have been different. The last words of gratitude go to my sweet girlfriend Judith, for her love, her patience and her unending enthusiasm whilst listening to me rambling on about the wonderful world of kites.

Jeroen Breukels 2010



### **An Engineering Methodology for Kite Design**

Kites have existed for nearly 3000 years [Fadul, 2009], yet they have seen little serious attention from the scientific community. Kites have been of paramount importance during the development of powered flight in the nineteenth century. By the beginning of the twentieth century, the widespread attention of the scientific community has made it possible for aeronautical science and technology to grow into a serious field of study. The scientific approach to the development of aircraft has enabled the technology to grow into what it is today. For kites, such a growth has not taken place.

Kites are still designed mostly by a sort of trial-and-error process. For the current application of kites such as kite surfing and other sports-related activities, this development process has proven to produce good results. This is possible due to a number of factors such as the availability of new materials and the fact that kites are cheap to make. building a large number of prototypes and testing them is not nearly as big of an investment as with conventional airplanes.

New industrial applications for kites have seen an increase in attention in the last decade. Systems for energy generation and ship propulsion are now under investigation at over 40 institutions and companies all over the world. Almost all of these groups are using the conventional surf kites as their platform. But the industrial application of kites puts far more stringent requirements on these kites. Not only do they need to be light and cheap, requirements governing safety and performance are far more complex than for the conventional kite surfing kites.

Using the old trial-and-error design method to design these industrial kites would lead to an unstructured and uncontrolled process which would yield a large amount of prototypes. This is undesirable. For industrial kites, an engineering methodology for kite design is required. A structured design process akin to the engineering of any other complex system.

The methodology proposed in this thesis is comprised of the following items.

- Knowledge on the dynamics, structure and design of kites and kite-related systems.
- Engineering tools for kite design. These tools are required to be intuitive and resource-friendly.
- Reproducible measurements in order to both further the understanding of kites and validate the design.

In order to build the basic knowledge of the dynamics of kites, first the most simple representation is evaluated. The rigid body model of a kite neglects the kite flexibility. Two rigid body models are developed and evaluated. The rigid body models show excellent agreement with regard to each other. Basic questions of stability can be addressed using this type of model. Furthermore, these rigid body models are comparable to the models for conventional aircraft. This in turn allows for a comparison between kites and airplanes. Such a comparison is made on the basis of the eigenmotions of both a conventional airplane and a kite.

The flexibility of a kite is one of the most important differences with regard to conventional aircraft. The flexibility of a kite is something to be embraced. It allows the kite to adjust and deform while in flight. Gusts and other disturbances are compensated for by gentle deformation, not a sudden departure from equilibrium. Therefore, for a highly flexible kite, the flexibility plays an important role in its stability. The deformation allows the kite to deal with disturbances in a very elegant manner. The flexibility does, however, pose a challenge for the designer. In order to simulate a flexible kite, a multi-body system based approach is used.

The kite simulation toolbox is a numerical simulation tool for flexible kite structures. The simulation tool is built as a toolbox which is easy and intuitive to use. Keeping this tool accessible is an important requirement because current kite companies do not have the financial resources to accommodate highly complex software running on a super computer. The current state of fluid structure interaction technology (coupling a finite element mesh to a computational fluid dynamics mesh and simulating their interactions) is such that a simulation of a complete kite is not feasible at this time (Groeneboom [2010]) due to the immense complexity and the massive amount of computational resources it would require.

The kite simulation toolbox uses three building blocks to build kite models: (1) Tethers, (2) inflatable beams and (3) Foils. These building blocks can be used to build any kite configuration. The cables are discretized by using rigid elements, joint together by hook joints. A general force on each element accounts for the aerodynamic drag on the cable. The tubes are built out of rigid cylindrical elements joint together by spherical joints. A three dimensional torque spring acts on these joints. The stiffness of this spring is governed by an algorithm which takes into account the beam radius, internal pressure and local deflection. The

algorithm is based on data obtained through beam bending tests. The foils are modelled as chordwise wires connecting every leading edge beam element with a trailing edge wire element. Lift and drag forces act on this chordwise wire. The aerodynamic forces are governed by an algorithm which takes into account the angle of attack, airfoil thickness and camber and outputs the appropriate aerodynamic coefficients. The algorithm is based on a CFD analysis of a database of airfoils.

Model validation was performed. First, the three building blocks are validated individually. The 3D canopy shape is validated using the data from a wind tunnel test at the University of Stuttgart. In a large 6.5m diameter windtunnel, an inflated kite was tested. Using photogrammetry, the shape of the wing was recorded. This shape was subsequently compared to the simulated shape. The comparison showed good agreement. Lastly, a number of surf kites were flown in loops and the forces on the lines, as well as the absolute velocity of the kite, were measured and compared to the simulation. Again, the comparison showed good agreement.

With the knowledge growing, the measurements stacking up and the simulation tools in place, a number of case studies are presented to show the benefit of this engineering methodology for kite design. First, the principle of effective cable length is introduced, showing that for very long tethers, only the top part directly influences the kite. Lateral motion of the kite results into lateral motion in the tether which is dampened out downwards along the tether.

The second case is that of a cornering surf kite. Conventional surf kites are flown on four lines: two power lines at the leading edge of the tips and two steering lines at the trailing edge of the tips. Pulling one of the steering lines makes the kite yaw (or corner). Exactly what mechanics are behind the reason why it corners is the subject of a fierce debate among kite designers and kite surfers. The engineering methodology of kite design presented in this thesis offers a new perspective on this issue. By simulating a cornering kite, the resulting data gives insight into a large array of parameters for every position on the kite. From the simulation it is concluded that the yaw motion of a kite as a result of a force on the steering line is the result from an asymmetric deformation of the entire kite. This deformation results in a yawing moment. The case study continues to explore what effects the cornering performance of a kite by comparison to an adapted kite.

The third case study is an investigation to the existing kiteplane design using the rigid body model. During flight testing, the kiteplane is found to have an unstable pendulum motion. The relation between lateral area and pendulum stability is investigated and from the analysis, a number of design changes are proposed. These design changes eventually lead to a new design which is built and tested. The flight tests of the new kiteplane show increased pendulum stability.

The thesis concludes that an engineering approach to the design of kites leads to a greater understanding and a more structured design process. It was shown that the engineering approach is capable of providing answers to existing questions

in the kite world. Both the rigid- and multi-body models are applicable in the design and analysis of kites. Furthermore, for a continued development of kites it is essential that cooperation between academics and kite designers is intensified.

---

## Nomenclature

---

### Latin Symbols

$\mathbf{x}$	State vector	
$\bar{c}$	Mean aerodynamic cord length	m
$\bar{y}$	Mean aerodynamic cord spanwise location	m
$\mathbf{R}$	resultant aerodynamic force	N
$A$	inertial acceleration	$\text{ms}^{-2}$
$a$	Azimuth angular velocity	$\text{s}^{-1}$
$a$	scaling factor for airfoil moment	[-]
$B$	inertial angular momentum	$\text{N}\cdot\text{m}\cdot\text{s}$
$b$	Bridle angular velocity	$\text{s}^{-1}$
$b$	Wing span	m
$c$	Cord length	m
$c_c$	Center cord length	m
$C_D$	Drag coefficient	[-]
$C_L$	Lift coefficient	[-]
$C_m$	Pitching moment coefficient evaluated at center of gravity	[-]
$c_r$	Root cord length	m
$c_t$	Damping constant	$\text{N}\cdot\text{s}/\text{m}$
$c_t$	Tip cord length	m
$C_{D_t}$	Tether drag coefficient	[-]

$C_{m_{ac}}$	Wing pitching moment coefficient evaluated at aerodynamic center	[-]
$C_{N_{\alpha}}$	Derivative of wing normal force coefficient with respect to $\alpha$	[-]
$C_{N_{HT\alpha}}$	Derivative of horizontal tail normal force coefficient with respect to $\alpha$	[-]
$C_{N_{HT\delta_e}}$	Derivative of horizontal tail normal force coefficient with respect $\delta_e$	[-]
$D$	Drag	N
$D_b$	dimensionless time	[-]
$D_c$	dimensionless time	[-]
$D_T$	Tether drag force	N
$d_T$	Tether diameter	mm
$D_{HT}$	Horizontal tail plane drag	N
$D_{VT}$	Vertical tail plane drag	N
$E$	E-modulus	N/m <sup>2</sup>
$E_B$	Body reference frame	[-]
$E_E$	Earth reference frame	[-]
$E_S$	Stability reference frame	[-]
$E_T$	Tether reference frame	[-]
$F$	Force	N
$F$	tether force along $X_S$ -axis	N
$f$	Frequency	Hz
$f$	Longitudinal tether velocity	ms <sup>-1</sup>
$f_m$	Measured longitudinal tether velocity	ms <sup>-1</sup>
$F_{tip}$	Cantilever tip force	N
$F_Z$	Gravity force	N
$F_{axial}$	Axial force on inflated tube	N
$F_{ext}$	sum of external forces	N
$G$	tether force along $Y_S$ -axis	N
$g$	Gravitational acceleration	ms <sup>-2</sup>
$H$	tether force along $Z_S$ -axis	N
$h$	Kite altitude	m
$I$	Inertia moment	kgm <sup>2</sup>
$i_{HT}$	Horizontal tail plane angle of incidence with respect to $X_a$	rad
$k_t$	Spring constant	N/m
$L$	Aerodynamic rolling moment about $X_S$	N·m
$L$	Lift	N
$L_T$	Tether lift force	N
$l_T$	Tether length	m



$l_t$	tether length	m
$L_{HT}$	Horizontal tail plane lift	N
$l_{HT}$	Distance between $ac_w$ and $ac_{ht}$	m
$L_{VT}$	Vertical tail plane lift	N
$l_{VT}$	Distance between wing and vertical tail plane aerodynamic center	m
$M$	Aerodynamic pitching moment about $Y_S$	N·m
$M$	Bending moment	Nm
$M$	Mach number	[-]
$m$	Kite mass	kg
$m_g$	Inertial kite mass excluding confined air	kg
$m_k$	Inertial kite mass including confined air	kg
$M_w$	Wrinkling moment	Nm
$N$	Aerodynamic yawing moment about $Z_S$	N·m
$P$	Motion period	s
$P$	Pendulum period	s
$P$	mechanical power	N·ms <sup>-1</sup>
$P$	tether moment about $X_S$ -axis	N·m
$p$	Pressure	Nm <sup>-2</sup>
$p$	Roll rate	rad/s
$p_{eff}$	Effective internal pressure	Nm <sup>-2</sup>
$Q$	tether moment about $Y_S$ -axis	N·m
$q$	Pitch rate	rad/s
$q_D$	Distributed drag force on tether	Nm <sup>-1</sup>
$q_g$	Distributed gravity force on tether	Nm <sup>-1</sup>
$Q_i$	Generalized force for generalized coordinate $i$	N
$q_i$	Generalized coordinate $i$	m
$R$	Specific gas constant	m <sup>2</sup> s <sup>-2</sup> K
$R$	resultant aerodynamic force	N
$R$	tether moment about $Z_S$ -axis	N·m
$r$	Beam radius	m
$r$	Radius	m
$r$	Yaw rate	rad/s
$r_t$	radius of tether cross section	m
$S$	Lifting surface area	m <sup>2</sup>
$s$	Coordinate along tether path	m
$s$	Laplace variable	[-]

$S_w$	Wing surface area	$m^2$
$S_{HT}$	Surface area of horizontal tail plane	$m^2$
$S_{VT}$	Vertical tail plane surface area	$m^2$
$T$	Kinetic energy	J
$T$	Temperature	K
$T$	Torsional moment	Nm
$t$	Time	s
$t$	membrane thickness	m
$T_G$	Tether force at the ground	N
$T_i$	Tether force at element $i$	N
$T_K$	Tether force at the kite	N
$T_w$	Wrinkling torsion moment	Nm
$T_{0.5}$	Time to damp to half the amplitude	s
$u$	velocity in $X_S$ -direction	$ms^{-1}$
$V$	Airspeed of wing	$ms^{-1}$
$V$	Potential energy	J
$v$	Deflection	m
$v$	velocity in $Y_S$ -direction	$ms^{-1}$
$V_0$	Undisturbed flow velocity	$ms^{-1}$
$V_a$	aerodynamic velocity	$ms^{-1}$
$V_{app}$	apparent velocity	$ms^{-1}$
$V_C$	Crosswind velocity	$ms^{-1}$
$V_k$	Kinematic velocity	$ms^{-1}$
$V_L$	Tether roll-out velocity	$ms^{-1}$
$V_W$	Wind velocity	$ms^{-1}$
$V_\infty$	Undesturbed flow velocity	$ms^{-1}$
$v_{collapse}$	Deflection at collapse	m
$V_{HT}$	Airspeed of horizontal tail plane	$ms^{-1}$
$V_{W_{eff}}$	Effective wind velocity in crosswind motion	$ms^{-1}$
$W$	Weight	N
$w$	velocity in $Z_S$ -direction	$ms^{-1}$
$W_x$	wind in $X_E$ direction	$ms^{-1}$
$W_y$	wind in $Y_E$ direction	$ms^{-1}$
$W_z$	wind in $Z_E$ direction	$ms^{-1}$
$X$	Aerodynamic force in $X_S$ direction	N
$x$	Crosswind factor	[-]

$x$	x coordinate	m
$x_t$	x position of tether attachment in aerodynamic reference frame	m
$x_{ta}$	Position of tow point control mechanism in $X_S$ direction	m
$x_{ac}$	x position of aerodynamic center in aerodynamic reference frame	m
$Y$	Aerodynamic force in $Y_S$ direction	N
$y$	Distance from the neutral line	m
$y_{ta}$	Position of tow point control mechanism in $Y_S$ direction	m
$Z$	Aerodynamic force in $Z_S$ direction	N
$z$	Zenith angular velocity	$s^{-1}$
$z$	z coordinate	m
$z_t$	z position of tether attachment in aerodynamic reference frame	m
$z_{ta}$	Position of tow point control mechanism in $Z_S$ direction	m

### Greek Symbols

$\alpha$	Angle of attack	rad
$\alpha_0$	Angle of attack at $C_L = 0$	rad
$\alpha_e$	Angle between $X_B$ and $X_S$	rad
$\alpha_T$	Angle of apparent wind with respect to the tether orientation	rad
$\beta$	Elevation angle	rad
$\beta_G$	Tether elevation angle at the ground	rad
$\beta_i$	Elevation angle of tether element $i$	rad
$\beta_K$	Tether elevation angle at the kite	rad
$\chi_k$	kinematic yaw angle	rad
$\chi_t$	Tether rotation angle around the tether longitudinal axis	rad
$\delta$	Lift vector tilting angle	rad
$\delta_e$	Elevator deflection angle	rad
$\delta_r$	Rudder deflection angle	rad
$\epsilon$	Downwash angle at the horizontal tail plane	rad
$\Gamma$	Circulation	rad
$\Gamma$	Dihedral angle	rad
$\gamma$	Path angle of apparent wind with horizontal	rad
$\gamma_a$	aerodynamic pitch angle	rad
$\gamma_k$	kinematic pitch angle	rad
$\kappa$	body pitch angle w.r.t. tether	rad
$\lambda$	Taper ratio	[-]

$\lambda$	eigenvalue	$s^{-1}$
$\Lambda_{LE}$	Leading edge sweep angle	rad
$\mu$	Poissons ratio	[-]
$\mu_a$	aerodynamic roll angle	rad
$\mu_b$	dimensionless mass	[-]
$\mu_c$	dimensionless mass	[-]
$\mu_k$	kinematic roll angle	rad
$\Omega$	angular velocity	rad/s
$\omega_0$	natural frequency	Hz
$\phi$	Roll angle	rad
$\phi$	Torsion angle	rad
$\psi$	Yaw angle	rad
$\psi_t$	tether azimuth angle	rad
$\rho$	Air density	$kgm^{-3}$
$\rho_T$	Tether density	$kgm^{-3}$
$\tau$	Nondimensional time variable	[-]
$\tau$	body roll angle w.r.t. tether	rad
$\theta$	Bending angle	rad
$\theta$	Pitch angle	rad
$\theta_t$	Tether angle with respect to the vertical in pendulum motion	rad
$\varepsilon$	error	m
$\vartheta$	Bridle angle	rad
$\xi$	body yaw angle w.r.t. tether	rad

## Abbreviations

<b>2D</b>	Two Dimensional
<b>3D</b>	Three Dimensional
<b>ac</b>	Aerodynamic Center
<b>ADAMS</b>	Automatic Dynamic Analysis of Mechanical Systems
<b>AR</b>	Aspect Ratio
<b>ASSET</b>	Aerospace for Sustainable Engineering and Technology
<b>CFD</b>	Computational Fluid Dynamics
<b>cg</b>	Center of Gravity
<b>DOF</b>	Degrees of freedom
<b>FEM</b>	Finite Element Method

<b>FSI</b>	Fluid Structure Interaction
<b>GPS</b>	Global Positioning System
<b>GUI</b>	Graphical User Interface
<b>GUM</b>	General Use Macros
<b>HAWP</b>	High Altitude Wind Power
<b>KPT</b>	Kiteplane Toolbox
<b>L/D</b>	Lift over Drag ratio
<b>LEI</b>	Leading Edge Inflatable
<b>LE</b>	Leading Edge
<b>MAC</b>	Mean Aerodynamic Cord
<b>ta</b>	Tether attachment points
<b>TE</b>	Trailing Edge
<b>TKC</b>	Toolkit Creator
<b>UDE</b>	User Defined Entity
<b>VLM</b>	Vortex Lattice Method

### Other Symbols

$\mathbb{T}_{BA}$	Transformation matrix from reference frame A to reference frame B
$\mathbb{I}$	mass matrix of inertia
$\mathbf{r}_\theta$	Position vector of the hinge line through the bridle attachment points
$\mathbf{r}_{cg}$	Position vector of the center of gravity
$\mathbf{r}_{ta}$	position of the tether attachment point w.r.t. $cg$ in body axes
$\mathbf{V}_{cg}$	Velocity vector of the center of gravity
$\mathcal{M}_{ext}$	sum of external moments
$\mathbf{F}_a^A$	Aerodynamic force vector in reference frame A
$\mathbf{Q}$	Generalized forces vector
$\mathbf{M}_a^A$	Aerodynamic moment vector in reference frame A
$\omega_{EB}$	Rotation vector of body reference frame
$\omega_{ET}$	Rotation vector of tether reference frame



---

# Contents

---

<b>Preface</b>	<b>vii</b>
<b>Summary</b>	<b>xi</b>
<b>Nomenclature</b>	<b>xv</b>
<b>1 Introduction</b>	<b>1</b>
1.1 Background . . . . .	1
1.2 Thesis objective . . . . .	2
1.3 Thesis structure . . . . .	3
<b>2 Preliminaries</b>	<b>5</b>
2.1 What is a kite? . . . . .	5
2.2 A brief history of kites . . . . .	7
2.2.1 The development of the flying machine . . . . .	7
2.2.2 The great divide . . . . .	10
2.2.3 The turning point . . . . .	10
2.2.4 The situation today . . . . .	11
2.3 Current state of the kite industry . . . . .	13
2.4 Kites and energy generation . . . . .	15
2.4.1 High altitude wind power . . . . .	15
2.4.2 The Laddermill . . . . .	16
2.4.3 Principle of crosswind power . . . . .	17
2.4.4 Kite requirements . . . . .	19
2.4.5 The kiteplane . . . . .	20
2.5 Previous research . . . . .	23

2.5.1	Materials and structures . . . . .	23
2.5.2	Kite aerodynamics . . . . .	25
2.5.3	Tether theory and models . . . . .	26
2.5.4	Kite structure models . . . . .	29
2.5.5	Flight dynamics of kites . . . . .	31
2.5.6	Kite measurements . . . . .	33
2.6	Concluding remarks . . . . .	34
<b>3</b>	<b>Rigid body kite dynamics</b>	<b>35</b>
3.1	Introduction . . . . .	35
3.2	Newton-based kite model . . . . .	36
3.2.1	External forces and moments . . . . .	37
3.2.2	Equations of motion . . . . .	40
3.2.3	Control inputs . . . . .	44
3.2.4	Tether model . . . . .	44
3.2.5	Linearized equations of motion . . . . .	45
3.2.6	Matrix notation of the symmetric equations of motion . . . . .	47
3.2.7	Matrix notation of the asymmetric equations of motion . . . . .	54
3.2.8	Simulation results . . . . .	59
3.3	Lagrange-based kite model . . . . .	63
3.3.1	Kite system kinematics . . . . .	63
3.3.2	Kinetic and potential energy . . . . .	65
3.3.3	Generalized forces . . . . .	65
3.3.4	Equations of motion . . . . .	66
3.4	Tethered vs non-tethered flight . . . . .	67
3.4.1	Eigenmotions of non-tethered flight . . . . .	67
3.4.2	Symmetric eigenmotions of tethered flight . . . . .	68
3.4.3	Asymmetric eigenmotions of tethered flight . . . . .	70
3.5	Effects of cable length . . . . .	72
3.5.1	Effects of cable length on symmetric flight . . . . .	72
3.5.2	Effects of cable length on asymmetric flight . . . . .	74
3.6	Concluding remarks . . . . .	76
<b>4</b>	<b>A Multi-body approach to kite simulations</b>	<b>77</b>
4.1	Introduction . . . . .	77
4.2	The principles of multi-body dynamics . . . . .	78
4.3	Building block 1: Cables . . . . .	82
4.3.1	Cable model definition . . . . .	82
4.3.2	Cable strain . . . . .	85
4.3.3	The cable toolbox implementation . . . . .	87
4.4	Building block 2: Inflatable tubes . . . . .	88
4.4.1	The mechanical behavior of inflatable structures . . . . .	88



4.4.2	Inflatable beam model definition . . . . .	89
4.4.3	Bending . . . . .	91
4.4.4	Torsion . . . . .	97
4.4.5	The combination of bending and torsion . . . . .	102
4.4.6	The inflatable beam toolbox implementation . . . . .	104
4.4.7	Complex inflatable structures . . . . .	105
4.5	Building block 3: Foils . . . . .	106
4.5.1	Airfoil model definition . . . . .	106
4.5.2	The aerodynamic forces . . . . .	108
4.5.3	The airfoil moment . . . . .	117
4.5.4	The airfoil toolbox implementation . . . . .	125
4.6	Building the complete model . . . . .	126
4.7	Concluding remarks . . . . .	127
<b>5</b>	<b>Multi-body kite simulation verification</b>	<b>129</b>
5.1	Introduction . . . . .	129
5.2	Cable model verification . . . . .	130
5.2.1	Simple pendulum . . . . .	130
5.2.2	Wave propagation . . . . .	130
5.2.3	Model convergence . . . . .	131
5.3	Inflatable beam verification . . . . .	132
5.3.1	Tapered beam comparison . . . . .	133
5.3.2	Beam bending comparison . . . . .	134
5.4	Airfoil verification . . . . .	137
5.4.1	Comparison of aerodynamic forces . . . . .	137
5.4.2	Comparison of 2D canopy shape . . . . .	138
5.5	3D canopy verification . . . . .	140
5.5.1	3D aerodynamic coefficients . . . . .	140
5.5.2	Comparison of canopy shape . . . . .	141
5.5.3	Canopy shape comparison . . . . .	143
5.6	Surf kite comparison . . . . .	147
5.6.1	3D aerodynamic coefficients of an arc wing . . . . .	147
5.6.2	Surf kite measurements . . . . .	153
5.6.3	Comparison between measured and simulated data . . . . .	155
5.7	Concluding remarks . . . . .	159
<b>6</b>	<b>Casestudies</b>	<b>161</b>
6.1	Introduction . . . . .	161
6.2	Effective cable length . . . . .	162
6.3	A cornering surf kite . . . . .	164
6.3.1	The model . . . . .	165
6.3.2	Cornering of a kite in detail . . . . .	166

6.3.3	The contribution of flexibility . . . . .	169
6.3.4	Influencing cornering performance . . . . .	171
6.4	Kiteplane stability . . . . .	173
6.4.1	Asymmetric inverted pendulum stability . . . . .	174
6.4.2	The effects of geometrical parameters . . . . .	179
6.4.3	Operational stability requirements . . . . .	182
6.4.4	Proposed design changes for stability . . . . .	185
6.4.5	Flight test results of the new Kiteplane 4 design . . . . .	187
6.5	Concluding remarks . . . . .	188
<b>7</b>	<b>Conclusions and recommendations</b>	<b>191</b>
7.1	Conclusions . . . . .	191
7.2	Recommendations to the scientific community . . . . .	194
7.3	Recommendations to kite designers . . . . .	195
	<b>References</b>	<b>199</b>
<b>A</b>	<b>Kite system definitions</b>	<b>211</b>
A.1	Frames of reference . . . . .	211
A.2	Transformation from $E_E$ to $E_T$ . . . . .	212
A.3	Transformation from $E_T$ to $E_B$ . . . . .	214
<b>B</b>	<b>Bridle line model</b>	<b>217</b>
<b>C</b>	<b>Linearization of the symmetric equations of motion</b>	<b>223</b>
<b>D</b>	<b>Linearization of the asymmetric equations of motion</b>	<b>229</b>
<b>E</b>	<b>Asymmetric control authority using shifting tow points</b>	<b>235</b>
<b>F</b>	<b>Comparison of rigid body models</b>	<b>243</b>
<b>G</b>	<b>Fitted constants</b>	<b>245</b>
G.1	Inflated tube constants . . . . .	245
G.2	Aerodynamic constants . . . . .	246
<b>H</b>	<b>Kiteplane properties</b>	<b>247</b>
H.1	Kiteplane geometry . . . . .	247
H.2	Kiteplane structure and inertia . . . . .	249
H.3	Kiteplane flexibility . . . . .	252
	<b>Samenvatting</b>	<b>255</b>
	<b>Curriculum Vitae</b>	<b>259</b>

# CHAPTER 1

---

## Introduction

---

### 1.1 Background

Compared to kites, airplanes (1903) and hot air balloons (1783) are recent inventions. Today, when thinking of flying, one envisions a seat on a Boeing 747. But in historical terms, these means of air travel have only just become available to us. Kites date back around 3000 years. That means that in all the time humans are able to create objects that fly, over 92% of that time kites were the only option.

In many respects, airplanes and gliders are all spin-off technology from kites. Louis Ferber (1862 - 1909), aviation pioneer and french army officer, stated that an airplane was nothing more than "an unanchored kite". The statement may somewhat oversimplify the specifics, but in its essence he was right. Kites and airplanes share many physics principles and challenges. Knowing this, one might wonder why today, the design of airplanes is an exact and meticulous science while the design of kites is mostly done by empirical data and rules of thumb.

The reason for this peculiarity appears mostly market driven and lies in the necessity of a design process. The design process of airplanes quickly became a very costly endeavor. Suddenly, a market opened where more and more stringent requirements were imposed upon on the system. This lead to an ever growing complexity which made a well-planned design process a necessity. Especially today, designing a new aircraft will cost many millions, if not billions of euros. The application of airplanes quickly became very serious. Public- and freight transport had put stringent requirements on aircraft and made the margins for error extremely small. With such a system, close control over the design proces is imperative in order to ensure the fulfilment of its requirements.

For kites, the more industrial applications haven't yet materialized on a large commercial scale. Even though kites were used in war scenarios and scientific experiments, most kites were simply flown for recreational purposes. Kite fabrics, rods and lines were fairly cheap. One could easily afford to try out a large number of different designs in order to find one that flew well. What exactly constituted "flying well" was left largely undefined. However, for recreational purposes such an approach may well still be favorable. It allows a natural evolution and is by far the cheapest method. One might also say that, because most kites are unmanned, there is no direct danger for loss of life in the event of a crash. But such a statement quickly becomes a dangerous one. Large and powerful kites put a large amount of tension in the lines. Careful consideration is required. With the advent of sports such as kite surfing, more stringent requirements were introduced. Materials became stronger and lighter which allowed for faster and more powerful kites.

The development of kites as a research tool for aviation and war applications in the 19th and early 20th century can be considered the first evolution of kites. The advent of kite surfing with its fast and powerful kites was to be the second kite evolution. And even though these kites have a much higher performance than the first evolution kites, they are still mostly designed like they were in the first kite evolution. The process of iterative design benefitted from better materials and other enabling technologies to yield better kites.

Nowadays, we find ourselves on the brink of the third kite evolution where kites are being used for industrial applications. These kites are fast and high performance designs which use computer control to fly them as if they were aircraft. Applications range from energy production to transportation and they put very stringent requirements on the design.

## 1.2 Thesis objective

This thesis proposes a scientific approach to the design of kites in order to have more control over the process and the eventual outcome. The objective of this thesis is threefold.

- To build the knowledge on the dynamics, structure and design of kites and kite-related systems.
- To develop the engineering tools for kite design. These tools are required to be intuitive and resource-friendly.
- To advocate proper measurements in order to both further the understanding of kites and validate the design.

The aim of this work is to benefit the kite designer directly. Kite companies are not large multi-nationals. And therefore, overly complex and resource-intense

software tools are avoided. The tools are designed to be easy to use and to run on a conventional desktop computer<sup>1</sup>. Furthermore, the knowledge on rigid body kite dynamics leans heavily on existing airplane dynamics and the measurement techniques are such that they do not require an enormous investment.

## 1.3 Thesis structure

The structure of the thesis is as follows. Chapter 2 contains the preliminaries to the work in this thesis. It starts with a discussion on the development history of the kite versus the conventional airplane. The chapter continues to explain the current kite market and the nature of the research done in this industry. Next, the subject of kites and energy generation is briefly explored. And lastly, Previous research into kites and kite-related fields is concisely laid out.

Chapter 3 Explores the rigid body dynamics of kites. The outlines are sketched of a kite model based on Newton's second law and a kite model based on Lagrangian equations of motion. Next, a comparison is made between tethered and untethered flight, based on the resulting eigenmotions. Lastly, the effects of cable length on the eigenmotions of tethered flight are investigated.

Chapter 4 outlines the specifics of a numerical kite model based on multi-body system dynamics. The chapter explains the toolbox nature of the model and outlines the three main building blocks: cables, inflated tubes and foils. The chapter concludes with a brief discussion on building the complete model.

Chapter 5 is a model verification for the model proposed in chapter 4. First, the three building block models are compared separately to measured data. Next, the shape of a three dimensional canopy is simulated and compared to measured data obtained by performing a photogrammetry analysis on an inflated kite in a large wind tunnel at the University of Stuttgart. Lastly, the simulated and measured flight performance of conventional surf kites are compared.

Chapter 6 presents a selection of case studies, using the knowledge and tools developed within this thesis. The chapter starts with a brief analysis of cable dynamics and introduces the concept of effective cable length. Next, the numerical model is used to investigate why a surf kite turns and what influences the cornering performance. The questions surrounding the cornering of surf kites has seen extensive debate among kite users and kite designers. This thesis proposes a new view on why a kite turns, based on the knowledge and tools which were developed. Lastly, the kiteplane comes under investigation using the rigid body model of chapter 3. The (then) current design (Kiteplane 3) is evaluated and its stability issues investigated. The model shows the same pendulum instability of the kite, which was also observed in flight testing. The chapter concludes with a number of design changes in order to stabilize the kiteplane. A new design

---

<sup>1</sup>Computer technology changes rapidly. With "current desktop computer" a configuration is meant with a 3Ghz Dualcore CPU and 4GB of RAM memory, running Windows XP

(Kiteplane 4) was built and tested. Flight testing shows increased lateral stability of the new design.

Chapter 7 ends the thesis with summing the conclusions and recommendations which were obtained through the course of the thesis work.

# CHAPTER 2

---

## Preliminaries

---

*The purpose of this chapter is to give a short overview of the current state of research in the fields of kites and kite related applications. Section 2.1 asks the question: what is a kite? and proposes a definition. Section 2.2 is a recount of the historical context of kites, especially in their relation to airplanes. Section 2.3 gives an overview of the kite industry, in particular the design proces. Section 2.4 focusses on one of the main applications of industrial kites: Energy generation. Section 2.5 touches on previous kite research and related fields of study, while section 2.6 closes this chapter with concluding remarks.*

### 2.1 What is a kite?

As was stated in the previous chapter, the goal of this thesis is to develop an engineering methodology for kite design. But what is a kite? What is its definition? The Cambridge Dictionary gives the following:

*An object consisting of a frame covered with plastic, paper or cloth that is flown in the air at the end of a long string, especially for pleasure.*

This definition confirms some of the preconceptions on kites this thesis will try to dismantle. Nowadays, high-performance kites are not just flown for pleasure. This thesis will show industrial applications where kites fulfill a more serious role than simple entertainment. The Oxford Dictionary expands on this definition and gives:

*[From its hovering in the air like the bird.] A toy consisting of a light frame, usually of wood, with paper or other light thin material stretched upon it; mostly in the form of an isosceles triangle with a circular arc as base, or a quadrilateral symmetrical about the longer diagonal; constructed (usually with a tail of some kind for the purpose of balancing it) to be flown in a strong wind by means of a long string attached. Also, a modification of the toy kite designed to support a man in the air or to form part of an unpowered flying machine (cf. AEROPLANE 1).*

The Oxford Dictionary does acknowledge the fact that kites can be used for other things than entertainment. However, like the definition before, the kite is seen primarily as a toy. It speaks of a "modification of the toy kite", clearly indicating the primary use of a kite as it is perceived. This thesis will aim to show that kites are not just toys. Large  $50m^2$  kites generate a pulling force of up to 600kg in the current 20kW Laddermill prototype (see section 2.4) and performance sports kites are now responsible for some of the highest sailing speeds. Kites such as these can hardly be called toys. In the 1828 Noah Webster's American Dictionary, the definition of a kite was given as follows:

*A light frame of wood and paper constructed for flying in the air for the amusement of boys.*

Suffice it to say that nowadays, girls enjoy the flying of kites as well.

From the survey of dictionaries as to the definition of a kite it became apparent that, because of the current state of kites and kite technology, a new definition is in order. This definition should not imply that a kite is only or mostly a toy. A kite is a heavier-than-air device which stays aloft by generating an aerodynamic force which is equal or greater than the combined mass of the kite and the tether, as well as the vertical component of the tether drag. Another essential aspect of a kite is that it is tethered to the ground. Its velocity vector is a vector sum of the wind velocity vector and its own velocity vector with regard to the fixed anchor point. Furthermore, a kite is able to achieve sustained flight for a certain period of time. This period of time is dependent, amongst other things, on its stability. The construction of a kite is not necessarily a frame with tensioned fabric, nor is it usually made of wood and paper. Considering these points, a new definition for kites could be formulated as:

*A kite is a tethered heavier-than-air device which is able to achieve flight by generating a resulting aerodynamic force which is countered by the mass of the device and the tension force in the tether.*

This definition is broader than the definitions obtained from the three aforementioned dictionaries and includes the type of industrial and sports performance kites which are covered in this thesis.



## 2.2 A brief history of kites

Kites have been known to man for nearly 3000 years [Fadul, 2009]. Throughout their history, kites have played a significant role in arts, religion and science. Kites are believed to have been invented in Asia. The first Chinese stories of kites are of Mo Tzu and his wooden kites amusing the crowd. Later tales tell of General Han Hsin who used kites to measure the distance to enemy fortifications. The invention of kites has an air of mystique to it. It is unknown how the invention came to be. Peter Lynn, one of the leading kite designers in the world wrote an interesting article in his newsletter of April 2005. Lynn states that for every invention, there is a gradual path leading up to the discovery. For instance, a boomerang was invented by aboriginals first throwing sticks at prey. They then discovered that the shape of the stick had an effect on its flight path. Gradually, the discovery was made that for certain shapes, the boomerang could actually swoop back towards the person who threw it. Similar paths can be postulated for other human inventions such as bows, needles and fishhooks. But for kites, such a gradual path is unknown. A kite is subject to a delicate balance of aerodynamic and gravitational effects. The system of forces is only stable for a limited number of combinations of shape, flexibility and bridle line positions. Without a proper understanding of its basic principles, the invention of a stable kite comes down to blind luck. Lynn states that due to the immensely large amount of permutations, it is somewhat of a miracle that kites were invented at all.

Kites only became known in the western world in the 13th century when Marco Polo came back from the far-east and described devices made of cloth, big enough to carry a man aloft. Man carrying kites were especially popular in Japan, centuries before the invention of airplanes. In the period from the 15th century to the beginning of the 20th century, kites became popular in the western world as well. Next to balloons, they were the only flying objects available. Leonardo DaVinci discovered in the 15th century how to span a river using a kite. In 1749, Scottish scientist Alexander Wilson used several kites, attached in a row, to measure and compare air temperatures at different altitudes. Benjamin Franklin used kites to pull boats and carriages and to experiment with electricity. And in 1901, Guglielmo Marconi used a kite to help transmit the first trans-Atlantic wireless telegraph message. Kites had become an important aerial platform for a large number of scientists. But even though kites have been tools in a number of scientific endeavors, they were never really subject of close examination themselves.

### 2.2.1 The development of the flying machine

The Wright brothers are often regarded as the first to invent the airplane. Even the Wright brothers themselves would disagree with this notion. They were the first to invent a successful airplane. But as they admitted themselves: "We stood on the shoulders of giants". The invention of the airplane goes back as far as the

work of Leonardo DaVinci. However, in that time, human flight was envisioned to mimic bird flight. Large flapping wings were considered the way to carry a man aloft. The first to ever consider a flying machine in the conventional configuration as we know it today was sir George Cayley. In 1804, in a stroke of genius, Cayley made a sketch of a hand-thrown glider which departed from the beating wing vision and adopted the fixed-wing design. Interesting to note is that kites had been using a fixed wing approach for centuries. But such a configuration was simply not perceived for human flight. It is a testament to the fact that in the minds of people at that time, kites were something entirely different than birds and flying machines. We will see later on how they grow closer in the minds of the aviation pioneers. Cayley's design was a revolution in the creation of the flying machine. Virtually every design henceforth adopted the fixed wing design.



**Figure 2.1:** *Sir George Cayley's glider (1804) [Co, 2006].*

Alexander Mozhaiski, responsible for what is called "the second powered hop" was one of the first people to realize the value of kites in the design of a flying machine. He was one of the first to experiment with kites in light of the development of human flight. Some of his kites were large enough to lift him off the ground when pulled at high speed by a horse-drawn carriage. From this point on, kites were considered a valuable research tool in understanding the mechanics of powered flight. Lawrence Hargrave from Australia invented the box kite in 1893. It was to play a vital role in the development of the flying machine. The box kite provided tremendous lift capabilities and admirable stability. On one occasion in 1894, Hargrave lifted himself more than 5 meters in the air in a mild wind using four box kites in a train configuration. In the following years, Hargrave experimented with powered flight, using box kite designs and even using box kites to carry the flying machine aloft before trying to fly it freely. But propulsion, or better yet the lack of propulsion, ensured his failure to realize powered flight. In 1899 Hargrave visited England with his family to make much needed contact with likeminded individuals. In England, he wrote a paper on box kites which was delivered to the Aeronautical Society in London. The head of this society was Percy Pilcher. Pilcher incorporated some of the box kite designs into his own triplane which he built in 1899.

Samuel F. Cody, who was a Klondike prospector, Wild West show-man and aviation pioneer designed the now famous Cody War Kite, a type of box kite which had excellent stability qualities. Patented in 1901, the British war office

became interested in using the Cody Kite as a man-lifting device for observation purposes. To convince the war office of his kite, he crossed the English Channel in 1903 using a boat, pulled along by a kite. The Cody War Kite was the first kite to be able to change its angle of attack, effectively powering and de-powering the kite. In another instance in 1902, Cody's kite is said to have reached a staggering altitude of 14000ft. It would be another decade before an airplane would reach that altitude. Research on the man-lifting Cody Kite was done between 1903 and 1906. Later on, Cody became interested in airplanes and used his kite knowledge to design and build his own aircraft. He eventually died in 1913 in a crash landing in one of his own inventions: the waterplane.

Otto Lilienthal had done extensive flight testing of gliders. The Wright brothers were aware of his exploits. Lilienthal controlled his gliders by shifting his weight and thereby changing the center of gravity. They started to investigate the matter and came up with the need for lateral control. Before the Wright brothers, only longitudinal control (pitch) and directional control (yaw) were identified to be useful for controlling a flying machine. The Wrights were the first to identify lateral control or roll as a necessary form of control by rotating the lift vector. In July of 1899 the Wright brothers tested their theory of lateral control using a kite, another instance where a kite played a crucial role in the development of the flying machine.

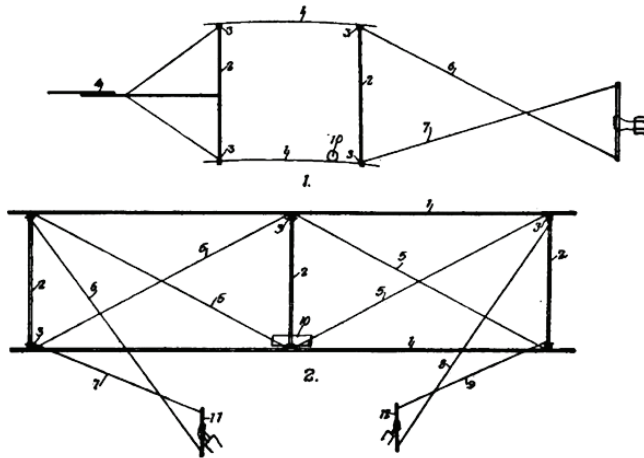


Figure 2.2: *The Wright brothers kite [Co, 2006].*

Up until their first powered flight on December 17th 1903, the Wright brothers continued to test many of their gliders as kites as well. The Wright brothers' successful flyer was a collection of cutting edge technologies. Even though many of these technologies were in their infancy, the Wrights' meticulous persistence forced a breakthrough. A breakthrough which was made possible through the use

of kites as a research tool.

### **2.2.2 The great divide**

With the exception of Otto Lilienthal, none of the aviation pioneers mentioned in the previous section had an academic education. As a matter of fact, all these people were self educated craftsmen. The designs they made borrowed little from the scientific community in the nineteenth century. Lord Kelvin, a revered scientist, stated at the end of the nineteenth century: "I have not the smallest molecule of faith in aerial navigation other than ballooning" This statement reflects the views of the scientific community on the exploits to invent a flying machine. In the nineteenth century, the advances in science were unprecedented. The atmosphere among scientists was that of supremacy. "Almost everything is known!" that was the sentiment of that day. Scientists were focussed on the physics and the mathematics while practical applications, such as the flying machine, were of little concern to them. This atmosphere of superiority stalled the scientific community into formulating very little new questions. The craftsmen, however, had plenty of questions. But a great divide existed between the scientists who struggled to understand the physics and the craftsmen who tried to design and build things, and make them work. This greatly hampered the development of the flying machine.

During the exploration of the flying machine in the nineteenth century, much of the theory needed to design a successful airplane was already known. Bernoulli's law, Navier-Stokes equations (not the solving), Vorticity (generation of lift), principles of friction drag and theory of laminar and turbulent flow had all been extensively explored. But unfortunately, the craftsmen attempting to design and build the first aircraft had no knowledge of this. As a matter of fact, the mature state of fluid dynamics contributed almost nothing to the development of the flying machine. Nowadays, aeronautical researchers in the academic community, researchers in government laboratories and designers in the aerospace industry all work closely together, optimizing the technology transfer between all parties through conferences and scientific publications. Such a situation is still not in place for kites. As a matter of fact, the community around kites more closely resembles the situation as it was for airplanes at the end of the nineteenth century. With regards to kites, a lot of applicable scientific theory and research tools are already available. Cable mechanics, aero-elastics, computational fluid dynamics and material sciences have reached a mature state. Yet, these powerful tools are rarely used in the development of kites.

### **2.2.3 The turning point**

At the end of the nineteenth century, researching flying machines was not a popular endeavor. It was viewed by the public as the exploits of mad men. Therefore, one of the biggest hurdles in the development of the airplane was not so much

the science, but the credibility. It is well known that credibility will pull people of different specialties on board to contribute. The lack of credibility creates isolation and makes existing expertise inaccessible. This was the situation for the airplane during the nineteenth century, and it is the situation for kites today. The craftsmen working on airplanes grew more and more disillusioned by the lack of interest from the scientific community and grew more frustrated by the fragmented nature of the knowledge they developed. In order to establish credibility, they employed the discipline of peer evaluation and widespread publishing of technical journals. As the number of craftsmen working on flying machines grew, and as the amount of knowledge grew, there was an increasing demand for a centralized organization. The first was the Societe Aerostatique et Meteorologique de France, founded in Paris in 1852. But by far the most important was the Aeronautical Society of Great Britain, founded in London in 1866. With the formation of this society, a formal mechanism for the establishment of technical credibility was in place. Through the Aeronautical Society, many important discoveries such as the effects of aspect ratio and the performance of cambered airfoils were available for all who were studying human flight. The establishment of the Aeronautical Society was a pivotal moment in the development of the flying machine. Through this establishment, the occupation of aeronautical engineer was first formulated. And even though nowadays, most aeronautical engineers are University educated, their profession was not established by the academic world, but by craftsmen and inventors of the late nineteenth century.

A similar establishment for kites is not in place today. Not even a sub-section within existing scientific societies devoted to kite research exists. As a matter of fact, searching for publications on kites within existing conferences and journals will yield limited results. And even though today kites actually constitute a business of significant size, within the scientific community there seems little interest to pursue its development. A reason for this seems to be the lack of credibility. Even today, kites are mostly seen as toys. Or at best, a means for adventurous people to pull them along the shoreline on a surfboard. It is hardly seen as a serious and valid research topic even though the mechanics behind a kite can be considered a challenge, its applications seem only limited by imagination and a market for existing applications is already in place.

## **2.2.4 The situation today**

Today, we are at a pivotal point in the life of the kite. The advent of sports such as kite surfing has created a surge in the application and research into kites. At this point, a third evolution can be seen. This evolution carries the kite from its current use to more industrial applications. Generation of clean energy and propulsion of ships put new requirements on the design of kites. Evermore sophisticated materials and construction principles allow the kite to grow to large proportions and create the possibility unprecedented control.

The airplane owes its existence to the kite. From the moment the first powered

airplane took off at Kitty Hawk, the kite took the backseat with regard to scientific research. This situation has allowed the airplane to steam ahead at full throttle, while the kite lagged behind. Hurt by a lack of direct applications, the kite slid back into the realm of toys, its contribution to aviation almost forgotten. But a hundred years after the invention of the airplane, the kite is back. In its future, a number of serious applications which provide clean energy and transportation. The kite is back and it is in dire need of attention from the scientific community in order to make the next leap. A leap which aircraft took well over a century ago.



**Figure 2.3:** *The three kite evolutions.*

## 2.3 Current state of the kite industry

Currently, the kite industry focus is mostly on entertainment and sports. Kites for entertainment include the toy kites for children and the large kites used for exhibitions. Kites used for sports are designed less for visual appearance and more for performance. These kites are used for applications such as kite buggying and kite surfing and are roughly sized between  $2m^2$  and  $16m^2$ . These performance kites bear the most resemblance to the industrial kites needed for, e.g. energy generation and therefore, the focus of this section lies with these performance kites.

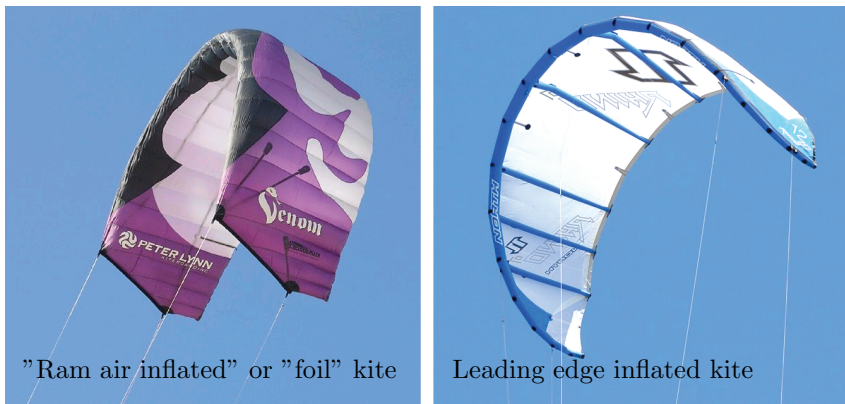


**Figure 2.4:** *The two types of kites: the ram-air inflated or foil kite [www.Airxpress.nl, n.d.] and the Leading edge inflated kite [Augustino, n.d.].*

Kites used for kite surfing generally fall into two categories. The first are the "foil", or "ram air inflated" kites. These kites are completely made out of slack fabric and rely on ram air pressure to maintain their shape. They are extremely flexible and quickly loose shape when their apparent velocity (the velocity of the kite with respect to the surrounding air) becomes too low. The second group of kites are the "leading edge inflatable" kites. These kites use inflated bladders to give their structure a certain amount of rigidity. This allows them to maintain their shape at low velocities, but it also makes them heavier due to the internal bladders.

The design of conventional surf kites today is not a highly structured design process such as we see in the aerospace sector. This is not necessarily a bad thing. Kites are cheap to build and simply trying out different configurations will yield a solution faster than a detailed design process. The process of kite design today bears a striking resemblance to a trial-and-error process. However, certain distinct differences are to be noted. A trial and error process does not investigate why a solution works. It shoots blindly and finds "A" solution, not "THE" solution. In

the kite industry, solutions are studied and evaluated, albeit in a limited fashion.

The design of kites, therefore, more resembles a Darwinian process of evolution by natural selection. Lets say, in the year  $N$ , a kite company starts its design of the new kites for the year  $N+1$ . It takes a look at the feedback it got from the previous year (year  $N$ ) and assesses what changes need to be made. Problems occur due to the inconsistent nature of the feedback. Feedback is generated by professional testriders and customers who state their findings in an arbitrary and often conflicting manner. This makes it difficult to formulate the new requirements. Therefore, the changes (or "mutations", to stay with the Darwinian analogy) are poorly structured and can lead the designer down the wrong path. In Darwinian evolution by natural selection, the mutations occur randomly. In the kite industry they are poorly structured. So there is a difference in how the mutations are brought about. But in practice, they both tend to lead to an enormous diversity of prototypes. These prototypes are then put through a natural selection type of process. Professional riders take them out and test fly the kites. This process eventually leaves the designer with a small number of kites from which the kites of year  $N+1$  are "bred". The crux is in the question: What design/mutation is the "fittest"? This is what drives the selection. For an engineering process, it is where the objective is defined.

This type of process, although mostly unstructured, has allowed the kite industry to make remarkable progress. This progress has been possible due to the fact that kites are cheap to build and prototyping is quickly done. Especially in the early days of kite surfing, finding "A" solution enabled a kite company to build a new generation of kites. The realm of possibilities was mostly unexplored. Nowadays, a trend is visible where more and more prototypes are needed to find "A" solution. Kites are becoming more complex, increasing the amount of variables. In discussions with kite designers such as Peter Lynn, Henry Rebeck and Don Montague it became apparent that they have warehouses full of prototypes which they simply don't have time for to test and evaluate. This fact, together with the poorly defined requirements resulting from ambiguous flight testing, has the potential to stagnate the innovation in the kite industry.

In many respects, the surf kites are moving more towards the industrial kites used for energy generation. These industrial kites already have to adhere to very strict requirements, increasing the complexity of the design process. For these types of kites, the conventional kite design process would lead to an unmanageable amount of prototypes. Furthermore, the lack of control over the output of the design process increases the project risk and project cost beyond acceptable limits. Therefore, an engineering methodology for kite design is required which gives the designer more control over the outcome. This engineering approach requires knowledge on the dynamics and structure of kites, simulation or virtual prototyping capabilities and parameter measurements for model validation and prototype evaluation. These three items are visualized in figure 2.5.

The arrows in figure 2.5 indicate the fact that the three items are closely related. For instance: a better understanding of kites leads to better simulation



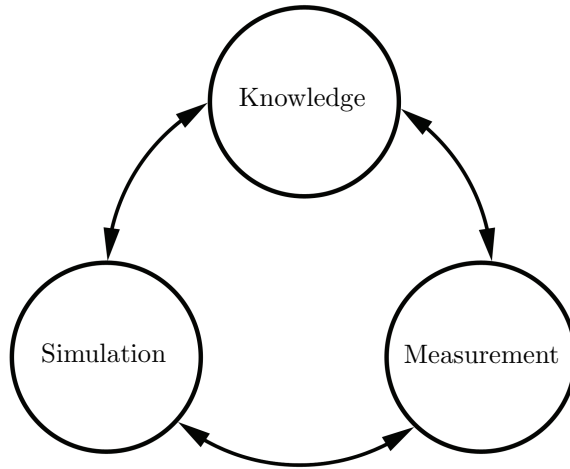


**Figure 2.5:** *The three prerequisites for an engineering approach to kite design.*

models. But also, good models can lead to a better understanding of kites (see section 6.3). The interaction between these items is what makes this type of engineering approach work. And in the continued development of the controlled kite system, the items in figure 2.5 become absolutely essential.

## 2.4 Kites and energy generation

In this section, one of the most promising industrial applications of kites is explored. In contrast to the past century where most of the generated energy comes from a single type of technology (namely fossil fuel burning plants) the future is expected to have a far more diverse energy mix using solar, wind, tidal and biomass technologies, to name but a few. This increased diversity of technologies is also expected to create a far more de-centralized energy generation infrastructure. The most extreme scenario projects energy generation on a per-zipcode or even per-address basis. For instance, houses with solar panels which generate the required energy for that particular house. In a far more diverse energy landscape there is an increased potential for innovation. One of the innovative ideas is to use the stronger winds at high altitude to generate electricity.

### 2.4.1 High altitude wind power

The winds at high altitude are far stronger and less turbulent than they are at low altitude. This means that current wind turbine technology generates energy using the worst possible conditions, namely those close to the ground. Archer

& Caldeira [2009] analyzed 28 years of wind statistics at altitudes between 500m and 12000m and established that there is an enormous amount of energy in the winds at high altitude. A number of areas such as over eastern China and north-eastern Africa were located where the mean value of the energy density at 10000m altitude was greater than 10kW per square meter. Archer & Caldeira [2009] calls this value "Unthinkable near the ground". Awareness of the value of the winds at high altitude has been steadily growing over the last decade. The number of organizations involved in high altitude wind power has grown from 3 in the year 2000 to more than 40 today (2010) [Furey, 2009]. The concepts under investigation at different companies and Universities are extremely diverse. However, they all share the same principle of "some sort of lifting body tethered to the ground". The lifting body is required to reach the high altitude winds and the ground-tethering is required in order to bring the energy down to the ground. These are the basic prerequisites of high altitude wind power and they show their kinship to conventional kites.

## 2.4.2 The Laddermill

The Laddermill [W. J. Ockels, 2001] is a novel concept which uses kites at high altitude to generate energy. Kites generally ascend without effort. In order to get them down, one has to physically pull them from the sky. For aircraft, the exact opposite holds true. An aircraft needs large engines to climb but can glide down under idle power. The kites in the Laddermill are a combination of kites and airplanes. Ideally, they ascend as kites and descend as gliding airplanes. While the kites ascend, they pull a cable off a drum, spinning the drum and the generator attached, thereby generating electricity. On the downstroke, kites are reconfigured for a lower pulling force and descend back towards the ground.

Initially, the Laddermill was envisioned as a large rotating loop of kites. The kites on one side would fly as kites and pull hard on the line, the kites on the other side of the loop would go into a gliding mode, minimizing their tug force on the main line. Early on it was established [Lansdorp & Ockels, 2005a] that the rotating loop, or rotating Laddermill, was an extremely complicated system requiring a number of enabling technologies which were not available at that time. The choice was made to start with the simplest kite power system and develop the enabling technologies, such as controlled kites, from there. This simple system became a single kite on a single line attached to a single ground station. This system would generate energy as the kite ascended. When the maximum altitude was reached, the kite would reconfigure for gliding and be pulled back down by the ground station. This downstroke would cost energy, instead of generating it. But because the tension in the main line was far less on the downstroke than it was on the upstroke, a nett amount of energy was produced at the end of a cycle. This intermittend kite power system was dubbed "the pumping Laddermill" and it has been the basis for the Laddermill project ever since. Figure 2.6 shows the two Laddermill concepts side by side.

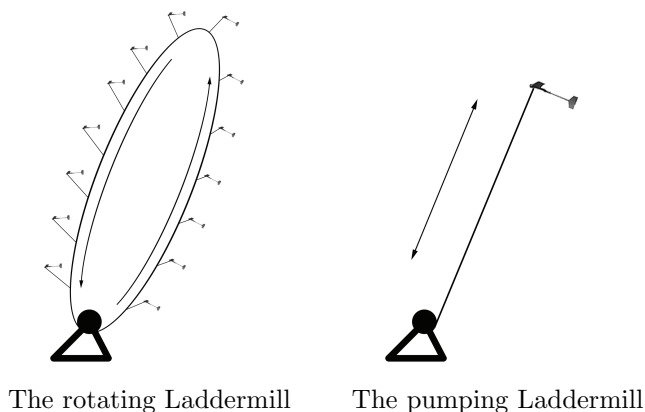


**Figure 2.6:** *The two Laddermill concepts.*

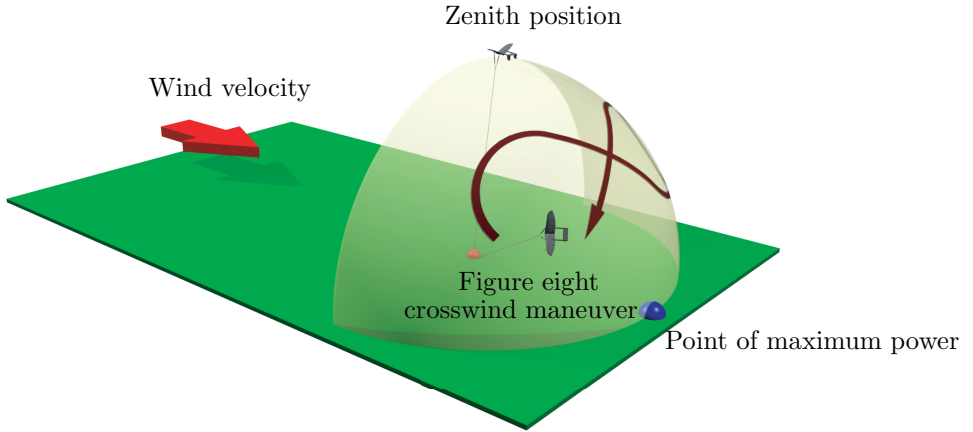
The pumping Laddermill has as a distinct disadvantage that it generates energy in an intermittent fashion. During the downstroke, no energy is generated. This discontinuous character of the system makes it difficult to connect it to the power grid. This problem can potentially be overcome by placing a number of these systems together and timing their operation in such a way that the combined output is continuous, like it were a very large piston engine.

### 2.4.3 Principle of crosswind power

When a kite flies high and straight downwind, it is said to be in the zenith position. In this position, the kite has no velocity with respect to the earth. It flies at a relatively low flight path angle and its tug force is relatively low. This region is where most toy kites will fly, gently coasting on the wind. For traction kites, however, a large tug force is of great importance. The tug force of the kite can be greatly increased by flying the kite from left to right through what is called "the wind window", an imaginary quarter sphere, as indicated in yellow in figure 2.7, where steady flight is possible.

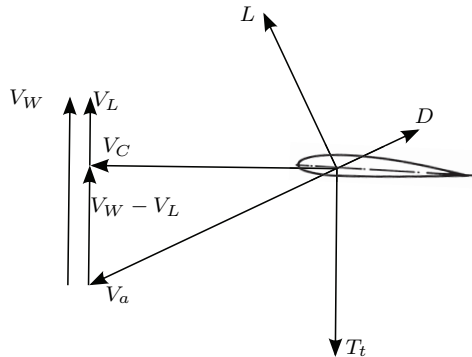
The idea of using crosswind motion to increase the force in the tether stems from Loyd [1980]. Moving in the plane normal to the wind vector allows the apparent wind velocity to become larger than the wind velocity itself. Since the force in the tether is more or less proportional to the square of the apparent wind velocity, this crosswind motion causes a strong increase in tether force.

Figure 2.8 shows the forces and velocities on a weightless kite in crosswind motion. This particular situation exists in the point of maximum power, indicated in blue in figure 2.7. Equilibrium of forces is obtained by the lift  $L$ , the drag  $D$  and the tether tension  $T_t$ . The velocities shown are the wind speed  $V_W$ , the speed



**Figure 2.7:** A graphic representation of the wind window and a crosswind pattern.

of the line  $V_L$ , the crosswind velocity of the kite  $V_C$  and the apparent velocity of the kite  $V_a$ .



**Figure 2.8:** Forces and velocities on a kite in crosswind motion.

In figure 2.8  $V_L$  is parallel to  $V_W$  and  $V_C$  is perpendicular to  $V_W$ . Because  $T_t$  is parallel to  $V_W$ ,  $D$  is parallel to  $V_a$ ,  $L$  is perpendicular to  $D$  and  $V_W$  is perpendicular to  $V_C$ , the following relation can be obtained for the apparent wind velocity of the kite:

$$V_a = (V_W - V_L) \left( \frac{L}{D} \right)_K \quad (2.1)$$

where  $(L/D)_K$  is the lift over drag ratio of the kite. because  $V_a$  and  $V_C$  are

approximately equal in magnitude, the lift force can be defined as:

$$\begin{aligned} L &= C_L \cdot \frac{1}{2} \rho V_a^2 S \\ &= C_L \cdot \frac{1}{2} \rho (V_W - V_L)^2 \left( \frac{L}{D} \right)_K S \end{aligned} \quad (2.2)$$

where  $C_L$  is the lift coefficient,  $\rho$  the air density and  $S$  the projected surface area of the kite. From equation (2.2) can be seen that the lift increases with the square of the lift over drag ratio. Furthermore, Loyd [1980] assumes that  $T_t$  is parallel to  $V_L$  and that  $L$  and  $T_t$  are approximately equal in magnitude. The power produced can now be given as:

$$P = C_L \frac{1}{2} \rho V_W^3 S \cdot F \quad (2.3)$$

where  $F$  is a function describing the operational mode of the kite. In this case the kite is flying in crosswind motion, which is thought of as a useful operational mode for the Laddermill [Lansdorp & Ockels, 2005a]. Loyd [1980] assumes that the inclination angle with the earth's surface is zero and that the kite is in perfect crosswind motion (indicated in blue in figure 2.7). The equation  $F$  for crosswind motion is given by:

$$F_{crosswind} = \left( \frac{L}{D} \right)_K^2 \left( \frac{V_L}{V_W} \right) \left( 1 - \frac{V_L}{V_W} \right)^2 \quad (2.4)$$

The maximum value of this relation is:

$$F^{\max} = \frac{4}{27} \left( \frac{L}{D} \right)_K^2 \quad (2.5)$$

which occurs at,

$$V_L/V_W = 1/3$$

$F^{\max}$  is again dependent on the square of the lift over drag ratio of the kite. So Loyd [1980] concludes that the  $(L/D)_K$  is the parameter to maximize to extract the most wind energy in crosswind motion.

## 2.4.4 Kite requirements

Using cross wind power allows the kite energy system to fly with the maximum allowable wing loading, independent of the actual wind velocity (within operational limits). For a wind turbine, this is not possible and therefore, a wind turbine will produce less power in lower wind speeds. The kite power system is far more flexibility in that respect. It has the vertical freedom to seek out regions of high wind velocities and it can supplement its power output by flying cross wind maneuvers.

As was shown in the previous section, the effective lift over drag is lowered as the cross wind factor is increased. This puts an important requirement on the design of energy generating kites. In order for the effective lift over drag to not become too small during cross wind sweeps, the kite needs to have a high lift over drag during symmetric flight to start with.

Another important requirement stems from the reel-in phase. During the reel-in phase, the kite should produce a low tug force on the main tether. A high tug force translates directly into a loss of energy. The capability of a kite to fly at low lift values is called the "depower" capability. Ram air inflated kites are generally unsuitable for high depower manoeuvres because they rely on the tension in the canopy to maintain their shape. A fully depowered kite has no tension in the canopy and for a highly flexible structure like a ram air inflated kite, this means a complete loss of shape and a potentially unrecoverable flight situation. Leading edge inflatable kites are more suited for high depower flight due to their ability to maintain their shape.

### 2.4.5 The kiteplane

From the realization that an ideal kite for energy generation can fly both as an airplane and as a kite, the Kiteplane was first conceptualized in Breukels [2003] and later evolved in Breukels & Ockels [2005] and Breukels [2005]. The initial application of this type of kite was as a high-altitude kite. As part of the KitEye project [Breukels, 2005] initial concepts were envisioned to break the world altitude record for a single kite on a single line. The motivation behind this project was to explore the field of high altitude kites as part of the Laddermill project. The philosophy behind its topology was that a kite which can fly as a kite and as an airplane needs the basic configuration of a conventional aircraft and the low weight characteristics of a kite. Furthermore, its depowered flight required it to exhibit a certain amount of rigidity, independent of the tension in the bridle lines or the canopy. Lastly, in order to properly operate under high cross wind conditions, its lift over drag should be high enough not to cause problems with the magnitude of the resulting elevation angle. Initial tests were performed on small foam models (Kiteplane 1) as presented in figure 2.9

The Kiteplane 1 from figure 2.9 was tested successfully. Control surfaces were added in the wingtips and on the horizontal stabilizer. Due to the low drag of the kite it was very volatile therefore difficult to control [Breukels, 2005]. An error in piloting the kite would quickly result in a crash. Any crash the kite endured immediately caused significant damage. Furthermore, the continued use of a foam structure would limit the ability to transport the scaled up versions of the kite. The need for durability and stowability during transport quickly led towards the principle of inflatable structures.

Subsequent versions of the Kiteplane were scaled up from the original foam kite and built as inflatable structures. This allowed the kite to be deflated and rolled up for transport. The first inflatable Kiteplane (Kiteplane 2) was built



**Figure 2.9:** *An early version of the Kiteplane made from Eperan PP (Poly-Propylene) foam.*

in-house at ASSET. It had a 4-meter wingspan and weighed between 2 and 2.5 kilograms, depending on bridle lines and control surfaces. Figure 2.10 shows this kite in flight.



**Figure 2.10:** *An early version of an inflatable Kiteplane.*

Kiteplane 2 has a relatively large dihedral angle that provides roll stability in sideslip. This is also the reason for the relatively small vertical tail planes, because they prevent sideslip by pointing the nose in the apparent wind direction. Furthermore, the camber in the airfoil is a direct result of the pressure distributions on the upper and lower surface. This Kiteplane uses an inflated beam at the nose of the airfoil and a single layer of fabric as the wing canopy. This configuration is known as a "single membrane airfoil" [Maughmer, 1972].

In 2008, Kiteplane 2 was mounted in a windtunnel to investigate its aerodynamic properties. The kite was hung upside down, because in this way gravity will keep it in place when the windtunnel is turned off. During the test, the forces in the lines are measured as well as the shape of the airfoil. Using photogrammetry the shape of the airfoil can be reconstructed after the test by post processing the data. The data was later used for model validation in section 5.5.2.

With increased complexity of the subsequent Kiteplane iteration, production in-house was taking up too much time. Therefore, the production of experimental kites was outsourced to Hong-kong-based Lam Sails. Lam Sails has extensive experience in the production of kites and parafoils and they indicated to be very interested in producing new experimental configurations. The subsequent Kiteplane 3 was scaled up to a wing area of 6 square meters and now had a double canopy forming the top and the bottom of the airfoil. This configuration is known as a "Double membrane airfoil" and it drastically reduces the pressure drag of the wing [Maughmer, 1972]. Further analysis of Kiteplane 3 can be found in section 6.4. Figure 2.11 shows this Kiteplane in flight.



**Figure 2.11:** *The double membrane airfoil Kiteplane in flight.*

For high altitude kiting, the maximum lift coefficient and the maximum  $L/D$  were regarded as most important [Breukels, 2003], as well as simplicity and manufacturing ease. It is for this reason that this concept with a straight but slender wing was chosen for further development. Since no payload needed to be carried in a fuselage, the two smaller diameter tail booms were preferred over a conventional fuselage because of better structural and aerodynamic properties. Structurally the tail booms are superior in all tail loads except for the bending load caused by the horizontal tail plane. Aerodynamically the tail booms interfere less with the



main wing than a larger diameter fuselage would. Secondly, the tail booms act as end plates for the horizontal tail plane and therefore increase the apparent aspect ratio.

Another important motivation for the use of an airplane like kite was that airplane theory is well developed, while kites were still not very well understood. Because the kite needed to go through some research and development to beat the altitude record, it was believed that airplane theory could help in the process. However, to be able to use airplane theory for a kite, it needs to be as similar as possible. Also for control it is convenient to have an airplane like kite, because of the extensive knowledge and experience on airplane control. Moreover, to reach high altitudes the kite should be connected to a single line, which means that conventional kite control with control lines is not an option.

In recent years it has been realized that in essence the requirements for the altitude record kite are not very dissimilar to the requirements for a lifting body for the Laddermill. A single line, high lift and  $L/D$ , a safe and light inflatable structure, all features that apply very well to the requirements for a lifting body on a Laddermill. Because of this, the main focus of the Kiteplane today is to become an efficient and effective lifting body for the Laddermill.

## 2.5 Previous research

Up to recently, limited research has been done on kites. No kite-specific research journals exist and only recently the first conferences on kites have been held such as the Kite Dynamics Conference 2009 held at the Faculty of Aerospace Engineering (TU Delft). Subsequently, publications with regard to kites are sparse, but some notable contributions have been made. The following section gives a brief overview of previous research on kites and kite related topics.

### 2.5.1 Materials and structures

Research on lightweight fabric materials and constructions has been extensive. Although very little of that research is geared specifically towards kites. The inflatable structures principle is often employed when designing and building kites and it has seen a great deal of research effort.

Inflatable tubular structures are a subgroup of air-inflated structures. Air-inflated structures, as opposed to air supported structures, consist of a closed envelope of pressurized gas. The pressured gas introduces a pre-stress which allows the membrane or thin shell structure to bear compressive loads. Veldman [2005a] positioned inflatable tubular structures together with dual-wall cushion structures as a high-pressure inflatable structure as opposed to air-supported structures, which require continuously replenishment of the inflation gas and operates at a lower pressure. This is not to say that a tubular structure can only function at high pressure. Breuer & Ockels [2007] speaks of tensairity which is a tubular structure

supported by a separate compression element and tension wires. The structure is in fact an air-inflated structure as it has a closed envelope, but it operates at a much lower pressure than a conventional tubular inflatable structure. Applications for tubular inflatable structures range from inflatable wings [Veldman, 2005a] [Brown et al., 2001] [Main, 1993] to habitats [Veldman, 2005a] and space-based antennae and solar reflectors [Jenkins, 2001]. The decreasing cost of high-strength materials allows the concept of tubular inflatable structures to expand to other areas. Areas such as kite surfing have seen an enormous surge as a result of modern materials science.

Mechanical behavior, in particular bending of inflated beams, has been subject of study for the last several decades. Several models for bending behavior have been published by Comer & Levi [1963], Main et al. [1995], Adler et al. [2000], Fichter [1966], Stein & Hedgepeth [1961] and Webber [1982]. All these models introduce three distinct states an inflatable structure can exist in.

The first state is the unwrinkled state in which the pre-stress, as a result of inflation, is larger than the compressive stress due to bending or torsion in every location of the inflatable structure.

The second state is that of the wrinkled state. In this state a location or locations exist where the compressive stress due to the externally applied load has become larger than the tensile pre-stress due to inflation. The different models treat the transition from unwrinkled to wrinkled in different ways. Comer & Levi [1963], Stein & Hedgepeth [1961] and Webber [1982] state that the wrinkling threshold is passed as soon as the principle stress becomes zero. In this model, the structure is treated purely as a membrane which has no capability to carry compressive loads whatsoever. Main et al. [1995] treats the wrinkling threshold based on a strain criterion, meaning that wrinkling will only occur as soon as the principle strain has become zero. This factors in the effect of contraction as a result of stresses in perpendicular direction. However, a problem occurs for materials with a Poisson's ratio of 0.5. For these materials, the theory of Main et al. [1995] gives a bending moment of zero.

The third and last state an inflatable structure can exist in is the collapsed state. In this state, the wrinkles have grown from the point of the lowest principle stress ([Comer & Levi, 1963], [Stein & Hedgepeth, 1961], [Webber, 1982]) or principle strain [Main et al., 1995] to a point past the neutral line of the beam. In this situation, a cross section exists within the structure where no more compressive stresses can be carried. This results in a local collapse of the beam and a sudden and large increase in deflection. Figure 2.12 shows the load-deflection curve of an inflatable tube with the three states identified.

Materials for making lightweight tubular inflatable structures have to be both light and durable when applied to kites. Furthermore, they have to be able to cope with the stresses of inflation and flight and have to be flexible enough to be deflated and stowed. [Verheul et al., 2009] takes a look at materials and joining methods suitable for kite structures. Materials generally fall in two categories: woven materials and laminates. Woven materials are cheap to make but cannot act as

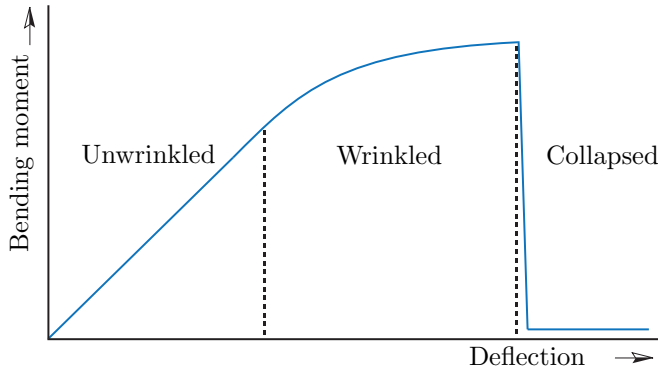


**Figure 2.12:** *The three states of an inflatable structure.*

a gas barrier for pressurized air. Tubular structures made out of woven materials need an extra inner bladder, generally made from thermoplastic polyurethane, in order to contain the inflation gas. Laminate materials consist of high tensile fibers laminated in a film material such as Mylar. These type of materials are able to fulfill both functions: structural integrity and gas containment.

Laminate materials are thus considered to enable lighter inflatable structures. However, joining them together can only be done by welding or bonding. In the kite industry, these types of joining techniques are rarely used. Woven materials can also be stitched together. The kite industry leans heavily towards the stitching process. Changing to a different joining process is a costly endeavour because the production facilities in China, India and Vietnam have only experience with sewing machines.

## 2.5.2 Kite aerodynamics

Leading edge inflatable kites all boast the same airfoil principle. The leading edge consists of an inflated beam. From the top of this beam, a fabric canopy spans to the trailing edge wire. This type of airfoil is commonly known as a sail wing. The fabric canopy is flexible and the resulting airfoil camber is a function of the pressure distribution over the upper and lower surface. Flexible sail wings have been subject to extensive research for half a century [Sweeney, 1961]. Nielsen [1963] Investigated the aerodynamic characteristics of two-dimensional flexible airfoils or sails without a leading edge tube. He used thin-airfoil theory to obtain the shape of the camber line as a function of angle of attack. Nielsen [1963] Found that there are stable camber line shapes for which there is no stagnation point. Experimental results partly agreed with the theory and he attributes the discrepancies

to fabric porosity and boundary-layer separation. Simultaneously Thwaites [1961] published work which was comparable. Fink [1969] And Fink [1967] launched an investigation into the aerodynamic characteristics of two full scale models with double membrane airfoils: one with an aspect ratio of 5.9 and one with an aspect ratio of 11.5. Tests were performed in the Langley wind tunnel facility in order to analyze (1) lift and drag, (2) static longitudinal and lateral stability and (3) lateral control. They found that a sail wing is able to produce comparable lift-drag ratios as a conventional hard wing. At low angles of attack, the sail wing obtained unusually steep lift-curve slopes. Interestingly Fink [1969] found that the shape of the leading edge nose only had a small effect on the characteristics of the wing. A round leading edge attained slightly higher lift coefficients but had a lower lift over drag ratio. At the Delft University of Technology, an experimental investigation was started into the low speed aerodynamic characteristics of a two-dimensional sail wing. Boer [1980] And Boer [1982] looked at airfoils with adjustable slack of sail to analyze its influence. Furthermore, a numerical model is presented which estimates the performance of both slightly and highly cambered double membrane airfoils. One of the most prominent conclusions was that the sail wing obtained a higher maximum lift over drag ratio than its rigid counterpart, which had a rigid circular plate with a 10% camber instead of a flexible sail. It was established that the higher lift over drag ratio can be attributed to the higher lift due to a higher camber and not due to a lower drag. Lastly, Maughmer [1972] performed extensive research into sail wings and presents a comparison between different sail wing configurations. It is shown that sail wings have very competitive characteristics compared to conventional hard wings, especially in low speed applications. Due to the variable camber, a higher maximum lift over drag ratio can be attained. Furthermore, it is concluded that sail wings have a fairly slow rise in drag coefficient, and consequently a slow decrease in lift to drag ratio with increasing values of the lift coefficient. The research also shows that double membrane airfoils exhibit a maximum lift over drag ratio roughly twice that of single membrane airfoils.

### 2.5.3 Tether theory and models

Imagine a single kite on a single tether. The tether force on the ground ( $T_G$ ) is not equal to the tether force near the kite ( $T_K$ ). The tether force near the kite is equal to the resultant aerodynamic force of the kite. In order to find the tether force at ground level, the aerodynamic forces (mostly drag) and gravitational forces on the tether need to be added to  $T_K$ . Figure 2.13 displays the problem, with distributed tether forces  $q_D$  and  $q_g$  denoting respectively the aerodynamic and gravitational forces. The path along the tether is described by coordinate  $s$ .

The force in the tether at ground level can be calculated using equation (2.6).

$$\mathbf{T}_G = -\mathbf{T}_K - \int_0^l (\mathbf{q}_g(s) + \mathbf{q}_D(s)) ds \quad (2.6)$$

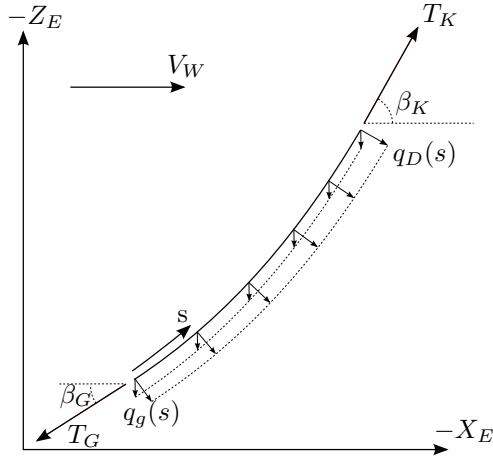


**Figure 2.13:** Free body diagram of a tether.

The force  $T_K$  is the tether force at the kite's end and considered known in this section, the force  $T_G$  is the force at the bottom end and the one to solve for. The distributed force  $q_g$  denotes gravity and the aerodynamic forces are denoted by  $q_D$ . To be able to find expressions for these distributed forces, the tether is discretized into a chain of rigid elements. Figure 2.14 displays an element of the tether with the local orientation angles and the forces acting on it. The centripetal acceleration necessary for the curved path of the tether when it rolls out, as well as any elastic or bending resistance effects of the tether are neglected. Moreover, it is assumed that the kite is flying straight downwind, so that the situation can be evaluated in 2D.

With the relations in figure 2.14,  $T_G$  can be found by stepwise integration over the tether elements, starting at the kite's end. The boundary conditions at the top of the last element are:

$$\begin{aligned} T_i &= T_K \\ \beta_i &= \beta_K \\ \alpha_T &= \arctan\left(\frac{L}{D}\right) \end{aligned}$$

However, these conditions do not completely define the tether. An additional parameter is required to identify the end of the tether, or ground point. Parameters suitable for identifying the ground point are: altitude of the kite, downwind ground distance of the kite or the tether angle  $\beta_G$ . Through  $\beta_i$  all these parameters can be linked to the tether path coordinate  $s$ . With either of these parameters set, the tether is uniquely defined by  $\beta_i$  for  $i = 1..N$ . Where  $\beta_{i-1}$  as well as  $T_{i-1}$  are merely the result of the zero resultant force condition for element  $i$  (with

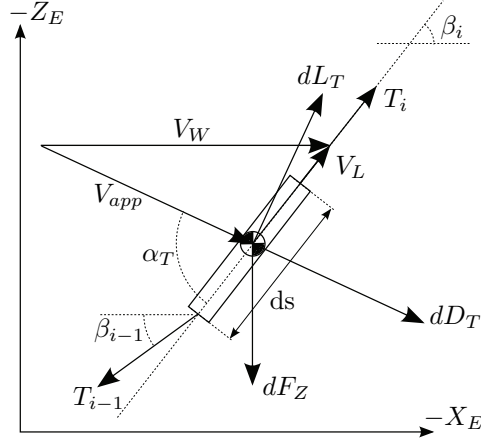


**Figure 2.14:** Forces on tether element  $i$ .

centripetal acceleration neglected).

The incremental lift and drag forces in figure 2.14 are defined by Eqs. (2.7) and (2.8).

$$dL_T = \frac{1}{2}\rho V_{app}^2 C_{L_T} d_T ds \quad (2.7)$$

$$dD_T = \frac{1}{2}\rho V_{app}^2 C_{D_T} d_T ds \quad (2.8)$$

According to Hoerner [1965b], the lift and drag coefficient on a tether at a subcritical Reynolds numbers can accurately be approximated by Eqs. (2.9) and (2.10) respectively.

$$C_{L_T} = 1.1 \sin(\alpha_T(s))^2 \cos(\alpha_T(s)) \quad (2.9)$$

$$C_{D_T} = 1.1 \sin(\alpha_T(s))^3 + 0.02 \quad (2.10)$$

The remaining incremental gravitational force is given by equation (2.11).

$$dF_Z = \frac{1}{4}\pi d_T^2 \rho_T g ds \quad (2.11)$$

Practical tether models are available in various complexities. The simplest one is a rigid one dimensional massless rod, however this is a very crude representation

of reality. On the other hand a continuum mechanics model of the tether adds unnecessary complexity. The aim is for the least complex model that describes all the relevant behavior.

The aspects of tether physics that are relevant for kites in general and the Laddermill in particular are listed below.

- Variable length tether (for rolling in and out)
- Influence of aerodynamic forces
- Increased length due to sagging
- Inertia of the tether

A model that takes these aspects into account is the lumped mass model as presented by Williams et al. [2007]. The basic idea of this model is displayed in figure 2.15.

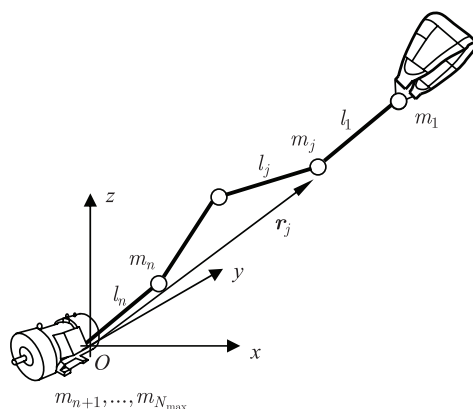


**Figure 2.15:** *Lumped mass tether model by Williams et al. [2007].*

In this model the tether consists of a series of point masses connected with massless inelastic rods. The length of the tether is varied by adding or removing elements, the length change is made continuous by resizing the first element. The aerodynamic forces are calculated for the rods and then divided over the two adjacent masses. These masses account for the inertia of the tether and their motion follows from Newton's second law, with the inelastic rod connections inserted as constraints in the equations.

## 2.5.4 Kite structure models

This section provides an overview of various kite models similar to Williams, Lansdorp, Ruitenkamp & Ockels [2008]. The models are discussed in an order

of increasing complexity. The equations of motion of the models are omitted because the purpose of this section is to give a qualitative overview and comparison between the models.

**Point mass model.** This is the simplest representation of a kite. It covers the translational dynamics, but attitude changes are instant. This means all forces act though the same point. The drag acts in the direction opposed to the apparent velocity and the lift vector is normal to this apparent velocity. The tilt angle of the lift vector is usually defined as a pseudo control variable. Point mass models are suitable for rough trajectory and performance analysis, but not of much use in control design of a flexible structure.

**Rigid body model.** In this model the point mass is replaced by a rigid body, which includes attitude dynamics. For this reason it is often called the 6 Degree Of Freedom (DOF) model, with 3 translational and 3 rotational degrees of freedom. This type of model is used in most flight dynamics and control studies of regular aircraft [Mulder et al., 2007]. The quality of these models depends strongly on the implementation of aerodynamic forces. The equations of the rigid body model are frequently linearized and converted to a state space representation, where the aerodynamic forces are present in the form of stability derivatives [Mulder et al., 2007].

**Flexible body model.** This model is an extension of the the rigid body model. It allows the body to deform through several predetermined mode shapes. The total deformation at a point comprises of the sum of the local values of the mode shape functions multiplied with the according mode amplitudes. In general these mode shapes are defined such that the mean inertia axes are equal to the principle inertia axes of the rigid body. In that case, the inertia can be assumed to be constant. If the structure is stiff enough, the flexible modes are separated from the rigid body motion in the frequency domain, such that these are uncoupled. For these structures, the flexibility modes have a significantly higher eigenfrequency than the rigid body modes, which makes their decoupling a valid assumption. For a kite however, the structure is presumably too flexible to uncouple these motions. The flexible modes and rigid body modes have comparable eigenfrequencies.

**Multi-plate flexible model.** Figure 2.16 illustrates the idea of a discrete plate model. Since kites in general twist their surface in response to a pull on the control lines, it seems relevant to include this behavior in the model. The multi-plate flexible model allows the plates to pitch and roll independently from each other and thereby including twisting and jellyfish<sup>1</sup> motion.

With the model able to describe deformation due to tether forces, the shape based on tether forces can be investigated. This way natural control of kites can

---

<sup>1</sup>Harmonic arc shape bending.



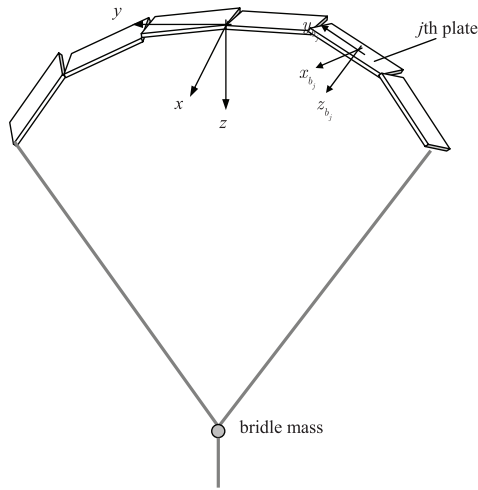


**Figure 2.16:** *Multiple flat plate kite model by Williams, Lansdorp, Ruiterkamp & Ockels [2008].*

be implemented in the model directly. A two plate model is in fact one of the simplest ways to represent a kite that can be controlled directly by tether force and tether attachment location [Williams, Lansdorp, Ruiterkamp & Ockels, 2008].

**Lumped mass membrane model.** Instead of adding a few sophisticated degrees of freedom one can also describe a kite at a fundamental lower level to find higher fidelity models. The membranes of the kite structure could for example be modeled by lumped masses connected with springs. In principle, with appropriate boundary conditions, a high fidelity kite model could be build out of these modeled membranes. Provot [1995] uses such a model to simulate a waving flag on a pole.

**FEM model.** Another step in complexity are finite element method models. In these models the distributed masses and connecting springs are replaced by elastic solid elements. Visualizations of the results of a FEM analysis are displayed in figure 2.17. However, it is much too extensive to find all the parameters and too costly in terms of computing time for kite applications.

## 2.5.5 Flight dynamics of kites

The behavior of atmospheric vehicles is studied by flight dynamics. With regard to flight dynamics for kites, some notable contributions have been made. Bryant et al. [1942] reports on collected research of kites for the purpose of wartime observation of enemy positions. It is stated that during the second world war,

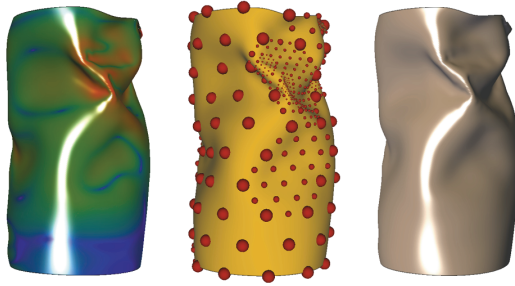


**Figure 2.17:** *FEM model using a conforming, hierarchical, adaptive refinement method to simulate a thin tube under compression, from Grinspun et al. [2002].*

kites as a means of observation received increased attention. It was thought that these kites required a "high performance", which was basically defined as a high lift-over-drag. A mathematical model was developed using a tether model which was largely empirical in nature and became singular for (nearly) straight tethers. A wood-and-linnen model was constructed for wind tunnel testing. These tests seemed to validate the model. However, flying in the turbulent conditions outside resulted in unstable flight and eventually a crash.

Melkert [1992] later employed the theory of Bryant et al. [1942] for the Stratow project in which a sailplane was towed behind a small powered aircraft using a long tether. By towing the glider, the glider was able to reach altitudes up to 10 kilometers. Similar cases of related research can be identified such as launching of gliders by towing, tethered aerostat dynamics, aerial-towed systems and even tethered underwater rovers. Even though these subjects seem very similar, notable differences to kites are present such as the buoyancy of aerostats and the larger weight and rigidity of gliders. Furthermore, because the kite remains tethered to the ground and is not detached from the cable after launch such as with gliders, different dynamic effects occur.

Alexander & Stevenson [2001] analyses the equilibrium points of single-line and two-line kites. The paper shows that these equilibrium points can be determined from the aerodynamic properties of the kite, the kite mass and the bridle lengths. While several equilibrium points are found, not all of them turn out to be stable equilibrium points. wind tunnel tests are shown to confirm the mathematical model.

Sanchez [2006] derived the Lagrangian equations of motion for a single-line kite for the purpose of control. The analysis is limited to symmetric motions. the paper continues to develop an open-loop control system to keep the kite at a constant altitude in changing atmospheric conditions.

Houska [2007] developed a 9 degree of freedom surf kite model to serve as a basis for control design. The model assumes the inertial tensor to be zero because the foil kites have such a low mass compared to the tether. Instead of deviding

the kite into several pieces, the paper introduces a small number of effective aerodynamic coefficients which can theoretically be obtained integrating over the aerodynamic properties of the entire kite.

To gain more insight in the behavior of a Laddermill, Meijaard [1997] performed a static analysis of a Laddermill in several wind conditions. This research was the starting point for Meijaard & Schwab [1999] that resulted in the Laddermill dynamic simulation program O-MILL. The model of the Laddermill in O-MILL is based on two types of elements, tether elements and wing elements. The tether elements are defined as one dimensional continuum with stiffness and damping in the normal direction, bending stiffness is neglected. Lift and drag forces are defined per wing element. The wing elements are assumed to be rigid and interference effects between them are neglected. The aerodynamic forces are assumed to be quasi static and the wind velocity is a function of altitude. Equations of motion are established for each element and the system is integrated using a fourth order Runge-Kutta integration scheme. Because the elements are parametric, the configuration and sizing of the Laddermill can easily be adjusted. This is convenient for a sensitivity study of various parameters.

## 2.5.6 Kite measurements

As part of the trinity depicted in figure 2.5, kite measurements are of paramount importance. Not only is it invaluable for model validation, measurements and observations directly establish increased knowledge and understanding of kites.

The early wind tunnel tests of Bryant et al. [1942] were mentioned in the previous section and seemed to concur with the theory which was developed. Jackson [1942] launched an analysis of kite performance using a 24-ft. wind tunnel. A total of six kites were tested in a wide range of wind velocities. These six kites included (A) a 3-ft. Cody kite Mk-II, (B) a 3-ft. reversed Cody or Dyco kite, (C) a 3-ft Haldon kite, (D) two 3-ft. Cody kites with lateral cross bracing, (E) a 2-ft. Cody kite Mk-III with bifucated inner bridle and (F) a 2-ft. Cody kite Mk-III with longitudinal bracing. It was concluded that the maximum value for lift-over-drag was no more than 2.5 with a maximum value for the lift coefficient of 0.9.

Wachter [2008] analyzed a ram-air inflated kite and its shape under loading. Of particular interest was the presence of ballooning of the surface and deformation of the original airfoil shapes. Their influences on the flow over the kite was analyzed using computational fluid dynamics and wind tunnel tests. Wachter [2008] employed two different techniques to capture the shape of the kite under loading. The first method was a wind tunnel test where an array of camera's took pictures simultaneously of the kite which was outfitted with a dot-pattern on its surface. Through photogrammetry the shape could be reconstructed as a wire-frame model in a computer. The second method was a three dimensional laser scanning technique which resulted in a large point-cloud, from which the shape of the kite could be deduced. This method was later dropped due to the

fact that the long cycle period of the laser scanner (over a minute long) gave rise to distortions in the data because during the cycle, the kite would not be perfectly still. The measurement using photogrammetry was instant and thus not subject to such distortions.

Although wind tunnel tests are a means of obtaining reproducible data on kites, there is a downside to its application. In contrast to conventional aircraft, kites cannot be scaled down due to their flexibility. A scaled down kite will deform differently than its full-scale counterpart. Therefore, only full-size kites can be tested in a wind tunnel. This makes wind tunnel testing of kites an expensive endeavor.

Stevenson et al. [2005] advocates a kite testing technique whereby the kite is flown close to the ground in a circle. In this manner, lift-over-drag ratios of kites can be determined. However, atmospheric conditions during the tests were critical to its accuracy. Only in wind-still conditions would the test yield good results.

Vlugt [2009] launched an extensive test program on surf kites in order to measure their performance. The work was part of an effort to optimize kite surfing for speed. Vlugt [2009] flew the kite in fast sweeps from left to right, while keeping the wind in his back. When the kite passed from upwind to downwind, dead-center in the wind window, measurements were taken of the wind velocity, the kite velocity and the line tension. Based on these parameters, the key aerodynamic coefficients on the kite could be obtained. The resulting data showed a small amount of scattering, but overall reasonably good results were obtained with this testing method.

## 2.6 Concluding remarks

One could argue that it is quite remarkable that for a device with such a wide field of applications, there has been so little interest from the scientific community. This chapter established that kites have been around for a long time and that they have been mostly ignored by scientists in the past, despite their multitude of applications and the scientific challenges posed by such a flexible flying craft. The study of kites is an open field of research which awaits discovery. The purpose of this thesis is to facilitate and inspire future research into this exciting field.

# CHAPTER 3

---

## Rigid body kite dynamics

---

*Two of the pylons on which the engineering methodology for kite design is based are knowledge and simulation (see section 2.3). In order to be able to quantify knowledge on kites and perform simulations, a calculation framework in the form of a mathematical model is required. This chapter explores the application of conventional rigid body flight dynamics to the modeling of kites. Section 3.1 gives a short introduction, section 3.2 and 3.3 formulate rigid body models for kites based on Newtonian equations of motion and Lagrangian equations of motion respectively. Section 3.4 explores the differences and similarities of tethered vs non-tethered flight based on the eigenmotions. Section 3.5 analyzes the effects of cable length on the dynamics of tethered flight. Lastly, section 3.6 closes this chapter with concluding remarks.*

### 3.1 Introduction

In the previous chapter it was established that for an engineering approach to the design of kites, simulation is one of the key components. Kite simulations can contribute to the understanding of kites and can be a valuable design and analysis tool for a kite designer. When modelling a kite, the question beckons: Can we use conventional airplane theory to model a kite? Conventional airplanes are often modelled as rigid bodies with six degrees of freedom while a kite is a highly flexible structure which is tethered to the ground. The question therefore becomes: can we model a kite as a rigid body? This chapter will make an attempt at doing so.

## 3.2 Newton-based kite model

In this section, a rigid body model is developed analogue to the theory of conventional flight dynamics [Mulder et al., 2007]. Significant work on this model was performed by Master Thesis student Stefan de Groot [Groot et al., 2010]. The equations of motion are based on a rigid body attached to a straight tether. The tether itself is modelled as a spring-damper between the ground and the cable attachment point on the kite. For this model, the following assumptions are made:

- The earth is assumed flat and non-rotating.
- The kite is a rigid body and is symmetric in the  $X^B - Z^B$ -plane.
- The tether is assumed to be straight and have no drag and no weight.

The straight tether assumption deserves justification. Comparing the amount of drag and weight of the tether to the tension in the tether forms the basis of this assumption. For a single kite on a single tether, the tension in the tether is:

$$T = \frac{1}{2}\rho V^2 S \sqrt{(C_L)^2 + (C_D)^2} \quad (3.1)$$

For the drag on the tether we can write:

$$D_t = C_{Dt} \frac{1}{2} \rho V^2 h d_t \quad (3.2)$$

In equation (3.2)  $h$  is the altitude above ground level of the kite and  $d_t$  is the diameter of the tether.  $C_{Dt}$  is the drag coefficient of the tether. Hoerner [1965a] reports the tether drag coefficient to be 1.065. To evaluate the ratio between the tether tension and the drag of the tether, we calculate:

$$\frac{D_t}{T} = \frac{C_{Dt}}{\sqrt{(C_L)^2 + (C_D)^2}} \frac{h d_t}{S} \quad (3.3)$$

For the type of kite under investigation here the lift- and drag coefficients will be in the order of resp. 0.9 and 0.2. With the tether drag coefficient from Hoerner [1965a] it becomes clear that the first quotient of equation (3.3) is close to 1. The second quotient of equation (3.3) is different. for a kite on a 100m line, the altitude  $h$  will be approximately 95 meters. The diameter of the cable is in the order of 2mm. With a wing surface of the kite  $S$  in the order of 10 square meters, the second quotient of equation (3.3), and therefore the ratio between

the tether tension and the tether drag becomes approximately 0.02. This means that the drag on the tether is only 2% of the tension in the tether. And with a small length and diameter, the weight of the dyneema tether is an even smaller portion of the tether tension. The sag of the tether was investigated using a multi-body tether model [Breukels & Ockels, 2007b], and it was concluded that the sag in these types of short cables with large kites attached is negligible. On the basis of this evaluation it was decided that the tether in the rigid body models would be represented by a massless and dragless straight rod stretching from the ground to the tether attachment point on the kite. This rod however, is allowed to extend and rotate freely about its longitudinal axis. A final remark to be made concerns the compression characteristics of the real tether and the spring-damper model. A tether is unable to sustain compression while a spring-damper can. During simulations, the tether tension was monitored for compression. During all simulations presented in this thesis, no compression occurred.

The definitions of the frames of reference, as well as the angle conventions can be found in appendix A.

### 3.2.1 External forces and moments

Types of external forces act on a kite:

- Aerodynamic forces
- Tether forces
- Gravity

The distributed aerodynamic- and gravity forces are replaced by point forces acting on particular points on the body, simplifying the equations of motion. The tether forces are already point forces acting on the tether attachment point.

The apparent velocity  $V_a$  is the result of the vector sum of the wind velocity vector  $V_w$  and the kinematic velocity vector  $V_k$ . When the tether force  $T$ , the aerodynamic forces  $L$  and  $D$  and the weight  $W$  are in equilibrium the kite is not accelerating with regard to the earth axis system. The aerodynamic force vector in the body-fixed reference frame is given by:

$$\mathbf{R}^B = \mathbf{F}_{aero}^B = \begin{bmatrix} X \\ Y \\ Z \end{bmatrix} \quad (3.4)$$

The tether force vector in the body-fixed reference frame is defined as:

$$\mathbf{T}^B = \mathbf{F}_{tether}^B = \begin{bmatrix} F \\ G \\ H \end{bmatrix} \quad (3.5)$$

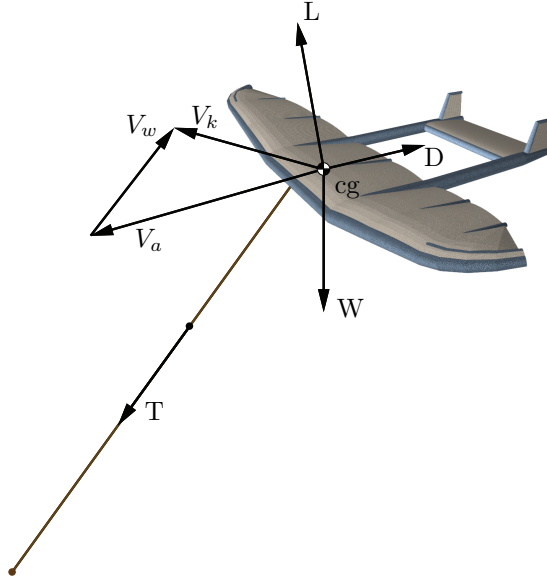


**Figure 3.1:** *Forces acting on the kite.*

The gravity vector in the body-fixed reference frame is given by:

$$\begin{aligned}
 \mathbf{W}^B &= m \cdot \mathbb{T}_{BE} \mathbf{g}^E \\
 &= m \cdot g \begin{bmatrix} -\sin \theta \\ \sin \phi \cos \theta \\ \cos \phi \cos \theta \end{bmatrix} \quad (3.6)
 \end{aligned}$$

In order to define the moments, a point of reference needs to be chosen. In conventional aircraft theory, this point is often the center of gravity. By choosing the center of gravity as the reference point, the gravity force is taken out of the moment equation. For a kite, one might be inclined to take the tether attachment point as the point of reference. For kite flyers, the cable attachment point has more physical significance than the center of gravity. However, the position of the cable attachment point can also be a control input for some of the more advanced industrial kites. Furthermore, for a rigid kite, the center of gravity is a fixed point. Therefore, the center of gravity is chosen as the point of reference around which the moments are defined. The external forces generate external moments about the center of gravity. The aerodynamic moment vector in the body-fixed reference frame is defined as:



$$\mathcal{M}_{aero,cg}^B = \begin{bmatrix} L \\ M \\ N \end{bmatrix} \quad (3.7)$$

The tether moment vector in the body-fixed reference frame is defined as:

$$\mathcal{M}_{tether,cg}^B = \begin{bmatrix} P \\ Q \\ R \end{bmatrix} = \mathbf{r}_{ta} \times \mathbf{F}_{tether}^B \quad (3.8)$$

where  $\mathbf{r}_{ta}$  is the position of the tether attachment point relative to the center of gravity in the body fixed reference frame. Figure 3.2 is a representation of the kite with the frames of reference as indicated.

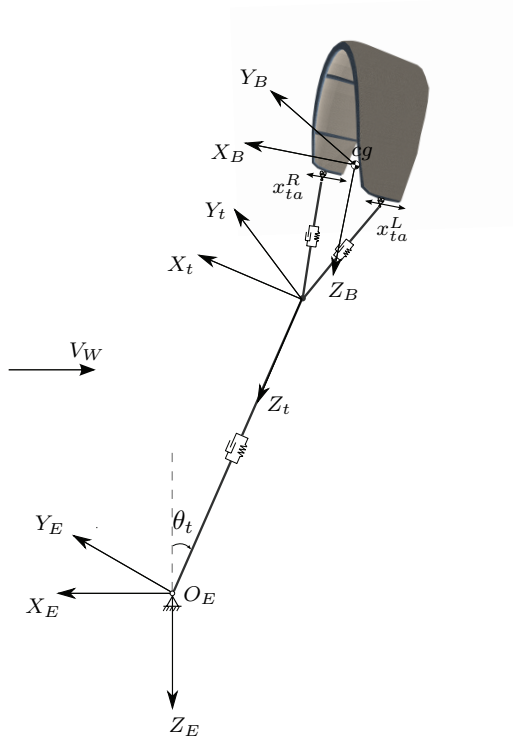


**Figure 3.2:** Kite system with the assumptions.

### 3.2.2 Equations of motion

In this section the equations of motion are derived. The general force and moment equations expressed in the earth-fixed reference are (Newton's second law):

$$m\mathbf{A}_{E,cg} = \mathbf{F}_{ext} \quad (3.9)$$

$$\frac{d\mathbf{B}_{cg}^E}{dt} = \mathcal{M}_{ext,cg} \quad (3.10)$$

where  $\mathbf{A}_{E,cg}$  and  $\frac{d\mathbf{B}_{cg}^E}{dt}$  are the inertial translational acceleration and the derivative of the inertial angular momentum respectively and  $\mathbf{F}_{ext}$  and  $\mathcal{M}_{ext,cg}$  are the applied external forces and moments with respect to the  $cg$  respectively. The inertial translational acceleration in the body-fixed reference frame can be expressed as:

$$\begin{aligned} \mathbf{A}_{E,cg}^B &= \frac{d\mathbf{V}_{E,rp}^B}{dt} + \boldsymbol{\Omega}_{BE}^B \times \mathbf{V}_{E,rp}^B = \begin{bmatrix} \dot{u}_k \\ \dot{v}_k \\ \dot{w}_k \end{bmatrix} + \begin{bmatrix} p \\ q \\ r \end{bmatrix} \times \begin{bmatrix} u_k \\ v_k \\ w_k \end{bmatrix} \\ &= \begin{bmatrix} \dot{u}_k + qw_k - rv_k \\ \dot{v}_k + ru_k - pw_k \\ \dot{w}_k + pv_k - qu_k \end{bmatrix} \end{aligned} \quad (3.11)$$

The derivative of the inertial angular momentum in the body-fixed reference frame can be written as:

$$\begin{aligned} \left( \frac{d\mathbf{B}_{cg}^E}{dt} \right)^B &= \frac{\mathbf{B}_{cg}^B}{dt} + \boldsymbol{\Omega}_{BE}^B \times \mathbf{B}_{cg}^B \\ &= \mathbb{I}_{cg}^B \frac{d\boldsymbol{\Omega}_{BE}^B}{dt} + \frac{d\mathbb{I}_{cg}^B}{dt} \boldsymbol{\Omega}_{BE}^B + \boldsymbol{\Omega}_{BE}^B \times (\mathbb{I}_{cg}^B \boldsymbol{\Omega}_{BE}^B) \end{aligned} \quad (3.12)$$

where  $\boldsymbol{\Omega}_{BE}^B$  and  $\mathbb{I}_{cg}^B$  are the rotational velocity and the inertia tensor respectively given by:

$$\boldsymbol{\Omega}_{BE}^B = \begin{bmatrix} p \\ q \\ r \end{bmatrix} \quad (3.13)$$

$$\mathbb{I}_{cg}^B = \begin{bmatrix} I_{xx} & -J_{xy} & -J_{xz} \\ -J_{yx} & I_{yy} & -J_{yz} \\ -J_{zx} & -J_{zy} & I_{zz} \end{bmatrix} \quad (3.14)$$

For the assumption of rigid body the time derivative of the inertia tensor is zero. The complete set of equations contains the equations of motion, kinematic relations and wind relations. The equations of motion for the forces and moments in the body-fixed reference frame are:

$$m \begin{bmatrix} \dot{u}_k + qw_k - rv_k \\ \dot{v}_k + ru_k - pw_k \\ \dot{w}_k + pv_k - qu_k \end{bmatrix} = mg_G \begin{bmatrix} -\sin\theta \\ \sin\phi \cos\theta \\ \cos\phi \cos\theta \end{bmatrix} + \begin{bmatrix} X \\ Y \\ Z \end{bmatrix} + \begin{bmatrix} F \\ G \\ H \end{bmatrix} \quad (3.15)$$

$$\mathbb{I}_{cg}^B \frac{d\boldsymbol{\Omega}_{BE}^B}{dt} + \boldsymbol{\Omega}_{BE}^B \times (\mathbb{I}_{cg}^B \boldsymbol{\Omega}_{BE}^B) = \begin{bmatrix} L \\ M \\ N \end{bmatrix} + \begin{bmatrix} P \\ Q \\ R \end{bmatrix} \quad (3.16)$$

The kinematic relations for the rotational rates of the body can be obtained from equations A.11 and 3.13:

$$\begin{bmatrix} \dot{\phi} \\ \dot{\theta} \\ \dot{\psi} \end{bmatrix} = \begin{bmatrix} 1 & \sin\phi \tan\theta & \cos\phi \tan\theta \\ 0 & \cos\phi & -\sin\phi \\ 0 & \frac{\sin\phi}{\cos\theta} & \frac{\cos\phi}{\cos\theta} \end{bmatrix} \begin{bmatrix} p \\ q \\ r \end{bmatrix} \quad (3.17)$$

For the kinematic relations due to the tether, we write the position and velocity of the tether attachment point out in spherical coordinates. If the kite is assumed to be a rigid body the velocity of the end point of the tether expressed in the tether-fixed reference frame  $\langle \dot{x}_t^t, \dot{y}_t^t, \dot{z}_t^t \rangle$  is determined from the kinematic velocity and the rotational speed of the kite. From the theory of the planar motion of rigid bodies [Török, 2000] the following equation is derived.

$$\begin{bmatrix} \dot{x}_t^B \\ \dot{y}_t^B \\ \dot{z}_t^B \end{bmatrix} = \begin{bmatrix} u_k^B \\ v_k^B \\ w_k^B \end{bmatrix} + \boldsymbol{\Omega}_{BE}^B \times \mathbf{r}_{ta} \quad (3.18)$$

Where  $r_{ta}^B$  is the position vector of the tether attachment point in the body-fixed frame of reference. If the velocity of the end point of the tether in earth axes is known, than the velocity of the end point of the tether can be transformed in tether-fixed axes by equation (3.19):

$$\begin{bmatrix} \dot{x}_t^t \\ \dot{y}_t^t \\ \dot{z}_t^t \end{bmatrix} = \mathbb{T}_{tB} \begin{bmatrix} \dot{x}_t^B \\ \dot{y}_t^B \\ \dot{z}_t^B \end{bmatrix} \quad (3.19)$$

The time derivative of  $\langle l_t, \theta_t, \psi_t \rangle$  is than given by equation (3.20).

$$\begin{aligned} \dot{l}_t &= -\dot{z}_t^t \\ \dot{\theta}_t &= -\frac{\dot{x}_t^t}{l_t} \\ \dot{\psi}_t &= -\frac{\dot{y}_t^t}{l_t \sin \theta_t} \end{aligned} \tag{3.20}$$

Equations 3.18, 3.19 and 3.20 now yield the kinematic relations due to the tether:

$$\begin{bmatrix} \dot{x}_t^t \\ \dot{y}_t^t \\ \dot{z}_t^t \end{bmatrix} = \mathbb{T}_{tB} \left( \begin{bmatrix} u_k \\ v_k \\ w_k \end{bmatrix} + \boldsymbol{\Omega}_{BE}^B \times \mathbf{r}_{ta}^B \right) \tag{3.21}$$

$$\begin{bmatrix} \dot{l}_t \\ \dot{\theta}_t \\ \dot{\psi}_t \end{bmatrix} = \begin{bmatrix} 0 & 0 & -1 \\ -\frac{1}{l_t} & 0 & 0 \\ 0 & -\frac{1}{l_t \sin \theta_t} & 0 \end{bmatrix} \begin{bmatrix} \dot{x}_t^t \\ \dot{y}_t^t \\ \dot{z}_t^t \end{bmatrix} \tag{3.22}$$

The aerodynamic forces and moments are dependent on the apparent velocity and acceleration. Since a kite flies under the influence of the wind, wind relations are required which describe the influence of the wind on the apparent velocity and acceleration. The apparent velocity  $V_a$  i.e. the actual wind velocity experienced by the kite, is given by the kinematic velocity of the kite  $V_k$  and the wind speed  $V_W$ . The wind velocity vector is defined as the velocity of an undisturbed air particle  $W$  in the center of gravity  $cg$  expressed in the earth-fixed reference frame  $E_E$  for a flat and non-rotating earth:

$$\mathbf{V}_W = \mathbf{V}_{W,cg} = \frac{d\mathbf{W}_{cg}^E}{dt} = \begin{bmatrix} W_x \\ W_y \\ W_z \end{bmatrix} \tag{3.23}$$

The kinematic velocity is the velocity of the kite relative to the earth, which determines the actual displacements in  $x$ ,  $y$  and  $z$ -direction. The apparent velocity can be split up in the kinematic velocity and the wind velocity expressed in the earth-fixed reference frame by:

$$\begin{aligned} \mathbf{V}_a &= \mathbf{V}_k + \mathbf{V}_w \\ \mathbb{T}_{EB} \begin{bmatrix} u_a \\ v_a \\ w_a \end{bmatrix} &= \mathbb{T}_{EB} \begin{bmatrix} u_k \\ v_k \\ w_k \end{bmatrix} + \begin{bmatrix} W_x \\ W_y \\ W_z \end{bmatrix} \end{aligned} \tag{3.24}$$

The equations of motion are written in the body-fixed reference frame. The apparent velocity in the body-fixed reference frame is given by:

$$\begin{bmatrix} u_a \\ v_a \\ w_a \end{bmatrix} = \begin{bmatrix} u_k \\ v_k \\ w_k \end{bmatrix} + \mathbb{T}_{BE} \begin{bmatrix} W_x \\ W_y \\ W_z \end{bmatrix} \quad (3.25)$$

where the wind velocity in body-fixed reference frame is equivalent to:

$$\mathbf{V}_W^B = \mathbb{T}_{BE} \mathbf{V}_W^E \quad (3.26)$$

To derive the aerodynamic acceleration the time derivative of the wind velocity in body axes needs to be known. Use is made of the theory of the transformation of the derivative of a vector [Etkin, 1972]:

$$\begin{aligned} \frac{d\mathbf{V}_W^B}{dt} &= \frac{d}{dt} \left( \mathbb{T}_{BE} \mathbf{V}_W^E \right) \\ \dot{\mathbf{V}}_W^B &= \mathbb{T}_{BE} \frac{d\mathbf{V}_W^E}{dt} + \frac{d\mathbb{T}_{BE}}{dt} \mathbf{V}_W^E \\ \dot{\mathbf{V}}_W^B &= \mathbb{T}_{BE} \cdot \dot{\mathbf{V}}_W^E + \mathbb{T}_{BE} \left( \boldsymbol{\Omega}_{EB}^E \times \mathbf{V}_W^E \right) \\ \dot{\mathbf{V}}_W^B &= \mathbb{T}_{BE} \cdot \dot{\mathbf{V}}_W^E - \boldsymbol{\Omega}_{BE}^B \times \mathbb{T}_{BE} \mathbf{V}_W^E \end{aligned} \quad (3.27)$$

equation (3.25) can now be differentiated with respect to time to obtain the expression for the aerodynamic acceleration vector in terms of the kinematic velocity vector, the wind acceleration vector and the wind velocity vector:

$$\begin{aligned} \frac{d\mathbf{V}_a^B}{dt} &= \frac{d\mathbf{V}_k^B}{dt} + \frac{d}{dt} \left( \mathbb{T}_{BE} \mathbf{V}_W^E \right) \\ \dot{\mathbf{V}}_a^B &= \dot{\mathbf{V}}_k^B + \mathbb{T}_{BE} \cdot \dot{\mathbf{V}}_W^E - \boldsymbol{\Omega}_{BE}^B \times \mathbb{T}_{BE} \mathbf{V}_W^E \end{aligned} \quad (3.28)$$

Now the set of kinematic relations can be completed by adding the wind relations describing the apparent velocity (3.25) and aerodynamic acceleration (3.28):

$$\begin{bmatrix} u_a \\ v_a \\ w_a \end{bmatrix} = \begin{bmatrix} u_k \\ v_k \\ w_k \end{bmatrix} + \mathbb{T}_{BE} \begin{bmatrix} W_x \\ W_y \\ W_z \end{bmatrix} \quad (3.29)$$

$$\begin{bmatrix} \dot{u}_a \\ \dot{v}_a \\ \dot{w}_a \end{bmatrix} = \begin{bmatrix} \dot{u}_k \\ \dot{v}_k \\ \dot{w}_k \end{bmatrix} + \mathbb{T}_{BE} \cdot \begin{bmatrix} \dot{W}_x \\ \dot{W}_y \\ \dot{W}_z \end{bmatrix} - \begin{bmatrix} p \\ q \\ r \end{bmatrix} \times \mathbb{T}_{BE} \begin{bmatrix} W_x \\ W_y \\ W_z \end{bmatrix} \quad (3.30)$$

### 3.2.3 Control inputs

Conventional aircraft are outfitted with control surfaces. For kites such devices are rare. Control of kites can be accomplished by changing the balance of forces in the tethers. Or, for single line kites, shift the attachment points of the bridle lines or tether to the kite. In this model, control can be established by shifting the two cable attachment points in the direction of the  $X_B$  axis (see figure 3.2). The position of the attachment points are defined in the body fixed frame of reference by:

$$\mathbf{r}_{taL} = \begin{bmatrix} x_{taL} \\ y_{taL} \\ z_{taL} \end{bmatrix} \quad \mathbf{r}_{taR} = \begin{bmatrix} x_{taR} \\ y_{taR} \\ z_{taR} \end{bmatrix} \quad (3.31)$$

Based on this definition it is possible to define an ‘average’ or central position. This is convenient when the controls are moved symmetrically and only one control variable has to be defined:

$$\mathbf{r}_{ta} = \begin{bmatrix} \frac{x_{taL} + x_{taR}}{2} \\ \frac{y_{taL} + y_{taR}}{2} \\ \frac{z_{taL} + z_{taR}}{2} \end{bmatrix} \quad (3.32)$$

For simplicity it is assumed that  $x_{taL}$  and  $x_{taR}$  are the only varying parameters. This holds when the displacement of the control positions in  $Y_b$  or  $Z_b$  direction is relatively small.

### 3.2.4 Tether model

The main tether force is modelled as a spring-damper and this is represented by equation (3.33):

$$\mathbf{T}_t \left( \delta l_t(t), \dot{l}_t(t) \right) = k_t \cdot \delta l_t(t) + c_t \cdot \dot{l}_t(t) \quad (3.33)$$

where  $k_t$  and  $c_t$  are the spring and damper constants. The initial tether length at ‘ $t = 0$  s’ is given by equation (3.34):

$$l_{t0} = l_{t,\delta l_t=0} + \delta l_{t0} \quad (3.34)$$

where  $l_{t,\delta l_t=0}$  is the unstretched tether length and  $\delta l_{t0}$  the initial tether elongation.

A system of bridle lines attach the main tether to the kite. The bridle lines constrain the kite in a mix of roll ( $p$ ) and yaw ( $r$ ) motion depending on the body

pitch angle with respect to the tether. A detailed discussion of the tether model can be found in appendix B. Figure 3.3 shows a graphical representation of the tether and control parameters.

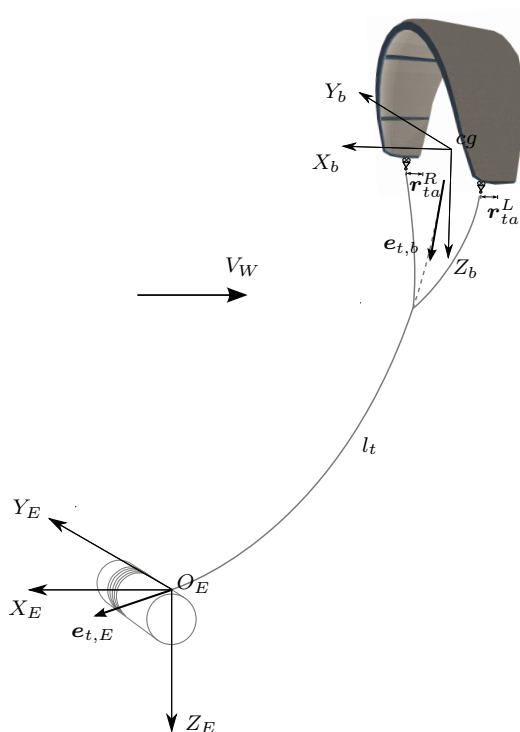


**Figure 3.3:** *Definition of tether and control parameters.*

### 3.2.5 Linearized equations of motion

In the previous sections a non-linear rigid body model of a kite was derived. This section outlines the linearized equations of motion. Extensive use is made of the linearization method for conventional aircraft flight dynamics which is described extensively in Mulder et al. [2007]. A more detailed discussion on the linearization of the equations of motion can be found in appendix C and D. A condensed discussion is given here.

The flight condition to be linearized is a steady straight symmetric flight condition where the initial kinematic velocity of the kite is zero. The initial condition is given by following parameters in the body-fixed reference frame, except for the

wind velocity components:

$$\begin{array}{cccccc}
u_a \neq 0 & u_k = 0 & \dot{u}_k = 0 & W_x \neq 0 & p = 0 & \dot{p} = 0 \\
v_a = 0 & v_k = 0 & \dot{v}_k = 0 & W_y = 0 & q = 0 & \dot{q} = 0 \\
w_a = 0 & w_k = 0 & \dot{w}_k = 0 & W_z = 0 & r = 0 & \dot{r} = 0 \\
\phi = 0 & \dot{\phi} = 0 & \delta l_t \neq 0 & \dot{l}_t = 0 & \tau = 0 & \dot{\tau} = 0 \\
\theta \neq 0 & \dot{\theta} = 0 & \theta_t \neq 0 & \dot{\theta}_t = 0 & \kappa \neq 0 & \dot{\kappa} = 0 \\
\psi = 0 & \dot{\psi} = 0 & \psi_t = 0 & \dot{\phi}_t = 0 & \xi = 0 & \dot{\xi} = 0 \\
X \neq 0 & F \neq 0 & L = 0 & P = 0 & & \\
Y = 0 & G = 0 & M \neq 0 & Q \neq 0 & & \\
Z \neq 0 & H \neq 0 & N = 0 & R = 0 & & 
\end{array}$$

The linearization of the states is done analogue to Mulder et al. [2007]. The equations of motion can be written as:

$$\begin{aligned}
F_x &= f(\dot{u}_a, v_a, w_a, q, r) \\
F_y &= f(\dot{v}_a, u_a, w_a, p, r) \\
F_z &= f(\dot{w}_a, u_a, v_a, p, q) \\
M_x &= f(\dot{p}, \dot{r}, p, q, r) \\
M_y &= f(\dot{q}, p, r) \\
M_z &= f(\dot{p}, \dot{r}, p, q, r)
\end{aligned} \tag{3.35}$$

Linearization of the forces and moments is largely analogue to conventional flight dynamics, except for the inclusion of the tether forces. The forces and moments are a function of the following states:

$$\begin{aligned}
F_x &= f(\theta, X, F) \\
F_y &= f(\theta, \phi, Y, G) \\
F_z &= f(\theta, \phi, Z, H) \\
M_x &= f(L, P) \\
M_y &= f(M, Q) \\
M_z &= f(N, R)
\end{aligned} \tag{3.36}$$

With:



$$\begin{aligned}
W &= f(\theta) \\
X &= f(u_a, w_a, q) & L &= f(v_a, p, r) \\
Y &= f(v_a, \dot{v}_a, p, r) & M &= f(u_a, w_a, \dot{w}_a, q) \\
Z &= f(u_a, w_a, \dot{w}_a, q) & N &= f(v_a, \dot{v}_a, p, r) \\
F &= f(x_{ta}, l_t, \dot{l}_t, \kappa) & P &= f(x_{ta}^L, x_{ta}^R, \tau) \\
G &= f(x_{ta}^L, x_{ta}^R, \tau) & Q &= f(x_{ta}, l_t, \dot{l}_t, \kappa) \\
H &= f(x_{ta}, l_t, \dot{l}_t, \kappa) & R &= f(x_{ta}^L, x_{ta}^R, \tau)
\end{aligned} \tag{3.37}$$

The control quantities  $\mathbf{r}_{ta}^L$  and  $\mathbf{r}_{ta}^R$  consist both of three components  $x_{ta}$ ,  $y_{ta}$  and  $z_{ta}$  as explained in section 3.2.3. The only variable components are  $x_{ta}^L$  and  $x_{ta}^R$ . Linearization of the control quantities will result in a dependency only of  $\Delta x_{ta}^L$  and  $\Delta x_{ta}^R$ .  $l_t$  and  $\dot{l}_t$  are states concerning the length and the change of length of the main tether.  $\kappa$  is the body pitch angle with respect to the tether and  $\tau$  is the body roll angle with respect to the tether. From here, linearization of the forces and moments is analogue to Mulder et al. [2007]

Linearization of the kinematic relations relating to the body is analogue to that for aircraft and is therefore omitted here. An extensive discussion can be found in Mulder et al. [2007]. Linearization of the kinematic relations relating to tether and the wind are done after applying the initial conditions in order to keep the linearization concise. Details on the linearization of the symmetric and asymmetric equations of motion and kinematic relations can be found in appendix C and D.

### 3.2.6 Matrix notation of the symmetric equations of motion

In appendix C a more detailed discussion can be found on the linearization of the equations of motion and the kinematic relations pertaining to the symmetric case. Grouping these equations as a function of  $\Delta \mathbf{X}$  and dropping the  $\Delta$ 's yields

the following set of equations:

$$\begin{aligned}
& -W \cos \theta_0 \cdot \theta + X_{u_a} \cdot u_a + X_{w_a} \cdot w_a + X_q \cdot q \\
& \quad + F_{x_{ta}} \cdot x_{ta} + F_{l_t} \cdot l_t + F_{\dot{l}_t} \cdot \dot{l}_t + F_\kappa \cdot \kappa = m \cdot \dot{u}_k \\
& -W \sin \theta_0 \cdot \theta + Z_{u_a} \cdot u_a + Z_{w_a} \cdot w_a + Z_{\dot{w}_a} \cdot \dot{w}_a + Z_q \cdot q \\
& \quad + H_{x_{ta}} \cdot x_{ta} + H_{l_t} \cdot l_t + H_{\dot{l}_t} \cdot \dot{l}_t + H_\kappa \cdot \kappa = m \cdot \dot{w}_k \\
& M_{u_a} \cdot u_a + M_{w_a} \cdot w_a + M_{\dot{w}_a} \cdot \dot{w}_a + M_q \cdot q \\
& \quad + Q_{x_{ta}} \cdot x_{ta} + Q_{l_t} \cdot l_t + Q_{\dot{l}_t} \cdot \dot{l}_t + Q_\kappa \cdot \kappa = I_y \cdot \dot{q} \\
& \quad \quad \quad \dot{\theta} = q \\
& \cos \kappa_0 \cdot u_k + z_{ta} \cos \kappa_0 \cdot q + \sin \kappa_0 \cdot w_k - x_{ta0} \sin \kappa_0 \cdot q = -l_{t0} \cdot \dot{\theta}_t \quad (3.38) \\
& -\sin \kappa_0 \cdot u_k - z_{ta} \sin \kappa_0 \cdot q + \cos \kappa_0 \cdot w_k - x_{ta0} \cos \kappa_0 \cdot q = -\dot{l}_t \\
& \quad \quad \quad \dot{\kappa} + \dot{\theta}_t = q \\
& \quad \quad \quad u_k + \cos \theta_0 \cdot W_x - W_{x0} \sin \theta_0 \cdot \theta = u_a \\
& \quad \quad \quad w_k + \sin \theta_0 \cdot W_x + W_{x0} \cos \theta_0 \cdot \theta = w_a \\
& \quad \quad \quad \dot{u}_k - W_{x0} \sin \theta_0 \cdot q = \dot{u}_a \\
& \quad \quad \quad \dot{w}_k + W_{x0} \cos \theta_0 \cdot q = \dot{w}_a
\end{aligned}$$

These 11 equations can be reduced to 6 equations. The equations for  $u_a$  and  $w_a$  can be used to replace the aerodynamic velocities in the force and moment equations. The same holds for  $\dot{w}_a$ . Furthermore a relation between  $\kappa$ ,  $\theta$  and  $\theta_t$  is obtained by integrating  $\dot{\kappa} + \dot{\theta}_t = q$ :

$$\begin{aligned}
q &= \dot{\kappa} + \dot{\theta}_c \\
\frac{d}{dt} \cdot \theta &= \frac{d}{dt} \cdot \kappa + \frac{d}{dt} \cdot \theta_c \\
\theta &= \kappa + \theta_c \\
\kappa &= \theta - \theta_c \quad (3.39)
\end{aligned}$$

where the integration constant is omitted, because it is represented in the initial state of equilibrium  $\mathbf{X}_0$ . By reducing the equations in (3.38) and collecting the

terms the following set of equations is obtained:

$$\begin{aligned}
& X_{u_a} \cdot u_k + X_{w_a} \cdot w_k \\
& + (-W \cos \theta_0 - X_{u_a} W_{x_0} \sin \theta_0 + X_{w_a} W_{x_0} \cos \theta_0 + F_\kappa) \cdot \theta \\
& \quad + X_q \cdot q + F_{l_t} \cdot l_t + F_{\dot{l}_t} \cdot \dot{l}_t - F_\kappa \cdot \theta_t \\
& + (X_{w_a} \sin \theta_0 + X_{u_a} \cos \theta_0) \cdot W_x + F_{x_{ta}} \cdot x_{ta} = m \cdot \dot{u}_k \\
\\
& Z_{u_a} \cdot u_k + Z_{w_a} \cdot w_k + Z_{\dot{w}_a} \cdot \dot{w}_k \\
& + (-W \sin \theta_0 - Z_{u_a} W_{x_0} \sin \theta_0 + Z_{w_a} W_{x_0} \cos \theta_0 + H_\kappa) \cdot \theta \\
& + (Z_q + Z_{\dot{w}_a} \cdot W_{x_0} \cos \theta_0) \cdot q + H_{l_t} \cdot l_t + H_{\dot{l}_t} \cdot \dot{l}_t - H_\kappa \cdot \theta_t \\
& + (Z_{w_a} \sin \theta_0 + Z_{u_a} \cos \theta_0) \cdot W_x + H_{x_{ta}} \cdot x_{ta} = m \cdot \dot{w}_k \\
\\
& M_{u_a} \cdot u_k + M_{w_a} \cdot w_k + M_{\dot{w}_a} \cdot \dot{w}_k \\
& + (-M_{u_a} W_{x_0} \sin \theta_0 + M_{w_a} W_{x_0} \cos \theta_0 + Q_\kappa) \cdot \theta \\
& + (M_q + M_{\dot{w}_a} \cdot W_{x_0} \cos \theta_0) \cdot q + Q_{l_t} \cdot l_t + Q_{\dot{l}_t} \cdot \dot{l}_t - Q_\kappa \cdot \theta_t \\
& + (M_{w_a} \sin \theta_0 + M_{u_a} \cos \theta_0) \cdot W_x + Q_{x_{ta}} \cdot x_{ta} = I_y \cdot \dot{q} \\
\\
& q = \dot{\theta} \\
\\
& \cos \kappa_0 \cdot u_k + \sin \kappa_0 \cdot w_k + (z_{ta} \cos \kappa_0 - x_{ta0} \sin \kappa_0) \cdot q = -l_{t0} \cdot \dot{\theta}_t \\
\\
& -\sin \kappa_0 \cdot u_k + \cos \kappa_0 \cdot w_k - (z_{ta} \sin \kappa_0 + x_{ta0} \cos \kappa_0) \cdot q = -\dot{l}_t
\end{aligned} \tag{3.40}$$

The equations of motion are made dimensionless in order to facilitate the possibility of comparison between different sized kites. The equations can be made dimensionless according to the divisors given in table 3.1 for the symmetric and asymmetric equations of motion.

	Symmetric motions	Asymmetric motions
Length [l]	$\bar{c}$	$b$
Velocity [ $lt^{-1}$ ]	$V_0$	$V_0$
Mass [m]	$\rho S \bar{c}$	$\rho S b$

**Table 3.1:** Divisors for the dimensionless linearized equations of motion.

In table 3.1  $\rho$  is the air density,  $S$  the projected surface area,  $\bar{c}$  the mean aerodynamic chord and  $b$  the wing span. In the symmetric equations (3.40) the force equations will be divided by  $\frac{1}{2}\rho V_0^2 S$  and the moment equation by  $\frac{1}{2}\rho V_0^2 S \bar{c}$ . In this process the states as well as the derivatives become dimensionless. The process is analogue to conventional flight dynamics [Mulder et al., 2007]

The resulting equations are:

$$\begin{aligned}
& C_{X_u} \cdot \hat{u}_k + C_{X_w} \cdot \hat{w}_k \\
& + (C_{Z_0} + C_{H_0} - C_{X_u} \frac{W_{x_0} \sin \theta_0}{V_0} + C_{X_w} \frac{W_{x_0} \cos \theta_0}{V_0} + C_{F_\kappa}) \cdot \theta \\
& + C_{X_q} \cdot \frac{q\bar{c}}{V_0} + C_{F_l} \cdot \frac{l_t}{\bar{c}} + C_{F_i} \cdot \frac{\dot{l}_t}{V_0} - C_{F_\kappa} \cdot \theta_t \\
& + (C_{X_w} \sin \theta_0 + C_{X_u} \cos \theta_0) \cdot \frac{W_x}{V_0} + C_{F_{x_{ta}}} \cdot x_{ta} = 2\mu_c D_c \cdot \hat{u}_k \\
\\
& C_{Z_u} \cdot \hat{u}_k + (C_{Z_w} + C_{Z_{\dot{w}}} D_c) \cdot \hat{w}_k \\
& + (-C_{X_0} - C_{F_0} - C_{Z_u} \frac{W_{x_0} \sin \theta_0}{V_0} + C_{Z_w} \frac{W_{x_0} \cos \theta_0}{V_0} + C_{H_\kappa}) \cdot \theta \\
& + (C_{Z_q} + C_{Z_{\dot{w}}} \frac{W_{x_0} \cos \theta_0}{V_0}) \cdot \frac{q\bar{c}}{V_0} + C_{H_l} \cdot \frac{l_t}{\bar{c}} + C_{H_i} \cdot \frac{\dot{l}_t}{V_0} - C_{H_\kappa} \cdot \theta_t \\
& + (C_{Z_w} \sin \theta_0 + C_{Z_u} \cos \theta_0) \cdot \frac{W_x}{V_0} + C_{H_{x_{ta}}} \cdot x_{ta} = 2\mu_c D_c \cdot \hat{w}_k \\
\\
& C_{m_u} \cdot \hat{u}_k + (C_{m_w} + C_{m_{\dot{w}}} D_c) \cdot \hat{w}_k \\
& + (-C_{m_u} \frac{W_{x_0} \sin \theta_0}{V_0} + C_{m_w} \frac{W_{x_0} \cos \theta_0}{V_0} + C_{Q_\kappa}) \cdot \theta \\
& + (C_{m_q} + C_{m_{\dot{w}}} \frac{W_{x_0} \cos \theta_0}{V_0}) \cdot \frac{q\bar{c}}{V_0} + C_{Q_l} \cdot \frac{l_t}{\bar{c}} + C_{Q_i} \cdot \frac{\dot{l}_t}{V_0} - C_{Q_\kappa} \cdot \theta_t \\
& + (C_{m_w} \sin \theta_0 + C_{m_u} \cos \theta_0) \cdot \frac{W_x}{V_0} + C_{Q_{x_{ta}}} \cdot x_{ta} = 2\mu_c K_Y^2 D_c \cdot \frac{q\bar{c}}{V_0} \\
\\
& \frac{q\bar{c}}{V_0} = D_c \cdot \theta \\
\\
& \cos \kappa_0 \cdot \hat{u}_k + \sin \kappa_0 \cdot \hat{w}_k + \frac{z_{ta} \cos \kappa_0 - x_{ta0} \sin \kappa_0}{\bar{c}} \cdot \frac{q\bar{c}}{V_0} = -\frac{l_{t0}}{\bar{c}} D_c \cdot \theta_t \\
\\
& -\sin \kappa_0 \cdot \hat{u}_k + \cos \kappa_0 \cdot \hat{w}_k - \frac{z_{ta} \sin \kappa_0 + x_{ta0} \cos \kappa_0}{\bar{c}} \cdot \frac{q\bar{c}}{V_0} = -D_c \cdot \frac{l_t}{\bar{c}} \\
\end{aligned} \tag{3.41}$$

with:

$$\begin{aligned}
\hat{u}_k &= \frac{u_k}{V_0} & C_{Z_0} + C_{H_0} &= -\frac{W \cos \theta_0}{\frac{1}{2}\rho V_0^2 S} \\
\hat{w}_k &= \frac{w_k}{V_0} & -C_{X_0} - C_{F_0} &= -\frac{W \sin \theta_0}{\frac{1}{2}\rho V_0^2 S} \\
\mu_c &= \frac{m}{\rho S \bar{c}} \\
\mu_c K_Y^2 &= \frac{I_y}{\rho S \bar{c}^3} \\
D_c &= \frac{\bar{c}}{V_0} \frac{d}{dt}
\end{aligned}$$

and

$$C_{F_\kappa} = -C_{H_0} \qquad C_{F_l} = -\frac{k_t \bar{c} \sin \kappa_0}{\frac{1}{2}\rho V_0^2 S} \quad (3.42)$$

$$C_{H_\kappa} = C_{F_0} \qquad C_{H_l} = \frac{k_t \bar{c} \cos \kappa_0}{\frac{1}{2}\rho V_0^2 S} \quad (3.43)$$

$$C_{Q_\kappa} = \frac{z_{ta}}{\bar{c}} C_{F_\kappa} - \frac{x_{ta0}}{\bar{c}} C_{H_\kappa} \qquad C_{Q_l} = -\frac{z_{ta} k_t \sin \kappa_0 + x_{ta0} k_t \cos \kappa_0}{\frac{1}{2}\rho V_0^2 S} \quad (3.44)$$

$$C_{F_i} = -\frac{c_t \sin \kappa_0}{\frac{1}{2}\rho V_0 S} \qquad C_{F_\delta} = 0 \quad (3.45)$$

$$C_{H_i} = \frac{c_t \cos \kappa_0}{\frac{1}{2}\rho V_0 S} \qquad C_{H_\delta} = 0 \quad (3.46)$$

$$C_{Q_i} = -\frac{z_{ta} c_t \sin \kappa_0 + x_{ta0} c_t \cos \kappa_0}{\frac{1}{2}\rho V_0 S \bar{c}} \qquad C_{Q_\delta} = -C_{H_0} \quad (3.47)$$

where the terms with the weight  $W$  come from the force equilibrium in the nominal flight condition.  $C_{X_u}, C_{X_w}, C_{X_q}, C_{Z_u}, C_{Z_w}, C_{Z_{\dot{w}}}, C_{Z_q}, C_{m_u}, C_{m_w}, C_{m_{\dot{w}}}$  and  $C_{m_q}$  are the so-called stability derivatives [Mulder et al., 2007].  $C_{F_\kappa}, C_{F_l}, C_{F_i}, C_{H_\kappa}, C_{H_l}, C_{H_i}, C_{Q_\kappa}, C_{Q_l}$  and  $C_{Q_i}$  are the derivatives related to the tether.  $C_{F_{x_{ta}}}, C_{H_{x_{ta}}}$  and  $C_{Q_{x_{ta}}}$  denote the input derivatives of the control system.

The equations (3.41) can be written in matrix notation depending on the dimensionless states  $\hat{u}_k, \hat{w}_k, \theta, \frac{q\bar{c}}{V_0}, \theta_t$  and  $\frac{l_t}{\bar{c}}$  with  $\frac{W_m}{V_0}$  and  $\frac{x_{ta}}{\bar{c}}$  as inputs:

$$\begin{bmatrix}
CX_u - 2\mu_c D_c & CX_w & CZ_0 + CH_0 - CX_u \frac{W_{x0} \sin \theta_0}{V_0} + CX_w \frac{W_{x0} \cos \theta_0}{V_0} + CF_\kappa & \hat{u}_k \\
CZ_u & CZ_w + (CZ_w - 2\mu_c) D_c & -CX_0 - CF_0 - CZ_u \frac{W_{x0} \sin \theta_0}{V_0} + CZ_w \frac{W_{x0} \cos \theta_0}{V_0} + CH_\kappa & \hat{w}_k \\
0 & 0 & -D_c & \theta \\
Cm_u & Cm_w + Cm_w D_c & -Cm_u \frac{W_{x0} \sin \theta_0}{V_0} + Cm_w \frac{W_{x0} \cos \theta_0}{V_0} + CQ_\kappa & \frac{\hat{u}^c}{V_0} \\
\cos \kappa_0 & \sin \kappa_0 & 0 & \theta_t \\
-\sin \kappa_0 & \cos \kappa_0 & 0 & \frac{\hat{L}_c}{c}
\end{bmatrix}
\begin{bmatrix}
CX_q & CF_l + CF_l D_c & \hat{u}_k \\
CZ_q + CZ_w \frac{W_{x0} \cos \theta_0}{V_0} & CH_l + CH_l D_c & \hat{w}_k \\
1 & 0 & \theta \\
Cm_q + Cm_w \frac{W_{x0} \cos \theta_0}{V_0} - 2\mu_c K_Y^2 D_c & CQ_l + CQ_l D_c & \frac{\hat{u}^c}{V_0} \\
\frac{z_{Ia} \cos \kappa_0 - x_{Ia0} \sin \kappa_0}{c} & 0 & \theta_t \\
-\frac{z_{Ia} \sin \kappa_0 + x_{Ia0} \cos \kappa_0}{c} & 0 & D_c
\end{bmatrix}
=
\begin{bmatrix}
-CX_u \cos \theta_0 - CX_w \sin \theta_0 & -CF_{xIa} \\
-CZ_u \cos \theta_0 - CZ_w \sin \theta_0 & -CH_{xIa} \\
0 & 0 \\
-Cm_u \cos \theta_0 - Cm_w \sin \theta_0 & -CQ_{xIa} \\
0 & 0 \\
0 & 0
\end{bmatrix}
\begin{bmatrix}
\frac{W_{x0}}{V_0} \\
\frac{x_{Ia}}{c}
\end{bmatrix}
\tag{3.47b}$$

A number of notable differences with the flight dynamics of conventional aircraft can be observed. Most notable is the fact that the matrix in the previous equation is a  $6 \times 6$  matrix instead of the  $4 \times 4$  matrix for conventional aircraft [Mulder et al., 2007]. The tether introduces new degrees of freedom ( $\theta_t$  and  $l_t$ ) which are responsible for the  $6 \times 6$  matrix configuration. The contribution of the tether can be found in the derivatives of the tether force coefficients  $C_F$ ,  $C_H$  and the derivatives of the tether moment coefficient  $C_Q$ . Because the tether is a spring-damper with known stiffness and damping, there is no need to measure the derivatives. For this model they can be calculated as is indicated in equations (3.2.6).

### 3.2.7 Matrix notation of the asymmetric equations of motion

In appendix D a more detailed discussion can be found on the linearization of the equations of motion and the kinematic relations pertaining to the asymmetric case. Grouping these equations as a function of  $\Delta \mathbf{X}$  and dropping the  $\Delta$ 's yields the following set of equations:

$$\begin{aligned}
 W \cos \theta_0 \cdot \dot{\phi} + Y_{v_a} \cdot v_a + Y_{\dot{v}_a} \cdot \dot{v}_a + Y_p \cdot p + Y_r \cdot r \\
 + G_\tau \cdot \tau + G_{x_{taL}} \cdot x_{taL} + G_{x_{taR}} \cdot x_{taR} &= m \cdot \dot{v}_k \\
 L_{v_a} \cdot v_a + L_p \cdot p + L_r \cdot r \\
 + P_\tau \cdot \tau + P_{x_{taL}} \cdot x_{taL} + P_{x_{taR}} \cdot x_{taR} &= I_x \cdot \dot{p} - J_{xz} \cdot \dot{r} \\
 N_{v_a} \cdot v_a + N_{\dot{v}_a} \cdot \dot{v}_a + N_p \cdot p + N_r \cdot r \\
 + R_\tau \cdot \tau + R_{x_{taL}} \cdot x_{taL} + R_{x_{taR}} \cdot x_{taR} &= I_z \cdot \dot{r} - J_{xz} \cdot \dot{p} \\
 p + \tan \theta_0 \cdot r &= \dot{\phi} \\
 \frac{1}{\cos \theta_0} \cdot r &= \dot{\psi} \quad (3.48) \\
 -v_k + z_{ta} \cdot p - x_{ta0} \cdot r &= l_{t0} \sin \theta_{t0} \cdot \dot{\psi}_t \\
 \dot{r} - \sin \kappa_0 \cdot \dot{\xi} - (\sin \theta_{t0} \cos \kappa_0 + \cos \theta_{t0} \sin \kappa_0) \cdot \dot{\psi}_t &= p \\
 \cos \kappa_0 \cdot \dot{\xi} - (\sin \theta_{t0} \sin \kappa_0 - \cos \theta_{t0} \cos \kappa_0) \cdot \dot{\psi}_t &= r \\
 v_k + W_{x0} \sin \theta_0 \cdot \phi - W_{x0} \cdot \psi + W_y &= v_a \\
 \dot{v}_k + W_{x0} \sin \theta_0 \cdot p - W_{x0} \cdot r &= \dot{v}_a
 \end{aligned}$$

These 10 relations can be reduced to a set of 6 equations, depending on the states  $v_k$ ,  $\phi$ ,  $p$ ,  $\psi$ ,  $r$  and  $\psi_t$ .

A relation can be found for  $\tau$  depending on  $\phi$ ,  $\psi$  and  $\psi_t$  by taking equations 4,5,7 and 8 of (3.48) together:

$$\dot{r} = \dot{\phi} + (-\sin \theta_0 + \tan \kappa_0 \cos \theta_0) \cdot \dot{\psi} + \frac{\sin \theta_{t0}}{\cos \kappa_0} \cdot \dot{\psi}_t$$



and equation (3.49) can be integrated, which yields:

$$\tau = \phi + (-\sin \theta_0 + \tan \kappa_0 \cos \theta_0) \cdot \psi + \left( \frac{\sin \theta_{t0}}{\cos \kappa_0} \right) \cdot \psi_t \quad (3.49)$$

Reducing the 10 equations to 6 and collecting terms the following set of equations is obtained:

$$\begin{aligned} & Y_{v_a} \cdot v_k + Y_{\dot{v}_a} \cdot \dot{v}_k + (W \cos \theta_0 + W_{x0} \sin \theta_0 Y_{v_a} + G_\tau) \cdot \phi \\ & \quad + (Y_p + W_{x0} \sin \theta_0 Y_{\dot{v}_a}) \cdot p \\ & + (-W_{x0} Y_{v_a} + G_\tau (-\sin \theta_0 + \tan \kappa_0 \cos \theta_0)) \cdot \psi \\ & \quad + (-W_{x0} Y_{\dot{v}_a} + Y_r) \cdot r + G_\tau \left( \frac{\sin \theta_{t0}}{\cos \kappa_0} \right) \cdot \psi_t \\ & \quad + W_y \cdot Y_{v_a} + G_{x_{taL}} \cdot x_{taL} + G_{x_{taR}} \cdot x_{taR} = m \cdot \dot{v}_k \\ & \quad \quad \quad p + \tan \theta_0 \cdot r = \dot{\phi} \\ & L_{v_a} \cdot v_k + (W_{x0} \sin \theta_0 L_{v_a} + P_\tau) \cdot \phi + L_p \cdot p \\ & \quad + (-W_{x0} L_{v_a} + P_\tau (-\sin \theta_0 + \tan \kappa_0 \cos \theta_0)) \cdot \psi + L_r \cdot r \\ & + P_\tau \left( \frac{\sin \theta_{t0}}{\cos \kappa_0} \right) \cdot \psi_t + W_y \cdot L_{v_a} + P_{x_{taL}} \cdot x_{taL} + P_{x_{taR}} \cdot x_{taR} = I_x \cdot \dot{p} - J_{xz} \cdot \dot{r} \\ & \quad \quad \quad \frac{1}{\cos \theta_0} \cdot r = \dot{\psi} \\ & N_{v_a} \cdot v_k + N_{\dot{v}_a} \cdot \dot{v}_k + (W_{x0} \sin \theta_0 N_{v_a} + R_\tau) \cdot \phi \\ & \quad + (W_{x0} \sin \theta_0 N_{\dot{v}_a} + N_p) \cdot p \\ & + (-W_{x0} N_{v_a} + R_\tau (-\sin \theta_0 + \tan \kappa_0 \cos \theta_0)) \cdot \psi \\ & \quad + (-W_{x0} N_{\dot{v}_a} + N_r) \cdot r + R_\tau \left( \frac{\sin \theta_{t0}}{\cos \kappa_0} \right) \cdot \psi_t \\ & \quad + W_y \cdot N_{v_a} + R_{x_{taL}} \cdot x_{taL} + R_{x_{taR}} \cdot x_{taR} = I_z \cdot \dot{r} - J_{xz} \cdot \dot{p} \\ & \quad \quad \quad -v_k + z_{ta} \cdot p - x_{ta0} \cdot r = l_{t0} \sin \theta_{t0} \cdot \dot{\psi}_t \end{aligned} \quad (3.50)$$

As for the symmetric equations of motion the asymmetric equations are made dimensionless as well. The divisors are given in table 3.1. The forces are divided by  $\frac{1}{2}\rho V_0^2 S$  and the moments by  $\frac{1}{2}\rho V_0^2 S b$ . The dimensionless quantities of  $p$  and  $r$  are  $\frac{pb}{2V_0}$  and  $\frac{rb}{2V_0}$  respectively, in accordance with conventional flight dynamics.

The dimensionless equations of motion can be written as:

$$\begin{aligned}
& (C_{Y_v} + C_{Y_v} D_b) \cdot \hat{v}_k + (-C_{Z_0} - C_{H_0} + C_{Y_v} \frac{W_{x0} \sin \theta_0}{V_0} + C_{G_\tau}) \cdot \phi \\
& \quad + (C_{Y_p} + 2C_{Y_v} \frac{W_{x0} \sin \theta_0}{V_0}) \cdot \frac{pb}{2V_0} \\
& \quad + (-C_{Y_v} \frac{W_x}{V_0} + C_{G_\tau} (-\sin \theta_0 + \tan \kappa_0 \cos \theta_0)) \cdot \psi \\
& \quad + (-2C_{Y_v} \frac{W_{x0}}{V_0} + C_{Y_r}) \cdot \frac{rb}{2V_0} + C_{G_\tau} \left( \frac{\sin \theta_{t0}}{\cos \kappa_0} \right) \cdot \psi_t + C_{Y_v} \\
& \quad \cdot \frac{W_y}{V_0} + C_{G_{x_{t\alpha L}}} \cdot \frac{x_{t\alpha L}}{b} + C_{G_{x_{t\alpha R}}} \cdot \frac{x_{t\alpha R}}{b} = 2\mu_b D_b \cdot \hat{v}_k \\
& \\
& \quad 2 \frac{pb}{2V_0} + 2 \tan \theta_0 \cdot \frac{rb}{2V_0} = D_b \cdot \phi \\
& \\
& \quad C_{l_v} \cdot \hat{v}_k + (-C_{l_v} \frac{W_{x0} \sin \theta_0}{V_0} + C_{P_\tau}) \cdot \phi \\
& \quad + C_{l_p} \cdot \frac{pb}{2V_0} + (-C_{l_v} \frac{W_x}{V_0} + C_{P_\tau} (-\sin \theta_0 + \tan \kappa_0 \cos \theta_0)) \cdot \psi \\
& \quad \quad + C_{l_r} \cdot \frac{rb}{2V_0} + C_{P_\tau} \left( \frac{\sin \theta_{t0}}{\cos \kappa_0} \right) \cdot \psi_t \\
& \quad + C_{l_v} \cdot \frac{W_y}{V_0} + C_{P_{x_{t\alpha L}}} \cdot \frac{x_{t\alpha L}}{b} + C_{P_{x_{t\alpha R}}} \cdot \frac{x_{t\alpha R}}{b} = 4\mu_b K_X^2 D_b \cdot \frac{pb}{2V_0} \\
& \quad \quad \quad - 4\mu_b K_X Z D_b \cdot \frac{rb}{2V_0} \\
& \\
& \quad \quad \quad \frac{2}{\cos \theta_0} \cdot \frac{rb}{2V_0} = D_b \cdot \psi \\
& \\
& \quad (C_{n_v} + C_{n_v} D_b) \cdot \hat{v}_k + (C_{n_v} \frac{W_{x0} \sin \theta_0}{V_0} + C_{R_\tau}) \cdot \phi \\
& \quad \quad + (2C_{n_v} \frac{W_{x0} \sin \theta_0}{V_0} + C_{n_p}) \cdot \frac{pb}{2V_0} \\
& \quad \quad + (-C_{n_v} \frac{W_x}{V_0} + C_{R_\tau} (-\sin \theta_0 + \tan \kappa_0 \cos \theta_0)) \cdot \psi \\
& \quad + (-2C_{n_v} \frac{W_x}{V_0} + C_{n_r}) \cdot \frac{rb}{2V_0} + C_{R_\tau} \left( \frac{\sin \theta_{t0}}{\cos \kappa_0} \right) \cdot \psi_t + \frac{W_y}{V_0} \cdot C_{n_v} \\
& \quad \quad \quad + C_{R_{x_{t\alpha L}}} \cdot \frac{x_{t\alpha L}}{b} + C_{R_{x_{t\alpha R}}} = 4\mu_b K_Z^2 D_b \cdot \frac{rb}{2V_0} \\
& \quad \quad \quad - 4\mu_b K_X Z D_b \cdot \frac{pb}{2V_0} \\
& \\
& \quad \quad \quad - \frac{v_k}{V_0} + 2 \frac{z_{t\alpha}}{b} \cdot \frac{pb}{2V_0} - 2 \frac{x_{t\alpha 0}}{b} \cdot \frac{rb}{2V_0} = \frac{l_{t0} \sin \theta_{t0}}{b} D_b \cdot \psi_t
\end{aligned} \tag{3.51}$$

where  $W \cos \theta_0$  has been replaced by  $-Z_0 - H_0$  as was done in the symmetric equations.  $C_{Y_v}$ ,  $C_{Y_{\hat{v}}}$ ,  $C_{y_p}$ ,  $C_{y_r}$ ,  $C_{l_v}$ ,  $C_{l_p}$ ,  $C_{l_r}$ ,  $C_{n_v}$ ,  $C_{n_{\hat{v}}}$ ,  $C_{n_p}$  and  $C_{n_r}$  are the so-called stability derivatives [Mulder et al., 2007].  $C_{G_\tau}$ ,  $C_{P_\tau}$  and  $C_{R_\tau}$  are the derivatives related to the tether.  $C_{G_{x_{t\alpha L}}}$ ,  $C_{G_{x_{t\alpha R}}}$ ,  $C_{P_{x_{t\alpha L}}}$ ,  $C_{P_{x_{t\alpha R}}}$ ,  $C_{R_{x_{t\alpha L}}}$  and  $C_{R_{x_{t\alpha R}}}$  denote the input derivatives of the control system.

The next step is to write the equations in matrix notation depending on the dimensionless states  $\hat{v}_k$ ,  $\phi$ ,  $\frac{pb}{2V_0}$ ,  $\psi$ ,  $\frac{rb}{2V_0}$  and  $\psi_t$  with  $\frac{W_y}{V_0}$ ,  $\frac{x_{t\alpha}^L}{b}$  and  $\frac{x_{t\alpha}^R}{b}$  as inputs:



A number of notable differences with the flight dynamics of conventional aircraft can be observed. Most notable is the fact that the matrix in the previous equation is a  $6 \times 6$  matrix instead of the  $4 \times 4$  matrix for conventional aircraft [Mulder et al., 2007]. The tether introduces new degrees of freedom which are responsible for the  $6 \times 6$  matrix configuration. The contribution of the tether can be found in the derivatives of the tether force coefficient  $C_G$  and the derivatives of the tether moment coefficients  $C_P$  and  $C_R$ . Because the tether is a spring-damper with known stiffness and damping, there is no need to measure the derivatives. For this model they can be calculated as is indicated in section D.

The coefficients  $C_{G_{x_{taL}}}$ ,  $C_{G_{x_{taR}}}$ ,  $C_{P_{x_{taL}}}$ ,  $C_{P_{x_{taR}}}$ ,  $C_{R_{x_{taL}}}$  and  $C_{R_{x_{taR}}}$  deserve deeper analysis. Appendix E presents a more thorough investigation on the influence of  $G$ ,  $P$  and  $R$  as a result of an anti-symmetric control input.

### 3.2.8 Simulation results

In order to build confidence in the validity of the Newton-based kite model, some simulation results are presented and commented. The purpose of the analysis is to provide a qualitative validation.

For the symmetric motions, the effects of the inputs on pitch angle  $\theta$  is of interest. Figure 3.4 shows the effect of one-second input pulses of different magnitudes.

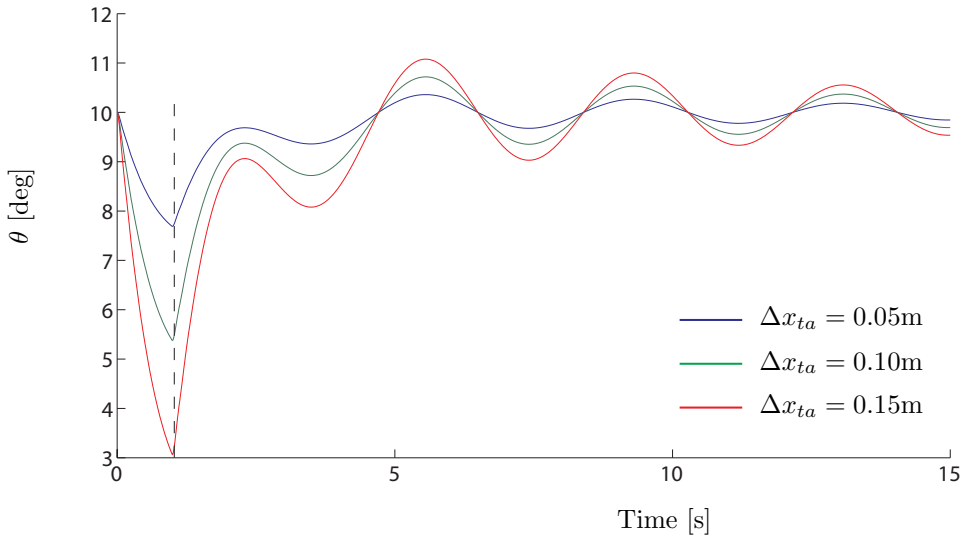


**Figure 3.4:** *The effect of a symmetric control input  $\Delta x_{ta}$  on pitch angle  $\theta$ .*

The input pulses consists of a shift in tow point along the  $X_B$ -axis ( $x_{ta}$ ). For the first second of the simulation, the tow point is shifted forward instantly for distances of resp. 5cm, 10cm and 15cm. This increases the moment arm of the tether force and creates a pitch-down moment which can clearly be seen in the resulting dip in pitch angle  $\theta$ . After the first second, the tow point is shifted back instantly to its original position, restoring the equilibrium of the initial conditions. Due to the pitch stability of the kite, a converging oscillation returns the kite to its original pitch angle.

In the second simulation, the kite is subjected to a wind gust  $\Delta W_x$  in  $X_E$  direction. The wind gust starts at 1 second and ends at 3.5 seconds. Figure fig:simresult2 shows the resulting effects on the pitch angle  $\theta$

Due to the temporarily increased wind velocity, the kite experiences an increased lift- and drag force. The resulting acceleration creates a decrease in angle of attack. Due to the static stability characteristics of the kite, a decrease in angle of attack results in a pitch-up moment. This in turn temporarily increases the

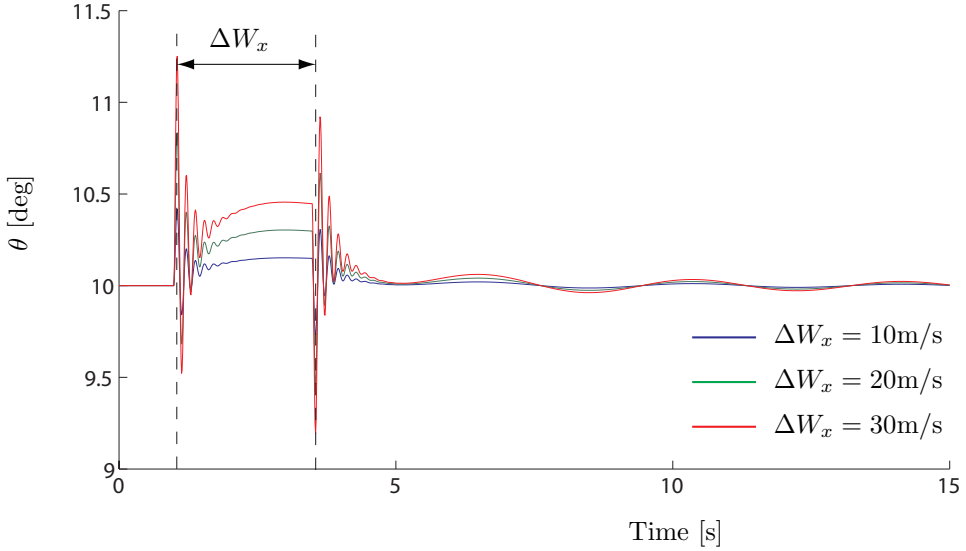


**Figure 3.5:** *The effect of a windgust input  $\Delta W_x$  on pitch angle  $\theta$ .*

pitch angle  $\theta$  as can be seen in figurefig:simresult2. Furthermore, the instantly changing gust creates some hysteresis at  $t = 1\text{s}$  and  $t = 3.5\text{s}$ . After the gust has passed, the kite converges back to its original pitch angle.

For the asymmetric motions, the tether angle  $\psi_t$  is of interest. In section 3.4.3, the eigenvalues of the equations of motion will be calculated. From this calculation, it becomes clear that one of the asymmetric eigenmotions of the kite is unstable. This instability is mostly manifested as a divergence in  $\psi_t$ . In figure 3.6 a 1-second anti-symmetric input pulse is introduced. This anti-symmetric input pulse consists of the right tow point ( $x_{taR}$ ) shifting forwards and the left tow point ( $x_{taL}$ ) shifting backwards such that  $x_{taR} = -x_{taL}$ .

After the one second input pulse, the tow points instantly shift back to their original position. As can be seen in figure fig:simresult3, the kite does not return to its equilibrium. The input pulse has created a divergent motion. In this thesis, this motion is called the asymmetric inverted pendulum motion, this particular instability mode is often observed in kites. In the kite world, a stable asymmetric inverted pendulum motion is called "auto-zenith capability". It is the ability of the kite to return to its zenith position high in the sky when no further control inputs are given. It is a characteristic favored by novice kite surfers.

Figure 3.7 shows the effects on tether angle  $\psi_t$  of an anti-symmetric control input of  $\Delta x_{taR} = -\Delta x_{taL} = 0.04\text{m}$  for different pulse lengths. The black line in figure 3.7 represents a sustained control input of the same magnitude.

Even though a short 1-second control input makes the kite diverge slower,

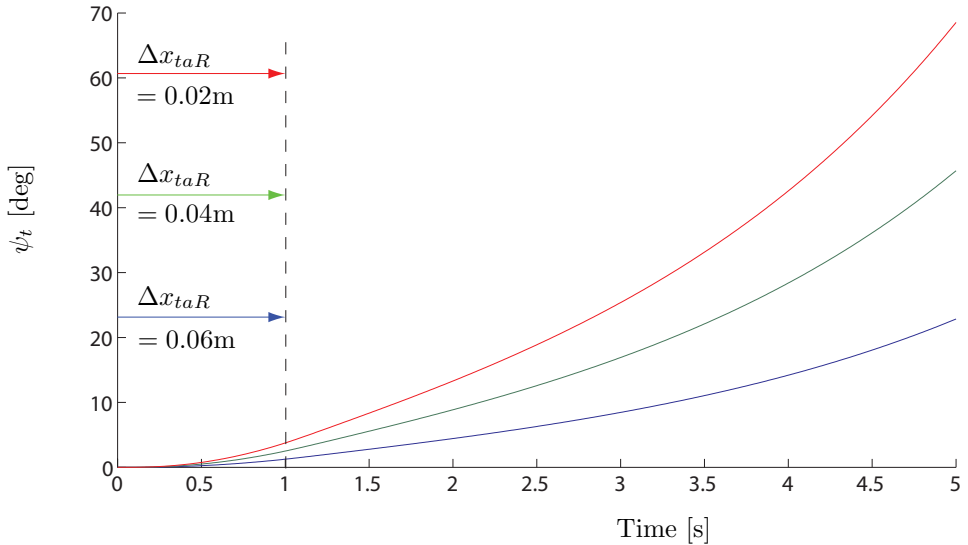


**Figure 3.6:** The effect of an asymmetric control input  $\Delta x_{taR} = -\Delta x_{taL}$  on tether angle  $\psi_t$ .

it diverges nonetheless. An interesting question is now how recoverable is this motion? Lets assume a person trying to control this particular kite by using instant control inputs of equal and opposing magnitude. Can this person keep the kite in the sky? Figure 3.8 shows the effects on tether angle  $\psi_t$  of an anti-symmetric control input, which is superceded by an opposing control input of the same magnitude. Three curves are plotted for three different lengths of the initial control input pulse.

When the kite controller reverses the control input after one second, the kite returns to it's zenith position and overshoots it to the other side. This maneuver takes significantly longer for an initial control input pulse of 1.5 seconds. For a initial control input pulse of 2 seconds, no recovery is possible with the prescribed control input.

In reality, a kite controller is not limited to just one set of opposing control inputs. Furthermore, the tow points do not shift instantly. And thus the analysis here is mostly hypothetical. However, it can be seen that for slow shifting controls, it becomes nearly impossible to control the kite. the kite flyer has to anticipate the motion of the kite and make corrections before the kite starts to diverge. This result agrees with the practical experience of controlling kites by shifting tow points.

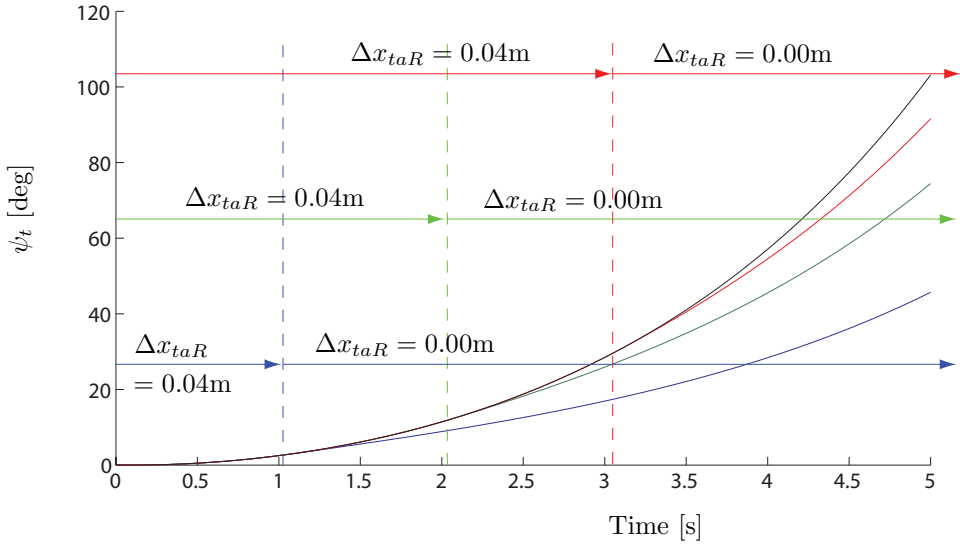


**Figure 3.7:** The effect of an asymmetric control input  $\Delta x_{taR} = -\Delta x_{taL} = 0.04\text{m}$  for different pulse lengths on tether angle  $\psi_t$ .

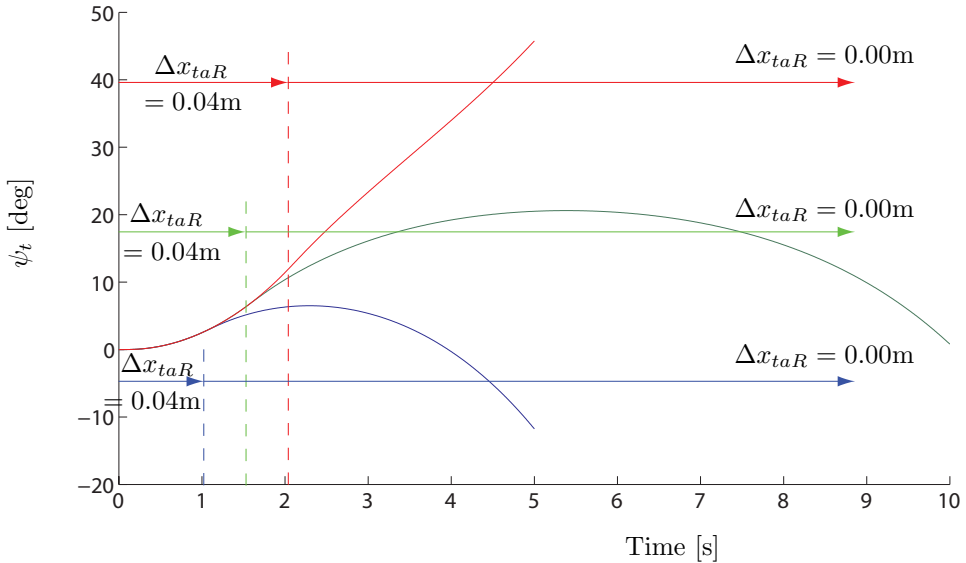


**Figure 3.8:** Recovery analysis with opposed control inputs  $\Delta x_{taR} = -\Delta x_{taL} = 0.04\text{m}$  after different pulse lengths.



### 3.3 Lagrange-based kite model

In this section, the equations of motion for the same kite system are derived. This time, Lagrange's equations of motion are used. Significant work on this model was performed by Master Thesis student Edwin Terink [Terink et al., 2010].

#### 3.3.1 Kite system kinematics

As was discussed in the previous section, the origin of the body reference frame is located at the *cg* of the Kite. In order to define the center of gravity in the earth frame of reference, the location of the cable attachment point with respect to the center of gravity is needed. The location of this point in the body-fixed frame of reference is denoted by  $r_{ta}^B$  and defined as:

$$\mathbf{r}_{ta}^B = \begin{bmatrix} x_t \\ 0 \\ z_t \end{bmatrix} E_B \quad (3.52)$$

The position vector of the center of gravity is now defined by equation (3.53):

$$\mathbf{r}_{cg} = \begin{bmatrix} 0 \\ 0 \\ -l_t \end{bmatrix} E_t + \begin{bmatrix} -x_t \\ 0 \\ -z_t \end{bmatrix} E_B \quad (3.53)$$

The velocity of the center of gravity is simply the time derivative of its position and thus equal to equation (3.54).

$$\mathbf{V}_{cg} = \begin{bmatrix} 0 \\ 0 \\ \dot{-l}_t \end{bmatrix} E_t + \begin{bmatrix} 0 \\ 0 \\ -l_t \end{bmatrix} \dot{E}_t + \begin{bmatrix} \dot{-x}_t \\ 0 \\ \dot{-z}_t \end{bmatrix} E_B + \begin{bmatrix} -x_t \\ 0 \\ -z_t \end{bmatrix} \dot{E}_B \quad (3.54)$$

In fact the third term can be left out because the time derivatives of  $x_t$  and  $z_t$  are zero. The time derivative of the tether length  $l_t$  can be replaced by the roll-out speed  $f$ . The velocity of the center of gravity can now be written as equation (3.55).

$$\mathbf{V}_{cg} = \begin{bmatrix} 0 \\ 0 \\ f \end{bmatrix} E_t + \begin{bmatrix} 0 \\ 0 \\ -l_t \end{bmatrix} \dot{E}_t + \begin{bmatrix} -x_t \\ 0 \\ -z_t \end{bmatrix} \dot{E}_B \quad (3.55)$$

What remains is to determine the derivatives  $\dot{E}_{E''}$  and  $\dot{E}_B$ , or more precisely, the derivatives of the unit vectors in these reference frames. However, a position vector multiplied by the derivative of a reference frame is equivalent to the crossproduct between the rotation vector of the reference frame and the position vector. Thus, the velocity of the center of gravity is equal to equation (3.56).

$$\mathbf{V}_{cg} = \begin{bmatrix} 0 \\ 0 \\ f \end{bmatrix} E_t + \boldsymbol{\omega}_{E_t}^T \times \begin{bmatrix} 0 \\ 0 \\ -l_t \end{bmatrix} E_t + \boldsymbol{\omega}_{E_B}^B \times \begin{bmatrix} -x_t \\ 0 \\ -z_t \end{bmatrix} E_B \quad (3.56)$$

According to the definitions in appendix A, the reference frame  $E_t$  rotates with  $\dot{\psi}_t$ ,  $\dot{\theta}_t$  and  $\dot{\chi}_t$ . These angular velocities are denoted by  $a$ ,  $z$  and  $b$  respectively. Transforming the angular velocities to the  $E_t$  reference frame results in the rotation vector  $\boldsymbol{\omega}_{E_t}^T$ , as displayed in equation (3.57).

$$\boldsymbol{\omega}_{E_t}^T = \begin{bmatrix} 0 \\ 0 \\ b \end{bmatrix} + \mathbb{T}_{TE''} \begin{bmatrix} 0 \\ z \\ 0 \end{bmatrix} + \mathbb{T}_{TE''} \mathbb{T}_{E''E'} \begin{bmatrix} 0 \\ 0 \\ a \end{bmatrix} = \begin{bmatrix} -\cos(\chi_t) \sin(\theta_t) a + \sin(\chi_t) z \\ \sin(\chi_t) \sin(\theta_t) a + \cos(\chi_t) z \\ b + \cos(\theta_t) a \end{bmatrix} \quad (3.57)$$

The rotation vector  $\boldsymbol{\omega}_{E_B}^B$  can be derived in a similar way, the result is displayed in equation (3.58).

$$\begin{aligned} \boldsymbol{\omega}_{E_B}^B &= \begin{bmatrix} 0 \\ p \\ 0 \end{bmatrix} + \mathbb{T}_{BT} \begin{bmatrix} 0 \\ 0 \\ b \end{bmatrix} + \mathbb{T}_{BT} \mathbb{T}_{TE''} \begin{bmatrix} 0 \\ z \\ 0 \end{bmatrix} + \mathbb{T}_{BT} f T E'' \mathbb{T}_{E''E'} \begin{bmatrix} 0 \\ 0 \\ a \end{bmatrix} \\ &= \begin{bmatrix} -\sin(\theta) b + \cos(\theta) \sin(\chi_t) z + (-\cos(\theta) \cos(\chi_t) \sin(\theta_t) - \sin(\theta) \cos(\theta_t)) a \\ p + \cos(\chi_t) z + \sin(\chi_t) \sin(\theta_t) a \\ \cos(\theta) b + \sin(\theta) \sin(\chi_t) z + (-\sin(\theta) \cos(\chi_t) \sin(\theta_t) + \cos(\theta) \cos(\theta_t)) a \end{bmatrix} \end{aligned} \quad (3.58)$$

With the rotation vectors derived, equation (3.55) can be evaluated to find the velocity vector. The reference frame in which the velocity vector yields the shortest expression is the tether reference frame. The velocity vector in this reference frame is given by equation (3.59).

$$\mathbf{V}_{cg}^T = \begin{bmatrix} -\cos(\chi_t) z l_t - \sin(\chi_t) \sin(\theta_t) a l_t - \cos(\theta) (p + \cos(\chi_t) z + \sin(\chi_t) \sin(\theta_t) a) z_t + \\ \sin(\theta) (p + \cos(\chi_t) z + \sin(\chi_t) \sin(\theta_t) a) x_t \\ \sin(\chi_t) z l_t - \cos(\chi_t) \sin(\theta_t) a l_t - (\cos(\theta) b + \sin(\theta) \sin(\chi_t) z + \\ (-\sin(\theta) \cos(\chi_t) \sin(\theta_t) + \cos(\theta) \cos(\theta_t)) a) x_t + \\ (-\sin(\theta) b + \cos(\theta) \sin(\chi_t) z + (-\cos(\theta) \cos(\chi_t) \sin(\theta_t) - \sin(\theta) \cos(\theta_t)) a) z_t \\ \sin(\theta) (p + \cos(\chi_t) z - \sin(\chi_t) \sin(\theta_t) a) z_t + \\ \cos(\theta) (p + \cos(\chi_t) z + \sin(\chi_t) \sin(\theta_t) a) x_t - f \end{bmatrix} \quad (3.59)$$

By using the transformation matrices of appendix A, the velocity vector can be expressed in any of the other reference frames as well.

### 3.3.2 Kinetic and potential energy

The total kinetic energy of the Kite system, which consists of translational and rotational energy, is obtained from equation (3.60) by substituting equation (3.59) for the velocity and equation (3.58) for the rotation vector.

$$T = \frac{1}{2}m_k \mathbf{V}_{cg} \cdot \mathbf{V}_{cg} + \frac{1}{2}\omega_{cg}^T \cdot \mathbb{I} \cdot \omega_{cg} \quad (3.60)$$

The potential energy of the Kite system is given by equation (3.62) using the definition in equation (3.61).

$$V = m_g \mathbf{g} \cdot \mathbf{r}_{cg} \quad (3.61)$$

$$V = m_g g (-\cos(\chi_t) \sin(\theta_t) (-\cos(\theta)x_T - \sin(\theta)z_T) + \cos(\theta_t) (-l_T + \sin(\theta)x_T \cos(\theta)z_T) \quad (3.62)$$

The gravitational acceleration vector is in the positive  $Z_E$  direction, thus the potential energy is simply the  $z$ -component of the position vector in the earth reference frame multiplied by the gravitational mass and  $g$ . The gravitational mass differs from the inertial mass, because it does not account for the confined air. In a light inflatable structure this makes a difference and implementing it this way avoids the inclusion of buoyancy forces. The calculated difference in center of gravity between  $m_k$  and  $m_g$  needs evaluation on a per-kite basis whether or not it can be neglected.

### 3.3.3 Generalized forces

Since the Kite model is subjected to nonconservative forces such as aerodynamic and ground station loads, generalized forces need to be included in Lagrange's equations of motion to account for this. For now it is assumed that the resulting aerodynamic loads can be expressed as a force vector and a moment vector that act on the Kite center of gravity. In the body reference frame, these two vectors are given by equations (3.63) and (3.64) respectively.

$$\mathbf{F}_a^B = \begin{bmatrix} X \\ Y \\ Z \end{bmatrix} \quad (3.63)$$

$$\mathbf{M}_a^B = \begin{bmatrix} L \\ M \\ N \end{bmatrix} \quad (3.64)$$

The force from the ground station acting on the tether in the tether reference frame is defined in equation (3.65).

$$\mathbf{F}_{GS}^T = \begin{bmatrix} 0 \\ 0 \\ F_{GS} \end{bmatrix} \quad (3.65)$$

With the nonconservative forces specified, the generalized force  $Q_i$  for generalized coordinate  $q_i$  can be derived using the principle of virtual work in Eq. (3.66).

$$Q_i = \frac{\partial \dot{\mathbf{r}}}{\partial \dot{q}_i} \cdot \mathbf{F} + \frac{\partial \dot{\boldsymbol{\omega}}}{\partial \dot{q}_i} \cdot \mathbf{M}, \quad i = 1, \dots, 5 \quad (3.66)$$

The results of applying Eqs. (3.66) to the generalized coordinates in the kite system are displayed in Eqs. (3.67) through (3.71). Note that the nonconservative forces are transformed to the reference frames corresponding to the generalized coordinates.

$$Q_\theta = \frac{\partial}{\partial \dot{\theta}} \left( \mathbf{M}_a^B \cdot \begin{bmatrix} 0 \\ \dot{\theta} \\ 0 \end{bmatrix} + \mathbf{F}_a^B \cdot \left( \begin{bmatrix} 0 \\ \dot{\theta} \\ 0 \end{bmatrix} \times \begin{bmatrix} -x_t \\ 0 \\ -z_t \end{bmatrix} \right) \right) \quad (3.67)$$

$$Q_{\chi_t} = \frac{\partial}{\partial \dot{\chi}_t} \left( \mathbf{M}_a^T \cdot \begin{bmatrix} 0 \\ 0 \\ \dot{\chi}_t \end{bmatrix} + \mathbf{F}_a^T \cdot \left( \begin{bmatrix} 0 \\ 0 \\ \dot{\chi}_t \end{bmatrix} \times \begin{bmatrix} -x_t \\ 0 \\ -z_t \end{bmatrix} \right) \right) \quad (3.68)$$

$$Q_{l_t} = \frac{\partial}{\partial \dot{l}_t} \left( (\mathbf{F}_a^T + \mathbf{F}_{GS}^T) \cdot \begin{bmatrix} 0 \\ 0 \\ -\dot{l}_t \end{bmatrix} \right) \quad (3.69)$$

$$Q_{\theta_t} = \frac{\partial}{\partial \dot{\theta}_t} \left( \mathbf{M}_a^{E''} \cdot \begin{bmatrix} 0 \\ \dot{\theta}_t \\ 0 \end{bmatrix} + \mathbf{F}_a^{E''} \cdot \left( \begin{bmatrix} 0 \\ \dot{\theta}_t \\ 0 \end{bmatrix} \times \mathbf{r}_{cg}^{E''} \right) \right) \quad (3.70)$$

$$Q_{\psi_t} = \frac{\partial}{\partial \dot{\psi}_t} \left( \mathbf{M}_a^{E'} \cdot \begin{bmatrix} 0 \\ 0 \\ \dot{\psi}_t \end{bmatrix} + \mathbf{F}_a^{E'} \cdot \left( \begin{bmatrix} 0 \\ 0 \\ \dot{\psi}_t \end{bmatrix} \times \mathbf{r}_{cg}^{E'} \right) \right) \quad (3.71)$$

### 3.3.4 Equations of motion

Lagrange's equations of motion are defined by equation (3.72) and provide a second order differential equation for each of the generalized coordinates.

$$\frac{d}{dt} \frac{\partial T}{\partial \dot{q}_i} - \frac{\partial T}{\partial q_i} + \frac{\partial V}{\partial q_i} = Q_i, \quad i = 1, \dots, 5 \quad (3.72)$$

With the previous equations, the Lagrangian equations of motion are known. The forces on the kite can be calculated using conventional strip theory. For instance, for the Kiteplane the body is divided into components such as the left wing, the right wing, the vertical fins and the horizontal tail surface. The aerodynamic forces on these components are calculated locally. Using the transformation matrix from the local component reference system to the body fixed reference system, the contributions of the aerodynamic forces and moments of the component to the body forces and moments are calculated. A more detailed derivation of this model with regard to the kiteplane can be found in Terink et al. [2010].

The question now beckons how this model relates to the Newton based model of section 3.2. Appendix F gives a comparison of the two models based on a scenario where a Cessna Ce500 Citation is modeled as a kite, tethered to the ground. The reason for choosing this scenario is that the stability derivatives of this airplane are readily available [Mulder et al., 2007].

## 3.4 Tethered vs non-tethered flight

With the two rigid body models completed in the previous sections, it is now possible to make a comparison between tethered and non-tethered flight. With the question whether or not conventional airplane theory can be used to model a kite, a new question gains significance. Exactly what happens to the dynamics of a flying object when it is tethered to the ground? To answer this question, the eigenmodes of a tethered and untethered Cessna CE500 Citation are compared. An accurate model for this aircraft is available [Mulder et al., 2007], because this particular aircraft is partly owned by the faculty of Aerospace Engineering and used as a flying laboratory. In order to make this model suitable for flying as a kite, a small change needs to be made. The mass of the tethered Citation is far too large to allow it to fly as a kite in conventional wind speeds. Therefore, the mass of the tethered Citation was reduced by 96%. Since the stability derivatives are dimensionless, they remain the same for this adapted Citation model. In the following text the reference "airplane" relates to the non-tethered Citation and the reference "kite" relates to the tethered Citation. The tethered Citation kite is bridled along the  $Y_B$  axis, inhibiting roll motion. The main cable is modeled as a spring-damper.

### 3.4.1 Eigenmotions of non-tethered flight

Mulder et al. [2007] gives a detailed analysis of the dynamics of the untethered Citation. Some of the results are repeated here for completeness. In the symmetric

regime, the Citation exhibits two distinct eigenmodes: a phugoid motion with a period of 32.1 seconds and a short period oscillation with a period of 5.6 seconds. In the a-symmetric regime, the citation exhibits a periodic dutch-roll motion with a period of 2 seconds and two a-periodic motions: a highly dampened roll motion and a slightly dampened spiral motion. Table 3.2 gives an overview of the symmetric eigenmotions of the non-tethered Citation.

**Table 3.2:** *Symmetric eigenmotions of the untethered Cessna CE500 Citation.*

Eigenmotion	Period [s]	Amplitude half-life [s]
Phugoid motion	32.1	81
Short period motion	5.6	0.6

Table 3.3 does the same for the asymmetric eigenmotions of the non-tethered Citation.

**Table 3.3:** *Asymmetric eigenmotions of the untethered Cessna CE500 Citation.*

Eigenmotion	Period [s]	Amplitude half-life [s]
Dutch roll motion	2	2.34
A-periodic roll motion	n/a	0.223
Spiral motion	n/a	6.782

The eigenmotions found for the untethered Citation are characteristic for conventional aircraft. The question now is how these eigenmotions change for the tethered Citation. The tether itself is modelled as a spring-damper between the ground and the cable attachment point on the kite and it is assumed to have no mass and no aerodynamic drag. The tether introduces new degrees of freedom which result in additional eigen values of the characteristic equation.

### 3.4.2 Symmetric eigenmotions of tethered flight

For the tethered Citation we find the following eigenvalues from the symmetric characteristic equation:

**Table 3.4:** *Eigenvalues from the symmetric characteristic equation.*

$\lambda_1$	-37.51
$\lambda_2$	-5.41 + 38.44i
$\lambda_3$	-5.41 - 38.44i
$\lambda_4$	-0.097 + 1.67i
$\lambda_5$	-0.097 - 1.67i
$\lambda_6$	-1.02

The eigenvalues in table 3.4 indicate the presence of two a-periodic eigenmotions, corresponding to  $\lambda_1$  and  $\lambda_6$  and two periodic eigenmotions, corresponding to  $\lambda_{2,3}$  and  $\lambda_{4,5}$ . In order to determine in which degrees of freedom these eigenvalues are dominant, we compute the eigenvectors. The values of the components of the eigenvectors can be found in table 3.4

**Table 3.5:** *The eigenvectors corresponding to the eigenvalues of table 3.4.*

States	$\lambda_1$	$\lambda_{2,3}$	$\lambda_{4,5}$	$\lambda_6$
$\hat{u}_k$	0.0429	$-0.0573 \pm 0.0286i$	$-0.9314 \pm 0.0000i$	-0.6523
$\hat{w}_k$	-0.0415	$0.7494 \pm 0.0000i$	$-0.0447 \pm 0.0062i$	-0.0410
$\theta$	0.6184	$-0.1192 \pm 0.1570i$	$-0.0340 \pm 0.0731i$	-0.6004
$\frac{q\bar{c}}{V_0}$	-0.7829	$-0.1819 \pm 0.1833i$	$-0.0040 \pm 0.0021i$	0.0208
$\theta_t$	0.0007	$0.0004 \pm 0.0004i$	$-0.0194 \pm 0.3336i$	-0.3816
$\frac{l_t}{\bar{c}}$	-0.0344	$0.0788 \pm 0.5679i$	$-0.1080 \pm 0.0249i$	-0.2575

In order to facilitate interpretation of the eigenvector matrix, the relative magnitude of the components are calculated. This method of interpretation of the eigenvector matrix is described both by Mulder et al. [2007] and Cook [1997]. The operation yields the amplitude of the components of the undamped characteristic motions. The values are displayed in table 3.6.

**Table 3.6:** *The relative magnitude of the components of the undamped characteristic, symmetric motions.*

States	$\lambda_1$	$\lambda_{2,3}$	$\lambda_{4,5}$	$\lambda_6$
$\hat{u}_k$	0.0429	0.0641	0.9314	0.6523
$\hat{w}_k$	0.0415	0.7494	0.0451	0.0410
$\theta$	0.6184	0.1971	0.0806	0.6004
$\frac{q\bar{c}}{V_0}$	0.7829	0.2583	0.0045	0.0208
$\theta_t$	0.0007	0.0005	0.3341	0.3816
$\frac{l_t}{\bar{c}}$	0.0344	0.5734	0.1108	0.5256

The eigenvector related to  $\lambda_1$  shows a strong dominance in pitch angle  $\theta$  and pitch rate  $q$ , which means this eigenmotion is mostly in pitch. The eigenvalue for  $\lambda_1$  is strongly negative, indicating a high level of damping on this a-periodic motion. The airplane also sees a fast pitching eigenmotion, namely the short period motion. For the kite it seems this motion is no longer periodic. It is plausible this is caused by the strong decrease in mass. The kite has little rotational inertia around its  $Y_B$ -axis while the flow over the kite offers ample damping.

The eigenvector related to  $\lambda_{2,3}$  shows a strong dominance in cable elongation  $l_t$  and velocity  $\hat{w}$ . This motion is a periodic motion which is relatively fast and strongly damped. The strong dominance in  $l_t$  suggests this motion relates to the elongation of the tether itself. The dominance in  $\hat{w}$  further supports this

conclusion because of the high lift over drag characteristics of the Cessna CE500 Citation kite. This high lift over drag of the kite will make it fly high at low tether elevation angle  $\theta_t$ , thus increasing the contribution of the vertical component to the elongation of the tether. The period and damping properties of this motion is directly related to the stiffness and damping values of the spring-damper which governs the tether force. Obviously, this eigenmotion is not present in non-tethered flight.

The eigenvector related to  $\lambda_{4,5}$  shows a strong dominance in  $\hat{u}$  and a reduced dominance in the tether zenith angle  $\theta_t$  and cable length  $l_t$ . This motion is a relatively slow periodic motion and is only slightly dampened. The dominance in  $\hat{u}$  together with the reduced dominance in  $\theta_t$  suggests this motion is a symmetric inverted pendulum motion. In fact, it seems related to the phugoid motion for aircraft. However, in the case of kites, the cable limits the motion in the  $X_E$ - $Z_E$  plane which transforms the traditional phugoid motion into this symmetric inverted pendulum motion. The elongation of the tether is a direct result of the acceleration in  $\hat{u}$ , generating a higher apparent velocity and thus a higher lift force.

The eigenvector related to  $\lambda_6$  shows a strong dominance in  $\hat{u}$ ,  $l_t$  and  $\theta$ . This motion is a slightly dampened a-periodic motion and seems related to the coupling of forward velocity  $\hat{u}$ , pitch and cable elongation. Its relation to the degrees of freedom resembles that of the eigenmotion related to  $\lambda_{4,5}$ . However, this eigenmotion sees a much stronger dominance in  $\theta$  which leads to the conclusion that this a-periodic eigenmotion is related to the pitch of the kite and the resulting position of the kite in the  $X_B$ - $Z_B$  plane. This position is strongly governed by the lift over drag of the kite and the resulting tether force.

### 3.4.3 Asymmetric eigenmotions of tethered flight

For the tethered Citation we find the following eigenvalues from the asymmetric characteristic equation:

**Table 3.7:** *Eigenvalues from the asymmetric characteristic equation.*

$\lambda_1$	$-24.98 + 38.76i$
$\lambda_2$	$-24.98 - 38.76i$
$\lambda_3$	$-6.78 + 6.32i$
$\lambda_4$	$-6.78 + 6.32i$
$\lambda_5$	$0.45$
$\lambda_6$	$-0.50$

The eigenvalues in table 3.4 indicate the presence of two a-periodic eigenmotions, corresponding to  $\lambda_5$  and  $\lambda_6$  and two periodic eigenmotions, corresponding to  $\lambda_{1,2}$  and  $\lambda_{3,4}$ . In order to determine in which degrees of freedom these eigenvalues are dominant, we again compute the eigenvectors.



**Table 3.8:** *The eigenvectors corresponding to the eigenvalues of table 3.7.*

States	$\lambda_{1,2}$	$\lambda_{3,4}$	$\lambda_5$	$\lambda_6$
$\hat{v}_k$	$0.0089 \pm 0.0154i$	$0.2214 \pm 0.1274i$	0.1027	-0.0925
$\phi$	$0.1036 \pm 0.1631i$	$-0.0988 \pm 0.1007i$	-0.1147	-0.1357
$\frac{pb}{2V_0}$	$-0.9555 \pm 0.0000i$	$0.1205 \pm 0.1458i$	0.0072	-0.0059
$\psi$	$0.0168 \pm 0.0396i$	$0.4759 \pm 0.4435i$	0.0887	-0.1094
$\frac{rb}{2V_0}$	$-0.2147 \pm 0.0374i$	$-0.6622 \pm 0.0000i$	-0.0049	-0.0054
$\psi_t$	$0.0018 \pm 0.0001i$	$0.1284 \pm 0.4435i$	0.9840	0.9803

In order to facilitate interpretation of the eigenvector matrix, the relative magnitude of the components are calculated. This method of interpretation of the eigenvector matrix is described both by Mulder et al. [2007] and Cook [1997]. The operation yields the amplitude of the components of the undampened characteristic motions. The values are displayed in table 3.9.

**Table 3.9:** *The relative magnitude of the components of the undampened characteristic, asymmetric motions.*

States	$\lambda_{1,2}$	$\lambda_{3,4}$	$\lambda_5$	$\lambda_6$
$\hat{v}_k$	0.0178	0.2554	0.1027	0.0925
$\phi$	0.1932	0.1411	0.1147	0.1357
$\frac{pb}{2V_0}$	0.9555	0.1891	0.0072	0.0059
$\psi$	0.0430	0.6505	0.0887	0.1094
$\frac{rb}{2V_0}$	0.2180	0.6622	0.0049	0.0054
$\psi_t$	0.0018	0.1318	0.9840	0.9803

The eigenvector related to  $\lambda_{1,2}$  shows a strong dominance in roll rate  $p$  and almost no effect on the tether azimuth angle  $\psi_t$ . It is a very fast and highly dampened periodic motion, most likely related to the bridle lines. The kite is bridled in  $Y_B$  direction by two bridle lines. This motion is a fast rolling motion in the bridle lines. It is related to the a-periodic roll motion of a conventional aircraft which is severely limited due to the presence of the bridle lines. The frequency of this periodic motion is strongly related to the stiffness of the bridle line spring-damper system. In practice, the high amount of damping of this motion makes it unlikely to significantly influence the stability of the kite.

The eigenvector related to  $\lambda_{3,4}$  shows a strong dominance in yaw angle  $\psi$  and yaw rate  $r$ . Reduced influence can be observed in all other states. This eigenmotion is a relatively fast periodic motion, strongly resembling the dutch roll motion of a conventional aircraft. For conventional aircraft, the dutch roll motion is a combination of yaw and roll. For bridled kites the roll is severely inhibited by the bridle lines, creating an eigenmotion which leans more to yaw than to roll. This yawing motion can be observed in many kites. Empirical

knowledge on kites suggests to add a long tail to the kite in order to overcome stability issues in this eigenmotion. This long tail then acts as a damper in yaw, increasing stability.

The eigenvectors related to  $\lambda_5$  and  $\lambda_6$  show a strong similarity. They both show a strong dominance in the tether azimuth angle  $\psi_t$  with only a slight contribution of roll angle  $\phi$  and yaw angle  $\psi$ . This motion is an asymmetric inverted pendulum motion and is related to the spiral motion of a conventional aircraft. Due to the presence of the tether, the spiral motion is inhibited, creating an inverted pendulum motion around the tether anchor point on the ground. In the case of this Citation kite, the motion is a-periodic. For other kites it was observed that this eigenmotion can also become either a stable or unstable periodic motion, often coupled with a yawing motion of the kite. In section 6.4 such an unstable periodic, asymmetric inverted pendulum motion is identified in the kiteplane. Design changes are suggested to overcome this stability issue.

## 3.5 Effects of cable length

In the previous chapter a comparison was made between the eigenmotions of a kite and an airplane. The cable for this model consists of a two-point force between the anchor point on the ground and the cable attachment point on the kite. This two-point force is modeled as a spring-damper to allow for cable elongation. As a model, this is not far from how an actual cable behaves. A cable between the ground and a kite will sag under gravitational and aerodynamic loads. The sagged cable behaves as a spring-damper. Short cables have only a slight amount of lag, making them act as a stiff spring with little damping. Long cables have a large amount of sag, making them act as weak springs with a large amount of damping. With these characteristics in mind for a real cable, we can now investigate the consequences of cable length in the rigid body model by varying the stiffness and damping of the modeled tether. Obviously, this comparison has its limits in that the actual tether length is not varied. Thus, this analysis is only valid for very short time intervals around equilibrium. By looking at the effects of stiffness and damping of the tether on the eigenvalues of the system, we can, in principle, say something about the effects of cable length on the stability of kites.

### 3.5.1 Effects of cable length on symmetric flight

In order to evaluate the effects of cable length on the symmetric eigenmotions of a kite, we compute these eigenvalues for a number of different values of cable stiffness and cable damping. Figure 3.9 shows the results of these computations.

Cable stiffness [ $N/m^2$ ]		Cable damping [ $Ns/m$ ]			
		E+0	E+1	E+2	E+3
E+11	$P[s]$	0.00551	0.00551	0.00552	0.00557
	$T_{0.5}[s]$	0.00452	0.00451	0.00433	0.00310
	$T_{0.5}[s]$	0.00062	0.00062	0.00062	0.00062
	$P[s]$	0.12726	0.12726	0.12726	0.12726
	$T_{0.5}[s]$	0.24222	0.24222	0.24222	0.24222
	$T_{0.5}[s]$	0.02284	0.02284	0.02284	0.02284
E+10	$P[s]$	0.01950	0.01952	0.01974	0.02317
	$T_{0.5}[s]$	0.00422	0.00420	0.00404	0.00290
	$T_{0.5}[s]$	0.00064	0.00064	0.00064	0.00065
	$P[s]$	0.13437	0.13437	0.13435	0.13408
	$T_{0.5}[s]$	0.14707	0.14697	0.14660	0.14276
	$T_{0.5}[s]$	0.02010	0.02010	0.02009	0.01997
E+9	$P[s]$	0.08755	0.08769	0.08907	0.09992
	$T_{0.5}[s]$	0.03139	0.03144	0.03201	0.03838
	$T_{0.5}[s]$	0.00065	0.00065	0.00065	0.00066
	$P[s]$	0.29760	0.29785	0.30025	0.32766
	$T_{0.5}[s]$	0.10173	0.10147	0.09893	0.08099
	$T_{0.5}[s]$	0.00215	0.00214	0.00205	0.00144
E+8	$P[s]$	0.10032	0.10045	0.10174	0.11318
	$T_{0.5}[s]$	0.06712	0.06695	0.06545	0.05886
	$T_{0.5}[s]$	0.00065	0.00065	0.00065	0.00066
	$P[s]$	1.16409	1.16537	1.17635	1.34153
	$T_{0.5}[s]$	0.78517	0.07722	0.67430	0.31281
	$T_{0.5}[s]$	0.00193	0.00192	0.00186	0.00136
E+7	$P[s]$	0.11311	0.11328	0.11495	0.13025
	$T_{0.5}[s]$	0.07246	0.07215	0.06939	0.05579
	$T_{0.5}[s]$	0.00065	0.00065	0.00065	0.00066
	$P[s]$	8.12631	8.12631	8.22080	9.86496
	$T_{0.5}[s]$	6.68516	6.49946	5.08653	1.74612
	$T_{0.5}[s]$	0.00191	0.00190	0.00184	0.00136

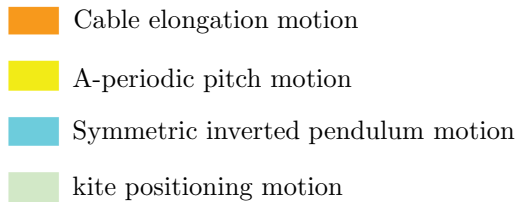


**Figure 3.9:** Values for the period  $P$  and time to damp to half the amplitude  $T_{0.5}$  of the symmetric motions for different values of cable stiffness and damping.

In figure 3.9 the values towards the top left of the figure are equivalent to a shorter tether and the values towards the bottom right are equivalent to a longer tether. For the a-periodic pitch motion, the eigenvalues in figure 3.9 show that the damping of the motion is independent of the tether stiffness and damping. This concurs with the earlier conclusion of section 3.4.2 that this motion is dominated by fast pitching motions and that it has little effect on the tether. The cable elongation motion, however, shows a strong dependence on the stiffness and damping of the main cable. The motion shows shorter periods for shorter cables and the increased damping for long cables enlarges the time to damp to half the amplitude. The symmetric inverted pendulum motion shows a more complex dependency on tether stiffness and damping. The motion shows to have a shorter period and is more damped for stiffer cables. However, tether damping shows to play only a marginal role. For the kite positioning motion, the dependency is clear. The a-periodic motion is faster for longer cables.

### **3.5.2 Effects of cable length on asymmetric flight**

In order to evaluate the effects of cable length on the asymmetric eigenmotions of a kite, we compute these eigenvalues for a number of different values of cable stiffness. In the model the cable damping has no effect on asymmetric motions as it was neglected during linearization of the equations of motion. Figure 3.10 shows the results of the eigenvalue computations.

Cable stiffness [ $N/m^2$ ]	E+11	$P[s]$	0.005471965		E+6	$P[s]$	0.005474225	
		$T_{0.5}[s]$	0.000936762			$T_{0.5}[s]$	0.00093572	
		$P[s]$	0.033559067			$P[s]$	0.033413151	
		$T_{0.5}[s]$	0.003450685			$T_{0.5}[s]$	0.003440992	
		$T_{0.5}[s]$	-0.051834419			$T_{0.5}[s]$	-0.335696653	
		$T_{0.5}[s]$	0.046871107			$T_{0.5}[s]$	0.991443082	
	E+10	$P[s]$	0.005471994			E+5	$P[s]$	0.005474239
		$T_{0.5}[s]$	0.00093675				$T_{0.5}[s]$	0.000935713
		$P[s]$	0.033556943				$P[s]$	0.033412099
		$T_{0.5}[s]$	0.003450532				$T_{0.5}[s]$	0.003440941
		$T_{0.5}[s]$	-0.052099881				$T_{0.5}[s]$	-0.467961135
		$T_{0.5}[s]$	0.047202051				$T_{0.5}[s]$	7.090320226
	E+9	$P[s]$	0.005472234			E+4	$P[s]$	0.005474239
		$T_{0.5}[s]$	0.000936638				$T_{0.5}[s]$	0.000935713
		$P[s]$	0.033541554				$P[s]$	0.033412099
		$T_{0.5}[s]$	0.003449514				$T_{0.5}[s]$	0.003440891
		$T_{0.5}[s]$	-0.054706703				$T_{0.5}[s]$	-0.496774029
		$T_{0.5}[s]$	0.050394264				$T_{0.5}[s]$	58.49514187
	E+8	$P[s]$	0.005473264			E+7	$P[s]$	0.005474084
		$T_{0.5}[s]$	0.000936158				$T_{0.5}[s]$	0.000935784
$P[s]$		0.033474323	$P[s]$				0.033422102	
$T_{0.5}[s]$		0.003444994	$T_{0.5}[s]$				0.003441549	
$T_{0.5}[s]$		-0.074873782	$T_{0.5}[s]$				-0.16015097	
$T_{0.5}[s]$		0.076514247	$T_{0.5}[s]$				0.221153655	

	Bridle rolling motion
	Dutch roll motion
	Asymmetric inverted pendulum motion

**Figure 3.10:** Values for the period  $P$  and time to damp to half the amplitude  $T_{0.5}$  of the symmetric motions for different values of cable stiffness.

In figure 3.9 the values towards the top of the figure are equivalent to a shorter tether and the values towards the bottom are equivalent to a longer tether. As expected, both the bridle rolling motion and the dutch roll motion show little dependency on cable length. The asymmetric inverted pendulum motion, however, shows to converge faster for short tethers and slower for longer tethers. As can be seen from the negative values for the time to damp to half the amplitude, one of the asymmetric inverted pendulum motions is unstable. As a matter of fact, this particular eigenmotion is often of great interest in new kite designs as it is often the source of instability. This particular motion with regard to the kiteplane is

further investigated in section 6.4.

### 3.6 Concluding remarks

The main goal of this chapter is to investigate whether or not conventional flight dynamics theory could be used to model the dynamics of a kite. As was stated earlier, conventional aircraft are often modeled as a rigid body, which transforms the question into: can we model a kite as a rigid body? This chapter shows that, with the proper assumptions concerning the main tether, such a model is indeed possible. The two different models show excellent agreement and the eigenmotions obtained from the Newton-based model seem to concur, in general, with observations of flying kites in reality. However, the question remains: how good are these models? Section 6.4 offers, to a certain extent, a comparison between the Lagrangian model and the real world. For the newtonian model, one would need to obtain the stability derivatives of a kite to perform this validation. Securing these stability derivatives is where many difficulties lie. For conventional aircraft, the stability derivatives are measured during controlled flight tests. For kites, these measurements are more difficult. A kite is such a light structure that the measurement equipment would account for a large part of the total mass of the system. Furthermore, attaching rigid objects to a highly flexible structure will make it deform severely. And thus, the kite fitted with the measurement equipment will be a substantially different kite than one without. Other problems arise from the slow flying nature of a kite. In conventional aircraft, small vanes are used to measure the direction of the flow. The low speed at which the kite flies generates too little aerodynamic force by which these vanes are aligned. Lastly, the measurement equipment needed for these type of measurements represent a significant financial investment. One which most kite companies are unable to make.

From the comparison of tethered and non-tethered flight, based on the Cessna CE500 Citation, a number of issues became clear. In symmetric flight, the familiar short period motion becomes a-periodic due to a decreased rotational inertia around the  $Y_B$  axis. The phugoid motion becomes a symmetric inverted pendulum motion due to the presence of the tether. Extra eigenmotions occur as a result of the tether. These motions seem highly dependent on the length of the tether. For asymmetric flight, the dutch roll motion is largely dominated by yaw due to the inhibiting effect of the bridle lines. The familiar spiral motion becomes an asymmetric inverted pendulum motion under influence of the cable. A fast and highly dampened extra eigenmotion occurs where the kite rolls in its own bridle. In practice, this eigenmotion is of little effect on the stability of the kite.

---

## A Multi-body approach to kite simulations

---

*The ability to simulate different kite designs is a vital part of the engineering-approach to kite design. The ability to assess a design before its actually built provides the designer with the ability to distinguish between concepts faster and cheaper. Furthermore, simulations allow the designer to explore theoretical situations and configurations which are not desirable or even not possible in reality. Theoretical cases such as cases where gravity is turned off or where the kite is infinitely rigid can provide new insights into the dynamics of a kite. Section 4.1 gives a short introduction into the numerical model and explains some of the requirements. Section 4.2 gives a concise overview of the multi-body dynamics theory. Sections 4.3, 4.4 and 4.5 explain in detail the three building blocks which lay at the foundation of the multi-body kite model. Lastly, section 4.6 outlines the building of complete kite models from the aforementioned building blocks.*

### 4.1 Introduction

The rigid body models presented in chapter 3 provide valuable insight. However, they are limited in the sense that they do not take into account the flexibility of the structure. With kites, flexibility is not simply a by-product of the loads on the structure. The flexibility itself is used to give the kite certain attributes such as cornering performance (section 6.3) or depower capability. A kite simulation which can be used as a design tool will have to take this flexibility into account.

For a designer, a fast and intuitive simulation is a valuable tool. Long CPU times create a long turn-around period for results on the latest design. This drastically slows down the design process. But the requirement dictating a fast

simulation can directly conflict with the requirement to include structural flexibility. For structures of fabric and battens, one is easily inclined to call upon the field of fluid-structure interaction, coupling computational fluid dynamics with a finite element code for the structure. Such a highly complex simulation requires an enormous amount of preparation and processing power. Small kite design companies often have no resources to invest in such simulations. Also, the question beckons: Is such a complex simulation really needed? In other words, is all the information such a simulation yields relevant? Many kite designers have indicated not to be overly concerned with details such as: where do wrinkles occur and at what angle and amplitude. They are interested in the general shape as a result of a specific flight condition.

In this thesis the simulation for kite design is positioned somewhere in between rigid models and complex fluid structure interaction models. Therefore, a choice was made to use the principles of multi-body dynamics to approximate a kite structure and dynamic behavior under load. Multi-body dynamics describes the motions of an assembly of rigid and constrained bodies. This principle is the backbone of the kite simulation presented in this chapter.

The kite simulation toolbox which was developed runs under MSC ADAMS, a well-known multi-body dynamics software package by MSC Software. The toolbox integrates into ADAMS and can be used from within the program. It consists of three elements or building blocks with which different kite configurations can be assembled. The building blocks are (1) cables, (2) inflatable beams and (3) foils. For every kite configuration, a parameterized macro can be written which can assemble the desired kite configuration from the aforementioned building blocks. The parameterization of the macro allows the designer to quickly change properties such as chord length or wing span. This allows for exploration of many different variations of a kite, without reprogramming the entire macro. The following three sections will outline the three main building blocks which lay at the root of every simulated kite within the kite simulation toolbox.

## 4.2 The principles of multi-body dynamics

Dynamics is a fundamental discipline in science and engineering. Dynamics describes the behavior of all things with time. And as such, the discipline of dynamics can be found in many fields. From particles such as electrons, through fluids and gasses, all the way to stars and galaxies are governed by the same principle laws of dynamics. In one of the more simple dynamic analyses, called "particle dynamics", mass and external forces are taken into account. A particle is considered to have infinitesimal small dimensions, and therefore no rotation of the particle around any body axis is considered. Rigid body dynamics governs the behavior of bodies which have both mass and dimensions. Therefore mass, external forces, as well as mass moments of inertia are accounted for.

Multi-body dynamics is the dynamic analysis of a collection of bodies connec-



ted by constraints. Constraints introduce the reaction forces on the bodies needed to enforce the constraints. They include joints such as revolute joints, spherical joints and translational joints. More complex constraints include gears, bearings and belt-drives. Rahnejat [1998] shows that these complex constraints are a combination of a number of simple constraint primitives. Other constraints include user imposed motions. These constraints prescribe a certain motion of a body or "part" in the assembly of bodies, regardless of external forces that may act on this particular body.

In the multi-body dynamic analysis, the Lagrange equations can be used to obtain the equations of motion of the entire assembly of bodies. However, for large assemblies with a large number of degrees of freedom, this can become a daunting task because one would have to consider the effects of all the system motions on all the bodies. Therefore, according to Rahnejat [1998], in large multi-body systems all parts are modelled separately, still using the Lagrange equations of motion. no coupling exists between the equations of motion of the different parts. A mathematical definition of the constraints is necessary to ensure the integrity of the multi-body system as a whole. Rahnejat [1998] gives an excellent summary of the multi-body dynamics methodology which is re-iterated here for clarity.

For each rigid body with 6 generalized coordinates we write:

$$[q] = [x, y, z, \psi, \theta, \phi]^T \quad (4.1)$$

With the rotational and translational components of  $q$ :

$$[q_t] = [x, y, z]^T \quad (4.2)$$

$$[q_r] = [\psi, \theta, \phi]^T \quad (4.3)$$

Lagrange's equation for each body yields:

$$F_j(\ddot{q}, \dot{q}, q, \lambda, t) = 0, \quad j = 1, \dots, 6 \quad (4.4a)$$

$$F_k(M_q, \dot{q}, q) = 0, \quad k = 1, \dots, 6 \quad (4.4b)$$

Where the later term gives the generalized moments. Because the translational components of  $F_k$  are already given by the translational velocities,  $F_k$  can be reduced to:

$$F_k (M_r, \dot{q}_r, q_r) = 0, \quad k = 4, 5, 6 \quad (4.5)$$

Furthermore:

$$[M] = [M_t, M_r]^T = [M_x, M_y, M_z, M_\psi, M_\theta, M_{phi}]^T \quad (4.6)$$

Thusfar we have 6 equations of motion and 3 equations of angular momentum for each body in the assembly. Rahnejat [1998] continues to introduce the additional variables:

$$[v] = [\dot{q}_t, \dot{q}_r]^T \quad (4.7)$$

Rahnejat [1998] continues to state that: "This satisfies the implicit formulation of the translational components of momenta as well as reducing the second order problem at hand to one of a first order. Therefore, there are six more equations specified by the vector,  $[v]$ ". In the previous equation the following relation holds:

$$[\ddot{q}] = [\dot{v}] \quad (4.8)$$

Now there are 15 equations for each body. these equations  $F_j = 0$ ,  $F_k = 0$  and  $[v] = [\dot{q}]$  are represented in a condensed format:

$$F \left( \dot{\xi}, \xi, \lambda, t \right) = 0 \quad (4.9)$$

With

$$\left[ \dot{\xi} \right] = \left[ \dot{v}, \dot{q}, \dot{M}_r \right] \quad (4.10a)$$

$$\left[ \xi \right] = \left[ v, q, M_r \right] \quad (4.10b)$$

At this point, the constraint equations need to be included. The reaction forces which the constraints introduce on the bodies are represented by Lagrange multipliers. These Lagrange multipliers can be obtained from the constraint functions.

$$c_i(q_t, q_r) = 0, \quad i = 1, \dots, 6 \quad (4.11)$$

Or in terms of  $\xi$ :

$$c(\xi) = 0 \quad (4.12)$$

The set of equations for a constrained multi-body system are now:

$$F\left(\dot{\xi}, \xi, \lambda, t\right) = 0 \quad (4.13)$$

$$c(\xi) = 0 \quad (4.14)$$

Equation (4.13) is a partial differential equation and equation (4.14) is an algebraic equation. The solution to the set of equation is obtained through implicit integration such that:

$$J\left(\xi, \lambda, \frac{s}{dt}\right) \cdot [\delta\xi, \delta\lambda]^T = -[F] \quad (4.15)$$

In equation (4.15),  $[\delta\xi, \delta\lambda]^T$  is the solution matrix,  $dt$  is the integration step size and  $s$  is the dimensionless scaling factor.  $J\left(\xi, \lambda, \frac{s}{dt}\right)$  is the Jacobian matrix defined as:

$$[J] = \begin{bmatrix} \left[\left(\frac{s}{dt}\right) \frac{\partial F}{\partial \dot{\xi}} + \frac{\partial F}{\partial \xi}\right] & \frac{\partial c}{\partial \lambda} \\ \frac{\partial c}{\partial \lambda} & 0 \end{bmatrix} \quad (4.16)$$

The jacobian is a sparse matrix. Furthermore, it contains a mix of linear- and non-linear algebraic equations, as well as partial differential equations. A solution method for such a set of equations is given by Orlandea et al. [1978]. This method is in fact used in the multi-body simulation software package MSC ADAMS, Which will be used extensively in the next chapters.

The remainder of this chapter outlines a model for flexible kites using a multi-body dynamics approach. This model uses existing multi-body dynamics theory. Therefore, the focus of the remainder of this chapter will be on the specifics of the model and the developed toolbox for MSC ADAMS, and not on the underlying conventional multi-body dynamics theory.

## 4.3 Building block 1: Cables

Cable dynamics is an important issue in the simulation of kites. The cable has a significant impact on the behavior of the kite and introduces modes of motion which are not present in free flying objects. Especially long cables exhibit a large amount of inertia. So much, in fact, that for a very long cable, one can consider the cable to have a memory of past motions and excitations. Modelling the cable force on the kite as a constant force vector would exclude the dynamic behavior of the cable. A proper dynamic simulation of the cable is required.

### 4.3.1 Cable model definition

Generally, the modes of motion in a cable can be divided into fast motions and slow motions. The fast motions are the longitudinal motions which are usually related to the high modulus of elasticity of the cable material. They are small in amplitude and travel through the cable very fast. Yen et al. [2009] investigated strain wave propagation velocities in steel cables and found these waves to travel through the cable with velocities in excess of 5000 m/s. The slow motions are the transversal motions which generally show a significant amount of inertia. They include waves that travel through the cable as a result of a lateral excitation. In modelling the flight behaviour of kites, the fast axial motions are of far lesser interest. Especially for cables made out of stiff materials such as Dyneema or Aramid, the fast motions are too fast and too short to have a significant impact on the stability of the kite. There are notable exceptions to this statement which will be dealt with in section 4.3.2(*Cable Strain*). The slow motions are able to tilt the cable force vector on the kite for a significant amount of time and therefore they have a larger impact on the stability of the kite. Subsequently, taking the fast motions into account would mean that the time integration step would have to be small. This would result in large calculation times and yield very little added value.

The cable model proposed in this thesis consists of a chain of discrete elements. These elements have a mass and they are infinitely stiff. Due to their infinite stiffness, they do not exhibit any strain under loading. In reality, a cable will elongate under stress. The maximum strain for cables made of high-tension fibers such as Dyneema and Aramid is approximately 2% to 4%. For short cables this strain amounts to an insignificant elongation. For long cables, however, strain can become more significant. An adaptation of this current model, which does take strain into account, is presented in section section 4.3.2(*Cable Strain*) The cable elements are hinged together using two hook joints on each end, allowing it to hinge in every direction but preventing it from twisting.

The reason for using the two hook joints and not a single spherical joint is because the fast oscillations that can occur around the axial direction of the cable element has little physical meaning. Furthermore, they have little effect on the flight dynamics of the kite. Therefore, it is taken out of the equation to speed up

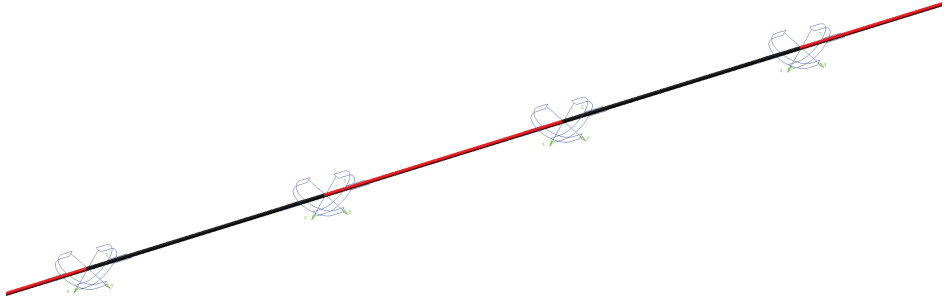


**Figure 4.1:** *Cable elements hinged by hook joints.*

the simulation process.

Damping of the cable motions comes in two forms. Material-based damping and Aerodynamic damping. Material-based damping is the dissipation of kinetic energy through heat, created by fibers rubbing against each other as the cable is bent and flexed. The material-based damping is dependent on the tension in the cable. The tension in the cable is a result of gravitational forces on the cable and the lift of the kite. Evaluating the damping using a simple analytical pendulum model is not possible due to the pretension which greatly effects the material based damping in the cable. For a cable we can say that the spring constant is equivalent to the tension divided by the element length. Therefore, the cable element equation of motion becomes:

$$\ddot{x} + \frac{c}{m}\dot{x} + \frac{T}{ml}x = 0 \quad (4.17)$$

This means that

$$2\beta\omega_0 = \frac{c}{m} \quad (4.18)$$

and

$$\omega_0^2 = \frac{T}{ml} \quad (4.19)$$

This results in the following equation:

$$c = 2\beta\sqrt{\frac{TM}{l}} \quad (4.20)$$

For rotational damping we divide by  $l$

$$c = 2\beta\sqrt{\frac{TM}{l^3}} \quad (4.21)$$

In equation (4.21) we see that the damping is dependent on the element length  $l$ , the element mass  $m$  and tension  $T$  in the element. The factor  $\beta$  is in the order of 1% to 5%, which is representative value for cable dynamics. In the model, the damping is introduced in the joints using torsion springs which have no stiffness, only damping. This is schematically represented in figure 4.2.

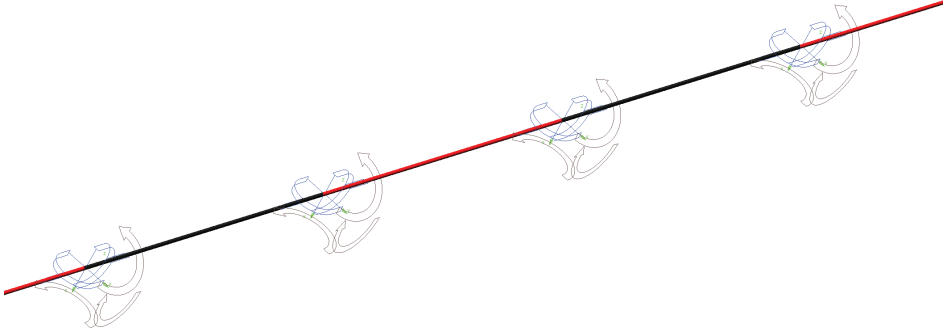


**Figure 4.2:** *The inclusion of rotational dampers on the hinge joints.*

The second damping effect the cable experiences is due to aerodynamic forces. The aerodynamic drag is one of the most prominent forces on the cable and it consists of two velocity components. The first is the wind speed. The wind speed vector does not necessarily have to be horizontal and constant with altitude. With increasing altitude, the wind velocity will increase as well. The second velocity component is that of the motion of the cable itself with respect to the earth axis frame of reference. While the cable moves, it experiences drag in the opposite direction. For the apparent velocity vector of a cable element we can write:

$$V_{cable}^E = \begin{bmatrix} V_{x,wind}^E + V_{x,element}^E \\ V_{y,wind}^E + V_{y,element}^E \\ V_{z,wind}^E + V_{z,element}^E \end{bmatrix} \quad (4.22)$$

We can transform this vector to the local tether frame of reference using the definitions from section A.2:

$$V_{cable}^T = \mathbb{T}_{TE} V_{cable}^E \quad (4.23)$$

For the drag force in the tether frame of reference we can write:

$$D_{cable}^T = \begin{bmatrix} C_{D,cable} \frac{1}{2} \rho \left( V_{x,cable}^T \right)^2 d dl \\ C_{D,cable} \frac{1}{2} \rho \left( V_{y,cable}^T \right)^2 d dl \\ C_{f,cable} \frac{1}{2} \rho \left( V_{x,cable}^T \right)^2 \pi d dl \end{bmatrix} \quad (4.24)$$

In equation (4.24),  $C_{D,cable}$  is equal to 1.065 and  $C_{f,cable}$  is equal to 0.0017 [Hoerner, 1965a].  $x$ ,  $y$  and  $z$  are the coordinates of the endpoints of the element.  $d$  is the cable radius and  $\rho$  is the air density. In the model, the aerodynamic drag on the kite is simulated as a three-axis force which acts on the center of the cable element. Figure 4.3 shows the final cable model.

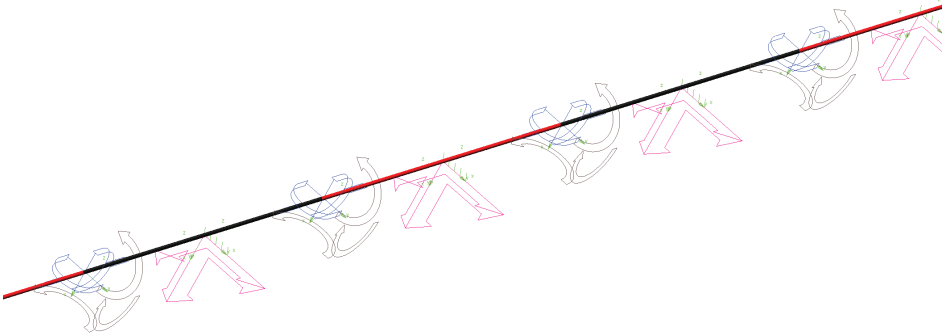


**Figure 4.3:** *The inclusion of aerodynamic drag using a force vector on the center of the element.*

### 4.3.2 Cable strain

In the previous section the distinction was made between fast motions and slow motions in the cable. It was stated that the fast motions are of lesser importance to the simulation of kites and, therefore, it was disregarded. There is a notable

exception to this statement with regard to the elongation of the cable due to strain. With varying wind conditions and gusts, the cable will constantly experience a varying strain in the cable. When, for instance, the kite experiences a wind gust, its temporary lift increase sends a wave of increased strain through the cable to the ground. The strain peaks can be of significant magnitude to break the cable, especially in situations where the cable is very long. During the attempts by Richard Synergy to break the world altitude record for a single kite on a single line, both the fruitless attempts he describes in his book *Synergy* [1994] failed due to a break in the line. For a static situation one would assume (and assume correctly) that the line would break at the kite where the gravitational component of the tension force is the largest. But in practice, a gust on the kite can create a strain wave in the cable which travels all the way down to the ground. If the cable is rigidly fixed to the ground, the strain wave will reflect and travel back up the cable. This can cause interference which can lead to tension peaks at the ground attachment point, which can easily result in cable failure.

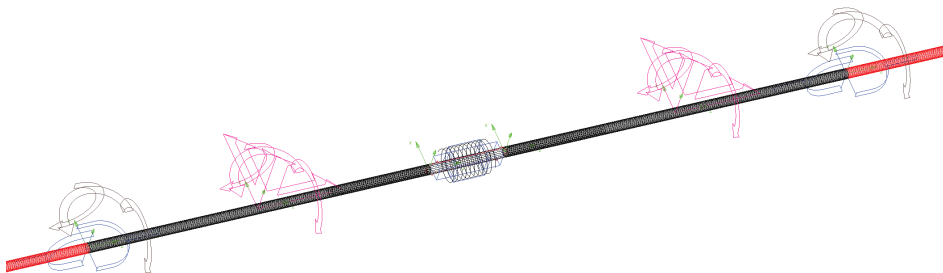


**Figure 4.4:** *The complete cable model incorporating elasticity.*

The model that was proposed thusfar is an infinitely rigid model which does not experience any strain. This results in a situation where strain waves due to a wind gust travel down the cable instantaneously. Large strain peaks are the result which are unrealistic. Especially for long cables, a certain amount of elasticity is required to obtain a more realistic simulation. In order to incorporate axial flexibility in the cable, the elements which make up the cable have been divided into two parts. In the middle, they are joint by a translational joint which only allows axial motion. A spring-damper provides the correct amount of elasticity. Figure 4.4 shows the final cable model incorporating cable elasticity.



### 4.3.3 The cable toolbox implementation

As part of a larger kite simulation toolbox, the cable simulation is implemented as a tool which is accessible from a toolbar. The the cable tool is able to quickly generate cables of the desired number of elements in between two markers. Markers are points in 3D space fixed on either the background or other elements such as rigid bodies, joints or force elements. This allows the designer to quickly test, for instance, different bridle systems by simply selecting the begin- and endpoint of a line and letting the cable tool generate the cable model in between. Figure 4.5 shows the GUI of the cable toolbox.

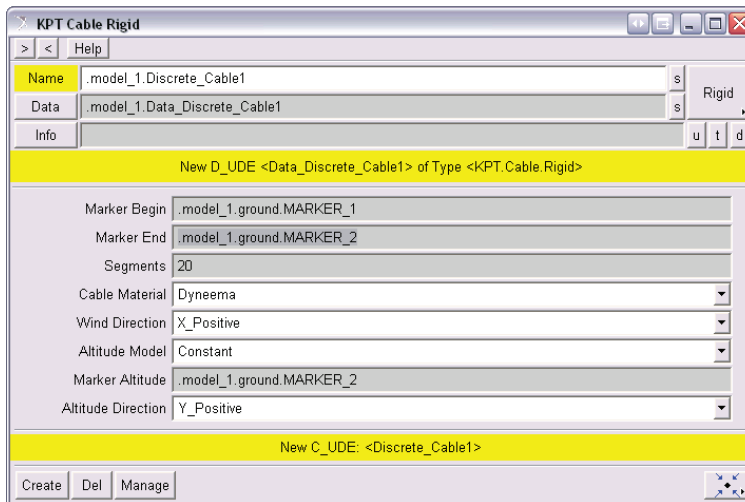


Figure 4.5: *The interface of the cable tool.*

At the top of this interface the choice can be made between the rigid and elastic cable models. Even though the rigid cable model is less realistic, it is still maintained within the toolbox because for short cables such as bridles, the extra complexity of elasticity has very little to no advantages. "Marker begin" and "Marker end" are the begin and end nodes of the cable. "Segments" indicates the number of cable elements used. "Cable material" indicates the material which the cable consists of. The material is important for determining its weight and elasticity. A choice can be made ranging from dyneema to steel and nylon. "Wind direction" states the direction of the wind velocity vector and "Altitude model" selects the wind velocity profile with altitude. A choice can be made between constant and KNMI. Constant assumes a constant wind velocity with altitude. Its magnitude is governed by a design variable which can be altered within the simulation. KNMI is a model based on measurements done by the Royal Dutch Meteorological Institute over the period of 20 years [W. J. Ockels, 2001]. It

assumes a steadily increasing wind velocity with increasing altitude. "Marker altitude" indicates the marker at ground level. This marker is important for cables which start at altitudes other than the ground and experience wind velocities governed by the KNMI model. Lastly, "Altitude direction" governs the direction of increasing altitude from the altitude marker.

## 4.4 Building block 2: Inflatable tubes

Even though wind speeds can be large, they are still relatively low when they are compared to minimum flight speeds of conventional aircraft. Kites are therefore very slow flying objects. In order to be able to fly the weight of the kite needs to be sufficiently low. Conventional kite structures were traditionally made from thin sticks and fabric. For small kites, such a structure is more than adequate. For larger kite structures, sticks tend to be too fragile. A more robust way of building kite structures is by using the principle of inflatable structures. Pressurized tubes provide rigidity whilst keeping the weight of the structure low. Furthermore, Inflatable structures are very durable and do not easily break during impact. An inflatable structure needs no hard parts. Once the pressure is released, all that is left is a soft fabric which can do no harm. For a structure which flies over populated areas, such a property is vital as it secures its position as a safe structure. In case of loss of control, all that needs to be done is release the pressure and the kite will gently fall to the ground like a flag which came loose from its pole.

### 4.4.1 The mechanical behavior of inflatable structures

A quick overview of previous research on inflated tubular structures was outlined in section 2.5.1. The section continues to identify the three different states in which an inflated beam under loading can exist in: "unwrinkled", "wrinkled" and "collapsed". Especially in the wrinkled and collapsed state, an inflated beam exhibits non-linear bending behavior.

For engineering purposes of current and future applications of inflated tubular structures there is a need for simulation of designs and concepts. The models mentioned in section 2.5.1 are applicable to simple cantilever beam type structures but not for more complex structures. Numerical codes are available for a finite element analysis approach to inflatable structures. Veldman [2005a] uses existing ABAQUS code to evaluate a straight and a tapered cantilever beam. In the unwrinkled state, the model produced good correlation with the experimental data. The wrinkling load was only 1.3% larger than the experimentally determined wrinkling load. Once wrinkles occur, the structure behaves non-linearly and the FEM model starts to significantly over-estimate the stiffness of the structure. Furthermore, it must be noted that mesh density plays a large role on the accuracy of the simulation. A coarse mesh will yield poor results while a fine mesh will

increase calculation time. Veldman [2005a] creates a fine mesh in the location where wrinkles are expected to occur. For simulations of more complex tubular structures, the location where wrinkles will occur is not obvious beforehand. Also, wrinkles may form in different locations under different loads. This means that the mesh would have to be fine everywhere which greatly increases the calculation time.

From discussions with kite designers such as Peter Lynn (Peter Lynn Kites) and Dr. Henry Rebeck (Mutiny kites) it became apparent that these designers are not necessarily interested in the level of detail a FEM analysis will yield. The exact location, size, amplitude and angle of wrinkles are of lesser interest. Kite designers are more interested in general flexible behavior of more complex tubular structures. The next section outlines a simulation of inflatable structures as the second building block of the kite simulation tool.

#### 4.4.2 Inflatable beam model definition

The state in which an inflatable structure finds itself is governed by geometry and internal pressure, as well as the externally applied loads. The model proposed in this thesis approximates a continuous inflated tubular beam as a linked chain of rigid elements. Consider a straight cantilever beam. The rigid sections are joint together using spherical joints. (See figure 4.6)

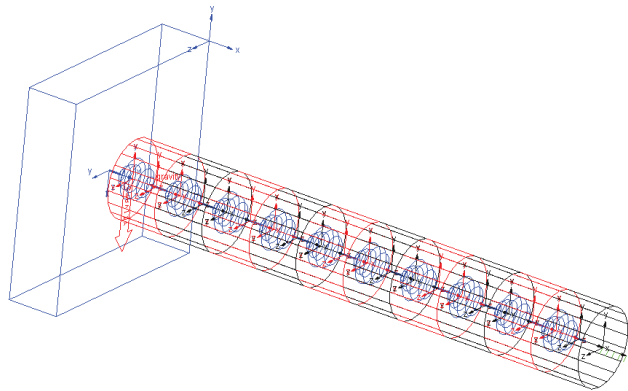


**Figure 4.6:** *An inflatable beam approximated by rigid elements joint by spherical joints.*

The spherical joints allow rotation along three axis. Two of these rotations can be considered as bending and one of these rotations can be considered as torsion. This beam is now nothing more than a chain of rigid bodies which exhibit no stiffness and no damping. The behavior of the structure is introduced by means of reaction forces which act on the joints themselves. In the case of these tubular structures, its behavior is modeled by introducing a three dimensional torque

vector on each of the joints. Figure 4.7 shows a close-up representation of the three dimensional torque vector.

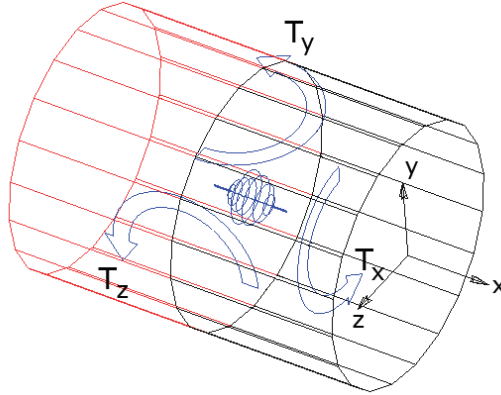


**Figure 4.7:** *A graphical representation of the 3D torque vector.*

In figure 4.7,  $T_y$  and  $T_z$  are the torque vectors which govern the bending behavior of the beam. The torque vectors act as springs which give the beam its bending rigidity.  $T_x$  is the torque vector which governs the torque of the beam. It acts as a torque spring, giving the beam its torsional stiffness. The stiffness of these springs determines the behavior of the inflatable beam. When the beam is in the unwrinkled state and both bending and torsion can be considered linear (for isotropic materials), the spring stiffness is a constant. In the wrinkled state, the stiffness of the springs starts to decrease with increasing deflection. Once the point of collapse is passed, the stiffness in the springs reduces to a value close to zero.

As was stated earlier, the algorithms governing the torque vectors determine the bending and torsion behavior of the beam. For a linear elastic beam, the stiffness would be a simple constant. In the case of an inflatable tube, the algorithm is far more complex. The goal of this simulation is to simulate the structural behavior of a kite which is made of a number of different fabrics. The tubular structure of the kite consists of a Dacron outer shell and a thermoplastic polyurethane (TPU) inner bladder. This constitutes a combination of anisotropic materials. Furthermore, in the theory proposed by Comer & Levi [1963], Stein & Hedgepeth [1961] and Webber [1982] the material of the inflatable tube is considered to be a membrane. This is a theoretical material which cannot carry any compressive loads. Main et al. [1995] introduces the possibility for a shell-type material but treats only isotropic materials. In order to come to a correct algorithm for the torque vectors, it was chosen to approach the solution from a venue of experimental data. Bending and torsional data will be obtained from

test beams which consist of the same Dacron/TPU materials. These experimental results will form a basis on which the algorithms for the torque vectors are based.

### 4.4.3 Bending

In order to determine the algorithms for the torque vectors which govern bending, a number of bending experiments were conducted. A set of three beams were built with diameters of 8cm, 13cm and 18cm. The beams were clamped on one end creating a cantilever setup. The beams were 1.20 meters long and loaded by a single force at 1 meter from the clamped end. Figure 4.8 shows the test setup.

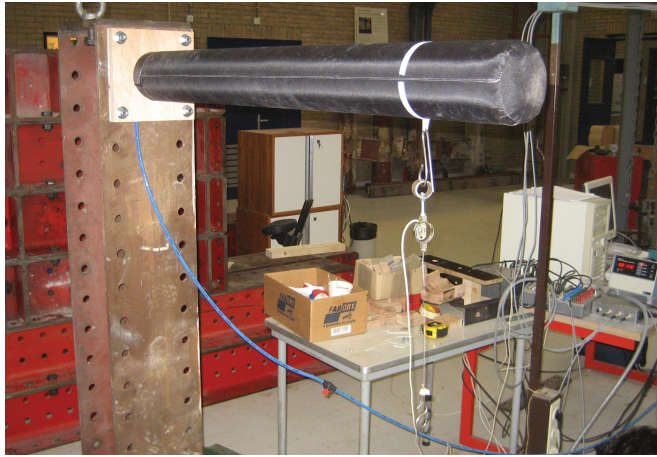


**Figure 4.8:** *The test setup for the bending test.*

The internal pressure in the beam is kept constant by use of a calibrated manometer and release valve. The load on the beam is measured using a load cell and the deflection of the tip is measured using a laser sensor, ensuring a zero-contact measurement of the deflection. Loads were introduced by hanging different weights on the attachment point. After the load was measured by the load cell, the deflection was recorded using the laser sensor. The weight of the load cell and wires were taken into account. During the test, it was observed that the pressure stayed relatively constant. A change of no more than 10 to 15 pascal was observed. The tests were conducted on all three beams at different internal pressures. Figure 4.9 shows a selection of the resulting load deflection curves.

For the simulation itself, an experimental data-fitting method was chosen for the governing torque vectors. Much in the same way tires are simulated ([Pacejka & Bakker, 1992]), this approach leads to an algorithm which is low CPU intensive, allowing the inflated tube simulation to run almost real time. Furthermore, an empirical data fit can yield accurate results, even with complicated multi-variable

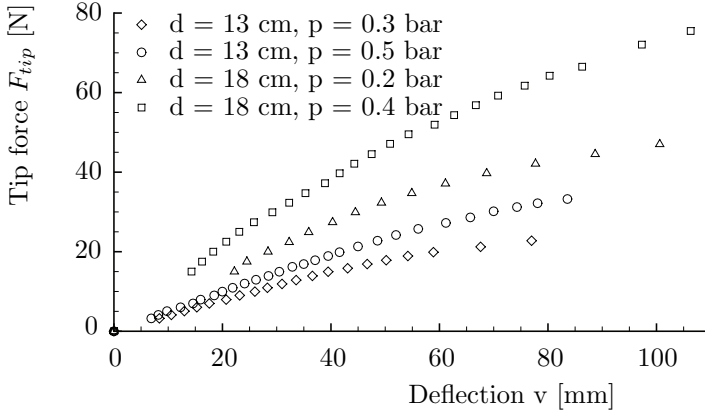


**Figure 4.9:** *The resulting load-deflection curves.*

systems.

The bending curve of an inflatable beam starts in the origin and continues at an angle, consistent with linear bending theory. However, once wrinkles start to occur, the curve arcs away from the initial stiffness due to the increased flexure introduced by the wrinkles. This characteristic leads to the proposition of a function which correlates to the data. This function acts as a basis to approximate the test data.

$$F_{tip} = \lambda_1 (1 - e^{-\lambda_2 v}) \quad (4.25)$$

In order to determine the dependency of  $\lambda_1$  and  $\lambda_2$  with regard to internal pressure and beam radius, a fit was made on a variable-by-variable basis. The goal of this method is to determine the topology of the function and to obtain a valid set of starting values for the coefficients. With these coefficients, an overall fit is made using the least squares method. This approach allows to carefully explore the function topology and locate any pitfalls early in the analysis. It greatly reduces the time spent during the actual final fit due to the fact that the dependencies of the different coefficients on the variables  $p$  (pressure),  $r$  (beam radius) and  $v$  (tip deflection) become more obvious during the procedure described in the following section. For instance: one can quickly see when a coefficient turns from positive to negative in a specific function topology. This change in sign can ultimately lead to a negative stiffness for some pressures or radii. Such problems are far less obvious during the final overall fit.

First, by using a least squares method, the values of  $\lambda_1$  and  $\lambda_2$  are determined for every combination of internal pressure and beam radius. The values of  $\lambda_1$  and

$\lambda_2$  which relate to the same beam radius are plotted in a graph against internal pressure and a set of functions is created through another least squares method which relates internal pressure to the values of  $\lambda_1$  and  $\lambda_2$ .

$$\lambda_1 = S_1 p^2 + S_2 \quad (4.26a)$$

$$\lambda_2 = S_3 p^2 + S_4 \quad (4.26b)$$

The form of the equations (4.26) have been obtained through an iterative process such that they yielded a close match to the experimental results. For both functions, the  $R^2$ -value (coefficient of determination) was over 0.99, which is very close to the ideal value of 1. Equations (4.26) yield four new coefficients  $S_1$ ,  $S_2$ ,  $S_3$  and  $S_4$ . These coefficients are plotted in a graph as a function of beam radius and a new least squares operation is used to find functions that relate the values of  $S_1$  through  $S_4$  to the beam radius  $r$ .

$$S_1 = C_1 r + C_2 \quad (4.27a)$$

$$S_2 = C_3 r^3 + C_4 \quad (4.27b)$$

$$S_3 = C_5 r^5 + C_6 \quad (4.27c)$$

$$S_4 = C_7 r + C_8 \quad (4.27d)$$

The values of  $C_1$  through  $C_8$  are numeric values which are determined in this operation. The  $R^2$ -values of the functions all lay above 0.99. By substitution of equations (4.26) and (4.27) into equation (4.25), a single equation is created which relates pressure, beam radius and deflection to a tip force.

$$F_{tip} = f(p, r, v) = [(C_1 r + C_2) p^2 + (C_3 r^3 + C_4)] \left[ 1 - e^{-\frac{(C_5 r^5 + C_6) p + (C_7 r + C_8)}{(C_1 r + C_2) p^2 + (C_3 r^3 + C_4)} v} \right] \quad (4.28)$$

This gives the topology and coefficients for a direct and complete fit of the test data. In this final fit, the error is defined as:

$$error = \frac{norm(\Delta F_{tip})}{norm(F_{tip})} \quad (4.29)$$

The final fit yielded a set of coefficients  $C_1$  through  $C_8$  which can be substituted into equation (4.28). The values of these coefficients are given in appendix A.

Figure 4.10 shows a comparison between measured and fitted data for a beam with a diameter of 13cm. The resulting error for this fit, defined in equation (4.29), was 1.91%.

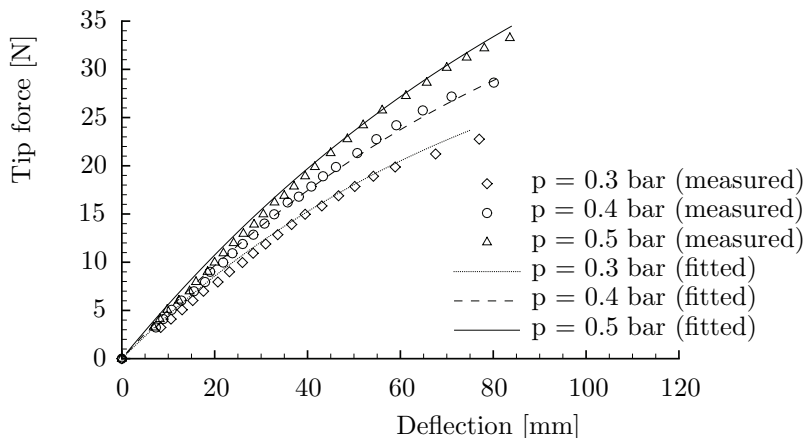


**Figure 4.10:** *The resulting load-deflection curves for a beam with a 13cm diameter.*

Looking at the curves in figure 4.10 one can immediately see that the transition from unwrinkled to wrinkled is not as pronounced in the experimental data as it is in the theoretical bending behavior depicted in figure 2.12. The different theories by Comer & Levi [1963], Main et al. [1995], Adler et al. [2000], Fichter [1966], Stein & Hedgepeth [1961] and Webber [1982] show a clear point at which wrinkling occurs and devoted a great deal of attention to this threshold. The matched data curves made in equation (4.28) don't indicate a wrinkling threshold at all. It simply approximates the smooth curves of figure 4.9. For a designer of kites and tents, the exact wrinkling load is less important than the overall shape of the load deflection curve.

A point which does require special attention is the point of collapse. The matched data curves made in equation (4.28) do not include the collapse behavior and simply extrapolate the curve for an increasing bending load. In the simulation, collapse is included by lowering the bending stiffness by a large factor after the collapse deflection is reached. It is therefore necessary to create a function which relates beam radius and internal pressure to a collapse deflection. In this function, the collapse deflection is the deflection of the beam right before the beam transitions from the wrinkled state to the collapsed state. During the experiments, collapse loads and collapse deflections were measured. All collapse deflections relating to the same beam radius  $r$  were plotted in a graph and a function was created to approximate the relation between internal pressure  $p$  and the collapse deflection.



$$v_{collapse} = T_1 p + T_2 \quad (4.30)$$

Analogue to the bending match, functions were created to relate the values of the coefficients  $T_1$  and  $T_2$  to the beam radius  $r$ .

$$T_1 = C_9 r^4 + C_{10} \quad (4.31a)$$

$$T_2 = C_{11} r^2 + C_{12} \quad (4.31b)$$

The values of  $C_9$  through  $C_{12}$  are numerical values obtained from the matching operation. The numerical values can be found in appendix G. By substituting equations (4.31) into equation (4.30), we obtain an equation for the collapse deflection as a function of internal pressure and beam radius.

$$v_{collapse} = (C_9 r^4 + C_{10}) p + C_{11} r^2 + C_{12} \quad (4.32)$$

At this point, the entire load-deflection curve is mapped out. It is now possible to write an equation for the bending stiffness as a function of internal pressure  $p$ , beam radius  $r$  and deflection  $v$ . Conventional beam bending theory [Gere & Timoshenko, 1991]:

$$\frac{d^2 v}{dx^2} = \frac{M}{EI} = \frac{1}{\rho} = \kappa \quad (4.33)$$

With:

$$\theta = \frac{l}{\rho} \quad (4.34)$$

The theory is only valid for small deflections. Deflections expected in an inflatable tube are much larger. But by dividing the beam into smaller elements, the deflections per element are much smaller, enabling the use of classical bending theory. For a beam divided into  $n$  elements we can write:

$$n = \frac{l}{\Delta l} \quad (4.35)$$

$$\Delta\theta = \frac{\theta}{n} \quad (4.36)$$

Substitution of equations (4.35) and (4.36) into equation (4.34) yields:

$$\Delta\theta = \frac{\Delta l}{\rho} \quad (4.37)$$

For the rotational spring stiffness in the joint between two elements we can write:

$$k\Delta\theta = M = \frac{EI}{\rho} \quad (4.38)$$

$$k\Delta\theta = k \frac{\Delta l}{\rho} \quad (4.39)$$

Combining equations (4.38) and (4.39) yields:

$$k = \frac{EI}{\Delta l} \quad (4.40)$$

Equation (4.40) gives us a relation between spring stiffness  $k$  and bending stiffness  $EI$  for an element length of  $\Delta l$ . We now include the experimental data. For a cantilever beam, conventional beam bending theory yields:

$$v = \frac{F_{tip}l^3}{3EI} \quad (4.41)$$

In case of an inflatable beam, the term  $EI$  is not a constant numeric value. It is a function of internal pressure  $p$ , beam radius  $r$  and bending deflection  $v$ . Equation (4.28) gives tip force  $F_{tip}$  as a function of  $p$ ,  $r$  and  $v$  and the beam length  $l$  equaled 1 meter in the experiments. This now allows the formulation of an equation which gives  $EI$  as a function of  $p$ ,  $r$  and  $v$ .

$$EI(p, r, v) = \frac{F_{tip}(p, r, v) l^3}{3v} \quad (4.42)$$

Substitution of equation (4.42) into equation (4.40) yields an expression for the spring stiffness:

$$k(p, r, v) = \frac{F_{tip}(p, r, v) l^3}{3v\Delta l} \quad (4.43)$$

The collapse deflection of equation (4.32) is used to determine at what deflection the stiffness should reduce to a minimal value. This is done through multiplication of the stiffness with a step function which equals 1 at values of deflection lower than the collapse deflection, and 0.001 for values of deflection higher than the collapse deflection.<sup>1</sup> This method was chosen above the option to simply reduce the stiffness to a constant small value for deflections greater than the collapse deflection because in this situation, a single and small value for the stiffness would have a range of large deflections. This is numerically undesirable. Because the initial stiffness creates a constant slope of the load deflection curve, multiplication by a small factor would reduce the stiffness considerably, and allow the stiffness to climb only marginally after collapse, ensuring only one stiffness relates to only one deflection.

With the functions for the coefficients of the polynomials, the simulation is complete. Figure 4.11 shows the measured and simulated data in a graph. The largest measured value in each of the bending experiments in this graph indicate the maximum tip force before collapse occurs.

#### 4.4.4 Torsion

In order to write an algorithm for the torsion vector governing the torsion of the beam, the same beams that were tested in bending were also tested in torsion. For this purpose, a beam torsion device was created to apply the torque loads on the beam and measure the angular deflection. The test setup clamps the test beam on one end and rotates the other end around the longitudinal axis of the test beam through the use of a double rotating arm. The first arm is rotated by a spindle. The second arm rests on the first arm and introduces the torque loads into the beam. Between the first and second rotation arm, a load cell measures the force. The maximum dimensions of the pressurized tubes are 2 m long and 0.3 m diameter. The shorter test beams were tested by placing the end fixture and the rotating arm closer together. Figure 4.12 shows the torsion setup.

---

<sup>1</sup>Within MSC ADAMS, a step function is a continuous and smooth transition from one value to another.

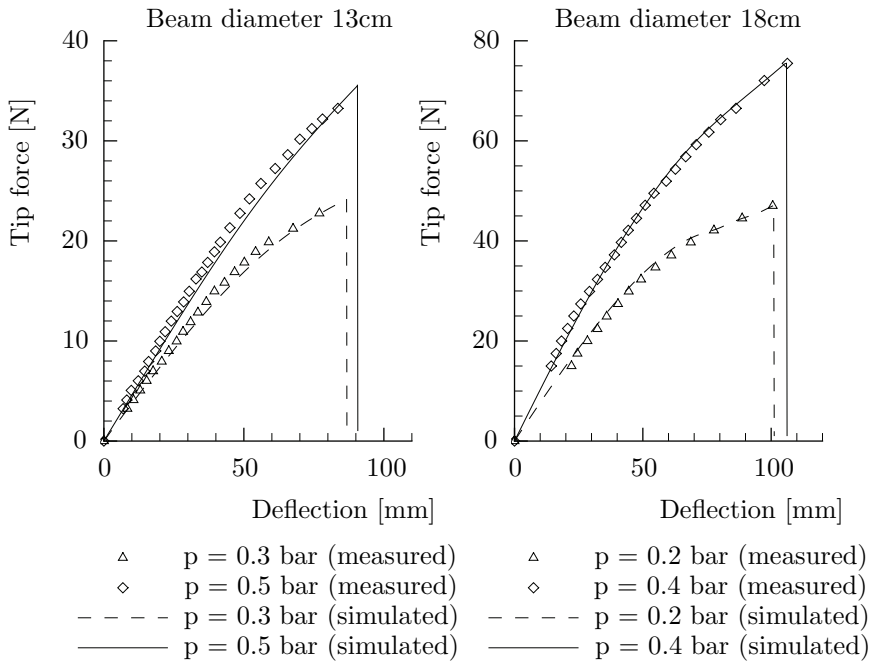


**Figure 4.11:** A comparison of measured and simulated bending data for different pressures and different beam diameters.

The 30 mm axis of the rotating arm is supported by 2 ball bearings on a distance of 200 mm. To prevent side ways forces on the load cell. The spindle rotates the first arm which then introduces the load through the load cell into the second arm. The second arm introduces the moment into the tube via 2 pins. The central axis of the load cell is aligned with the pins and the 30 mm axis. The distance between the load cell and the 30 mm axis is 500 mm.

The deflection angle is measured using a digital inclinometer and the pressure is regulated using a digital manometer and a release valve. The beams were tested at different internal pressures up to deflection angles of at least 40 degrees. Figure 4.14 shows some of the torsion test results.

From the torsion test it became clear that for the first part of the torsional rotation, the behavior of the beam was only marginally dependent on internal pressure. The curves with the same beam diameters are very close and seem to have the same slope. Once wrinkles are formed, the lines start to deviate from each other, with the highest pressures reaching the highest torque loads. Unlike the bending behavior, the stiffness does not rapidly drop. It simply levels out. In torsion, the beam knows only two states, unlike beams in bending which can exist

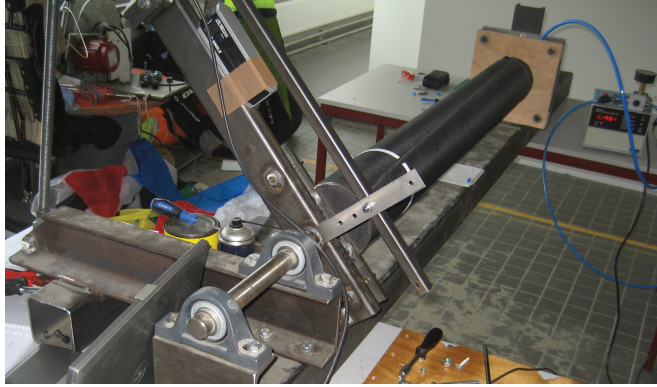


**Figure 4.12:** *The torsion test setup.*

in three states [Breuer, 2007]. The two states are "unwrinkled" and "wrinkled". According to Adler et al. [2000] wrinkles form perpendicular to the direction of the lowest principle stress. In the unwrinkled state, the lowest principle stress has a positive value. This means that compressive stress due to torsion is smaller in absolute value than the tension in that same direction. In the wrinkled state, the lowest principle stress is equal to zero. Theory suggests that the wrinkling threshold is a distinct point which leads to a clear shift in the slope of the torsion deflection curve. Figure 4.14 shows that the transition from unwrinkled to wrinkled is a more gradual process. For the purpose of the simulation proposed in this thesis, an approach similar to the one taken for bending in section 4.4.3 was chosen for torsion as well. In order to approximate the experimental results, the following function was proposed.

$$T = \lambda_3 \arctan(\lambda_4 \varphi) \quad (4.44)$$

As with the bending analysis, function topology and initial values for the coefficients were found by fitting the data in a variable-by-variable method. First, by using a least squares method, the values of  $\lambda_3$  and  $\lambda_4$  are determined for every combination of internal pressure and beam radius. The values of  $\lambda_3$  and  $\lambda_4$  which relate to the same beam radius are plotted in a graph against internal pressure and a set of functions is created through another least squares method which relates internal pressure to the values of  $\lambda_3$  and  $\lambda_4$ .

$$\lambda_3 = S_5 p + S_6 \quad (4.45a)$$

$$\lambda_4 = S_7 \ln(p) + S_8 \quad (4.45b)$$

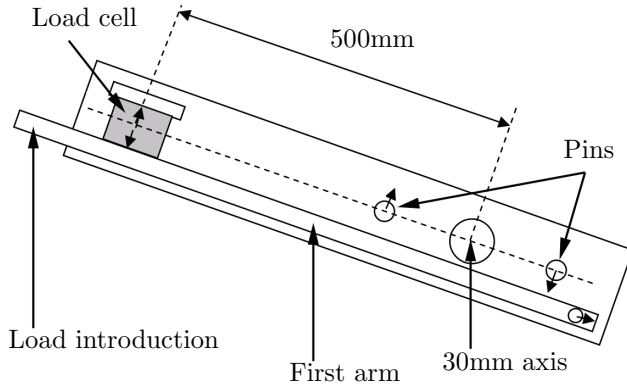


**Figure 4.13:** A schematic representation of the torsion test apparatus [Breuer, 2007].

The form of the equations (4.45) have been chosen as such due to the fact that they yielded the closest match to the experimental results. For both functions, the  $R_2$ -value was over 0.99. Equations (4.45) yield new coefficients  $S_5$ ,  $S_6$ ,  $S_7$  and  $S_8$ . These coefficients are plotted in a graph as a function of beam radius and a new least squares operation is used to find functions that relate the values of  $S_5$  through  $S_8$  to the beam radius  $r$ .

$$S_5 = C_{13}r + C_{14} \quad (4.46a)$$

$$S_6 = C_{15}r + C_{16} \quad (4.46b)$$

$$S_7 = C_{17}r^4 \quad (4.46c)$$

$$S_8 = C_{18}r^3 + C_{19} \quad (4.46d)$$

The values of  $C_{13}$  through  $C_{20}$  are numeric values which are determined in this operation. The  $R_2$ -values of the functions all lay above 0.99. By substitution of equations (4.45) and (4.46) into equation (4.44), a single equation is created which relates pressure  $p$ , beam radius  $r$  and deflection angle  $\varphi$  to a torque moment  $T$ .

$$T = f(p, r, v) = [(C_{13}r + C_{14})p + (C_{15}r + C_{16})] \arctan [(C_{17}r^4) \ln(p) + (C_{18}r^3 + C_{19})] \quad (4.47)$$

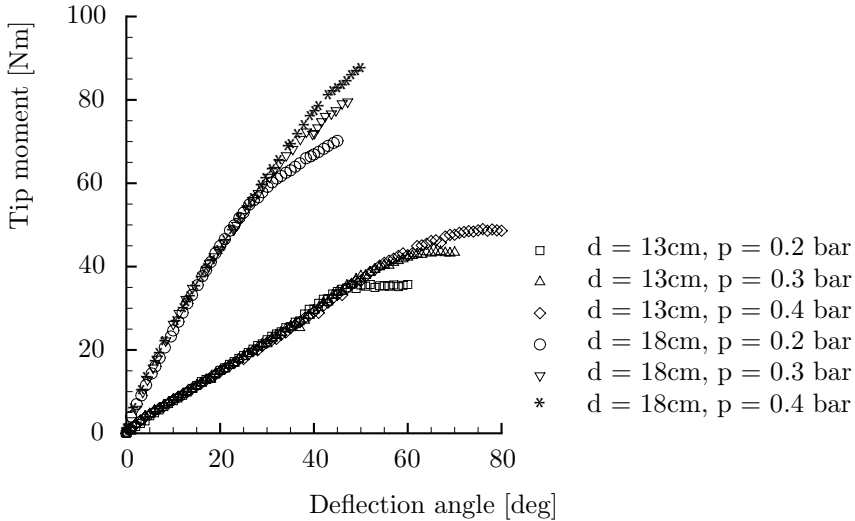


**Figure 4.14:** Test results from the torsion tests on inflatable beams.

As was done for bending in the previous section, the values found for the coefficients  $C_{13}$  through  $C_{19}$  can now be used to perform an overall fit of the test data to equation (4.47). This yields a new set of values for constants  $C_{13}$  through  $C_{19}$  which can be found in appendix A. The error for this final fit is defined as:

$$error = \frac{norm(\Delta T)}{norm(T)} \quad (4.48)$$

The error for the best fit turned out to be 2.78%. Figure 4.15 shows a comparison between measured and fitted data.

For the torsion spring stiffness we can use the angular form of Hooke's law:

$$T = -k\varphi \quad (4.49)$$

Substitution of equation (4.47) into equation (4.49) yields an expression for the torsional spring stiffness. This expression is now only valid for beam elements with a length of 1 meter because it was directly derived from the experimental tests on the 1 meter long test beams. But because the torsion angle increases linearly with increasing beam length, we can write the following expression for a beam element with length  $\Delta l$ .

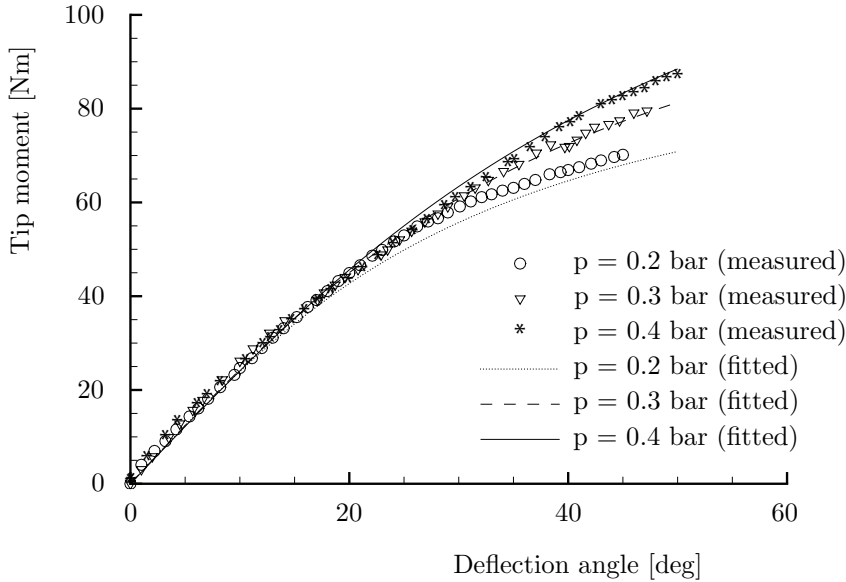


**Figure 4.15:** A comparison of measured and fitted torsion data for a beam with a diameter of 18cm.

$$k = -\frac{T}{\varphi} \frac{1}{\Delta l} \quad (4.50)$$

With equation (4.50), the torsion algorithm is complete and ready for implementation in the simulation.

#### 4.4.5 The combination of bending and torsion

Up until this point, bending and torsion in inflatable tubular beams have been considered independent of each other. In reality, this is not the case. Webber [1982] analyzed cantilever inflatable beams under bending and torsion. In his paper, he assumed the material to behave as a membrane. Veldman [2005a] later showed that assuming the material to behave as a thin shell yields better correlation with the experimental data on wrinkling loads. Veldman [2005b] investigates the interaction of torsion and bending and their effect on the wrinkling load. A comparison between analytical theory and numerical FE simulation is made. For the interaction between the wrinkling torque and the bending moments, the following expression was derived in Veldman [2005a]:



$$\frac{M}{M_w} + \left[ \frac{T}{T_w} \right]^2 = 1 \quad (4.51)$$

with:

$$(M_w)_{T=0} = \frac{\pi}{2} p r^3 \quad (4.52)$$

$$(T_w)_{M=0} = \sqrt{2} \pi p r^3 \quad (4.53)$$

The equations (4.52) and (4.53) are the wrinkling loads in resp. pure bending and pure torsion situations. Webber [1982] found similar expressions. Equation (4.52) is only valid if the material is considered to be a membrane (wrinkling criterion based on stress, Comer & Levi [1963], Webber [1982] and Stein & Hedgepeth [1961]). Gerard & Becker [1957] and Donell [1933] have each derived their own equations for wrinkling loads in thin-walled tubes in torsion which consider the material to be a shell. These tubes contained no overpressure. Crate et al. [1944] first published a theory on the interaction between wrinkling in thin walled shells and internal overpressure. He derived the following expression:

$$\left[ \frac{T_w}{(T_w)_{p=0}} \right]^2 + \frac{p}{(p_w)_{T=0}} = 1 \quad (4.54)$$

With an empirically determined expression for  $(p_w)_{T=0}$ :

$$(p_w)_{T=0} = -2.6E \frac{2r}{l} \left( \frac{t}{2r} \right)^{2.5} \quad (4.55)$$

Veldman [2005b] makes a combination between membrane and shell theory to write an expression for the torque wrinkling load.

$$(T_w)_{M=0} = \sqrt{2} \pi p r^3 + 0.544 \pi E r t^2 \sqrt{\frac{t}{r} \frac{1}{(1-\nu^2)^{0.75}}} \sqrt{1 + 4.35 \frac{p}{E} \frac{r}{l} \left( \frac{r}{t} \right)^{2.5}} \quad (4.56)$$

The interaction of bending and torsion is implemented into the simulation by creating a scaling factor which is based on the wrinkling load in pure bending  $(M_w)_{T=0}$  or torsion  $(T_w)_{M=0}$  and the wrinkling load during a combination of bending  $M_w$  and torque  $T_w$ . With  $T_w$  obtained from equation (4.54) and  $M_w$  obtained from equation (4.51).

$$K_{bending} = \frac{M_w}{(M_w)_{T=0}} \quad (4.57)$$

$$K_{torsion} = \frac{T_w}{(T_w)_{M=0}} \quad (4.58)$$

In the simulation, the spring stiffness algorithm of the torque vectors which govern the bending and torsion behavior are multiplied by the scaling factors in equations (4.57) and (4.58).

#### 4.4.6 The inflatable beam toolbox implementation

The simulation is set up within MSC ADAMS. In order to create an intuitive interface, a toolbox was created with which beam models can easily be produced. For every beam element, the radius and internal pressure are automatically substituted into the equations. This ensures that the bending stiffness of every joint is only dependent on the variable bending deflection and the equations reduce in complexity before the simulation starts. On every joint, the angles between the adjacent elements are constantly measured and values are related back to the stiffness algorithm. This creates a loop during the simulation where every joint allows for the correct deflection at a specific local bending moment. This allows the simulation to function in loading situations other than a cantilever beam as well. The experimental data is only used to formulate a general stiffness algorithm which relates the local bending moment, the local internal pressure and the local beam radius to a local bending angle between the elements. Figure 4.16 shows the beam toolbox user interface.

In the beam toolbox "Tube Props" indicates the location of the beam properties file. This file contains data such as the fitted coefficients and beam radii. By switching tube property files one can load in other inflatable beams as well, consisting of different materials or different sizes. "Marker Beg" and "Part Beg" indicates respectively the marker at the beam start and the part to which it is connected. The same goes for "Marker End" and "Part End" but then for the other end of the beam. "Marker XY" governs the orientation of the beam. Usually, its X-axis is directed from the beginning marker to the end marker. The last two options, "Conn Beg" and "Conn End" is where the type of connections at

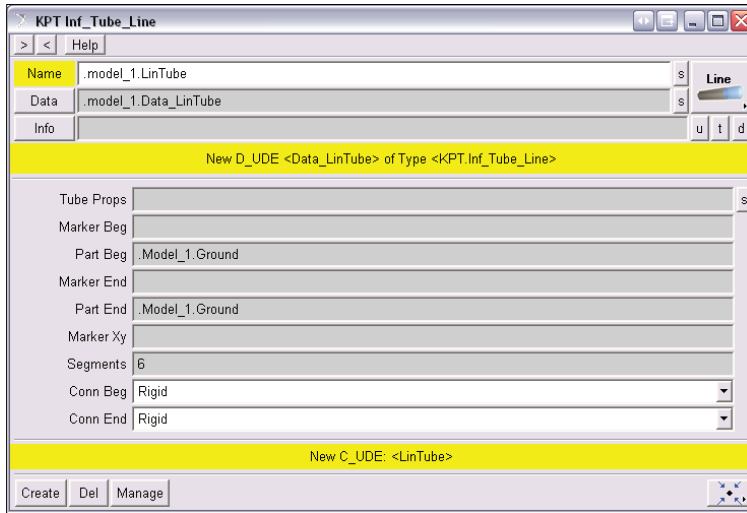


**Figure 4.16:** *The inflatable beam toolbox.*

the beginning and end of the beam are chosen. Whether it is a free end, a flexible end or a rigid end. After the model has been generated, the properties above remain changable. In this way it is relatively simple for a designer to change the radius of a specific beam in the kite without regenerating the entire model.

#### 4.4.7 Complex inflatable structures

The simulation was set up from the outset to be able to simulate structures which consist of more than just one simple beam. Building complex inflatable tubular structures is a simple task using the inflatables toolkit which was created. The user simply draws out the nodes of the structure and connects them using inflatable beams. However, a few remarks on more complex inflatable structures need to be made.

Up until now, only bending and torsion have been considered. For simple cantilever beams loaded by torques or tip forces, bending and torsion are the only loads on the elements which are of significance. In more complex inflatable structures, beams may also come under pure compression in axial direction. Axial compression is a load which works in the exact opposite direction of the longitudinal tension as a result of the internal overpressure. In essence, axial compression lowers the effective internal overpressure. The axial compression can be obtained from the joints between the elements. For the effective internal pressure at that location we can write:

$$p_{eff} = p + \frac{F_{axial}}{2\pi r t} \quad (4.59)$$

In equation (4.59),  $F_{axial}$  is negative for compression and positive for tension. Axial tension creates an increased pre-tension in the skin of the beam in longitudinal direction, increasing the effective pressure.

The second remark that needs to be made concerns the connections between the individual beams. As long as beams are connected in each others longitudinal direction, the algorithm governing that joint is no different than the algorithms governing the joint between the individual elements. But when beams are connected at an angle, stress concentrations occur which need to be taken into account. This means that the algorithms governing the connections of the individual beams need to be adjusted to take into account the stress concentration factor. This can be done by multiplying the local stiffness by the reciprocal of the stress concentration factor. The stress concentration factor is dependent on geometry and has been investigated intensively. Yakup et al. [1978] has conducted a number of experiments and determined the stress concentration factor for a T-joint to be between 2.6 and 3. For each joint between beams, the stress concentration factor can be determined and incorporated in the model.

## 4.5 Building block 3: Foils

With the two previously discussed building blocks, cables and tubes, it is possible to build the backbone of a kite. What is missing is the fabric that makes up the airfoil and introduces the aerodynamic forces. Kites that are supported by inflatable tubes obtain their lift and drag from an airfoil which is, in essence, a sail wing. Sail wings are a particular type of wing structure which consist of a (semi)-rigid leading edge nose and a flexible fabric surface. Figure 4.17 shows two variations of the sailwing. A single and a double membrane airfoil.

Flexible sailwings have been subject to extensive research ever since their invention at Princeton University in the 1960s [Sweeney, 1961]. An overview of previous research into the behavior of sail wings was given in section 2.5.2.

### 4.5.1 Airfoil model definition

From previous research it has become apparent that the change in camber has a significant effect on the aerodynamic performance of the sail wing. Simply assuming constant camber results in a performance which greatly differs from the performance of a flexible foil (Fink [1969] and Fink [1969]). In the kite simulation tool, the wing is divided into a number of chordwise wing elements. The aerodynamic forces on these elements are summed and superimposed onto a leading

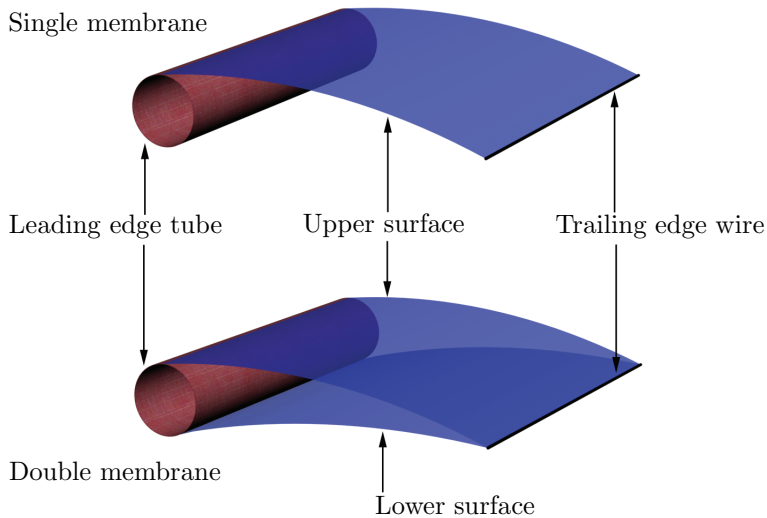


**Figure 4.17:** *A schematic representation of a single and a double membrane airfoil.*

edge to trailing edge wire which replaces the actual foil. Figure 4.18 shows the simplification

In the actual sail wing, lift is produced as a result of the pressure difference between upper and lower surface. the actual aerodynamic force is a distributed force on the canopy surface. In the model, the aerodynamic force is summed in spanwise direction and superimposed on the chordwise wire as a chordwise distributed force. The chordwise wire itself is modelled in the same manner as the cables in the previous section. it consists of five elements from leading to trailing edge and connects the trailing edge wire to the leading edge beam. The elements are joint together by hook joints allowing all rotations except axial rotation. The aerodynamic force on the wing element is introduced as force vectors which act on the four joints between the chordwise wire elements. Figure 4.19 shows the wing model in MSC ADAMS with the chordwise wires and local aerodynamic force vectors.

The last element required is the connection between the different chordwise wires. Up to now, they remain unconnected. In reality The canopy fabric itself has a negligible bending stiffness, but it does act as a shear web between arbitrary nodes on the canopy. This function in the model is fulfilled by cross-wires connecting the chordwise wires. The cross wires consist of a spring connecting the nodes. The spring stiffness is a measure for the shear modulus of the fabric. Figure 4.20 shows the complete wing model, including the cross wires.

The model depicted in figure 4.20 is a single membrane airfoil with a canopy as

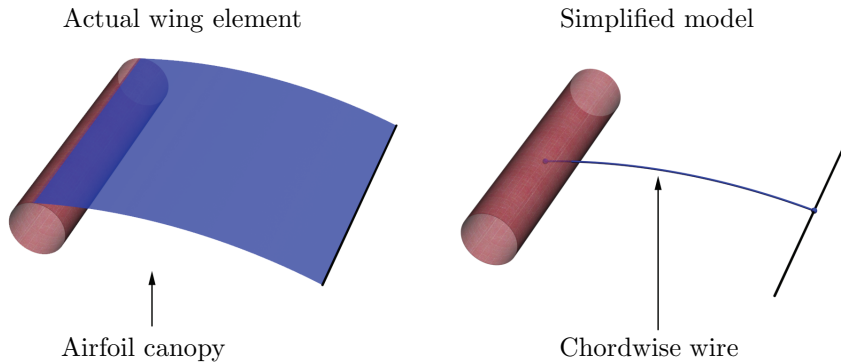


**Figure 4.18:** *Schematic representation of an actual sail wing and its modelled counterpart.*

the upper surface of the wing. It is important to realize that the structural model and aerodynamic forces are only indirectly coupled, in contrast to conventional fluid structure interaction simulations. The canopy created by the cross wires acts as a structural member in the flexible camber behavior of the wing under the load introduced by the local force vectors. The local force vectors are governed by a lift and drag coefficient which is dependent, among other parameters, on the local camber of the wing. The algorithm which determines the lift and drag coefficients has the local camber as an input parameter. The model finds itself constantly striving for equilibrium between parameters such as camber, aerodynamic forces, trailing edge wire tension and deformations of the inflatable beams. Adding a lower surface in the model only affects its structural flexibility. as long as the aerodynamic coefficient algorithm doesn't change, the extra lower surface has no direct aerodynamic implications.

## 4.5.2 The aerodynamic forces

As was stated in the previous section, the aerodynamic properties are introduced through an algorithm which takes into account a number of parameters to obtain its local lift, drag and moment coefficients. These input parameters consist of camber, angle of attack and airfoil thickness. The camber of the airfoil changes the aerodynamic characteristics. The angle of attack for every section is measured locally, taking into account the wind direction, flexure of the trailing edge wire in vertical direction (body axis) and velocity vector of the local wing section. The airfoil thickness introduces the effects of tube radius and the changes in chord-length due to the flexure of the training edge wire in horizontal direction (body

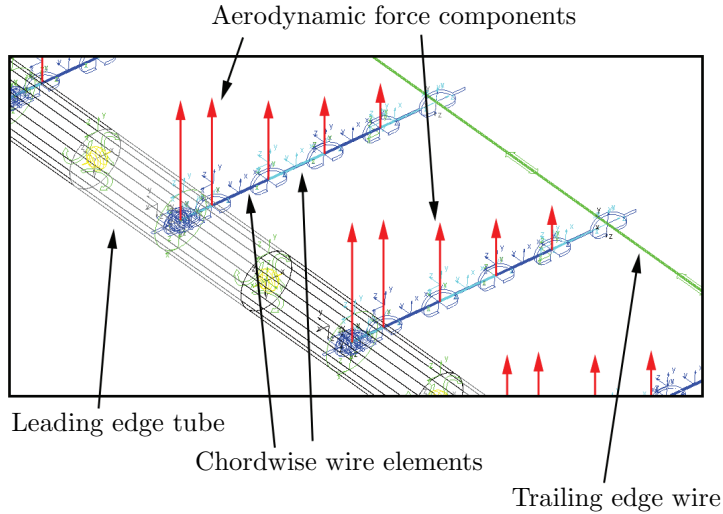


**Figure 4.19:** *The sail wing model showing the chordwise wire elements.*

axis). When the trailing edge wire moves towards the leading edge, the chord length is reduced. For the sail wings modelled here, this equals to a subsequent increase of the airfoil thickness (in percentage).

In order for the model to use the correct aerodynamic coefficients, an algorithm is developed which produces these coefficients as a function of aforementioned camber, angle of attack and airfoil thickness. previous research by e.g. Nielsen [1963] and Boer [1982] yielded rudimentary numerical models. however, its application within the scope of this simulation proved to be difficult. None of the models were suited for the type of wings and airfoils which are of prime interest. Furthermore, some of the models require iterative operations which are resource. It was therefore decided to employ the same approach as was done with the bending of tubular inflatable beams. But instead of obtaining data experimentally, a computational fluid dynamics (CFD) analysis was used to obtain the aerodynamic coefficients of a number of airfoils with differing thicknesses and camber values at different angles of attack. It was also attempted to obtain the data using a simpler approach using software such as xfoil, but it was quickly concluded that the high amount of turbulent flow on the sail wing airfoil created large discremancies with reality.

As was stated earlier, the algorithm for the aerodynamic coefficients determines the aerodynamic properties of the simulated wing. Therefore, this algorithm is where characteristics such as single or double membrane, leading edge nose shape and fabric roughness effects on the boundary layer can be found. The different wing configurations exist within the simulation as different aerodynamic coefficient

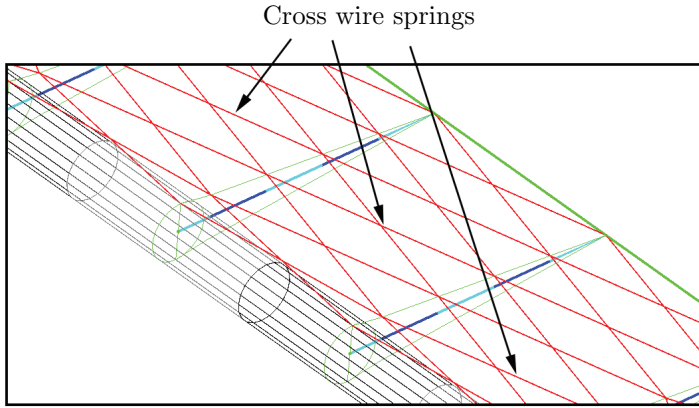


**Figure 4.20:** *The sail wing model showing the cross wires between the chordwise wire elements.*

algorithm packages which can be selected at will. The type of wing discussed in this section is a single membrane airfoil with a circular leading edge tube. This airfoil is most commonly used in surf kites and functions as a base for further investigations.

The CFD analysis was performed on three sets of airfoils with 15%, 20% and 25% thicknesses. The airfoils within each set ranged in camber from 0% to 12%. To obtain the airfoil polars, a two-dimensional grid was created. Figure 4.21 shows the grid of a 20% thick airfoil with a 4% camber.

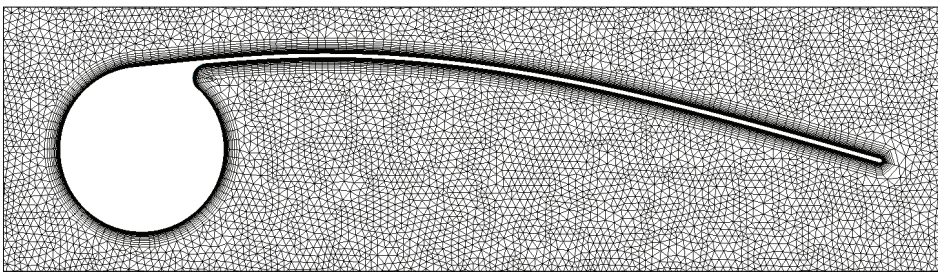


**Figure 4.21:** *A zoomed in view of the two-dimensional grid used.*

The airfoil analysis uses a one meter chord airfoil. Around the airfoil there is a 20-cell thick boundary layer which amounts to an absolute thickness of 18mm. The airfoil is encompassed in a density box with a maximum cell size of 10mm. The outer edges of the grid model is a box of 10 meters long and 8 meters high.



The size of this box agrees with the common rule for airfoil CFD analyses. This rule states the boundary box should be 10 times as wide as the chord of the airfoil. While this rule is hardly substantiated by scientific evidence, the fact that this rule is common practice will secure analogy with other airfoil CFD analyses. The maximum cell size is 50mm at the outer edges of the grid. The grid model was imported into Fluent from the ICEM grid program. The left end and bottom of the outer box is defined as a pressure inlet and the right side and top of the outer box is defined as a pressure outlet. The solver was configured as pressure-based, steady and two-dimensional with a Green-Gauss node based gradient option. For the viscous effects a K-Omega SST model was chosen incorporating transitional flows. for the solution, the SIMPLEC pressure-velocity coupling was chosen, as well as a second order discretization of pressure, momentum and turbulent kinetic energy. The specific dissipation rate was left on first order. Calculations were done with under-relaxation factors of 0.5 for pressure, 0.7 for momentum, 0.7 for turbulent kinetic energy and 0.7 for specific dissipation rate. The case was iterated for angles of attack ranging from 0 degrees to 25 degrees and aerodynamic coefficients were recorded for each angle of attack step. As an example, figure 4.22 shows the turbulence intensity around an airfoil with an 8% camber and at 0 degrees angle of attack.

As can be seen in figure 4.22 even at a low angle of attack there is a considerable amount of turbulence intensity around the airfoil, most of which is concentrated below the canopy of the airfoil. The presence of this amount of turbulent flow is why codes such as x-foil produce poor and inconsistent results for these type of airfoils.

Figure 4.23 shows the same airfoil at an angle of attack of 8 degrees. An increased turbulence intensity can be observed above the canopy at the trailing edge where flow separation starts to occur. A reasonable amount of turbulence is also still present on the lower side of the canopy.

Figure 4.24 shows the same airfoil at 20 degrees angle of attack. The flow has separated from the top of the canopy and a large wake is formed as a result. At this angle of attack, the airfoil has stalled and the steady CFD case does not converge. Unsteady analysis of this case revealed that a Von Karmann vortex street is formed behind the airfoil. From figures 4.22 through 4.24 it is clear that the amount of turbulence intensity rules out the use of panel codes to base the aerodynamic model of the kite on. Therefore, the CFD analysis is used for this purpose.

For all large number of combinations of different airfoil thicknesses and cambers, the aerodynamic coefficients were plotted against angle of attack. Figure 4.25 shows the lift coefficients for the 15% thick sail wing at different values of camber.

Figure 4.25 shows an increasing lift coefficient with increasing camber. Also, the zero lift angle of attack becomes more and more negative. Figure 4.26 shows the drag of the same airfoil with angle of attack.

Increasing camber shows an increase in drag on the airfoil as well. Figure 4.27

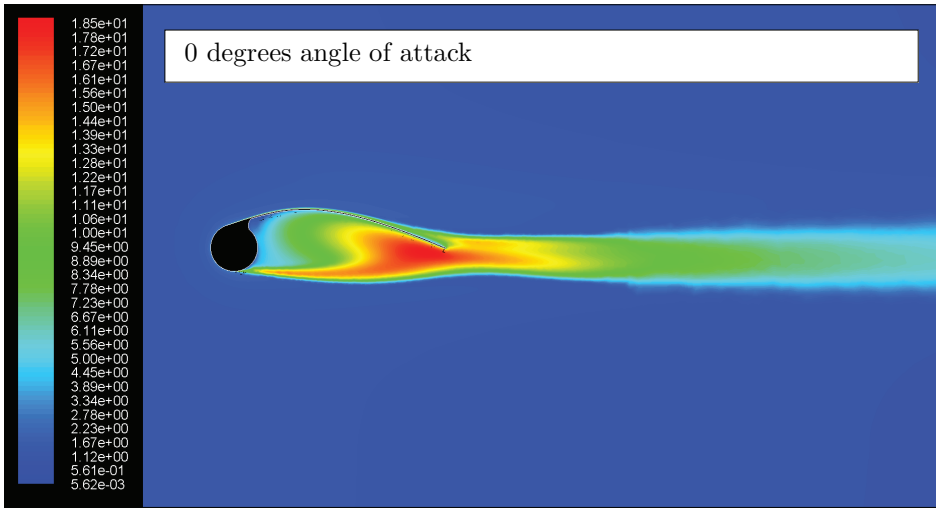


Figure 4.22: Plot of turbulence intensity at 0 degrees angle of attack.

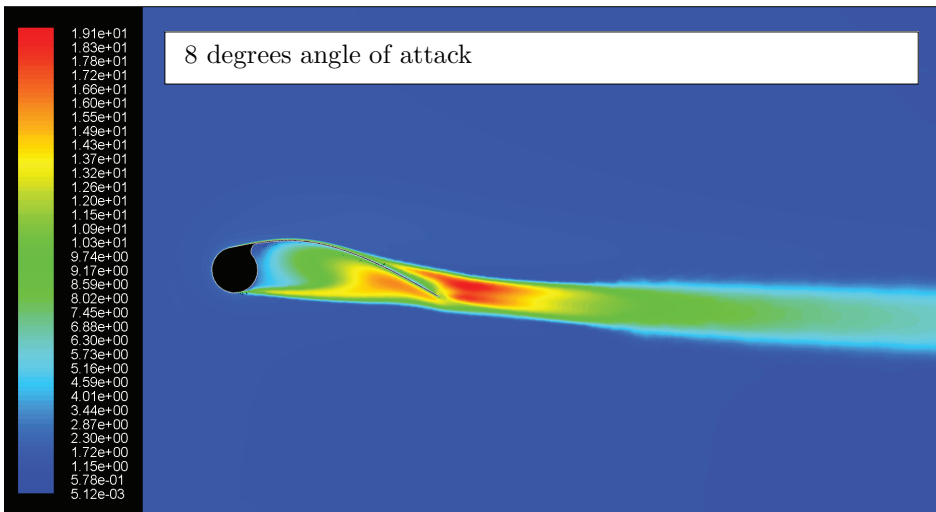
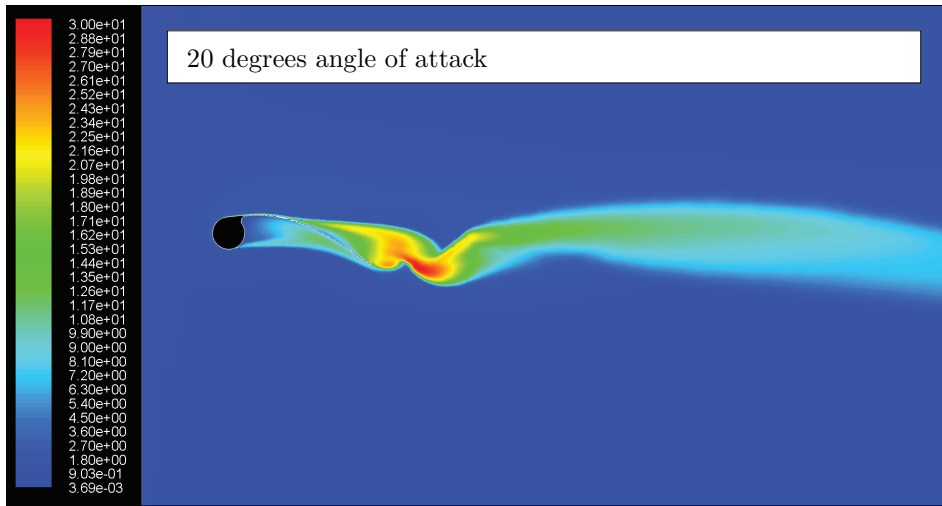


Figure 4.23: Plot of turbulence intensity at 8 degrees angle of attack.

shows the moment coefficient of the same airfoil.

Again, one can see that a change in camber has significant effects. The moment coefficient rapidly becomes more negative with increasing camber. Because of the highly flexible nature of the wing, the camber is closely linked to the pressure



**Figure 4.24:** *Plot of turbulence intensity at 20 degrees angle of attack.*

difference between the top side and the bottom side of the airfoil. During flight, one can expect to see a range of cambers occurring with all the differences in aerodynamic performance that figures 4.25, 4.26 and 4.27 indicate.

In the previous sections it was shown how the camber flexibility was simulated from a structural point of view. In order to have the correct aerodynamic performance to go with the flexible wing, an algorithm is devised which looks at the momentary airfoil thickness, camber and angle of attack and gives a lift- drag- and moment coefficient to match that particular configuration. This algorithm is established in the same manner as was used for the bending and torsion of the inflatable tubular structures.

In order to approximate the lift curve with respect to angle of attack, a third order polynomial is chosen. The characteristic shape of the  $Cl$ - $\alpha$  curve between -20 degrees and 20 degrees is such that the choice for a third order polynomial is shown to be a good starting point for the approximation. For the lift coefficient as a function of angle of attack, we write:

$$Cl = \lambda_5 \alpha^3 + \lambda_6 \alpha^2 + \lambda_7 \alpha + \lambda_8 \quad (4.60)$$

This yields different values for  $\lambda_5$  through  $\lambda_8$  which can be plotted with regard to camber.

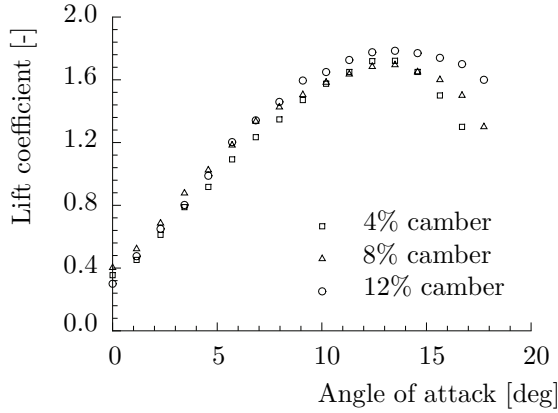


**Figure 4.25:**  $C_l$  -  $\alpha$  curves for a 15% thick sail wing airfoil at different values of camber.

$$\lambda_5 = S_9 \kappa + S_{10} \quad (4.61a)$$

$$\lambda_6 = S_{11} \kappa + S_{12} \quad (4.61b)$$

$$\lambda_7 = S_{13} \kappa + S_{14} \quad (4.61c)$$

$$\lambda_8 = S_{15} \kappa + S_{16} \quad (4.61d)$$

The first order polynomial was chosen here because, once plotted, the data appeared to fall onto a straight line. Therefore, a first order polynomial was deemed as a good starting point. From the equations (2) a new set of coefficients  $S_1$  through  $S_8$  is obtained. The new coefficients  $S_9$  through  $S_{15}$  are plotted in a graph as a function of airfoil thickness. This yields:

$$S_9 = C_{20}t^2 + C_{21}t + C_{22} \quad (4.62a)$$

$$S_{10} = C_{23}t^2 + C_{24}t + C_{25} \quad (4.62b)$$

$$S_{11} = C_{26}t^2 + C_{27}t + C_{28} \quad (4.62c)$$

$$S_{12} = C_{29}t^2 + C_{30}t + C_{31} \quad (4.62d)$$

$$S_{13} = C_{32}t^2 + C_{33}t + C_{34} \quad (4.62e)$$

$$S_{14} = C_{35}t^2 + C_{36}t + C_{37} \quad (4.62f)$$

$$S_{15} = C_{38}t^2 + C_{39}t + C_{40} \quad (4.62g)$$

$$S_{16} = C_{41}t^2 + C_{42}t + C_{43} \quad (4.62h)$$

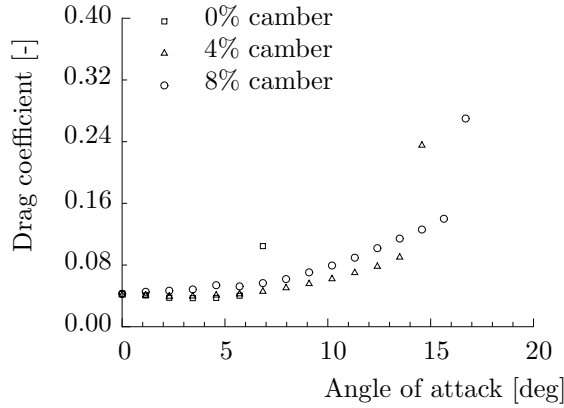


**Figure 4.26:**  $C_d$  -  $\alpha$  curves for a 15% thick sail wing airfoil at different values of camber.

In order to make a best fit, a Matlab program was written to take the data and make a fit based on the least squares method. This resulted in numerical values for the coefficients  $C_{20}$  through  $C_{43}$ . The numerical values are given in appendix A

The error introduced by this fitting procedure deserves special attention. The error under investigation here is the error between the data obtained through the CFD analysis and the data resulting from the fitted algorithm. The fit error is defined as the square root of the sum of all the squared differences between the CFD and matched algorithm data, divided by the square root of the sum of the squared CFD data. In essence, the values of the differences between CFD and fitted data are used as components of a large  $1 \times n$  vector. This vector is then normalized. The same is done with the coefficient values of the CFD data and the quotient between the two are a measure for the error made in the fit procedure:

$$error = \frac{norm(C_{l,fit} - C_{l,CFD})}{norm(C_{l,CFD})} \quad (4.63)$$

For this fit this yielded an error of 5.5%. With the values  $C_{20}$  through  $C_{43}$  known, the algorithm for the lift coefficient is known. To be more precise, it is known for a range of angles of attack from -20 degrees to 20 degrees. The simulation, however, also requires values for all the other angles of attack from -180 degrees to -20 degrees and from 20 degrees to 180 degrees. At these angles of attack, the flow is highly turbulent and a steady CFD analysis does not converge with residuals small enough to be considered reliable. Therefore, a more empirical

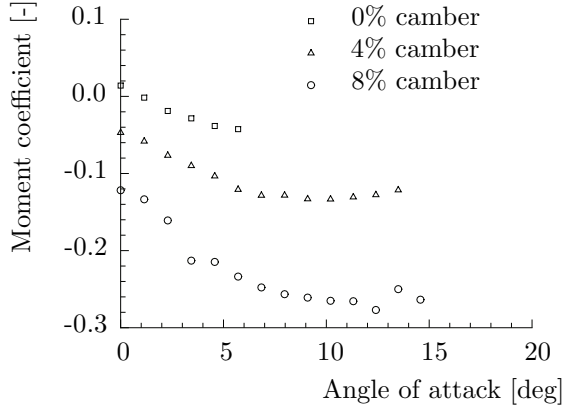


**Figure 4.27:**  $C_m$  -  $\alpha$  curves for a 15% thick sail wing airfoil at different values of camber.

approach is taken in these ranges of angles of attack by assuming the aerodynamic properties to be close to that of a flat plate. For the range of angles of attack from -180 degrees to -20 degrees and from 20 degrees to 180 degrees we assume the lift coefficient to equal [Spiereburg, 2005]:

$$C_{l_{high\alpha}} = 2 \cos(\alpha) \sin^2(\alpha) \quad (4.64)$$

For a numerical simulation it is imperative to create functions which are continuous differentiable. If they are not, numerical integration problems can occur. Therefore, in order to continuously switch between the lift algorithm for low angles of attack and equation (4.64) for high angles of attack, a step function is used to create a smooth transition. <sup>2</sup>.

For the drag and moment coefficients, a very similar method is used to obtain an algorithm which uses camber, airfoil thickness and angle of attack as an input and produces resp. a drag and a moment coefficient. For conciseness, the derivation is omitted here. The algorithm for drag yields:

$$C_d = [(C_{44}t + C_{45})\kappa^2 + (C_{46}t + C_{47})\kappa + (C_{48}t + C_{49})]\alpha^2 + [(C_{50}t + C_{51})\kappa + (C_{52}t^2 + C_{53}t + C_{54})] \quad (4.65)$$

---

<sup>2</sup>Within MSC ADAMS, a step function is a continuous and smooth transition from one value or function to another.

The numerical values of  $C_{44}$  through  $C_{54}$  can be found in appendix A. For the airfoil moment the same method yields:

$$Cm = [(C_{55}t + C_{56})\kappa + (C_{57}t + C_{58})]\alpha^2 + [(C_{59}t + C_{60})\kappa + (C_{61}t + C_{62})] \quad (4.66)$$

Flat plate theory for high angles of attack yield for Cd:

$$Cd_{high\alpha} = 2\sin^3(\alpha) \quad (4.67)$$

As with the previous coefficients the numerical values of  $C_{55}$  through  $C_{62}$  can be found in appendix A.

With the coefficients  $C_{20}$  through  $C_{62}$  known, the entire behavior of the aerodynamic forces as a function of angle of attack, airfoil thickness and camber are known. This approach allows for a modular simulation. One could quite easily apply the entire procedure with regard to a different airfoil and in the process obtain a different set of coefficients. Within the kite simulation toolbox, these different airfoil models are then selectable. This approach allows the use of experimental data, as well as numerical data giving it added flexibility and new avenues of analysis.

### 4.5.3 The airfoil moment

Up to this point, we now have three functions which approximate the lift-, drag- and moment coefficients as a function of angle of attack, thickness and camber. But this is not the only information which was obtained from the CFD analysis. The CFD data also gives us the pressure distribution over the chord of the airfoil. In this section we will make use of that information to distribute the lift force over the nodes of the airfoil model.

In section 4.5.1 it was shown that the lift and drag forces are introduced in the model as resultant forces on the nodes between the chordwise wire elements. Each vector depicted in figure 4.19 is a resultant force vector of the local lift- and drag fraction. Adding the fractions would yield the total resultant force vector for that particular sliver of wing. The aerodynamic moment of an airfoil is the result of the moment introduced by the pressure distributions on the upper and lower surface. These pressure distributions are a result of the flow over the airfoil. With changing angle of attack, airfoil thickness or camber, the force fractions on the nodes also change, not just in absolute sense but with respect to each other as well. The objective is to distribute the total aerodynamic force over the nodes and maintain the same airfoil moment. Figure 4.28 shows a schematic view of a single airfoil as it is represented in the model.

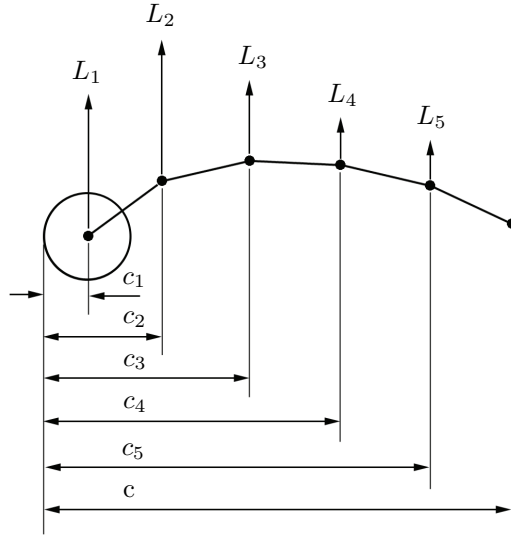


**Figure 4.28:** A schematic representation of the airfoil model.

A method of introducing the aerodynamic forces and moments to the structure is to make separate fits for each force component. Figure 4.29 shows this procedure. In this figure an arbitrary pressure difference between the upper and lower airfoil surface is defined to serve the purpose of this example.

By taking the mean average of the intervals it is possible to obtain the aerodynamic force components:

$$F_i = \frac{\int_{\frac{x_i}{c}}^{\frac{x_{i+1}}{c}} \Delta p \left(\frac{x}{c}\right) d\left(\frac{x}{c}\right)}{\left(\frac{x_{i+1}}{c}\right) - \left(\frac{x_i}{c}\right)} \quad (4.68)$$

With equation (4.68), the airfoil moment becomes:

$$M = F_i \left( \frac{\frac{x_{i+1}}{c} - \frac{x_i}{c}}{2} + \frac{x_i}{c} \right) \quad (4.69)$$

This procedure, in essence, gives us the weight factors with which the total lift force is distributed over the airfoil. For these weight factors  $w_i$  we can write:

$$\sum_{i=1}^n w_i = 1 \quad (4.70)$$



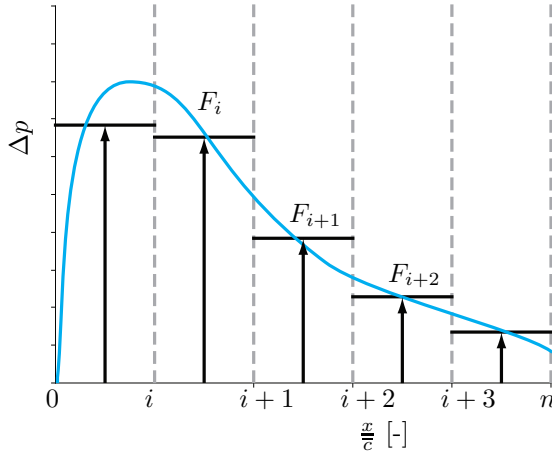


**Figure 4.29:** A schematic representation using the mean average of the intervals depicted to calculate the aerodynamic force components.

Figure 4.30 Shows these weight factors.

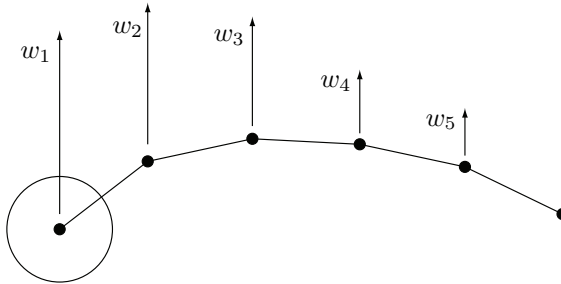


**Figure 4.30:** The weight factors for distribution of the aerodynamic lift force over the nodes.

The airfoil moment, however, is not necessarily equivalent to the airfoil moment obtained from the continuous pressure distribution. Due to the coarse discretization, the contributions from the forces  $F_i$  to the airfoil moment will be different from the contribution of the distributed force in interval  $(\frac{x_i}{c}, \frac{x_{i+1}}{c})$ . This difference is the result of the variation of the gradient of the curve within the interval which creates a different "center of effort" than the mid point of the interval. This discrepancy reduces with increasing resolution of the discretization.

At this point, the number of nodes is limited by currently available processing

power. To stay within the requirements for this simulation with regard to processing capabilities a low amount of nodes is required to approximate the actual airfoil moment as well. Therefore a different approach is suggested.

Changing flight conditions will vary the airfoil lift and moment. This variation is represented by a variation of the weight factors. The rate of variation of the weight factors on the nodes is governed by  $u_i$ . Figure 4.31 shows the weight factors  $w_i$  and the variation of the weight factors  $u_i$ .

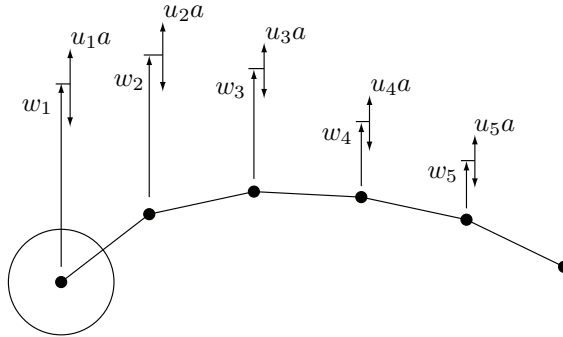


**Figure 4.31:** A schematic representation the changing lift force components.

We now seek to develop a class of discrete functions with which to approximate the distribution of pressure on the airfoil surface. For the factors  $u_i$  we can write the following condition:

$$\sum_{i=1}^n u_i = 0 \tag{4.71}$$

The actual variation of the force components is introduced by variable  $a$ . The distribution is now written as a function of one single variable  $a$  using the constant coefficients  $w_i$  and  $u_i$ . For the lift we can now write:

$$L = \sum_{i=1}^n L(w_i + u_i a) \tag{4.72}$$

The variation of  $a$  does not change the sum of the aerodynamic forces, it only changes their distribution and thus only the airfoil moment. The aerodynamic moment is obtained from the moment algorithm derived in the previous section. It is therefore known for every combination of angle of attack, airfoil thickness and camber. This moment is taken around the quarter chord point of the airfoil. For the airfoil moment we can write:

$$M = \sum_{i=1}^n L(w_i + u_i a)(0.25c - c_i) \quad (4.73)$$

For a set of coefficients  $w_i$  and  $u_i$  which satisfy equations (4.70) and (4.71) we can solve for the variable  $a$ .

$$a = \frac{M - L(0.25c - \sum_{i=1}^n (w_i u_i))}{-L(\sum_{i=1}^n (u_i c_i))} \quad (4.74)$$

In the simulation, the lift fractions can now be determined at every time step. In this approach, only the lift force varies in order to incorporate the correct aerodynamic moment. In reality, due to the camber of the airfoil, the drag force fractions also introduce a moment with regard to the quarter chord point. However, the moment arm of the drag force is small compared to the moment arm of the lift force. Furthermore, the drag force itself is also significantly lower than the lift force. Therefore, the moment introduced by the drag force fractions is much smaller than the moment of the lift force fractions and therefore it has been neglected.

The crux of this procedure lies within the coefficients  $w_i$  and  $u_i$ . It must be noted that for given boundary conditions of  $L$  and  $M$  there are an infinite amount of coefficient sets  $w_i$  and  $u_i$  possible which satisfy equations (4.70) and (4.71). Figure 4.32 shows for a given value of  $L$  and  $M$  and for a number of arbitrary sets of coefficients  $w_i$  and  $u_i$  the resulting force distributions.

The numerical values of the series in figure 4.32 can be found in table 4.1

	$i$	1	2	3	4	5
Series 1	$w_i$	0.2	0.2	0.2	0.2	0.2
	$u_i$	0.5	0.5	-0.4	-0.4	-0.2
Series 2	$w_i$	0.4	0.3	0.1	0.1	0.1
	$u_i$	0.2	0.1	-0.1	-0.1	-0.1
Series 3	$w_i$	0.7	0.1	0.1	0.05	0.05
	$u_i$	0.4	-0.1	-0.1	-0.1	-0.1
Series 4	$w_i$	0.3	0.2	0.2	0.2	0.1
	$u_i$	0.2	0.1	-0.1	-0.1	-0.1
Series 5	$w_i$	0.4	0.2	0.2	0.1	0.1
	$u_i$	0.1	0.1	0	-0.1	-0.1

**Table 4.1:** Arbitrary values for coefficients  $w_i$  and  $u_i$ .

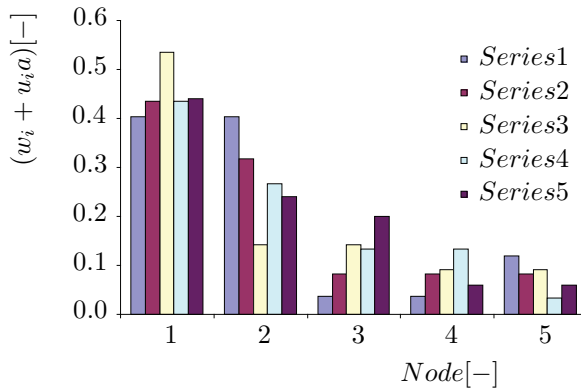


**Figure 4.32:** The distribution of aerodynamic force components in terms of weight factor  $(w_i + u_i a)$  as a result of arbitrary sets of values for  $w_i$  and  $u_i$ .

For each of the series in table 4.1 the conditions of equations (4.70) and (4.71) are met. Furthermore, the sum of the forces all equal the same value for  $L$  and the moment introduced in the airfoil all equal the same value for  $M$ . What is left is an undetermined distribution. In order to come to a set of coefficients  $w_i$  and  $u_i$ , a comparison is made with the original CFD data. Through an iterative procedure, a set of coefficients  $w_i$  and  $u_i$  is determined which satisfies the aforementioned conditions and results in force components which are comparable to the result of the averaged CFD data as depicted in figure 4.29. Table 4.2 displays the chosen coefficients.

$i$	1	2	3	4	5
$w_i$	0.4	0.2	0.2	0.1	0.1
$u_i$	0.1	0.1	0	-0.1	-0.1

**Table 4.2:** Values for coefficients  $w_i$  and  $u_i$ .

We now have reduced the distribution of the lift force components to a one dimensional operation. A particular airfoil moment results in a single value of  $a$ , which is then used to determine the distribution weight factors  $w_i + u_i a$ . The assumption of the shape of the pressure distribution is contained within the coefficients  $w_i$  and  $u_i$ . Figure 4.33 depicts the values for the weight factors  $w_i + u_i a$  for different values of airfoil moment coefficient  $C_M$ .

The question is now: How good is this choice? To evaluate the validity of these values, a set of five lift fractions are directly obtained from the CFD data for a certain airfoil shape and angle of attack and compared to the outcome of the procedure described in this section. Figure 4.34 shows the resulting lift force fractions for both the values obtained directly from the CFD data and the

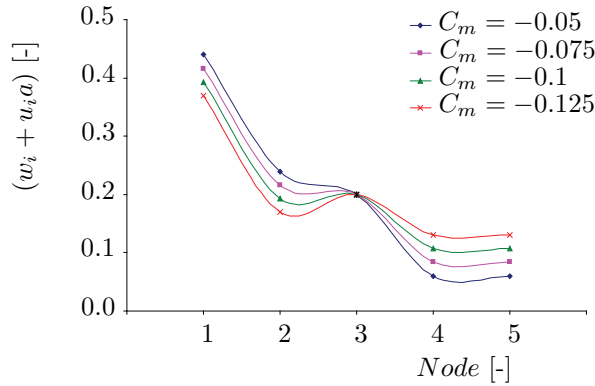


**Figure 4.33:** The values for the weight factors  $(w_i + u_i a)$  for different values of airfoil moment coefficient  $C_M$ .

approximation method described in this section for an airfoil with a 15% thickness and a 4% camber, at an angle of attack of 10.2 degrees.

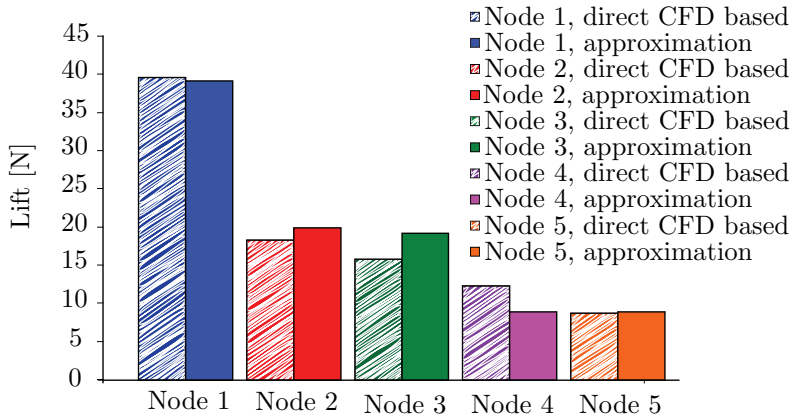


**Figure 4.34:** A comparison of lift fractions for the approximated and direct CFD based values for an airfoil with a thickness of 15%, a camber of 4% and at an angle of attack of 10.2 degrees.

Some discrepancies can be seen in figure 4.34, but overall the two methods show good agreement. Figure 4.35 shows a similar comparison for a 20% thick airfoil with a 4% camber at an angle of attack of 8 degrees

Figure 4.35 shows the same level of agreement between the values obtained using the method described in this section and the values obtained directly from the CFD analysis. Note that an exact agreement between measured and simulated

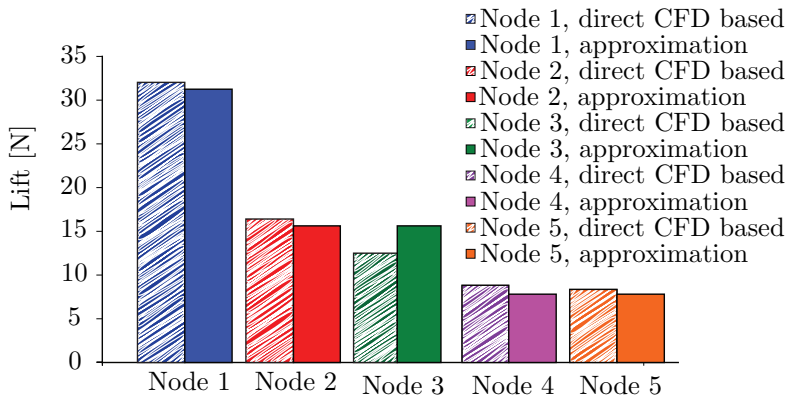


**Figure 4.35:** A comparison of lift fractions for the approximated and direct CFD based values for an airfoil with a thickness of 20%, a camber of 4% and at an angle of attack of 8.0 degrees.

values is not sought. For reasons explained in the beginning of this section, some discrepancies are to be expected as a result of the center of effort position of the distributed aerodynamic force within the intervals (see figure 4.29). The comparison of figures 4.34 and 4.35 only serves as a check whether or not the force components are comparable to the CFD data.

Another critical note must be made concerning this approach. From the CFD analysis of section 4.5.2 a pressure distribution over the airfoil is obtained. This pressure distribution consists of close to 140 discrete values in chordwise direction. This amount of values is a direct result of the coarseness of the CFD mesh. These 140 values are then condensed into one single value for aerodynamic lift, drag and moment. This section proposes to expand the single value of lift into  $n$  values again (where  $n$  is larger than 1). This expansion step makes use of an assumed shape for the pressure distribution. This assumed shape is contained within the  $w_i$  and  $u_i$  coefficients. This is a somewhat odd procedure. Why reduce the data to single values only to continue to increase the number of values again.

The desire to keep the number of chordwise nodes variable is also responsible for the choice to employ the method described in this section. During the development of this method, the flexibility of the number of chordwise nodes was essential in assessing the limits of current hardware. The pre-processed nature of the fitting procedure ensured that the procedure described in this section resulted in more analytical flexibility than a procedure where every number of chordwise nodes required new fitting and new sets of coefficients. It was therefore concluded that the fitted method of this section provides an adequate amount of accuracy and serves the purpose of the simulation.

## 4.5.4 The airfoil toolbox implementation

Building these models by hand is extremely laborious and introduces a high chance of errors due to bad construction. Therefore, a toolbox was created to generate the model. The airfoil tool is a building block in a larger kite simulation toolbox. Figure 4.36 shows the airfoil tool.

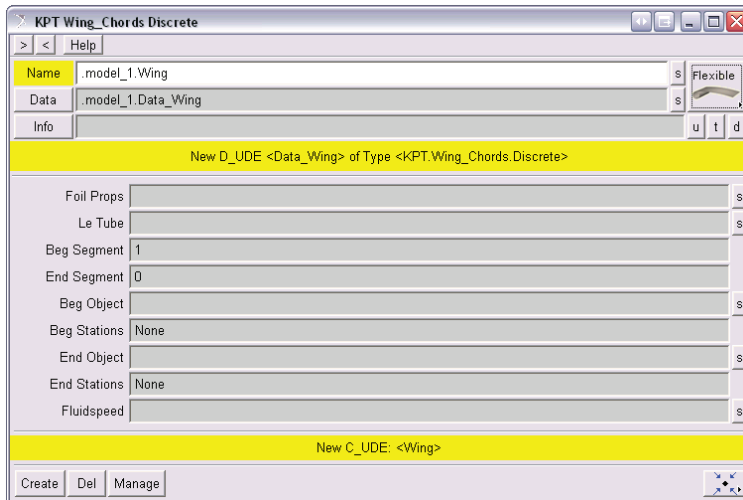


**Figure 4.36:** *The airfoil toolbox.*

”Foil props” reverts to the data file containing the coefficients which govern the lift, drag and moment coefficients. This is where different airfoils can be selected in the simulation. It is therefore possible to have multiple wings with different airfoils operating within the same model. The airfoil model requires an inflatable beam as a base from which it is built. This is indicated in the field next to ”LE Tube”. ”Beg Segment” and ”End Segment” are indicators for the beginning and the end of the foil. ”Beg object” and ”End Object” indicate to what object the beginning and the end of the foil are attached. This could be another inflatable tube, a rigid rod or another foil. ”Beg Stations” and ”End Stations” indicate the specific markers on the objects where the foils are attached. For instance, the foil can be attached along the top of an inflatable strut or on the side of the strut. Lastly, ”Fluid speed” indicates which wind model the airfoil adheres to. For instance, a wind model which introduces a constant wind with increasing altitude or a wind model which introduces a steadily increasing wind as the kite gains altitude. The wind within the simulation is a separate module so that changing the wind properly affects all aspects of the simulation.

## 4.6 Building the complete model

With the three building blocks of section 4.3, 4.4 and 4.5 in place it is now possible to build complex kite models. From within the toolbox, the building blocks can be directly accessed to build a model on the fly. For more complex models it is advisable to build these models from an assembly file. An assembly file is a macro which accesses the building blocks and any other ADAMS-specific items to build the model. This method has the advantage that it is faster and quickly repeatable. It also makes the building process more transparent which lowers the chance of building errors. Figure 4.37 shows a schematic representation of the model building process.

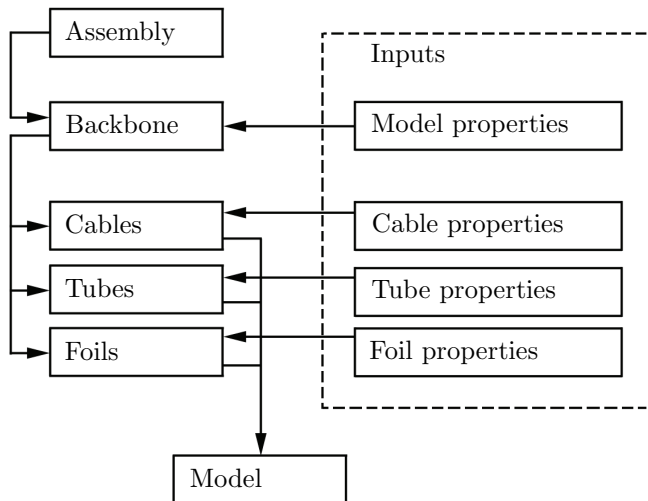


**Figure 4.37:** A schematic representation of the model generation process.

Using the structure in figure 4.37 a fully parametric model can be constructed. The inputs are data files with properties belonging to the assembly or the building blocks themselves. They are called within the assembly and define the model. The model properties has geometric and visualization properties. These properties include items such as wing span, chord lengths, tube diameters, internal pressures and cable attachments. From these properties, a backbone is generated. The backbone of the model is a collection of coordinates indicated by dummy parts which make up the nodes of the model. These nodes indicate where parts such as tubes or cables begin and end. Once the backbone is completed, the model is filled in by calling the three building blocks and building these components. Cable, tube and foil properties govern the specific behavior of these components.



The generation process has been set up like this so that changes made after the model is generated are correctly implemented. This is crucial for a design tool. In this way, changes to properties such as chord length or tube diameter are quickly implemented and simulated. Figure 4.38 shows the resulting model for an airplane-like kite called a "Kiteplane".

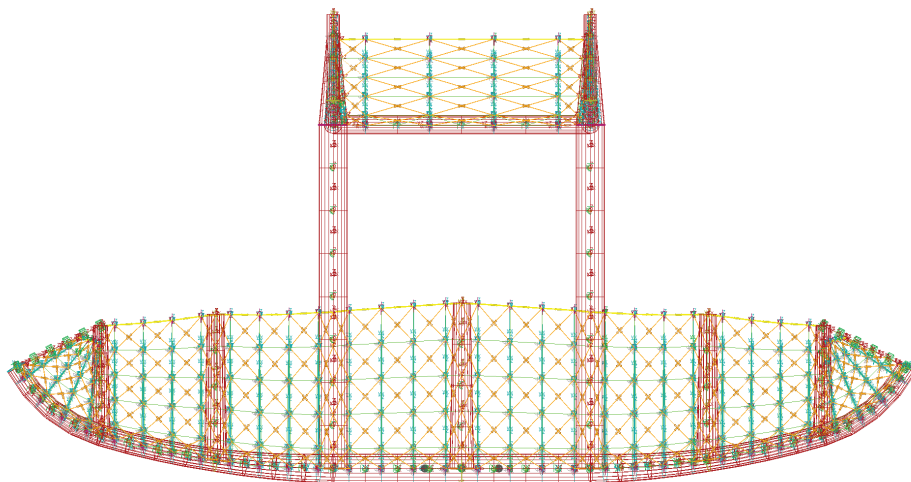


**Figure 4.38:** *A completed model of a "Kiteplane".*

## 4.7 Concluding remarks

This chapter proposes a numerical simulation of kites based on multi-body dynamics. The nature of this simulation is strongly governed by the requirements which were set in section 4.1. Requirements on resource intensity and intuitive use are brought forth by the current state of the kite industry. One could argue that for industrial kites, the industry is expected to be far bigger and thus the need for a simple tool less important over detail. First of all, leaving out the current kite industry would be an enormous mistake. There is a wealth of knowledge available in this industry. Fast and intuitive simulation tools will allow this industry to focus on further improvement by quantifying their knowledge and designs. Second, A fast and intuitive tool is a powerful tool during the conceptual stage of any design effort.



---

## Multi-body kite simulation verification

---

*This chapter provides a validation for the flexible kite model outlined in Chapter 4. In sections 5.2, 5.3 and 5.4 evidence is presented for the validity of the three building blocks in the simulation: The cables of section 4.3, the Inflated tubes of section 4.4 and the airfoils of section 4.5 respectively. Next, section 5.5 presents the results of a windtunnel test where the shape of the three dimensional canopy is measured using photogrammetry and compared with the simulated canopy shape. Lastly, in section 5.6 measurement are presented of the flight performance of a number of surf kites and the results are compared to their simulated counterparts.*

### 5.1 Introduction

Verification performed in this chapter is done mostly on the basis of measurements. In the first three sections the building blocks of the kite simulation toolbox are validated individually. This establishes the validity of the building blocks on their own, but it says little on the validity of combining these building blocks. A kite model integrates these three building blocks into a single model. The validity of this integration of models into a bigger single model is validated in two cases. These two cases are designed to validate the two important results from the simulation, shape under load and flight performance. The first case validates the resulting 3D shape of a canopy under aerodynamic load. The second case validates the flight performance of surf kites.

## 5.2 Cable model verification

In order to verify the physics, an analytically solvable situation and a real world measured situation are compared with their modelled counterpart.

### 5.2.1 Simple pendulum

The first situation is a simple pendulum. For the period of a rod pendulum, we can write:

$$P = 2\pi\sqrt{\frac{\frac{1}{3}ml^2}{\frac{1}{2}mgl}} = 2\pi\sqrt{\frac{2l}{3g}} \quad (5.1)$$

For a pendulum with a length of 1 meter, this results in a period of 1.638 seconds. Modelling this in ADAMS creates the following graph.

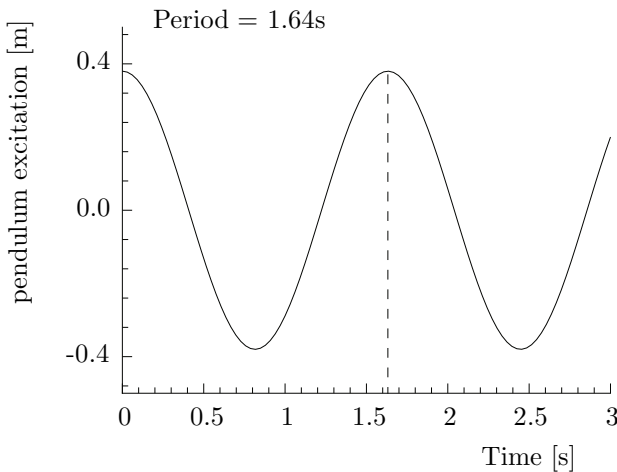


**Figure 5.1:** *Excitation graph of a simulated pendulum.*

As can be seen in figure 5.1, the period of the motion closely resembles the analytical value.

### 5.2.2 Wave propagation

The second case is a real world measured case where a 32-meter long tether was hung from the faculty building on a breezeless day. The tether had a radius of 4mm. The top of the tether was excited and the time was measured which it took

for the maximum of the first wave to travel down to the other end of the tether. A large number of experiments were done which led to an average of 3.3 seconds with a standard deviation of 0.25 seconds. The same situation was modelled in ADAMS using the proposed cable model. In this model, 32 elements were used with a length of 1 meter. At the top, the tether was excited with the function:

$$F = 4\sin\left(8t + \frac{1}{2}\pi\right) \quad (5.2)$$

Figure 5.2 shows the excitation graph for the top and bottom node.

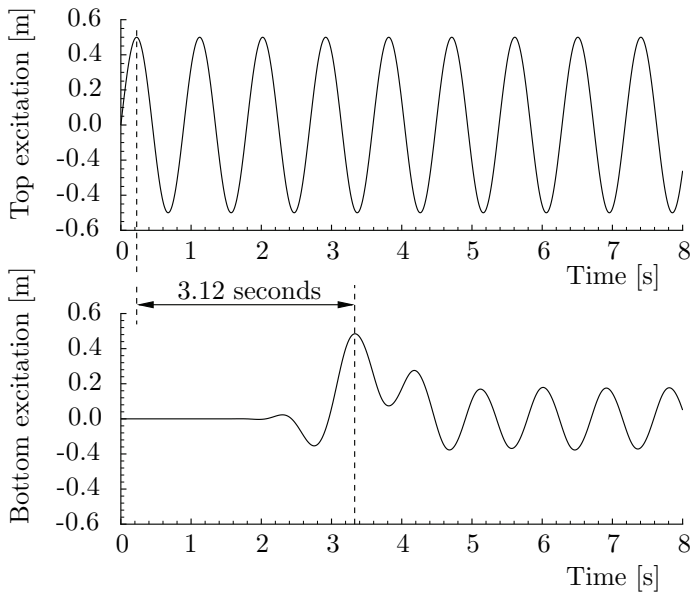


**Figure 5.2:** *Excitation graph of top and bottom node.*

As can be seen, the time for the first wave to travel down the tether is 3.12 seconds, which is close to the measured 3.3 seconds and falls within the standard deviation of 0.25 seconds.

### 5.2.3 Model convergence

The number of elements used in the model is of great influence on the speed with which the calculations can be made. In order to evaluate the sensitivity of the model to the number of elements used, several simulations were conducted with models of the same length (25 meters) but with ever increasing number of

elements. The cable was fixed at the bottom node and a force is introduced on the top node, pulling that end straight up. The cable is simulated and finds an equilibrium between cable mass, external force and aerodynamic drag. Figure 5.3 shows the X and Y coordinates of the top node at equilibrium for cables consisting of different numbers of elements.

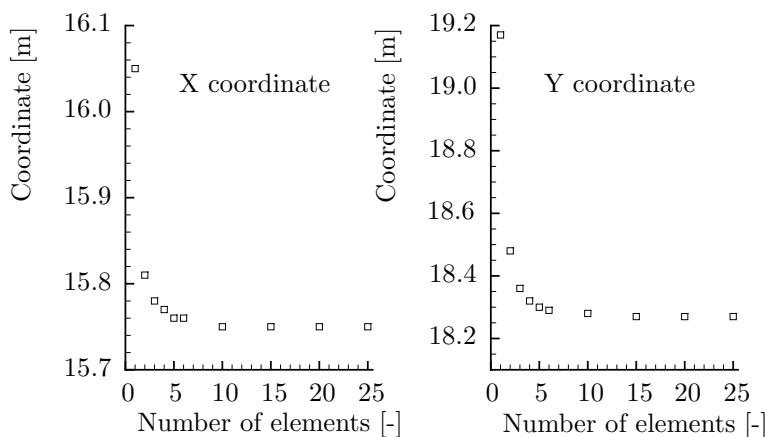


**Figure 5.3:** *Convergence of the cable model.*

As can be seen in figure 5.3, the model will quickly converge with increasing number of elements. For this model, no more than 10 elements would be enough to describe the cable equilibrium with an error smaller than 5%.

### 5.3 Inflatable beam verification

The inflatable beam simulation uses fitted functions to interpolate and extrapolate the experimental data to fit beams of all manner of diameters and internal pressures. One must therefore be aware that such an approach is dependent on the test data itself. The simulation can only be considered valid for beams which have comparable dimensions. Extrapolation of the data is possible, but there are limits to the extent. It can be expected that the validity will suffer under extended extrapolation. The simulation proposed in this thesis is meant as a basis for the simulation of inflatable kites which have a tubular inflatable structure. Such tubes have comparable dimensions as the test beams and consist of the same combination of Dacron fabric and inner TPU bladders. The same materials and dimensions are used in tent structures, making the simulation valid for such structures as well. This is not to say that a simulation with other dimensions and materials is not possible. In such a case, bending and torsion tests of comparable

dimensions and materials would have to be conducted and the resulting test data would have to be used to obtain the constants  $C_1$  through  $C_{19}$ .

On the other hand, this simulation is far less resource intensive than a FE analysis. Setting up the simulation is a matter of minutes using the toolbox. One simply dictates the nodes and the toolbox will create the model automatically. Parameters such as diameter and internal pressure can be changed in an instant. The simulation runs almost real time on a conventional desktop, making it an intuitive tool for designers of e.g. kites.

### 5.3.1 Tapered beam comparison

Up until this point, only straight cylindrical beams have been discussed. In the simulation, conical beams are approximated by varying the radius of each of the elements linearly over the length of the beam. Because the local three dimensional torque vector determines the local bending and local torsion behavior, conical beams are a simple extension of straight cylindrical beams. To compare the performance of conical beams in the simulation with the analytical theory, the location of collapse along the length of the beam is compared. For conical cantilever beams, wrinkling will not necessarily occur at the root of the beam, as is the case with straight cylindrical beams. The location of wrinkling is the result of the balance between local beam radius and local bending moment. For this comparison, we use the wrinkling theory of Comer and Levi ([Comer & Levi, 1963]) which is based on stress. It is also important to note that the location where the first wrinkles occur is also the location where collapse will occur due to the nature of both wrinkling and collapse and their dependence on the principle stress [Veldman, 2005a]. Consider a conical beam with a radius  $r_1$  at the root and a radius  $r_2$  at the tip. For the radius  $r(x)$  along the length of the beam we write:

$$r(x) = \left( \frac{r_2 - r_1}{l} \right) x + r_1 \quad (5.3)$$

For the bending moment we write:

$$M(x) = F_{tip}x \quad (5.4)$$

Using the stress criterion ([Comer & Levi, 1963]), we combine conventional beam theory with the boiler formula for stress in a pressure vessel in longitudinal direction [Gere & Timoshenko, 1991]. The stress criterion dictates that wrinkles will occur as soon as the compressive stress due to bending becomes equal to the tensile stress due to the internal pressure.

$$\frac{My}{I} = \frac{pr}{2t} \quad (5.5)$$

For the conical beam with a radius which is a function of coordinate  $x$ , we write:

$$\frac{F_{tip}(l-x)}{\pi r^3(x)} = \frac{p}{2} \quad (5.6)$$

Or:

$$F_{tip} = \frac{\frac{\pi}{2} p r^3(x)}{l-x} = \frac{\frac{\pi}{2} p \left( \left( \frac{r_2-r_1}{l} \right) x + r_2 \right)^3}{l-x} \quad (5.7)$$

The value for  $x$  which results in the lowest value for  $F_{tip}$  is determined. This is the location at which wrinkles will occur first since it requires the lowest external load for wrinkles to form. In order to obtain the location of the first wrinkles (and thus the location where collapse will occur), we differentiate equation 39 with respect to  $x$ . For each taper ratio we solve for:

$$\frac{dF_{tip}}{dx} = 0 \quad (5.8)$$

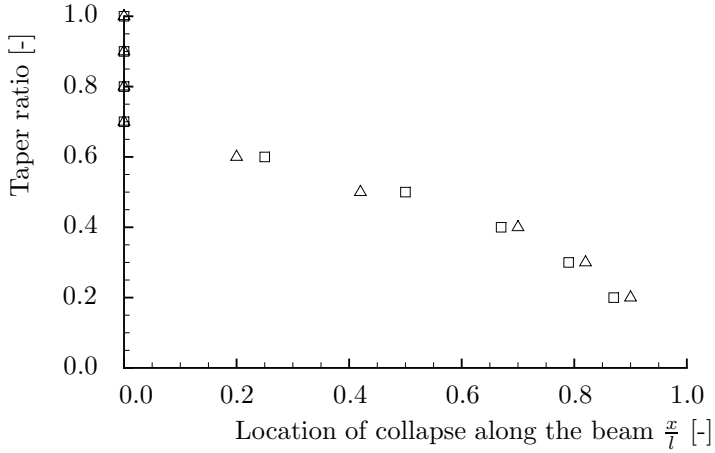
Figure 5.4 shows the correlation between collapse location determined by the analytical theory and the simulation for different taper ratios.

Figure 5.4 shows there is a clear correlation between the measured and calculated data. Some discrepancies occur which can be attributed to the discrete nature of the model. The beam can only collapse between two elements. The point of this comparison is to show that while the test beams were straight cylindrical beams, a simulation for conical beams can still be derived from them with a reasonable measure of accuracy.

### 5.3.2 Beam bending comparison

As was stated earlier, this simulation is tailored particularly with the materials of the test beams in mind. A comparison between bending data from the inflated beams and the simulation can be found in figure 4.11. The simulation makes use of the experimental data these tubes yielded. We now compare the simulation to bending in beams made from a different material to assess the applicability





**Figure 5.4:** A comparison of the location of collapse for different taper ratios.

of different materials with respect to its bending behavior. Figure 5.5 shows the bending deflection curves of a beam with a radius of 5 centimeters at three different pressures.

For the beam tested in figure 5.5 a polyester fiber cloth was used, which was coated in soft PVC. This made for an airtight fabric. The beam was built slightly differently as the other Dacron/TPU beams. Two 1 meter long strips were cut and glued together to form a sleeve. This resulted in not one but two seams, one on each side of the beam. The seams are in the plane of the neutral axis to limit their influence on the bending behavior. The radius was chosen to be 5cm. The cloth was bonded using a PVC adhesive, which would remain somewhat elastic after curing. Most PVC adhesives cure to a hard substance. Such bonds would rip loose in a "breathing" structure such as an inflatable beam. The elastic PVC adhesive is able to move with the beam as it is inflated and deflated. The polyester fiber/PVC material of the beam has a thickness of approximately 1mm, making it twice as thick as the Dacron/TPU material. The simulation underestimates the experimental data by approximately 10%. This can be attributed to the thicker material which makes the collapse of the beam a less sudden event. The thick material allows the wrinkled area to carry a small compressive load. Also, the double seams in the plane of the neutral line can delay collapse as well.

Comparing the simulation to a beam with a larger radius and a less thick material is expected to yield better results. The beam used for this comparison is (again) a straight, untapered beam, fully enclosed on one end and loaded by a single tip force on the other end. The beam consists of Plexiglas caps. Plexiglas was used because of its transparency, letting in enough light enabling the tester

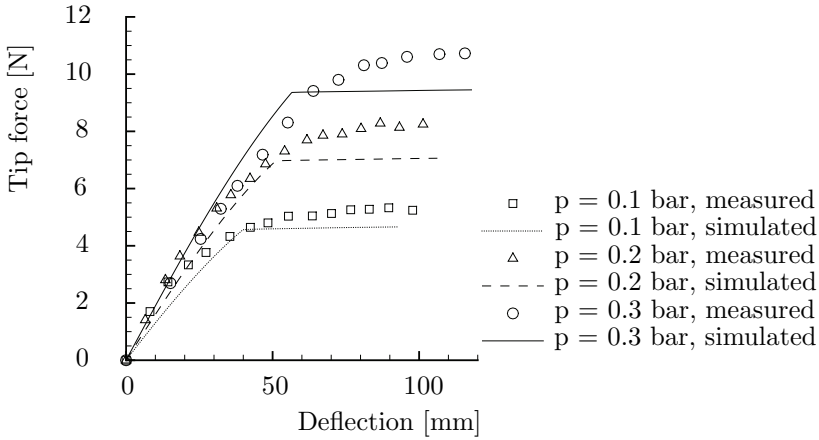


**Figure 5.5:** A comparison of bending data for a measured and simulated polyester fiber cloth beam.

to see inside the beam during testing. The enclosed end cap was glued onto a larger Plexiglas plate, which was subsequently attached to the back plate of a fixture. The free end cap was outfitted with an aluminum bracket. This bracket functioned as an attachment of the load cell. The inner bladder consists of a single layer of nylon 6 flat cast film (Capran 980). Two strips bonded on the long edges form a tube. The two seams are present along the sides of the beam to maintain symmetry. The diameter of the beam was chosen to be 15 cm and the length of the beam is 100cm. A glass-fiber braid was applied over the gas barrier. The braid was clamped into place by a hose clamp on both ends of the beam. This clamp fixed the fibers in place. The fibers are only fixed at the ends of the beam. Between the ends the fibers are not attached to the nylon bladder. The beam was tested in bending for different internal pressures. Figure 5.6 shows a comparison between the tested beam and the simulation results.

As can be seen there is a clear correlation between experimental and simulated data for this beam. The most notable difference is the point of collapse, which the simulation predicts to happen at a lower value of the tip force. This comparison shows that for materials of comparable thickness, the simulation still gives a reasonable prediction of bending behavior. At low bending moments, the simulation is accurate within a few percent. With increasing bending moment, the error increases as well to approximately 5% to 10% at the collapse load. Even though the results are not as detailed as a FE analysis, the results are considered accurate enough for a designer to predict the general shape of a beam under load.

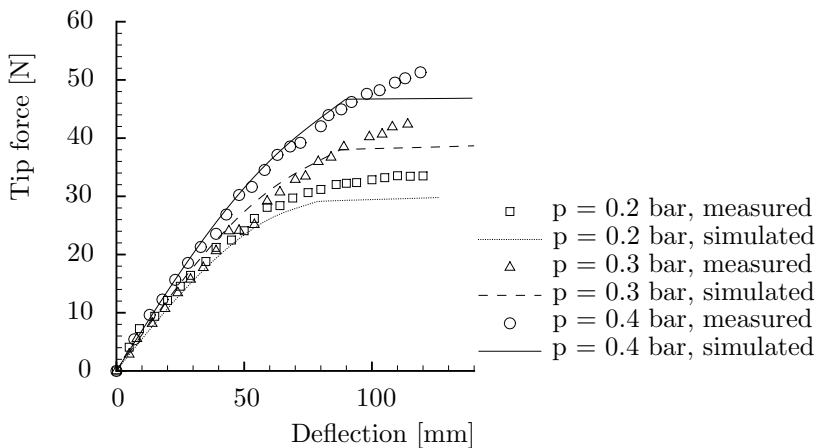


**Figure 5.6:** *A comparison of bending data for a measured and simulated glass-fiber braid beam.*

## 5.4 Airfoil verification

In this section the model is compared to existing wind tunnel tests on the basis of the shape and forces.

### 5.4.1 Comparison of aerodynamic forces

For the comparison, the measurements of [Boer, 1980] are used. Experimental data on single membrane airfoils is scarce. [Boer, 1980] gives good data on the particular airfoil used in kites. In [Boer, 1980] a two dimensional sail wing has been tested at different angles of attack and different values for slack of sail. The model consisted of a round metal bar with a fabric wrapped around it. The other end of the fabric was stretched backwards to create a sail wing. The airfoil of that wing had a 9.33% thickness. By rotating the bar, it was possible to add a slack of sail to the airfoil. For this comparison, only the results with no slack of sail are used for comparison since slack of sail is not included in the present simulation as such.

In order to do a comparison, a model was created with the same dimensions and properties as the wind tunnel model of Boer [1980]. The model is a rectangular sailing wing with a wingspan of 1.2m and a chord of 0.325m. The diameter of the leading edge beam was 3.25cm bringing the thickness of the airfoil to 10%. In the tests of Boer [1980], the canopy of the wing was made from dacron with a weight of 150 grams per square meter. The porosity of the material was measured using a Gurley meter and was considered to be negligible. Figure 5.7 show

a comparison between measured and simulated lift coefficients at two different Reynolds Numbers ( $0.195 * 10^6$  and  $0.295 * 10^6$ )

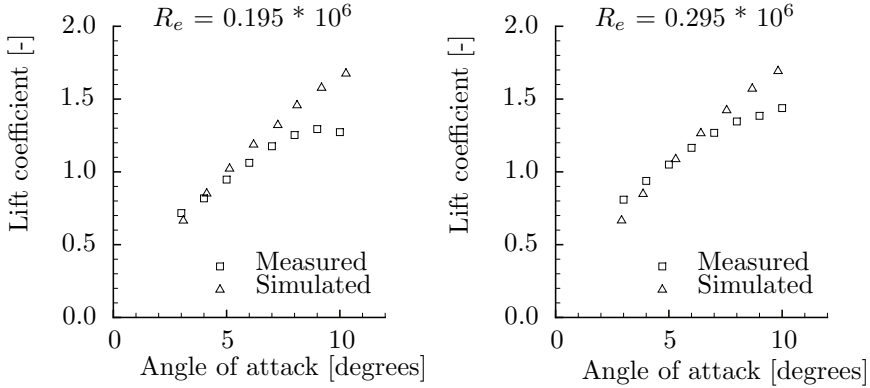


**Figure 5.7:** A comparison of measured and simulated lift coefficients.

At  $R_e = 0.195 * 10^6$  the simulated data shows the same slope as the measured data at low angles of attack, but stall occurs earlier for the simulated data. At  $R_e = 0.295 * 10^6$  the simulated slope agrees less with the measured slope. The discrepancy in stall behavior is likely the result of the CFD data used to build the lift coefficient algorithm. The CFD analysis is notorious for delayed stall and inaccurate drag predictions when significant turbulent flow is present. The single membrane airfoil has such a significant amount of turbulent flow, especially at higher angles of attack. From this consideration, it is worth looking at a comparison between measured and simulated drag. A discrepancy is expected.

From figure 5.8 it can be seen that the simulation overestimates the amount of drag, especially for higher angles of attack.

## 5.4.2 Comparison of 2D canopy shape

The interesting question is now whether or not the discrepancy observed in section 5.4.1 is indeed the result of poor CFD results or whether it is the result of the simulation itself and the resulting shape of the airfoil. To evaluate this, the shapes of the measured and simulated airfoils are compared. [Boer, 1980] Gives the airfoil shapes for different values for the slack of sail. Only the plots with zero slack of sail are useful in this comparison. [Boer, 1980] gives the shape of the airfoil for two Reynolds numbers ( $R_e = 0.195 * 10^6$  and  $R_e = 0.295 * 10^6$ ) an angle of attack of 7 degrees. At this angle of attack, the lift coefficients of both the measured and simulated airfoil are comparable, as can be seen in figure 5.7. The question now is whether or not the airfoils have a comparable shape under

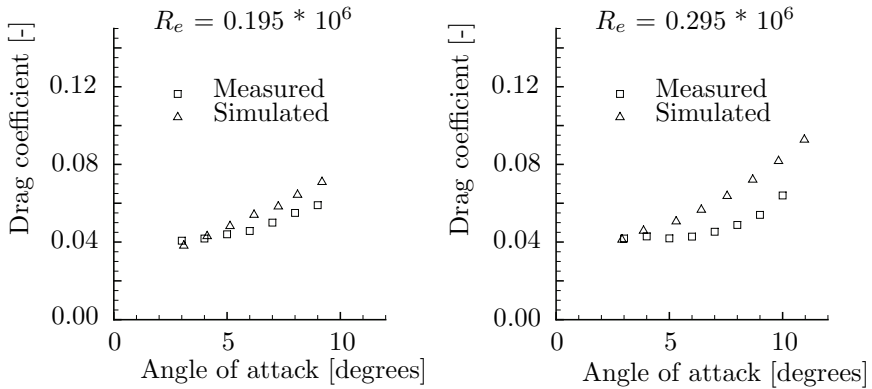


**Figure 5.8:** A comparison of measured and simulated drag coefficients.

this equal aerodynamic load. Figure 5.9 shows the comparison between simulated and measured shape.

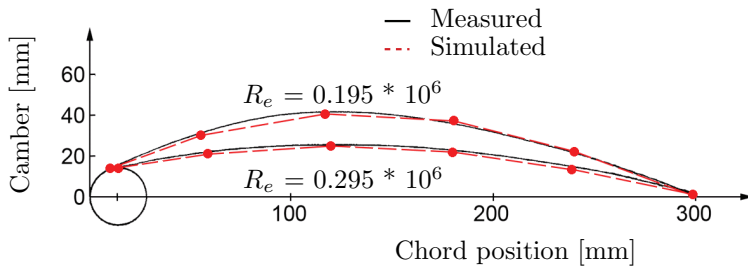


**Figure 5.9:** A comparison of measured ([Boer, 1980]) and simulated airfoil shapes at 7 degrees angle of attack.

Figure 5.9 was composed by overlaying the coordinates of the simulated airfoil onto the plot of the measured airfoil shape from [Boer, 1980]. It can be seen that the simulated and measured airfoil shapes are very close. This gives rise to the idea that the deviation between simulated and measured airfoil shapes at high angle of attack is the result of the data on which the aerodynamic coefficients are based.

## 5.5 3D canopy verification

In this section, a comparison will be made between the simulated three dimensional canopy shape of a Kiteplane and a measured dataset which was obtained using a photogrammetry analysis in the Boen wind kanal at the University of Stuttgart. The aim of this section is to verify the canopy shape and resulting aerodynamic force.

### 5.5.1 3D aerodynamic coefficients

Up to now, the chords of the wing make use of aerodynamic coefficients which have been obtained by analysis of two dimensional airfoil sections. In reality, downwash and tip vortices influence the lift distribution of the wing in such a way that the actual local lift coefficients are slightly lower than their two dimensional counterparts. This effect on the aerodynamic properties of a wing has been subject of extensive research since the 1910s. There are several models to choose from to incorporate this effect. In light of the nature of this simulation, a model was required which gave reasonable results at low computation cost. Due to the fact that this computation would have to be done for every wing chord and at every time step, Prandtl's lifting line theory [Anderson, 1991] was selected. Prandtl's lifting line theory is relatively simple to compute and produces excellent results for planar wings [Anderson, 1991].

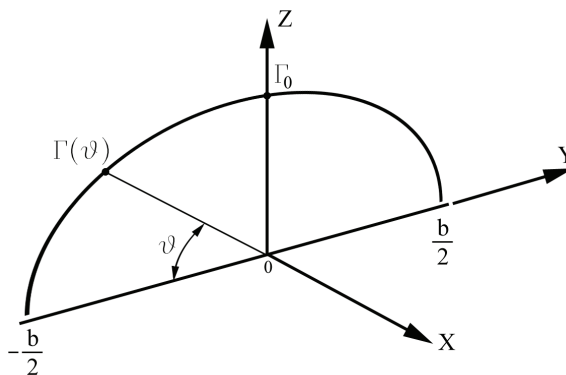


**Figure 5.10:** A schematic representation of Prandtl's lifting line theory.

According to [Anderson, 1991], Prandtl proposes a vortex sheet with a circulation as a function of angle  $\theta$ .

$$\Gamma(\theta) = \Gamma_0 \sin(\theta) \tag{5.9}$$

We can write equation (5.9) as a Fourier sine series:

$$\Gamma(\theta) = 2bV_\infty \sum_{n=1}^N A_n \sin(n\theta) \quad (5.10)$$

With  $n = (1, 2, \dots, N)$  and  $N$  can be as many as is required for accuracy. The coefficients  $A_1$  through  $A_N$  are unknowns. However, they have to satisfy Prandtl's fundamental equation of the lifting line theory [Anderson, 1991]. Differentiating equation (5.10) with respect to  $y$ , we obtain:

$$\frac{\partial \Gamma}{\partial y} = \frac{\partial \Gamma}{\partial \theta} \frac{\partial \theta}{\partial y} = 2bV_\infty \sum_{n=1}^N n A_n \cos(n\theta) \frac{\partial \theta}{\partial y} \quad (5.11)$$

Substitution of equations (5.10) and (5.11) into the fundamental equation of Prandtl's lifting line theory yields:

$$\alpha(\theta_0) = \frac{2b}{\pi c(\theta)} \sum_{n=1}^N A_n \sin(n\theta) + \alpha_{L=0}(\theta_0) + \frac{1}{\pi} \int_0^\pi \frac{\sum_{n=1}^N A_n \cos(n\theta)}{\cos(\theta) - \cos(\theta_0)} \partial \theta \quad (5.12)$$

According to [Karamcheti, 1966], the integral in equation (5.12) can be rewritten to form:

$$\alpha(\theta_0) = \frac{2b}{\pi c(\theta)} \sum_{n=1}^N A_n \sin(n\theta) + \alpha_{L=0}(\theta_0) + \sum_{n=1}^N A_n \frac{\sin(n\theta_0)}{\sin(\theta_0)} \quad (5.13)$$

For any arbitrary span wise location, specified by  $\theta_0$ , the only unknowns in equation (5.13) are the coefficients  $A_1$  through  $A_N$ . By evaluating equation (5.13) at  $N$  different stations on the wing (and therefore  $N$  different values of  $\theta_0$ ), a system of  $N$  equations with  $N$  unknowns is created which can be solved. We are left with values of effective angle of attack  $\alpha(\theta_0)$  for every wing station. These values for effective angle of attack are then used to determine the local aerodynamic coefficients using the algorithms of chapter 4.

## 5.5.2 Comparison of canopy shape

A series of wind tunnel tests were performed on a full-scale inflatable sail wing. Tests were performed at the Boenwindkanal of the University of Stuttgart in

Germany. The Boenwindkanal is a suction tunnel with a circular test section diameter of 6.3 meters and a maximum velocity of 17 m/s. The kite was positioned in the tunnel upside down and suspended by attaching the bridle lines to the load cells in the ceiling of the tunnel. The shape of the canopy was recorded using photogrammetry. The surface of the canopy and part of the leading edge tube were covered in 300 equidistantly spaced dots with a diameter of 12mm. By taking photographs of these dot patterns from different angles, photogrammetry software is able to orient the cameras and the dots in three-dimensional space. This allows for a construction of a wireframe model of the sail wing canopy. Figure 5.11 shows the actual kite in the tunnel and its wireframe model from the same vantage point.

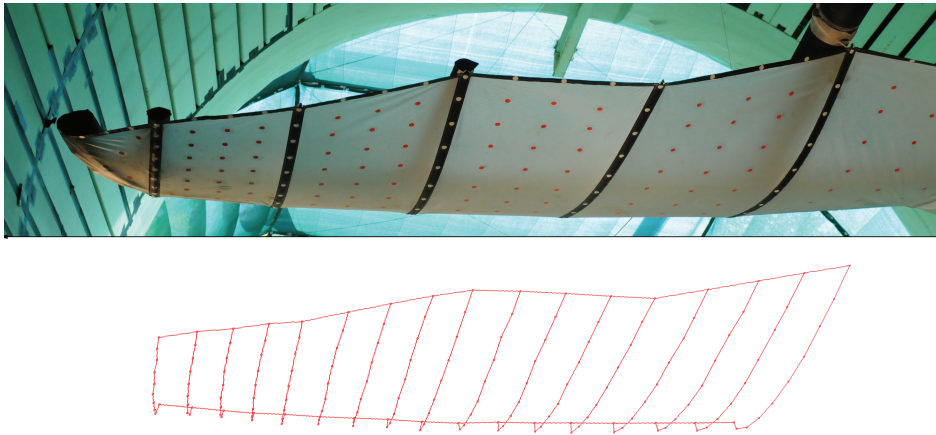


**Figure 5.11:** *Side-by-side view of the actual wing in the tunnel and the wireframe model.*

In order to build an accurate wireframe model, each dot needs to be clearly visible on photographs taken from at least two different angles. Dots that are only visible on one photograph can not be oriented in 3D space. In order to have all these dots photographed, 14 different pictures were taken from different angles. For a completely stationary object, these 14 pictures can be taken by a single camera. By moving around the object and making pictures one can end up with enough photographic material to build the wireframe model. In the case of the kite in the tunnel, this posed a number of problems. Moving about in the tunnel during a test disturbs the flow in such a degree that its influence taints the measurement. Furthermore, the kite in the tunnel is never perfectly still. This would lead to different photographs of different shapes which result in an error in the final wireframe model. In order to capture the shape of the wing, an array of 14 Nikon D300 digital cameras was installed in the tunnel to take photographs simultaneously from 14 different angles. All cameras were connected to a single



shutter switch allowing for all 14 cameras to snap simultaneously, and thereby instantly capture the shape of the wing. This yielded models with an X- Y- and Z-precision error of no more than 1.7mm.

In the determination of the angle of attack the assumption was made that the flow in the tunnel is parallel to the longitudinal axis of the tunnel. This assumption was made for other research projects in the tunnel as well and was deemed reasonable for a tunnel of such configuration. In the floor of the tunnel there is a square panel with markers on it which are used to create a line parallel to the longitudinal wind tunnel axis. These markers were imported into the photogrammetry model as well which allowed an accurate reconstruction of the angle of attack.

During the test phase the wing was placed under different angles of attack and in flows of different velocities. For each combination of angle of attack and flow velocity, the load on the load cells was recorded and three different series of 14 simultaneously taken photographs were stored. During the post processing phase very little difference was observed between the three series of pictures taken, giving rise to the belief that the kite was stable during the tests and that very little vibration occurred. All test data was post-processed into wireframe models of the shape of the wing.

### **5.5.3 Canopy shape comparison**

In order to perform a comparison, a model was created using the toolkit with the same geometry as the kite tested in the wind tunnel. The model was suspended in the same manner as was done in the tunnel and the same flow conditions were introduced. The forces were obtained by measuring the tension in the bridle lines and the shape of the wing was recorded by exporting the deformed model to a 3D CAD program (Rhino 4) where the simulated model could be overlaid with the wireframe model obtained through photogrammetry. In the simulation, the model achieved equilibrium and displayed no significant vibrations. All runs were done on a conventional desktop computer and required approximately two minutes to achieve five hundred 0.01s time steps, resulting in a total run length of 5 seconds. All simulations managed to reach equilibrium within the first 2 seconds of simulated time. After the first two seconds, the displacement of the simulated components was negligible.

The first case to be discussed is a case where the free stream velocity equals 5.3 m/s and the angle of attack equals 12 degrees. This angle of attack is taken at one of the tail booms. It is a reference angle of attack based on the angle between the longitudinal axis of the tunnel and the longitudinal axis of the tail boom. The local angle of attack along the span of the wing can differ greatly from this reference angle of attack. The angle meant here is only used to reference the measured model to the simulated model and it is not used for any calculation of aerodynamic coefficients. Only local angles of attack are used for that purpose. Figure 9 shows the resulting measured shape in red and the simulated shape in

black.

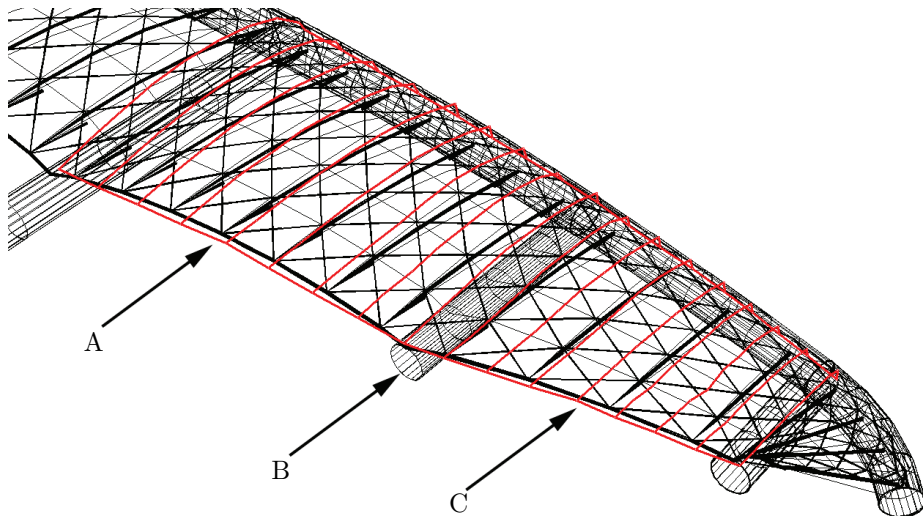


**Figure 5.12:** A comparison between the measured (red) and simulated (black) shape at a wind velocity of 5.3m/s and a reference angle of attack of 12 degrees.

To get a better view of the differences between the simulated and measured shape, three different airfoil cut-outs are made at the location indicated in figure 5.12 by the letters A, B and C. Figure 5.13 shows those cut-outs.

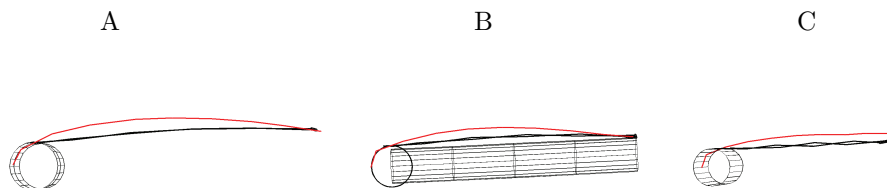


**Figure 5.13:** A comparison between the measured (red) and simulated (black) shape at the three wing stations ( $V_{wind} = 5.3m/s$ ).

The difference in shape between the measured and simulated model are quite significant. A possible reason could be that this measurement was taken at a low velocity and a resulting low wing loading. The wing which was placed in the wind tunnel was hand-made and had a reasonable amount of flights under its belt prior to wind tunnel testing. As a result, the fabric was not perfectly taut as the simulated model assumes. Therefore, initially only a very small amount of force

is required to exhibit quite a significant camber in the canopy. This slack in the sail is possibly the cause of this discrepancy in canopy shape. The force on the bridle was measured to be 39.6N. The simulated model registers 35.25N, which is comparable to the measured value.

For second case to be discussed the wind velocity is 8 m/s and the reference angle of attack is 11 degrees. Figure 5.14 shows the cross sections.

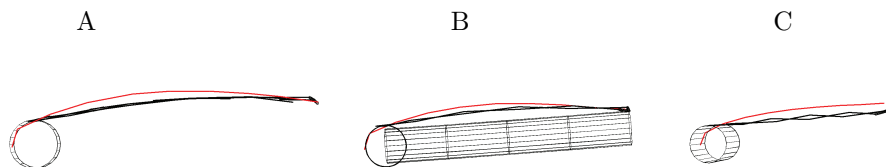


**Figure 5.14:** A comparison between the measured (red) and simulated (black) shape at the three wing stations ( $V_{wind} = 8m/s$ ).

This case sees a higher pressure in the canopy and a closer correlation between the simulated and measured shapes. Especially cross section B shows an improved match. This can be explained by the fact that the strut which exists there keeps the trailing edge in place as much as it can. Only flexure or torsion of the strut or leading edge beam can displace the trailing edge in that location. A discrepancy does exist at cross section C where the trailing edge displacement of the simulated and measured model shows a significant difference. Due to the fact that this discrepancy increases towards the tip, it is plausible that this is caused due to increased torsion of the leading edge beam. This idea is further substantiated by the fact that the outer most strut of the measured model exhibits a slightly decreased angle of attack with respect to the same strut on the simulated model. A local weakness or production fault in the inflated tube could be the cause of this phenomenon. Which of the two might become apparent when models of higher wing loading are compared. If the discrepancy in tip angle of attack stays relatively constant with increasing wing loading, it is more likely the result of a fault in production whereby the leading edge beam has a slight twist. If the discrepancy grows with increasing wing loading a local weakness lowering the torsional stiffness is more plausible. The resulting force in the beam was measured in the wind tunnel to be 75.28N. The simulation showed a value of 69.43N, a value comparable to the measured bridle force.

The third case was measured at a wind speed of 12 m/s and at a reference angle of attack of 22 degrees. Figure 5.15 shows the cross sections.

In this case, the wing is close to  $C_{L,max}$  and the pressure in the canopy is considerable. At this configuration the wing introduced a total force in the bridle lines of 173.97N in the bridle lines. The simulated force in the bridle lines was

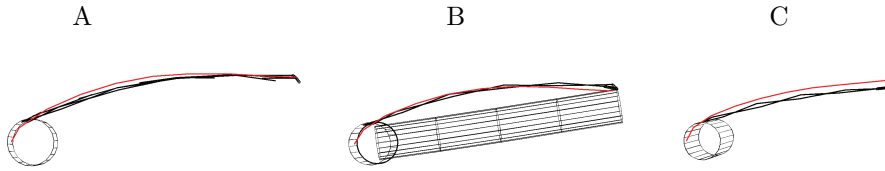


**Figure 5.15:** A comparison between the measured (red) and simulated (black) shape at the three wing stations ( $V_{wind} = 12\text{m/s}$ ).

169.8N, a value very close to the measured bridle force. In this high canopy stress case the measured and simulated model show good correlation at cross sections A and B. For cross section C the same discrepancy is visible as was observed in the previous two cases.

The last case was taken at close to the maximum tunnel speed of 16m/s and at a reference angle of attack of 21.5 degrees. Figure 5.16 shows the resulting cross sections.

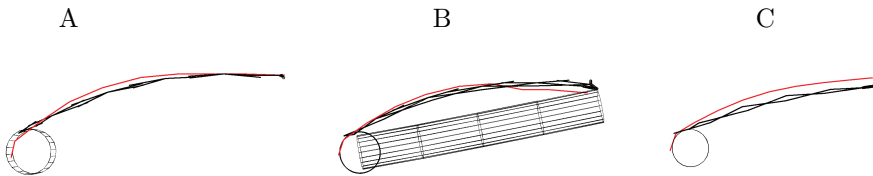


**Figure 5.16:** A comparison between the measured (red) and simulated (black) shape at the three wing stations ( $V_{wind} = 16\text{m/s}$ ).

Again, at this high canopy stress case, good agreement is shown between the measured and simulated models. This seems to substantiate the hypothesis that the larger discrepancies seen in the first two cases are indeed the result of initial slack in the foil. As the tension increases and the displacements grow larger, the relative contribution of the initial slack becomes smaller. Better shape correlation is reached and more accurate bridle force values present themselves. For this case, the bridle force was measured in the wind tunnel to be 262.28N, the simulated value turned out to be 257.7N. Furthermore, the discrepancy in cross section C seems to remain equal for whatever wing loading acts on the canopy. This further substantiates the idea that the wing indeed has a slight twist in the outer area of the inflated leading edge tube. Such a twist could have easily come about as the result of a production fault or due to damage sustained during flight testing.

One last issue that requires attention is the kink which is present in the measured canopy at station B. At about 30% chord from the trailing edge the canopy has a bend downwards. This bend is clearly visible in figure Figure 5.16 at 16m/s but was also beginning to become visible in figure Figure 5.15 at 12m/s. A possible explanation of this kink is that at this station, due to the increasing tension, wrinkles start to form in the canopy fabric. These wrinkles were clearly observed during testing. These wrinkles may have disturbed the flow to such a degree that an area of turbulence occurs. The simulated model does not take into account such local effects and therefore the kink does not show itself.

## 5.6 Surf kite comparison

To evaluate the simulation, a comparison is made with measured data using existing surf kites. These kites are flown and the forces in the lines are measured, as well as the absolute velocity of the kite using a GPS Doppler based velocity estimation .

### 5.6.1 3D aerodynamic coefficients of an arc wing

The aerodynamic coefficients determined in section 4.5.2 are obtained by a two dimensional CFD analysis. Therefore, these coefficients are purely two dimensional coefficients. On finite wings, effects as span wise flow and tip vortices cause the aerodynamic coefficients of a three dimensional wing to be substantially different. For straight tapered wings, Prandtl's lifting line theory produces good correlation between calculated and measured values of the 3D aerodynamic coefficients in relation to their 2D counterparts. However, for an arc-shaped wing such as a surf kite, Prandtl's lifting line theory does not hold ([Anderson, 1991]). To investigate the lift distribution on an arc-shaped surf kite, the Tornado vortex-lattice method ([Stockholm Sweden & Bristol, 2008]) was used. The vortex-lattice method approximates a lifting surface as an infinitely thin sheet of discrete vortices in order to calculate the lift and induced drag. The influences of viscosity and thickness are neglected. A model was created using a total of 1000 panels which was subsequently used to calculate the lift distribution on the arc shaped kite at different angles of attack and slip angles. Figure 5.17 shows the 2D and calculated 3D lift distribution graph. In this graph, the horizontal axis has the coordinate along the arc of the kite. It is the coordinate along the wetted surface, not the projected surface. The lift coefficient depicted in figure 5.17 represents the lift perpendicular to the local wing surface, not the body axis.

At 0 degrees slip angle, the curves of figure 5.17 are symmetrical with respect to the vertical axis at span coordinate = 0. A significant difference can be observed between the 2D and 3D coefficients. In contrast to the center, towards the tips the 3D coefficient is larger than its 2D counterpart. [Lowson, 1990] reports an increased efficiency towards the tips for arc shaped wings. It is plausible that span

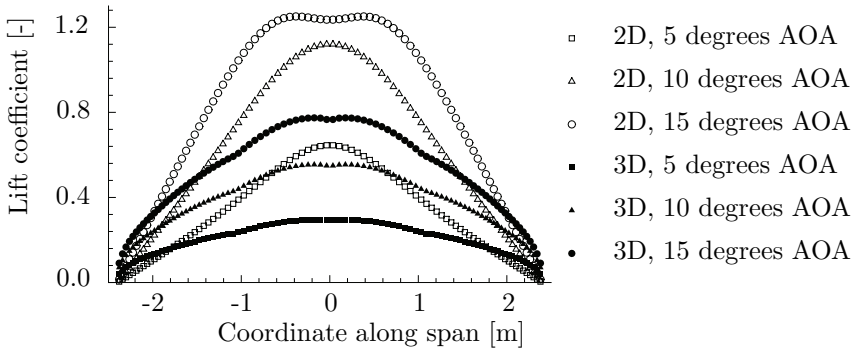


**Figure 5.17:** 2D and 3D lift distribution on a surf kite at different angles of attack (0 degrees slip angle).

wise flow along the arc of the wing from center to the tips results in an increased pressure which subsequently results in increased lift. At the tips, the lift drops to zero for both the 2D and 3D curves. This is due to the fact that the angle of attack at the tips is zero for a zero degree slip angle. Figure 5.18 shows a similar set of curves for a kite at a slip angle of 5 degrees.

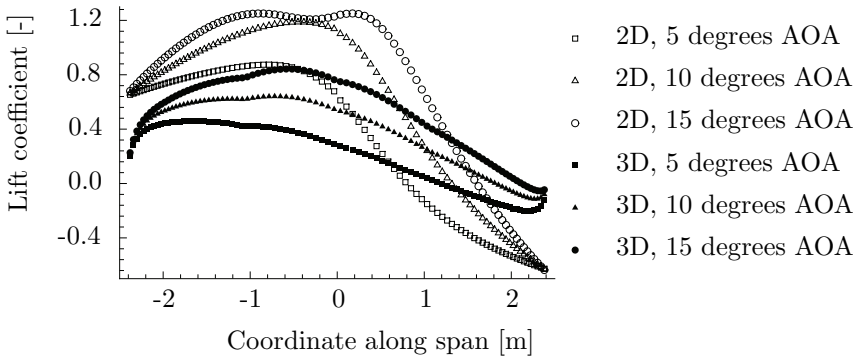


**Figure 5.18:** 2D and 3D lift distribution on a surf kite at different angles of attack (5 degrees slip angle).

In figure 5.18, the curves are no longer symmetrical with regard to the vertical axis. The same differences can be observed between the 2D and 3D lift distribution curves. The slip angle of 5 degrees shifts the local angle of attack along the arc wing. In order to get a better understanding, the arc shaped wing is subjected to a range of different angles of attack and slip angles. These variations create different local angles of attack along the arc. For this analysis, the wing is assumed

to be rigid. The procedure has been repeated for the same wing with a number of different airfoils. These airfoils all had the same single membrane characteristics, but differed in airfoil thickness and camber. We can now plot the lift coefficients obtained at a certain location of the arc as a result of varying local angle of attack.

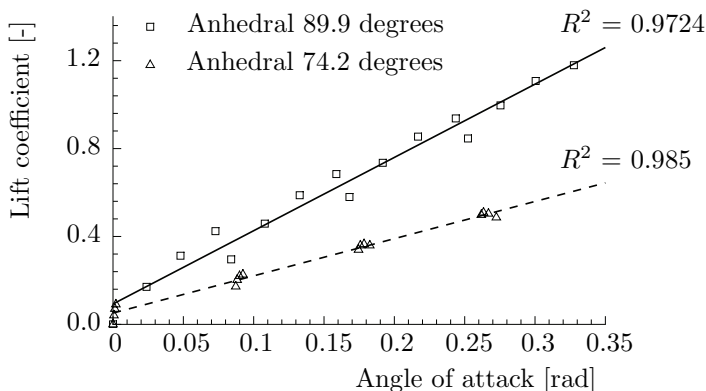


**Figure 5.19:** Lift coefficients and their corresponding angles of attack for two locations along the arc.

Figure 5.19 shows the lift coefficients at two locations along the arc wing with a single membrane airfoil with 15% thickness and 4% camber. The anhedral angle indicates the coordinate of the two locations. An anhedral angle of 90 degrees indicates the tip of the kite and an anhedral angle of 0 degrees indicates the top of the kite. With a degree of error, indicated in figure 5.19 as the  $R^2$ -value, the lift coefficients at the locations on the arc wing can be approximated using a fitted linear function. Although the error at certain angles of attack can be clearly visible in figure 5.19, the approximation is deemed acceptable in regard to the fidelity of the entire model. With the linear functions fitted at different locations along the arc wing, it is now possible to determine a constant local lift curve slope  $dC_L/d\alpha$ . Figure 5.20 is a plot of these slopes as a function of dihedral.

Figure 5.20 shows a relatively constant  $dC_L/d\alpha$  for the center wing locations. Towards the tips, the  $dC_L/d\alpha$  values increase slightly, only to drop sharply at the edge of the tips. Very little variation is observed in the curves for different airfoils. With the largest difference only resulting in marginal differences in the lift coefficients, the relation between lift curve slope and anhedral angle is assumed to be independent of airfoil shape. With this relation between dihedral angle and  $dC_L/d\alpha$  known, we can now determine the local 3D lift coefficient for any location and any angle of attack where the lift curve is linear. The simulation uses a 10-step procedure to come from a 2D coefficient to a 3D coefficient.

**Step 1:** Each location on the arc has its own angle of attack, camber and

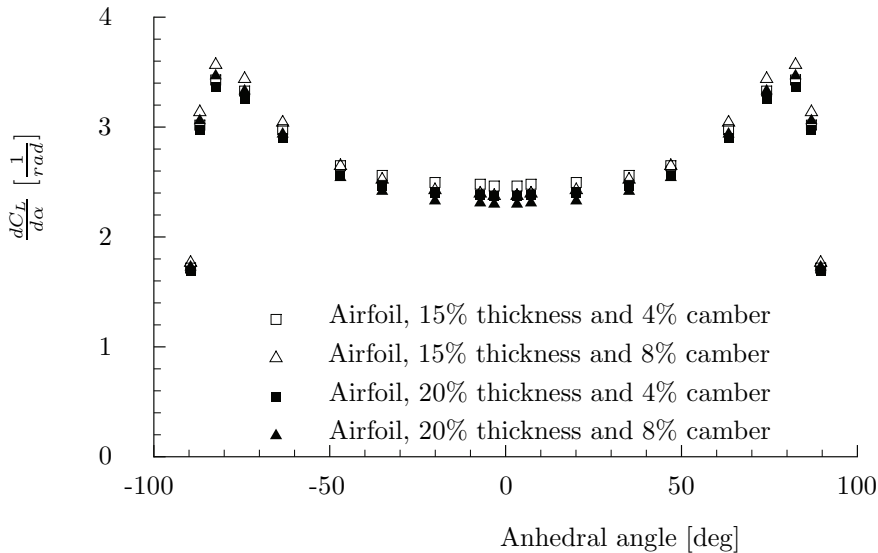


**Figure 5.20:** Lift curve slope  $\frac{dC_L}{d\alpha}$  as a function of anhedral angle.

airfoil thickness. Based on these parameters, a 2D coefficient is determined as was explained in section 4.5.2. Along with this coefficient, two other 2D coefficients are determined as is indicated in fig 5.21.

Using the fitted algorithm, two other points on the curve are determined.  $Cl_{\alpha,0}$  is the lift coefficient at angle of attack zero and  $Cl_{\alpha,x}$  is the lift coefficient close to the end of the linear part of the lift curve.

**Step 2:** The values obtained in step 1 are used to create a linear function for the linear part of the lift curve.

$$Cl = \frac{Cl_{\alpha,x} - Cl_{\alpha,0}}{\alpha_x} \alpha + Cl_{\alpha,0} \quad (5.14)$$

**Step 3:** Equation (5.14) is now used to obtain the zero lift angle  $\alpha_{ift,0}$

$$\alpha_{ift,0} = -\frac{\alpha_x Cl_{\alpha,0}}{Cl_{\alpha,x} - Cl_{\alpha,0}} \quad (5.15)$$

**Step 4:** Determine the  $dC_L/d\alpha$  from the relation as indicated in figure 5.20.



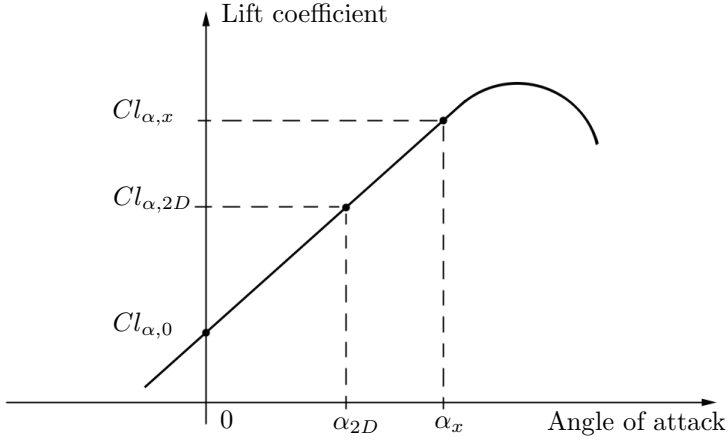


**Figure 5.21:** Step 1: determine  $Cl_{\alpha,2D}$ ,  $Cl_{\alpha,0}$  and  $Cl_{\alpha,x}$  using the fitted algorithm.

**Step 5:** For both the 2D and 3D lift angle, the zero lift angle of attack is the same (figure 5.21 from [Anderson, 1991]). With the lift curve slope  $dC_L/d\alpha$  we can now determine a linear function for the linear part of the 3D lift curve.

$$CL = \frac{dCL}{d\alpha} (\alpha - \alpha_{lift,o}) \quad (5.16)$$

**Step 6:** With equation 4 it is now possible to determine  $CL_{\alpha,x}$ .

$$CL_{\alpha,x} = \frac{dCL}{d\alpha} (\alpha_x - \alpha_{lift,o}) \quad (5.17)$$

**Step 7:** At this juncture, it is possible to obtain the effective angle of attack belonging to  $CL_{\alpha,x}$ . The effective angle of attack is the angle of attack which the airfoil "feels" as opposed to the actual angle of attack. The difference between these two angles is created by the losses induced by the 3D flow effects such as span wise flow and the tip vortices. Figure 12 shows the effective angle of attack for  $CL_{\alpha,x}$ .

$\alpha_{eff,x}$  can be obtained by solving the fitted algorithm equation from section 4.5.2:

$$CL_{\alpha,x} = \lambda_1 (\alpha_{eff,x})^3 + \lambda_2 (\alpha_{eff,x})^2 + \lambda_3 (\alpha_{eff,x}) + \lambda_4 \quad (5.18)$$

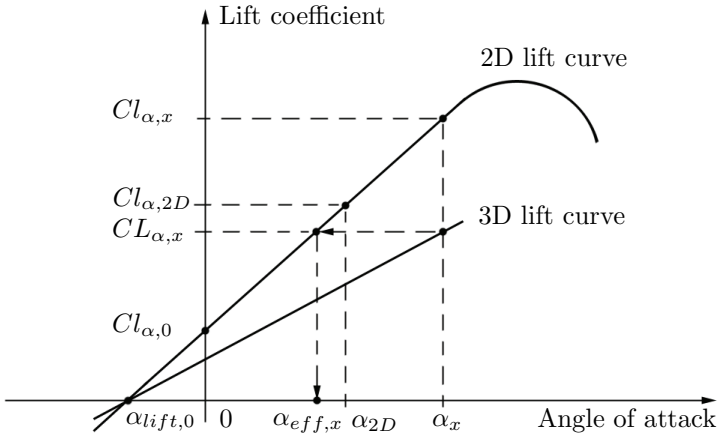


**Figure 5.22:** Step 7: determine  $\alpha_{eff,x}$ .

Solving for  $\alpha_{eff,x}$  involves solving the 3rd order polynomial. This can yield up to three roots and thus three different values for  $\alpha_{eff,x}$ . Moreover, the occurrence of complex numbers is more than likely. Complex numbers are a problem for MSC ADAMS code. There are no provisions for solving equations with complex numbers in MSC ADAMS. It is therefore imperative to obtain  $\alpha_{eff,x}$  from equation (5.18) without the use of complex numbers. For this purpose, Cardano's method is used. More on Cardano's method can be obtained in [Bronstein & Semendjajew, 1991].  $\alpha_{eff,x}$ , Cardano's method states:

$$\alpha_{eff,x} = \left[ 2(X_i)^{\frac{1}{3}} \cos\left(\frac{\phi}{3} - \frac{4}{3}\pi\right) \right] - \frac{\lambda_2}{3\lambda_1} \tag{5.19}$$

With:

$$X_i = -\frac{\frac{\lambda_3}{\lambda_1} + \frac{\lambda_2^2}{3\lambda_1^2}}{27} \tag{5.20}$$

And:

$$\phi = -\frac{\frac{\lambda_4 - CL_{\alpha,x}}{\lambda_1} + \frac{2\lambda_3^3 - 9\frac{\lambda_2\lambda_3}{\lambda_1^2}}{3\lambda_1^2}}{2X_i} \tag{5.21}$$

With equations (5.19), (5.20) and (5.21) it is possible to obtain the value of  $\alpha_{eff,x}$ .

**Step 8:** With  $\alpha_{eff,x}$  and  $\alpha_{lift,0}$  known, it is possible to determine  $(\alpha - \alpha_{eff})$  as a function of  $\alpha$ :

$$\Delta\alpha = (\alpha - \alpha_{eff}) = \left[ \frac{\alpha_x - \alpha_{eff,x}}{\alpha_x - \alpha_{lift,0}} \right] (\alpha - \alpha_{lift,0}) \quad (5.22)$$

**Step 9:** With equation (5.22), it is now possible to calculate the effective angle of attack at which the airfoil is flying.

$$\alpha_{eff} = \alpha - \Delta\alpha \quad (5.23)$$

**Step 9:** With the effective angle of attack of the local airfoil known, we can obtain the value of the 3D lift coefficient by substituting this effective angle of attack into the lift coefficient algorithm.

$$CL = \lambda_1 (\alpha_{eff})^3 + \lambda_2 (\alpha_{eff})^2 + \lambda_3 (\alpha_{eff}) + \lambda_4 \quad (5.24)$$

At this point, CL has been determined and is used for calculation of lift forces in the model.

## 5.6.2 Surf kite measurements

In order to determine the validity of the simulation, its performance is compared to measured data. Several flight tests were undertaken, using a variety of kites ranging from  $6m^2$  to  $16m^2$ . Tube kites are generally flown on four lines. Figure 5.23 is a simplified representation of the lines on a common tube kite.

The power lines support most of the pulling force of the kite. The steering lines allow the kite to be steered in both pitch and yaw. Pulling on a steering line will shift the resultant force on the particular tip from the leading edge towards the trailing edge. If the entire bar is pulled towards the rider, both steering lines are equally loaded. The resultant cable force on each tip shifts towards the trailing edge equally. This makes the kite fly at a higher angle of attack. In other words: it "powers" the kite. If the bar is rotated, only one of the steering lines is tensioned and therefore only on one tip does the resultant cable force shift towards the trailing edge. This induces a yawing motion in the kite. More on steering the kite will be presented in chapter 6

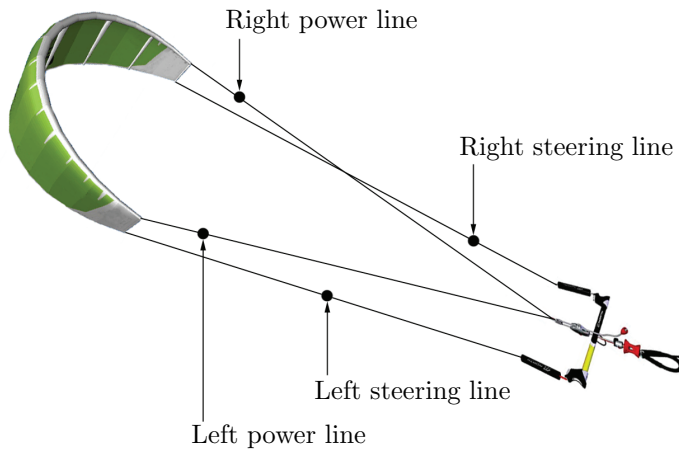
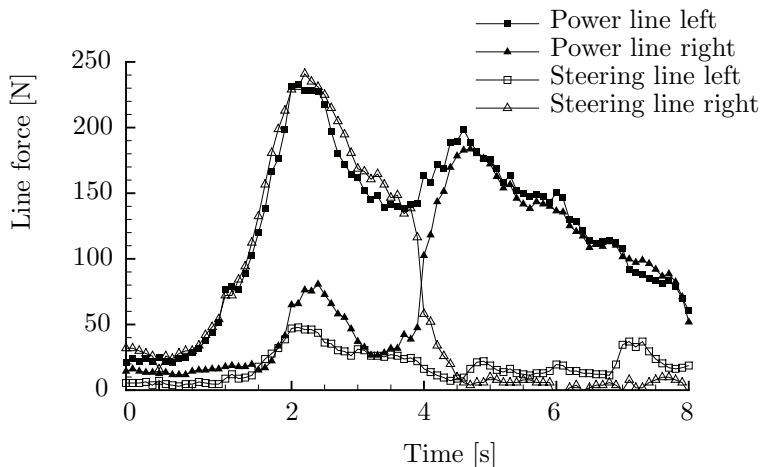


**Figure 5.23:** *The line plan of a conventional tube kite.*

For the comparison with the model, surf kites of different sizes were flown. A set of four load cells were placed in the four lines, measuring the line tension. The load cells were connected to a small logging unit and time-stamped using GPS time. To measure the velocity of the kite, a small GPS receiver was placed on the top-center strut in the kite. The velocity used for the comparison is a Doppler-based velocity measurement which gives the velocity as a scalar. There is also an option to determine the velocity vector by integration of the GPS position, but this data proved to be too inaccurate for a proper determination of the velocity vector. The Doppler-based velocity measurement uses the slightly changing frequency of the GPS D-band carrier signals to determine a velocity scalar. The accuracy of such a measurement is reported to be within 0.2m/s ([Zhang et al., 2006]). Lastly, wind measurements were used from a local weather station which measures wind speed at an altitude of 10 meters above MSL in 10 second intervals. The test was performed at the beach with calm conditions and a steady breeze from the sea between 5m/s and 7m/s. 3 second interval gusts were reported to be no larger than 2m/s above the average value.

At the start of a measurement, the kite was brought into its zenith position in the top of the wind window. This means the kite is flying center and level, high above the kite flyer. In this position, the steering lines are slack and the tug force is fully supported by the power lines. Once the kite is in this position, a control input is given by rotating the bar to one side and tensioning one of the steering lines. This makes the kite yaw and dive. During this dive, the kite picks up speed rapidly. Because of this speed and the still tensioned steering line, the kite keeps yawing and loops until it is facing nose up again. If the steering line is kept under tension, the kite will continue to loop. This maneuver was performed

on a number of kites of different sizes to both the left and the right. Figure 5.24 shows the resulting line forces for a North Rhino  $16m^2$  kite.



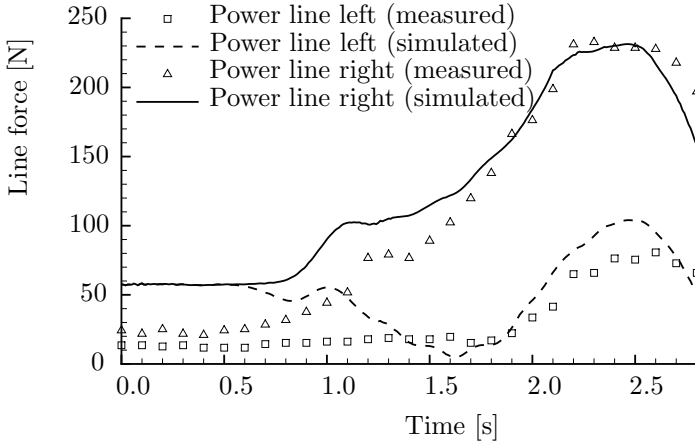
**Figure 5.24:** *The line force of a North Rhino 16m<sup>2</sup> kite while performing a loop.*

Figure 5.24 shows a turn to the right. At 16:43.3 the right steering line is tensioned and the kite begins its turn. As the velocity increases it makes one loop after which the tension on the right steering line is released. Once both the steering lines are slack, the velocity reduces and the kite flies back to its zenith position. It is interesting to note that during the turn, this particular kite hangs almost completely by its left power line and its right steering line. The forces on the other lines are significantly lower.

### 5.6.3 Comparison between measured and simulated data

In order to make a comparison between the measured data, as represented in figure 5.24, and the data obtained from the simulation model it was first attempted to reproduce the steering inputs at the bar during the flight test into the simulation model. This procedure leads to unsatisfactory results due to the fact that a correct representation could not be guaranteed. The exact position and angle of the bar is difficult to measure. The person flying the kite is not always able to perform perfect block-shaped control inputs. The body of the person flying the kite is flexible as well and the bar is not rigidly attached to the kite flyer. Some thought went into making a rigid ground station with a carefully controlled bar. This idea was abandoned for the simple fact that connecting a kite to a rigid point on the ground can be dangerous. When the kite accelerates it can easily rip itself to pieces.

Ultimately, it was decided to use the forces on the steering lines as control input for the model and make a comparison based on the forces in the power lines and the absolute velocity of the kite. This circumvents the practical problems involving the measurements of the bar and allow for a solid comparison where the only uncertainty in the validity of the control inputs lie with the accuracy of the load cells.

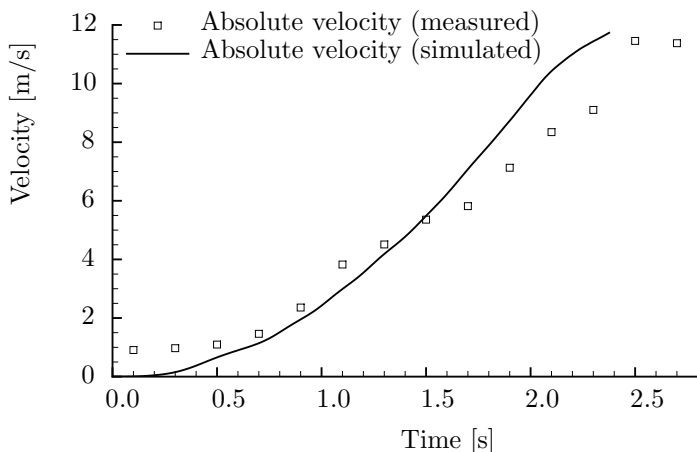


**Figure 5.25:** Comparison of power line forces between the measured and simulated data of the  $16m^2$  North Rhino.

Figure 5.25 shows a comparison between the forces in the power lines of the model and the measurement for a  $16m^2$  North Rhino kite. The forces on the steering lines were used as control inputs and the force on the power lines, as well as the absolute velocity were recorded. The model anatomy is such that it represents the actual kite as close as possible. The model consists of a kite and four lines. The power lines are attached in a rigid point. Force vectors act on the end of the steering lines and are directed towards the ground attachment point of the power lines. The physical inclusion of the steering lines is done because the measurement of the steering line force is done close to the ground. Due to drag on the line and its inertia both the direction and the magnitude of the steering line force can be expected to differ between the end of the steering line and at the kite tip.

Figure 5.25 shows a Left hand loop performed from a zenith position. As the kite starts to turn, its velocity increases and the kite starts to pull. For this particular kite we see a discrepancy in line force in the first second. This is the result of the fact that it is difficult to keep the kite completely still at the beginning of the maneuver due to fluctuating winds. And with a large surface area such as this North Rhino has, these small variations in wind quickly translate to

line forces. Apart from the initial discrepancy, figure 5.25 shows good correlation between the flight test and the simulation. Figure 5.26 shows the comparison between measured and simulated velocities.



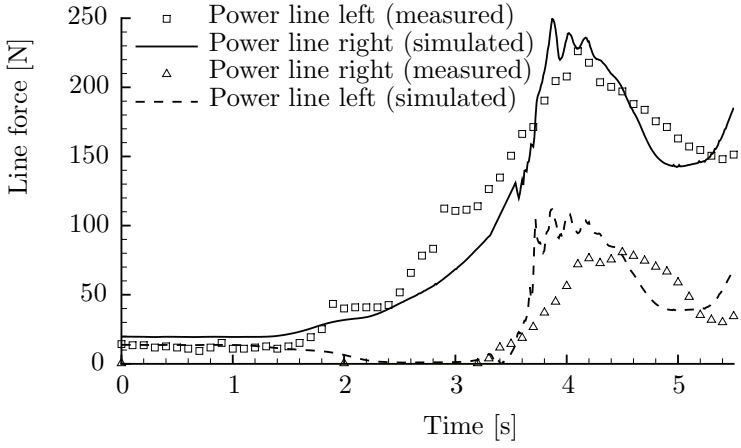
**Figure 5.26:** A comparison between measured and simulated velocities of the  $16m^2$  North Rhino.

Figure 5.26 shows good correlation between simulated and measured data. The initial discrepancy in line force in the first second of figure 5.25 seems to agree with the fact that the initial velocity in that first second is higher for the measured data. This is due the aforementioned issue with keeping a large kite still in varying winds.

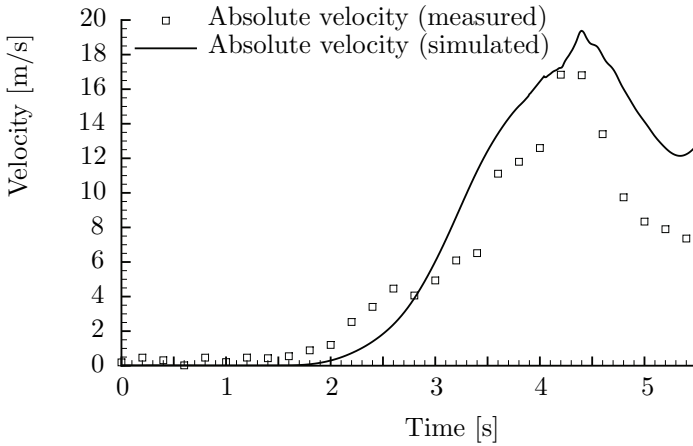
A far smaller kite is the Naish Aero 6. This kite is far less susceptible to wind variations and is able to fly much faster than the big North Rhino. This smaller kite was tested in the same manner, figure 5.27 shows the resulting line forces of the measured and simulated kite.

Figure 5.27 represents a right-hand turn of the kite from a stable zenith position. In this figure some differences can be seen clearly, most notably in the data for the right steering line. The force in the line seems to pick up faster and reach a higher value. The left power line shows good correlation between the model and the test. Lastly, the model shows an oscillation at the peak tug force that is not present in the test. This coupled with the fact that the force buildup is faster in the model suggests the model is under-dampened.

Figure 5.28 shows a comparison of absolute velocity of the measured and simulated  $6m^2$  Naish Aero kite. The figure shows that the simulated kite accelerates slightly faster and obtains a higher top velocity during the loop. This observation is in line with the earlier statement that the kite is slightly under-dampened. It



**Figure 5.27:** Comparison of power line forces between the measured and simulated data of the  $6\text{m}^2$  Naish Aero.



**Figure 5.28:** A comparison between measured and simulated velocities of the  $6\text{m}^2$  Naish Aero.

is possible that this stems from an under-estimated drag coefficient.



## 5.7 Concluding remarks

From the comparisons presented in the previous sections it can be concluded that the kite simulation toolbox produces models which show acceptable agreement with actual measured kites. The response to manual (operational) input is slower than predicted by the simulation. It is plausible that this is a result from the under-estimated drag force on the kite as can be seen in figure 4.26.



# CHAPTER 6

---

## Casestudies

---

*With the models of chapters 3 and 4 in place, the question arises: how useful are these models? In order to show the benefit of an engineering approach to kite design, a number of case studies will be done. Section 6.2 deals with the issue of effective cable length. It has been known in kiting that for a long cable only the top part of that cable is directly influenced by small perturbations of the kite. This section will quantify this effect. Section 6.3 addresses a heated debate within the kite community. In this section, the multi-body model of chapter 4 is used to find an answer to the question: what makes a surf kite corner. The multi-body model offers new insight into this issue and proposes modifications which influence the cornering behavior. Lastly, section 6.4 uses the Lagrangian equations of motion of section 3.3 to investigate an unstable eigenmotion of the kiteplane. Modifications are proposed and tested in the field.*

### 6.1 Introduction

The aim of this thesis is to complement the engineering methodology to the design of kites with accurate and workable models. Once these models are in place, they can be an invaluable tool in the design of a kite to a large set of stringent requirements. The models also allow to study the kite in its behavior, bringing about a deeper understanding. This chapter presents a number of case studies which show the benefit of the models developed in this thesis.

## 6.2 Effective cable length

A long tether exhibits a large amount of inertia. For a kite on a long tether, this means that the motions of the kite do not necessarily travel all the way down the cable. The damping effect of the aerodynamic drag and the internal damping of the cable will ensure that only the top part of the cable will actually experience the motions of the kite. This holds true for small motions such as the motions a kite would exhibit when it experiences a wind gust. This effected length of the cable is called "effective cable length". It is important to notice that the effective cable length is applicable to large out-of-plane motions of the cable. The axial strain wave phenomenon mentioned in section 4.3.2 is a different phenomenon altogether which travels through the cable much faster than the wave propagation effects as a result of large displacements of cable nodes.

In order to grasp the effective cable length, the cable model proposed in this thesis is used. A 50 element, 500 meter non-elastic cable is generated using the cable toolbox. The bottom of this cable is attached to the ground and at the top of the cable a constant lift and drag force are introduced. Perpendicular to both the lift and drag force, a disturbance is introduced by a force which is governed by a step function. The force generates a one second pulse of 20 newtons. This pulls the cable out of its plane of symmetry and results in a three-dimensional, transient cable shape. In this simulation, the deflection of the cable in the direction perpendicular to the lift and drag force vectors are measured at different positions along the cable. Figure 6.1 shows the results for three different values of damping in the joints between the cable elements (internal structural damping).

As one can see, the excitation quickly dissipates along the length of the cable. After 200 meters, the maximum amplitude in the cable is less than 20% of the amplitude in the top. What is interesting to note is that the different values of damping coefficient  $c$  seem to have no effect on the dissipation of the original excitation. The maximum amplitude at the top, as well as the maximum amplitudes along the cable are equal for all three values of  $c$ . At low values of damping  $c$ , the cable moves in a more erratic way. The internal structural damping seems to merely dampen the faster, erratic motions and not the slower motions.

To study the effect of external aerodynamic damping only, the same experiment is conducted, but now at a constant value of damping  $c$  ( $c = 0.1$ ). To vary the effect of the external aerodynamic damping, the air density is varied. At  $\rho = 0$ , the experiment is effectively conducted in a vacuum and no aerodynamic drag exists. In this situation, there is also no external aerodynamic damping. The more interesting figures are presented in figure 6.2 which show the excitation curves at  $\rho = 0.4kg/m^3$ ,  $\rho = 0.8kg/m^3$  and  $\rho = 1.225kg/m^3$ .

Figure 6.2 shows that the peaks in the graphs still occur at the same points in time. The velocity at which the wave travels through the cable is constant. But the amount of dissipation varies quite significantly. At  $\rho = 0.4kg/m^3$ , the maximum amplitude of the cable at 100m altitude is still about 15% of the maximum amplitude at the top of the cable. With increasing air density, the external

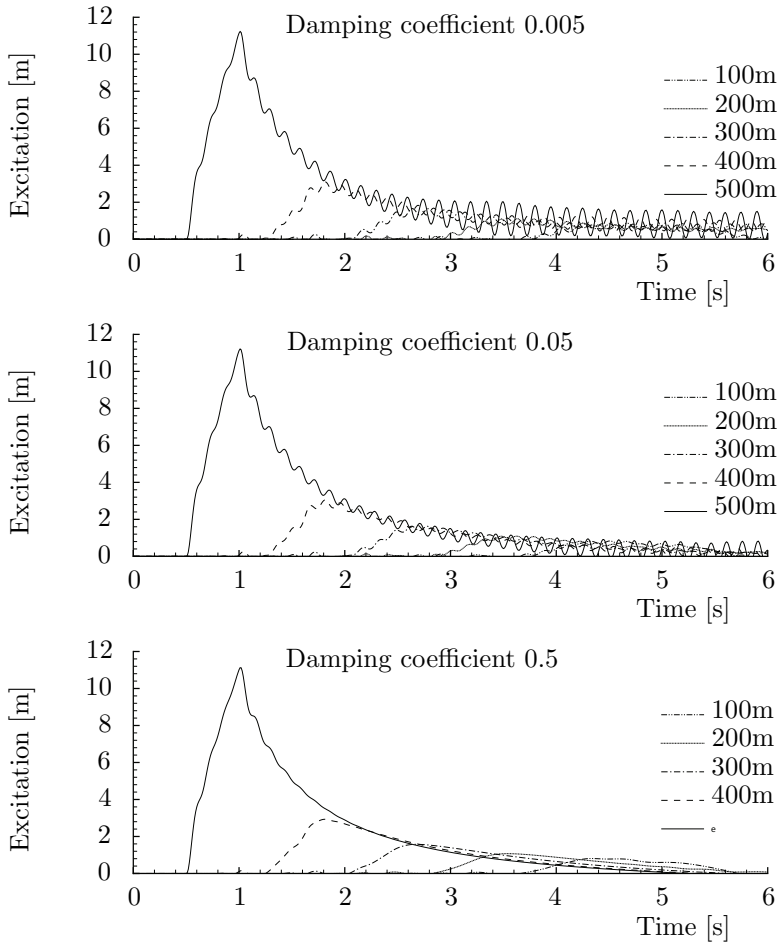


**Figure 6.1:** Excitation of the cable for different values of internal structural damping.

aerodynamic damping effect also quickly increases.

The two evaluations of external aerodynamic damping and internal structural damping show that it is the external aerodynamic damping which has the most effect on the effective cable length. The internal structural damping has more effect on the small, fast vibrations which occur as a result of numerical instability. For kite dynamics, it is the external aerodynamic dampening which is of most interest. It determines the effective cable length and therefore has a large impact in the flight dynamics of the kite.

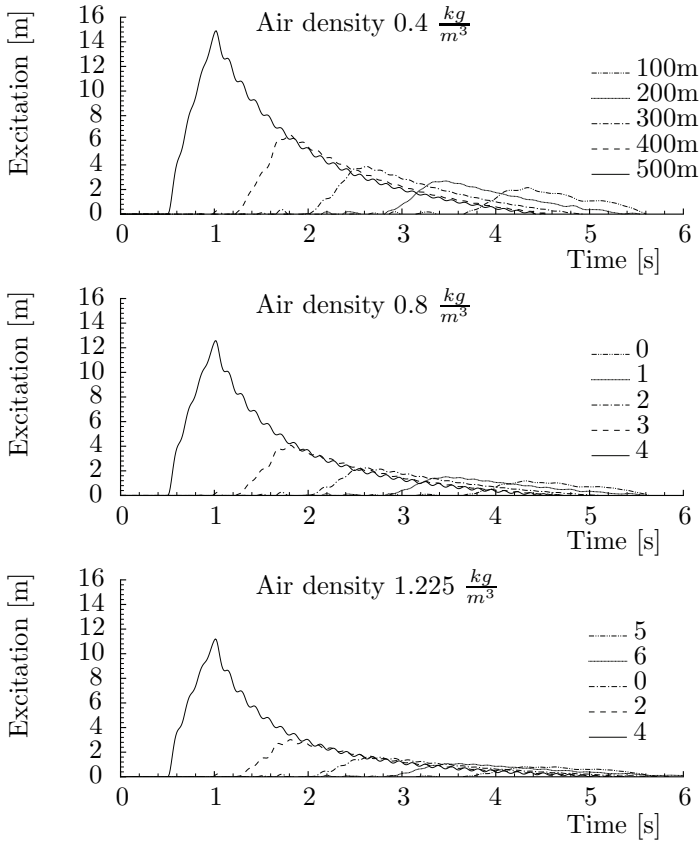


**Figure 6.2:** Excitation of the cable for different values of external aerodynamic damping.

### 6.3 A cornering surf kite

The cornering of a surf kite has been subject of great debate amongst kite designers and enthusiasts. The cornering ability of a kite plays a large role in its attractiveness as a traction kite. A professional kite surfer with years of experience would want his kite to turn fast. Controlling such a volatile kite would be a daunting task for a beginner. Safety-wise, there is also much to be gained with regard to the cornering ability of a kite. With cornering comes acceleration. And acceleration leads to a large increase in tug force of the kite. For these reasons, a kite designer benefits significantly from his knowledge on what makes a kite turn. In order to "dial in" the correct cornering speed for a particular type of kite, a thorough understanding of the mechanics of a cornering kite is required. This is why cornering of kites has been such a heated debate. When talking to designers

it becomes clear that there are a large number of conjectures as to what makes a kite corner. One such conjecture states that an increase of steering line force on one side of the kite increases its local angle of attack. This angle of attack increase leads to a local lift increase which then turns the kite. Others speak of an increased drag due to an increase in steering line force. The resulting asymmetric drag force on the arc is then believed to turn the kite.

### 6.3.1 The model

With the model presented in chapter 4, it is possible to formulate a new hypothesis on the mechanics of a turning kite. The model allows for detailed step-by-step study of all the forces, velocities and shape changes of the kite while it is turning. For this analysis, we use the following model.

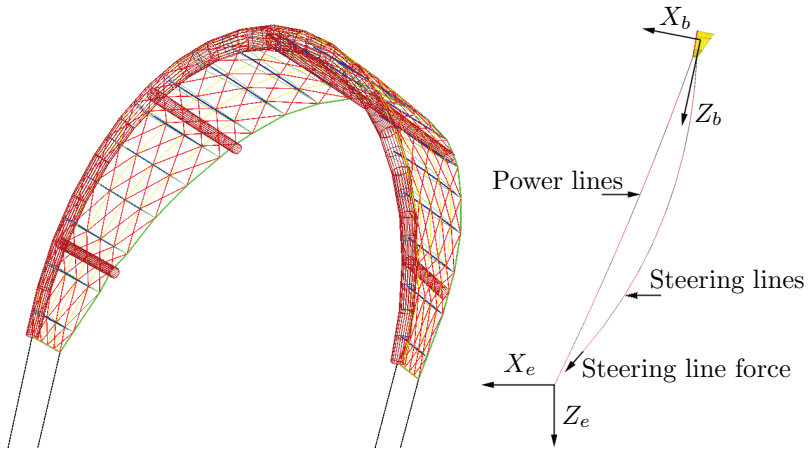


**Figure 6.3:** *The kite model used for cornering analysis.*

The model of figure 6.3 is based on the Naish Aero 6 kite. It is connected to the ground by the same line plan as was given by figure 5.23 with a length of 27 meters. The power lines are directly connected to the ground; the steering lines are one meter shorter and are only slightly pulled towards the cable attachment point to the ground by a 5N force. This is done to approximate the real case where the kite pulls on the power lines and the steering lines are kept slack. The kite is brought into its zenith position, keeping both steering lines loaded with only the 5N force. At a certain moment in time, henceforth called  $t_0$ , a steering input is generated by shifting the lower end of the right steering line downwards over a distance in the direction of the cable attachment point to the ground. This is done by increasing the right steering line force to 30N. Figure 6.4 shows the resulting displacement of the lower end of the right steering line.

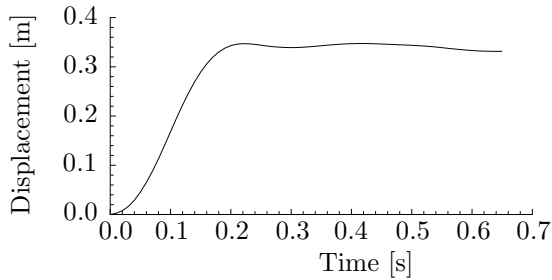


**Figure 6.4:** *The absolute displacement of the lower end of the right steering line as a result of a steering line force increase from 5N to 30N.*

The increase in steering force results in a displacement of approximately 35cm, which is consistent with what is to be expected during actual kite surfing.

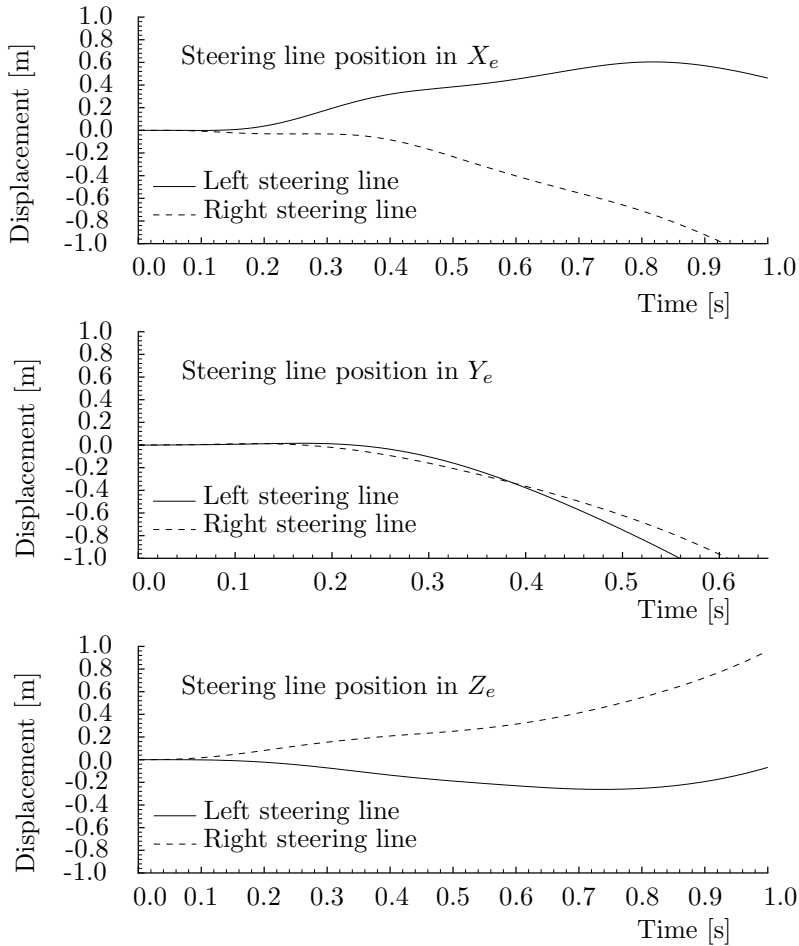
### 6.3.2 Cornering of a kite in detail

Figure 6.5 shows the displacement of the upper end of both steering lines at the kite. In this figure, the zenith position of the kite is taken as the origin; all displacements are measured from this initial position.

The simulation shows a delay in the control input reaching the kite. This is a direct result of the fact that a sagged cable acts like a spring-damper. The more sag the cable has, the more it dampens the steering input. This phenomenon also puts a limit on the maximum length of a steering line. Whilst a kite surfer might want to go higher with his kite to use stronger winds, the damping effect of the steering lines inhibits his ability to steer de kite. To overcome this issue it was suggested by W. J. Ockels [n.d.] to guide the steering lines along the power lines. The power lines are in higher tension and therefore less prone to sagging due to aerodynamic drag. This configuration, however, is outside of the scope of this case study.

As the right steering line is tensioned, the kite starts to move to the right as can be seen from the  $Y_e$  displacement in figure 6.5. This motion in negative  $Y_e$  direction is brought about by the fact that with an increased tension in the right steering line, the kite deforms. This deformation results in a slightly larger tip surface on the right and a slightly smaller tip surface on the left. Also, the increased tension in the right steering line shifts the resultant force of the right power- and steering lines towards the trailing edge of the tip. This creates an asymmetric loading and therefore an asymmetric deformation of the kite structure. Because the center of elasticity of the canopy cross-section is located forward, approximately in the center of the leading edge tube, a resultant line force shifting towards the trailing edge creates a component of that force in  $Y_b$ -direction. This component creates a moment around the center of elasticity of the airfoil cross





**Figure 6.5:** *The displacement of the top end of both steering lines in the earth axis frame of reference.*

section which results in an increased angle of attack. Figure 6.6 shows the angles of attack of the left- and right tips.

The difference in tip surfaces and angles of attack lead to a larger lift force on the right, pulling the kite to the right. It is important to note that at this point, there is no reason for the kite to yaw, other than a difference in drag forces on the left and right tip caused by the difference in angle of attack. This drag force difference has often been cited by kite designers and enthusiasts as the main contributor to the cornering ability of a surf kite. Figure 6.7 shows the drag forces on the left and right wing tips. The results in this figure are composed of the sum

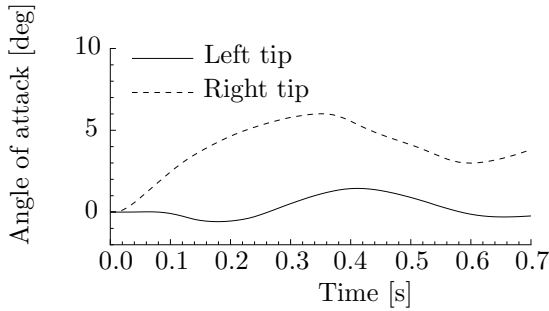


**Figure 6.6:** *The angle of attack of the left- and right tips.*

of the drag forces on the left and right last 30% of half the kite arc.

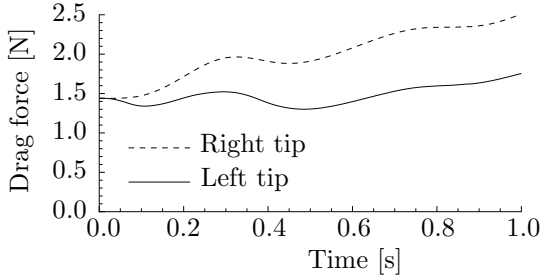
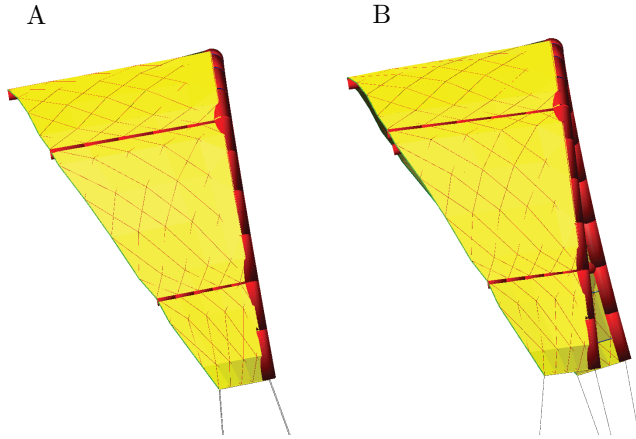


**Figure 6.7:** *The drag at the tips of the kite.*

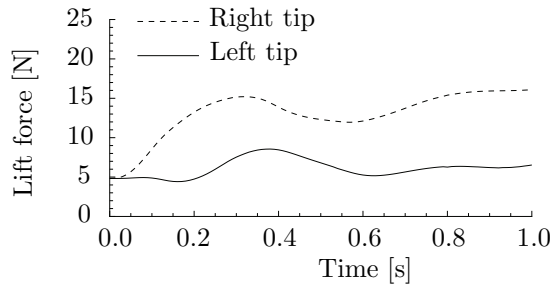
The asymmetry in the drag forces on both tips is clearly visible. But the magnitude of the difference is small and cannot be solely responsible for the fast cornering of a surf kite. The asymmetric loading of the kite by the resultant forces of the power lines on the left and the right side deform the kite in a distinct manner. The asymmetric loading causes the right tip to bend forwards and the left tip to bend backwards. Figure 6.8 shows the kite structure from the side along the  $Y_b$ -axis before and after the control input.

Figure 6.8 shows the shape of the kite before the control input (A) and one second after the control input is introduced (B). The kite shows a skewing deformation as a result of the asymmetric cable loads. This skewing deformation creates an offset in the lift forces in  $Y_b$  direction. Figure 24 shows the lift forces on the left and right wing tips. The results in this figure are composed of the sum of the drag forces on the left and right last 30% of half the kite arc.

The control input not only increases the lift forces, it also offsets the tips with respect to each other. Especially the right tip is pushed forward of the center of gravity and introduces an increased lift force. This results in a yaw moment which



**Figure 6.8:** *The shape of the kite before the control input (A) and after (B).*



**Figure 6.9:** *The lift at the tips of the kite in  $Y_b$  direction.*

makes the kite corner. Furthermore, the left tip moves slightly aft with respect of the center of gravity, further increasing the yaw moment of the kite.

### 6.3.3 The contribution of flexibility

From the analysis of this model it can be concluded that the flexibility of the kite model plays a large role in its ability to corner. Its deformation under an asymmetric cable load creates an asymmetric aerodynamic load which allows the kite to turn. The model allows taking the flexibility out of the equation by making the kite completely rigid. If the previous statement on the importance of flexibility on a cornering kite holds, this hypothetical kite should not corner, or corner much less rapid. Figure 6.10 shows the yaw angle of the flexible and rigid kite with respect to the earth axis frame of reference.

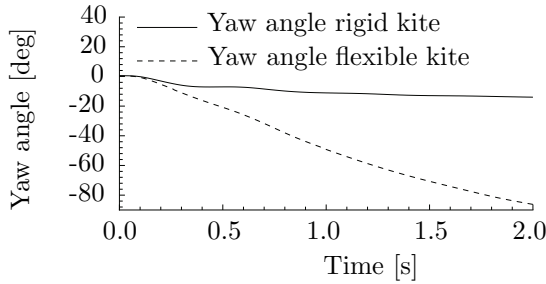


**Figure 6.10:** *Yaw angle of the flexible and the rigid kite.*

Figure 6.10 seems to concur with the statement that a rigid kite is barely able to corner. While the flexible kite is able to corner a full 90 degrees in little over two seconds, the rigid kite is barely able reach a yaw angle of 15 degrees. This inability to yaw also makes it hard to steer the kite from left to right along the  $Y_e$  axis. Figure 6.11 shows the  $Y_e$  displacement of both the flexible and rigid kites.

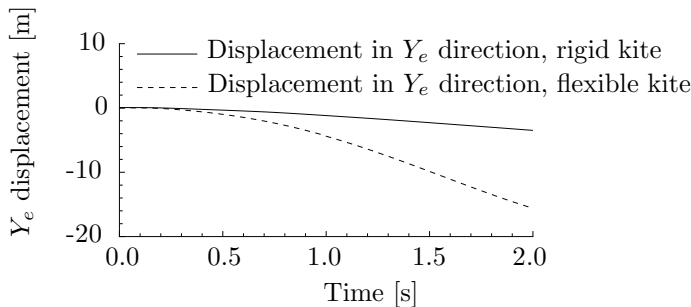
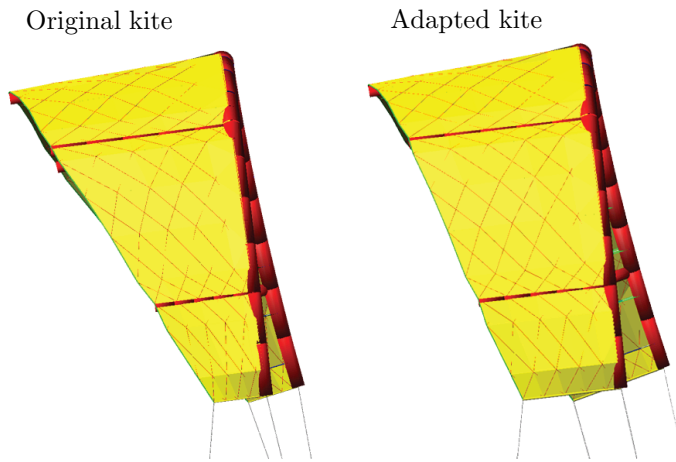


**Figure 6.11:**  *$Y_e$  displacement of the flexible and the rigid kite.*

It can be seen that the rigid kite is hard to move along the  $Y_e$  axis. This inability of the kite to fly rapidly from left to right along the  $Y_e$  axis seriously inhibits its capability to use crosswind power [Loyd, 1980]. Crosswind power is a maneuver whereby the kite flies figure eight patterns and greatly increases its velocity and therefore its tug force. It is an essential maneuver used in kite surfing and a kite's inability to perform this maneuver will render it practically useless. A fast cornering kite is of special interest to professional kite surfers. The quick change in direction gives the rider a more responsive tug force with which he can perform his various jumps and stunts.

### 6.3.4 Influencing cornering performance

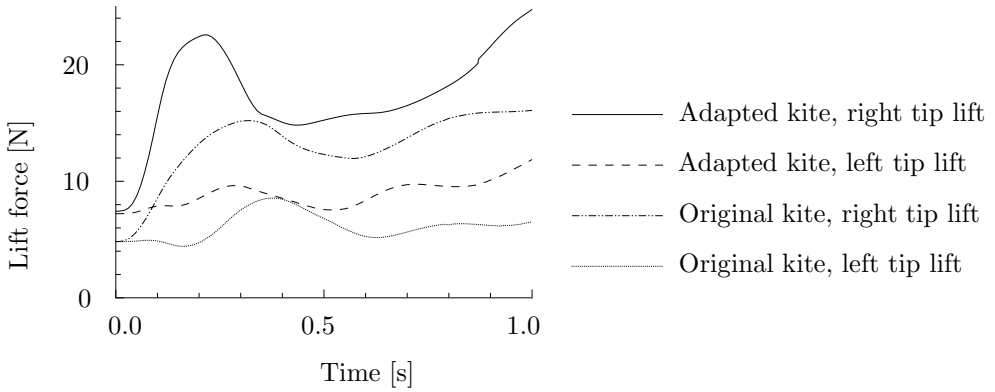
Now that the model established that rigidity is detrimental to the cornering performance, the question beckons: What makes cornering performance increase? Based on the model it was established that the main contribution to the cornering of a surf kite comes from the skewing deformation of the kite structure creating an offset in the lift forces on the left and right side of the kite. Increasing cornering performance could possibly be established by simply increasing the lift force and/or increasing the skewing deformation. Increasing the lift force in the tips would require a better airfoil or simply more tip surface. The latter also allows for a larger deformation if the increase in surface area is established by increasing the tip chord. A larger tip chord creates a larger distance between the power and steering line attachments. This larger distance will ensure a more asymmetric loading of the kite when one of the steering lines is tensioned. In order to investigate this claim, a new model is generated with a 100% increase in the chord length in the tips. Figure 6.12 shows the resulting deformation while cornering for the original and adapted kite.



**Figure 6.12:** *Skewed deformation of the original and adapted kite while cornering.*

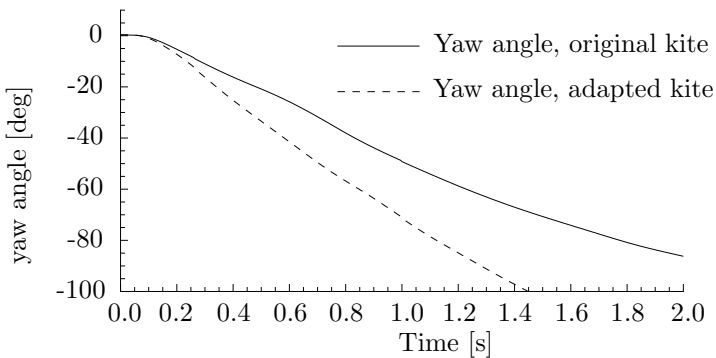
Figure 6.12 shows a clear increase in deformation of the adapted kite. This increased deformation is responsible for an enlarged moment arm the offset lift forces have with respect to the yawing pivot point. The increased chord in the tip not only increases this moment arm, it also increases the surface area at the tip, and with it the lift generated by the tip. Figure 6.13 shows the resulting lift forces of both tips for the original and adjusted kite.

Figure 6.13 indeed shows a significant increase in the lift at both the left and the right tip of the adjusted kite. This increase in lift, combined with the enlarged



**Figure 6.13:** *Lift at both the left and right tip of the original and adjusted kite.*

moment arm is expected to increase the cornering velocity of the kite. In order to evaluate this claim, the yaw angles of the original and adapted kites are plotted against time in figure 6.14.



**Figure 6.14:** *Yaw angle of the original kite and an adapted kite with a 50% chord length increase.*

Figure 6.14 confirms the reasoning of the previous paragraph. A larger lift force in the tips, together with a larger deformation increases the cornering velocity of the surf kite significantly. This result further establishes confidence in the notion that the cornering velocity of a kite is dependent on the flexibility of the kite structure and the lift in the tips.

## 6.4 Kiteplane stability

Section 2.4.5, the concept of the kiteplane was introduced. The kiteplane is a kite with the configuration of a conventional twin-boom aircraft. The reason for this design stems from the desire to create a kite with a high lift-over-drag which is able to fly both as a kite on a tether and as an airplane with a slack tether. The need for an airplane-like flight regime came forth from the desire to minimize the energy loss resulting from the retraction phase of the pumping laddermill. Earlier kiteplane prototypes such as depicted in figure 2.9 and 2.10 were mainly a structural technology testbed. The kiteplane depicted in figure 2.11 was the first kiteplane whose design was based on a number of rudimentary static stability rules. This particular kiteplane, henceforth called "kiteplane 3", was the first kiteplane which was meant as a testbed to analyze the flight dynamics of tethered flight. The properties of kiteplane 3 can be found in appendix H.

Flight testing of kiteplane 3 revealed that the kite was longitudinally stable. Laterally, however, an a-periodic unstable inverted pendulum motion occurred. The kite launched with ease, but would fall to either the left or the right side after a short period of flight. Figure 6.15 gives a representation of this unstable motion.



**Figure 6.15:** *A composite representation of the unstable a-symmetric inverted pendulum motion of kiteplane 3.*

This particular instability mode, either periodic or a-periodic, often plagues kites. In the kite world, the ability of a kite to remain at a 12 o'clock position in the sky is called its "auto-zenith capability". Some kites are auto-zenith, others are not. The reasons for auto-zenith capability are subject of intense debate among kite flyers. Conventional wisdom in the kite world dictates that adding a long tail can overcome this type of instability. For the kiteplane, however, this is undesirable because a long tail would add a significant amount of drag. The added drag would have a detrimental effect on the lift-over-drag of the kite. Another rule-of-thumb in the kite world is that increased dihedral can help alleviate this type of instability. For a kite which is bridled only in its  $X_B$ - $Z_B$  plane, dihedral in the wing will result in static roll stability as a result of slipping flight which occurs as the kite falls to the side. The static roll stability then rotates the lift vector of the kite such that the kite moves back into the zenith position. The Kiteplane, however, is bridled in spanwise direction in order to support the wing. Therefore it is limited in roll.

In this section, the kite model based on Lagrangian equations of motion (section 3.3) is used to investigate the asymmetric inverted pendulum instability characteristics of Kiteplane 3. A more detailed derivation of this model with respect to the kiteplane can be found in Terink et al. [2010]

### 6.4.1 Asymmetric inverted pendulum stability

In this section, the stability of the path that results from revolving the tether endpoint in equilibrium position about the  $X_E$ -axis is investigated. For this inverted pendulum motion, the tether is assumed to have a fixed length so that the indicated path projected on the  $Y_E$ - $Z_E$  plane describes a circle. A second simplification states that the pitch angle is fixed as well. The state of Kiteplane 3 on this path is now completely defined by the bridle rotation angle and an angle that defines the location on the projected circle. This latter angle is called  $\theta_t$  and equal to zero in the uppermost (zenith) position. The situation for this case study is visualized in figure 6.16.

Pendulum stability requires Kiteplane 3 to converge to the situation displayed in figure 6.16 from a disturbance in  $\theta_t$ . The disturbances  $\dot{\theta}_t$  and  $b$  correspond to sideslip stability and the  $\dot{b}$  disturbance to stability of angular velocity about the tether longitudinal axis. Nevertheless, if these disturbances are combined with a nonzero  $\theta_t$ , gravity can no longer be neglected and its effect may destabilize the system. Also, the wind power in the operating space provides more than enough energy to make an oscillating motion diverging.

To investigate the pendulum stability, a case study is performed on the situation in figure 6.17. This is the typical scenario where, for the observer, Kiteplane 3 is located on the left side, falling to the left side and pointing to the left side. Initial body axis rotational velocities are set to zero for convenience. The sum of the lateral forces is given by equation (6.2), the sum of moments about  $X_B$  is given by equation (6.3) and the sum of moments about  $Z_B$  is given by equation



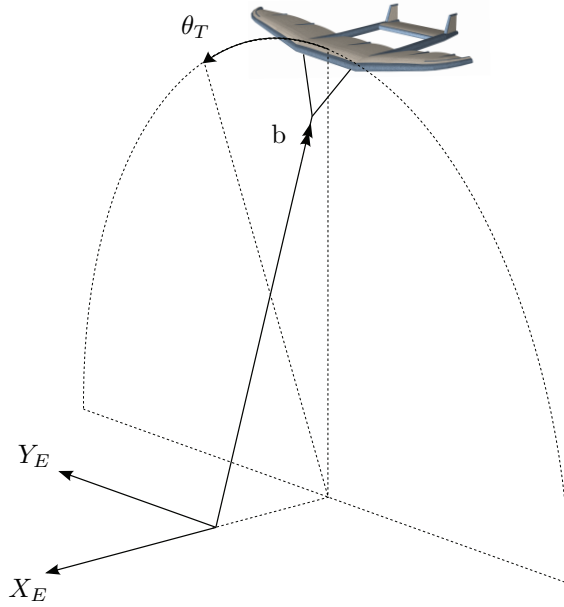


**Figure 6.16:** *Kiteplane 3 pendulum motion.*

(6.4).

$$\sum F_{Y_B} = -2(L_f \cos(\beta) + D_f \sin(\beta)) - Y_{rw} + Y_{lw} \quad (6.1)$$

$$+ F_Z \sin(\theta_t) \sin(\beta) \quad (6.2)$$

$$\sum M_{X_B} = (L_{lw} - L_{rw}) \bar{y}_w - 2(L_f \cos(\beta) + D_f \sin(\beta)) \bar{y}_{VT} + F_Z \sin(\theta_t) z_t + (T_{K_r} - T_{K_l}) y_b \cos(\delta) \quad (6.3)$$

$$\sum M_{Z_t} = (X_{rw} - X_{lw}) \bar{y}_w \cos(\Gamma) + 2(L_f \cos(\beta) + D_f \sin(\beta)) l_{VT} - F_Z \sin(\theta_t) x_t \quad (6.4)$$

Sufficient conditions for static pendulum stability in the case displayed in figure 6.17 are displayed below.

$$\begin{aligned} dF_{Y_B}/d\theta_t &< 0 \\ dF_{Y_B}/d\beta &< 0 \\ dM_{X_B}/d\theta_t &< 0 \\ dM_{X_B}/d\beta &< 0 \\ dM_{Z_B}/d\theta_t &< 0 \\ dM_{Z_B}/d\beta &> 0 \end{aligned}$$

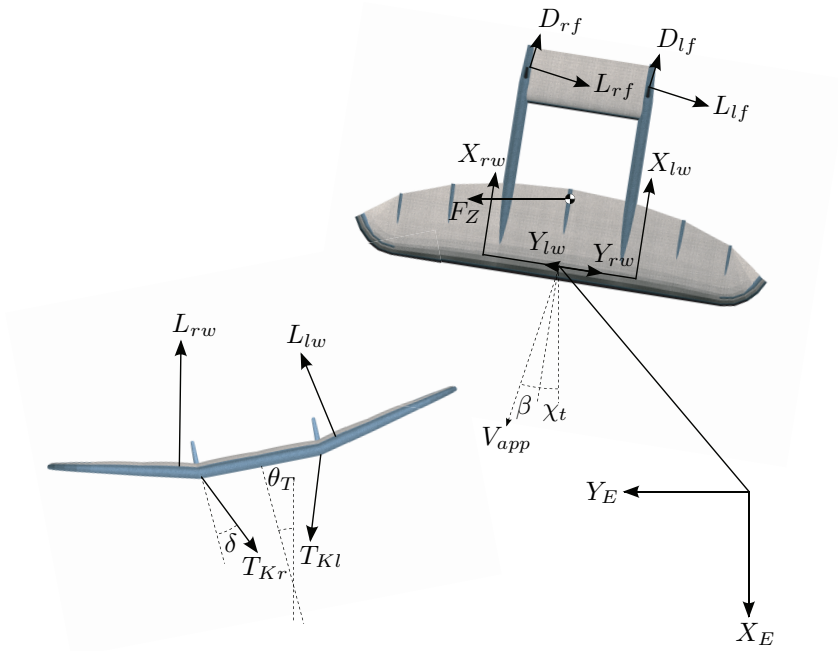


**Figure 6.17:** Top view of Kiteplane 3 in pendulum motion.

Necessary conditions are difficult to define, because the pendulum motion is a combination of  $\theta_t$  and  $\chi_t$ . However, by using equation (6.5), the six sufficient conditions above can be translated to the four conditions below.

$$M_{Z_t} = M_{Z_B} \cos(\theta) + M_{X_B} \sin(-\theta) \quad (6.5)$$

$$\begin{aligned} dF_{Y_B}/d\theta_t &< 0 \\ dF_{Y_B}/d\beta &< 0 \\ dM_{Z_t}/d\theta_t &< 0 \\ dM_{Z_t}/d\beta &> 0 \end{aligned}$$

In order to evaluate equations (6.2) through (6.4), the following relations are needed:

$$L = \frac{1}{2}\rho V_{app}^2 S_w C_L \quad (6.6)$$

$$D = \frac{1}{2}\rho V_{app}^2 S_w C_D \quad (6.7)$$

$$C_L = C_{L_\alpha} \alpha \quad (6.8)$$

$$C_D = C_{D0} + \frac{C_L^2}{\pi A R_w e_w} \quad (6.9)$$

$$L_{HT} = \frac{1}{2}\rho V_{app}^2 \left( \frac{V_t}{V_{app}} \right)^2 S_{HT} C_{L_{HT}} \quad (6.10)$$

$$D_{HT} = \frac{1}{2}\rho V_{app}^2 \left( \frac{V_t}{V_{app}} \right)^2 S_{HT} C_{D_{HT}} \quad (6.11)$$

$$C_{L_{HT}} = C_{L_{HT\alpha}} \alpha \left( 1 - \frac{d\epsilon}{d\alpha} \right) \quad (6.12)$$

$$C_{D_{HT}} = C_{D0_{HT}} + \frac{C_{L_{HT}}^2}{\pi A R_{HT} e_{HT}} \quad (6.13)$$

$$M_{ac} = \frac{1}{2}\rho V_{app}^2 S_w \bar{c} C_{m_{ac}} \quad (6.14)$$

$$\epsilon = \frac{d\epsilon}{d\alpha} \alpha \quad (6.15)$$

$$\theta_t = \alpha - \theta \quad (6.16)$$

$$F_Z = m_g g \quad (6.17)$$

$$X_{rw} = \frac{1}{2}\rho V_{app}^2 \frac{S_w}{2} C_{X_{rw}} \quad (6.18)$$

$$X_{lw} = \frac{1}{2}\rho V_{app}^2 \frac{S_w}{2} C_{X_{lw}} \quad (6.19)$$

$$L_f = \frac{1}{2}\rho V_{app}^2 \left( \frac{V_t}{V_{app}} \right)^2 \frac{S_{VT}}{2} C_{L_{VT}} \quad (6.20)$$

$$D_f = \frac{1}{2}\rho V_{app}^2 \left( \frac{V_t}{V_{app}} \right)^2 \frac{S_{VT}}{2} C_{D_{VT}} \quad (6.21)$$

$$C_{L_{VT}} = C_{L_{VT\alpha}} \beta \quad (6.22)$$

$$C_{D_{VT}} = C_{D0_{VT}} + \frac{C_{L_{VT}}^2}{\pi A_{VT} e_{VT}} \quad (6.23)$$

By substituting the relations (6.6) through (6.23) and constants from appendix H in equations (6.2) through (6.4), and using equation (6.5), equations for the force in  $Y_B$  and the moment about  $Z_t$  are obtained. The resulting equations depend on  $\beta$ ,  $\theta_t$ ,  $\theta$ ,  $V$  and  $\alpha$  only. For the variables  $\theta$ ,  $V$ , and  $\alpha$ , the following representative constants are substituted.

$$\begin{aligned}
\theta &= -5 \text{ Deg} \\
V &= 6 \text{ ms}^{-1} \\
\alpha &= 5 \text{ Deg}
\end{aligned}$$

With these values substituted,  $F_{Y_B}$  and  $M_{Z_t}$  can be plotted as functions of  $\beta$  and  $\theta_t$ . Figure 6.18 displays the lines  $F_{Y_B} = 0$  and  $M_{Z_t} = 0$  in  $\theta_t$ - $\beta$  space. The lines in fact represent the equilibrium condition for  $Y_B$  and  $Z_t$ . The only equilibrium condition for the pendulum motion is the point (0,0) in figure 6.18. The arrows in figure 6.18 indicate in which direction Kiteplane 3 is accelerated. They are, if aerodynamic effects of roll and yaw velocity can be neglected, a measure for the acceleration vector in  $\theta_t$ - $\beta$  space with  $x$ -component  $\ddot{\theta}_t$  and  $y$ -component  $\ddot{\beta}$ .

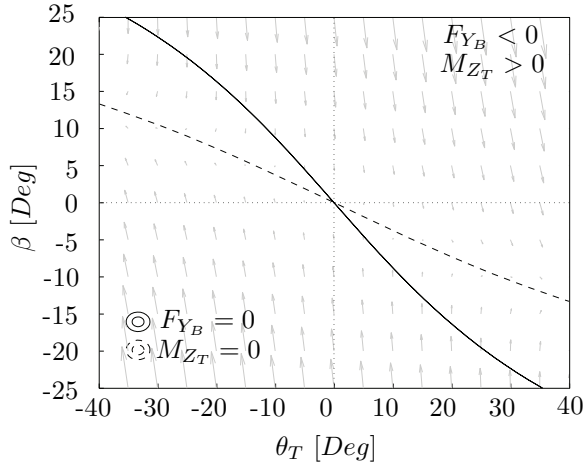


**Figure 6.18:** *Pendulum stability space with  $\theta_t$  equilibrium — and  $\beta$  equilibrium --.*

The variation in magnitude of the arrows is approximately linear, which can be observed in figure 6.19 that displays horizontal and vertical slices of figure 6.18. Figure 6.19 displays a horizontal slice at  $\beta = 10^\circ$  (left) and a vertical slice at  $\theta_t = 20^\circ$  (right) to get an impression of the gradients  $dF_{Y_B}/d\beta$  and  $dM_{Z_t}/d\beta$ .

As stated before, the sufficient conditions for static pendulum stability equals  $dF_{Y_B}/d\theta_t < 0$ ,  $dM_{Z_t}/d\theta_t < 0$ ,  $dF_{Y_B}/d\beta < 0$  and  $dM_{Z_t}/d\beta > 0$ . However, the derivative  $dF_{Y_B}/d\theta_t$  is positive as can be observed from figure 6.19 (left). The sufficient conditions for static stability are therefore not met.

However, if the equilibrium  $\beta$  is sufficiently stable and yields a negative value for  $F_{Y_B}$ , the system may still be stable. This means that in figure 6.18 the dashed  $M_{Z_t}$  line should be above the solid  $F_{Y_B}$  line for  $\theta_t > 0$ , but observation of figure 6.18 quickly learns that this is neither the case. Similar conclusions can be drawn from following the arrows in figure 6.18, which results in either diverging to the left or the right.

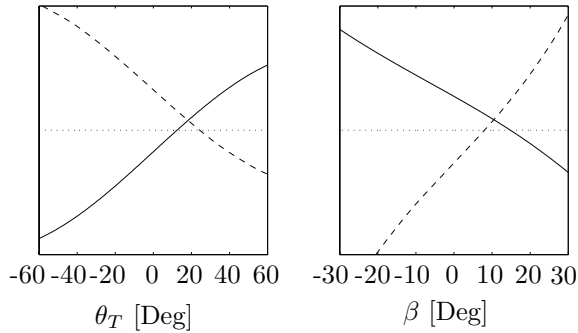


**Figure 6.19:**  $F_{Y_B}$  — and  $M_{Z_t}$  -- gradients at  $\beta = 10^\circ$  and  $\theta_t = 20^\circ$ .

The analysis in this section shows that the Kiteplane restricted to pendulum motion is unstable. By means of this analysis this cannot be guaranteed for the unrestricted Kiteplane system. However, as was shown in figure 6.15, field tests revealed a similar instability mode. In sections 6.4.2 and onwards the analysis in this section is extended to a parameter analysis to determine how the pendulum motion can be stabilized. The results obtained in this section are summarized below.

#### Pendulum stability

---

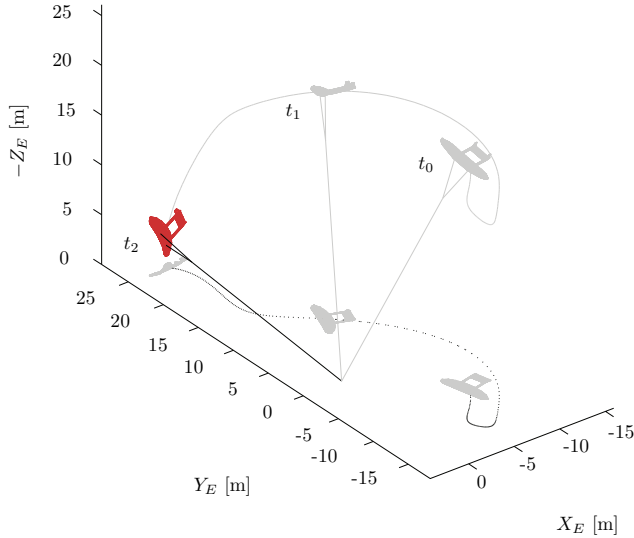
Sideslip:	Statically and dynamically stable
Tether pendulum angle:	Statically unstable

Figure 6.20 shows the simulated unstable inverted pendulum motion of kiteplane 3.

### 6.4.2 The effects of geometrical parameters

Inspection of Table H.1 yields many geometrical parameters to investigate, but only the ones with the largest impact on the geometry are interesting for the scope of this text. For the lateral stability the interesting parameters are vertical tail surface area  $S_{VT}$ , vertical tail distance  $l_{VT}$  and dihedral  $\Gamma$ . Next to these parameters, the inclusion of an additional lateral surface on top or below the wing is regarded interesting as well. The main effect of such a surface can be achieved with dihedral as well, but secondary effects are inherently different. The most noticeable difference is the effect of dihedral on the yaw moment, which is absent for a single vertical surface in the middle of the Kiteplane.

Nevertheless, the parameters  $S_{VT}$  and  $\Gamma$  are selected for the initial lateral stability investigation. Keeping the tail boom length constant avoids side effects on longitudinal stability and adjusting  $\Gamma$  is simply found more elegant than the addition of a vertical surface. The impact of variations in  $S_{VT}$  and  $\Gamma$  on the inertia



**Figure 6.20:** 3D path of diverging motion with asymmetric initial conditions:  $\theta = -10^\circ$ ,  $\chi_t = -60^\circ$ ,  $l_t = 25$  m,  $\theta_t = 25^\circ$ ,  $\psi_t = 45^\circ$ ,  $\dot{\mathbf{x}}_0 = 0$  and a final time of 17 s.

is neglected to keep the results depending on geometry only. Indirect effects due to changing inertia is assessed at a later stage.

The stability is assessed based on simulation results in the range  $-10^\circ < \Gamma < 40^\circ$  and  $0 < \frac{S_{VT}}{S_{VT0}} < 8$  for two different wind velocities. The arrangement of the stability domains for  $V_W = 6$  ms $^{-1}$  and  $V_W = 10$  ms $^{-1}$  are displayed in figure 6.21.

Small vertical tail planes seem to cause diverging oscillations and low dihedral angles seem to cause aperiodic divergence. Stability requires a large dihedral angle and a vertical tail plane of about 1 to 3 times the original size. Furthermore, the stable region increases with increasing wind velocity.

For low dihedral angles and low wind velocities, increasing the vertical tail size quickly leads from unstable oscillations to aperiodic divergence, but if the dihedral angle and wind velocity are large enough, a stable region emerges in between. The stable region itself consists of three domains. The first, for the smallest vertical tail plane, is the stable oscillation. The second, for a larger vertical tail plane, is the converging oscillation. For very large vertical tail planes and low dihedral angles, a domain of aperiodic convergence exists. For higher wind velocities the aperiodic convergence domain increases in size at the cost of the size of the converging oscillation domain.

At the boundary of diverging oscillation and stable oscillation something peculiar happens, for this reason Figure 6.22 zooms in on this particular area.

At a vertical tail plane size slightly too small for stable oscillation, there seems to be a small band of  $\Gamma$  values that still yield a stable oscillation. When the

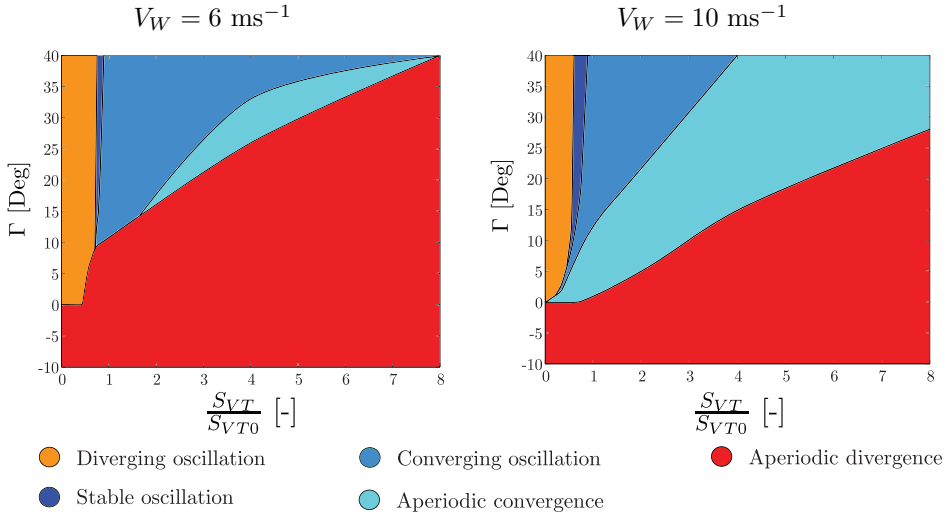


**Figure 6.21:** Stability chart depending on  $\frac{S_{VT}}{S_{VT0}}$  and  $\Gamma$  for  $V_W = 6 \text{ ms}^{-1}$  and  $V_W = 10 \text{ ms}^{-1}$ .

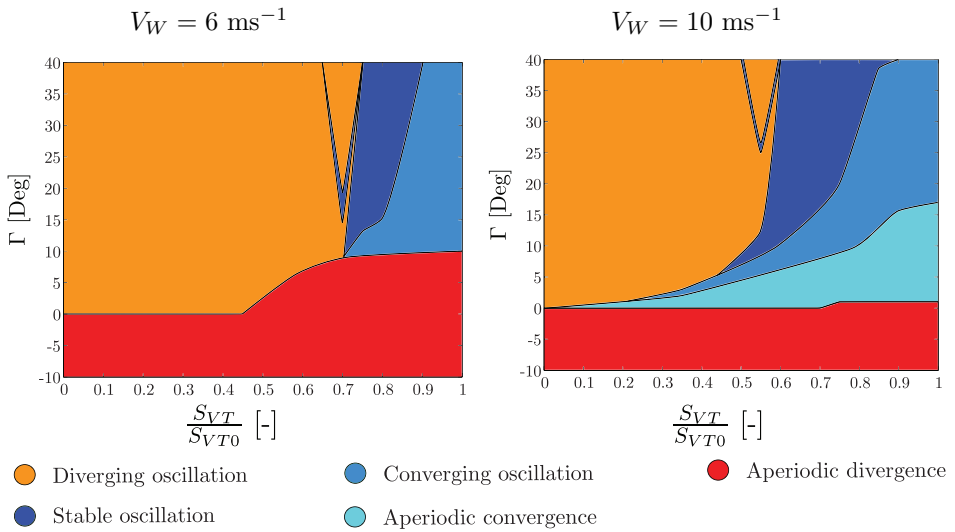


**Figure 6.22:** Stability chart depending on  $\frac{S_{VT}}{S_{VT0}}$  and  $\Gamma$  for  $V_W = 6 \text{ ms}^{-1}$  and  $V_W = 10 \text{ ms}^{-1}$ .

vertical tail plane area is reduced slightly from stable oscillation, the stable figure-

eight pattern starts to oscillate itself. This behavior can be compared with the precession of the rotation axis of a spinning top. For most cases, the crossing of the figure-eight starts to move in  $Y_E$  direction, one circle becomes larger than the other and eventually Kiteplane 3 crashes into the ground.

Another feature that is invisible in Figures 6.21 and 6.22 are the roots of the different stable domains. These figures reveal that there is always a converging oscillation domain below the stable oscillation domain and that the arrangement of the aperiodic convergence domain is depending a lot on wind velocity.

The pendulum stability spaces according to the five stability domains with a sample trajectory are displayed in figure 6.23. In fact, the shown stability spaces are based on average values of the sample trajectories and therefore loose accuracy if the motion is erratic.

The first thing to notice is that small changes in the stability space have a large impact on the resulting behavior that indicated by the red line. Another interesting aspect is the similarity between the stability spaces of the two unstable domains, even while the behavior and geometry is significantly different. It appears that if the difference between the slope of the solid and dashed line becomes too large, the system becomes unstable. In these cases the acceleration arrows are more or less vertical, which means that the  $\theta_t$  motion is dominated by gravity.

The stable oscillation domain displayed in figure 6.23b is the desired stability space according to the analysis in Section 6.4.1. The dashed line is steeper than the solid line, which means that Kiteplane 3 converges to a sideslip angle that generates a resultant force towards  $\theta_t = 0$ . However, it seems that this configuration lacks damping at small  $\theta_t$  angles because of the continued oscillations.

At the border of stable oscillation and converging oscillation, the dashed line is on top of the solid line. From the sole pendulum motion point of view, this is the border to unstable behavior. However, the longitudinal stability improves lateral stability and is in fact essential in the entire converging domain [Terink et al., 2010].

If the solid line is only slightly steeper than the dashed line the motion is still oscillatory, but if the difference in slope becomes slightly larger, the oscillations disappear. This is the domain of aperiodic convergence and illustrates the improved apparent lateral stability very clearly. According to the acceleration arrows the motion should diverge instead of converge, but evidently the longitudinal stabilization is able to overcome the pendulum instability.

Nevertheless, if the lateral instability becomes too large for the longitudinal stabilization, the motion finally diverges as displayed in figure 6.23e. The absolute difference in slope in Figs. 6.23d and 6.23e are about equal, but the relative difference is larger because the slopes in figure 6.23e are shallower.

### 6.4.3 Operational stability requirements

During flight the Kiteplane system encounters various operational conditions. Also the model is a simplification of reality based on assumptions that have an



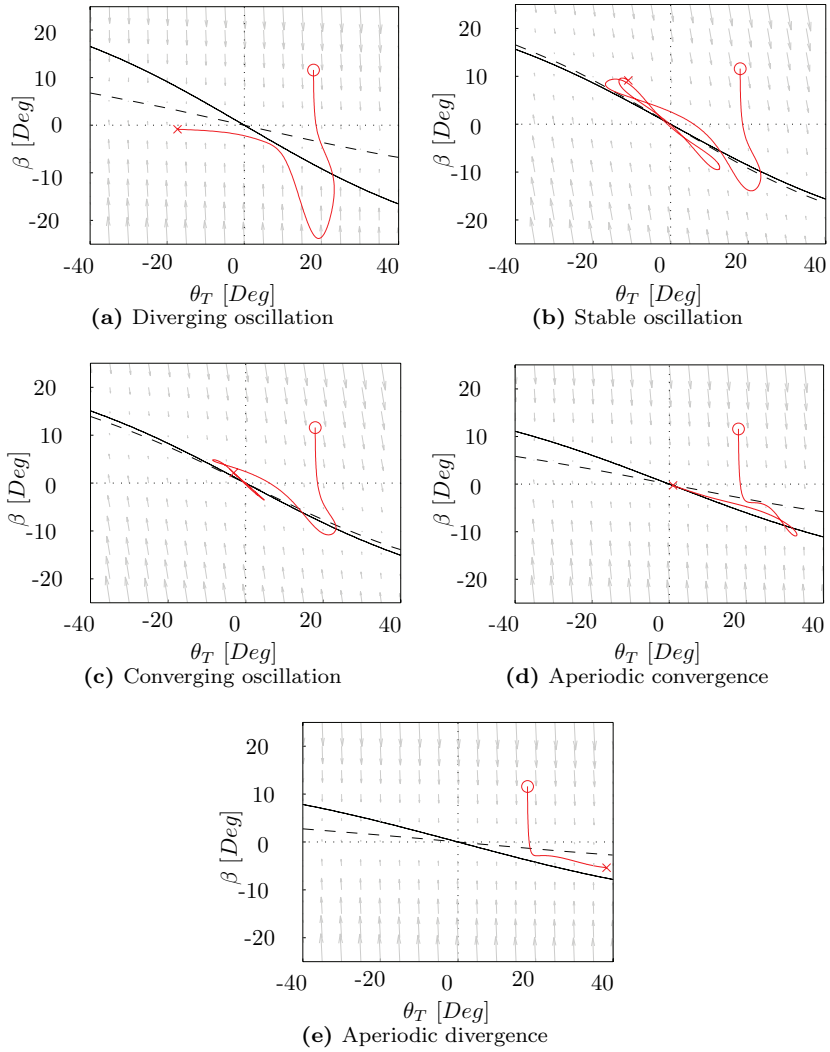


**Figure 6.23:** Pendulum stability space with  $\theta_t$  equilibrium — and  $\beta$  equilibrium -- according to the five different stability domains.

impact on accuracy. For these reasons, it is important that stability holds for both varying conditions and small design variations.

To determine the impact of these variations on stability, the following range of operating conditions are simulated.

- Design variations
  - Mass and Inertia tensor  $\pm 20\%$
  - $\Gamma \pm 20\%$
  - $\frac{S_{VT}}{S_{VT0}} \pm 20\%$
- Operational variations
  - $x_t$  ranging from 0 to 0.6 m
  - $l_t$  ranging from 10 to 100 m
- External condition variations
  - $V_W$  ranging from 4 to 16  $\text{ms}^{-1}$
  - Instantaneous lateral wind gusts of 50%  $V_W$

On the basis of this list, a series of simulations was performed where each simulation varies a single parameter. The results of these simulations are compared to the converging oscillation reference case with the following parameter values:

- $\Gamma = 20^\circ$
- $\frac{S_{VT}}{S_{VT0}} = 1.5$
- $V_W = 8 \text{ ms}^{-1}$
- $l_t = 25 \text{ m}$
- $x_t = 0.3 \text{ m}$

All other parameters are equal to the original design values. The simulation results are summarized in Table 6.1.

The stability of the reference case seems robust, since only one of the variations leads to unstable behavior. If Kiteplane 3 is properly trimmed in pitch, only the case that increases  $x_t$  to 0.6 m leads to unstable behavior. To find out if the robustness holds for combined variations, the following cases are assessed.

1. Inertia +30%,  $\Gamma$  +30% and  $\frac{S_{VT}}{S_{VT0}} -30\%$
2. Inertia -30%,  $\Gamma$  -30% and  $\frac{S_{VT}}{S_{VT0}} +30\%$

Both the first case that leans towards diverging oscillations and the second case that leans towards aperiodic divergence are in fact still converging. Although the latter is on the verge of aperiodic divergence, these results are promoting the idea of a configuration that is stable in the entire operating domain. In Section 6.4.4 this idea is explored.

**Table 6.1:** *Impact of operating conditions on stability.*

Parameter variation		Asymmetric initial conditions	Lateral step gust of $0.5V_W$
Reference		Converging oscillation	Converging oscillation
Inertia	-30%	More damped oscillation	More damped oscillation
	+30%	Less damped oscillation	Less damped oscillation
$\Gamma$	-30%	Aperiodic convergence	Aperiodic convergence
	+30%	Less damped oscillation	Less damped oscillation
$\frac{S_{VT}}{S_{VT0}}$	-30%	Less damped oscillation	Less damped oscillation
	+30%	More damped oscillation	More damped oscillation
$x_t$	0.0 m	More damped oscillation	More damped oscillation <sup>1</sup>
	0.55 m	Aperiodic convergence	Aperiodic convergence
	0.6 m	Aperiodic divergence	Aperiodic divergence
$l_t$	10 m	More damped oscillation	More damped oscillation
	100 m	Equal damping, longer period	Equal damping, longer period and lower amplitude
$V_W$	$4 \text{ ms}^{-1}$	Less damped oscillation <sup>1</sup>	Less damped oscillation <sup>1</sup>
	$16 \text{ ms}^{-1}$	More damped oscillation <sup>1</sup>	More damped oscillation <sup>1</sup>

<sup>1</sup> Requires new trim setting for proper longitudinal equilibrium in  $\alpha$ .

#### 6.4.4 Proposed design changes for stability

From the flight tests, the conclusion that the Kiteplane 3 design is unstable quickly arises. A first idea of the cause of this behavior was formed in section 6.4.1 where the pendulum motion is analyzed. Then in Section 6.4.2 the simulations finally yield the conclusion that lateral stability is closely related to the amount and distribution of lateral area.

This result can now be used to improve the stability of Kiteplane 3 and come up with some design changes. Due to the requirement for control, it is preferred that the lateral stability is sufficiently susceptible to oscillations. The preferable features and requirements of the new Kiteplane design are listed below.

- Converging oscillation in worst case scenario
- Minimize non-lifting surface area (vertical tail plane, dihedral angle)
- Low weight (reduces effective L/D, improves stability and decreases minimal  $V_W$ )
- Quick longitudinal convergence

The listed features are partly conflicting on the design parameters and thus a compromise is required. Nevertheless, Terink et al. [2010] indicates that shortening the tail booms improves longitudinal stability. A similar result can be obtained by a smaller horizontal tail plane. Since the vertical tail plane size is not particularly large and shorter tail booms certainly require a larger vertical tail plane, the option of horizontal tail plane reduction is preferred over a decrease in tail boom length.

For lateral stability, values for  $\Gamma$  and  $S_{VT}$  need to be found that (a) ensure stability in the worst case scenario and (b) provide sufficient susceptibility to oscillations. Looking at Figure 6.21, while keeping in mind that the lateral area and dihedral angle should be minimized for performance, a dihedral angle of  $20^\circ$  and a  $S_{VT}$  of 1.5 times the original size are deemed appropriate values. The proposed design changes are summarized below.

- Equivalent dihedral angle of  $20^\circ$ .
- Vertical tail plane area enlarged by 50%
- Horizontal tail plane area reduced by 25%

These changes do have an effect on the inertia of the Kiteplane, but the increase in vertical tail plane weight is approximately canceled out by the decrease in horizontal tail plane weight. Furthermore, for the purpose of this analysis it is assumed that the effect of the increase in  $\Gamma$  on the inertia can be neglected.

To assess the stability of the new design, the changes are incorporated in the SIMULINK model and subjected to the simulations listed in Table 6.1. The results are equal or better for each of the cases in Table 6.1.

After the simulations were completed, the new design features were incorporated into a new kiteplane design, henceforth called "Kiteplane 4". This kiteplane was to be a new design from the ground up and not simply an adapted old kite. Adapting Kiteplane 3 from figure H.1 presented a number of practical issues such as maintaining symmetry while increasing the dihedral. The Kiteplane 4 design will take the new knowledge of kiteplanes into account. The choice was made, for simplicity of construction, to have the dihedral originate from the center of the wing and not have a horizontal part of the wing in the center like the old design of figure H.1. By reducing the number of kinks in the wing to one, it is easier to build the wing symmetrical. Furthermore, the increased amount of lateral area will be beneficial to the stability of the kite.

Another change which was incorporated was to move the fins to the underside of the tailbooms. The fins on top resulted from the desire to have the kiteplane design analogue to conventional aircraft. However, the fins on top have a destabilizing effect. While in yaw motion, the fins on top introduce a destabilizing roll moment which is usually overcome by the dihedral of the main wing. Moving the fins to the bottom introduces a stabilizing moment while yawing. In essence, this design change increases the effective dihedral of the kite, making the stability

derivative  $C_{l_v}$  more negative (see section 3.2). For conventional aircraft, ground clearance ensures that the vertical fins have to be on top. For a kiteplane, a ground clearance requirement like that for conventional aircraft does not exist.

The new kiteplane 4 design is visualized in figure 6.24.

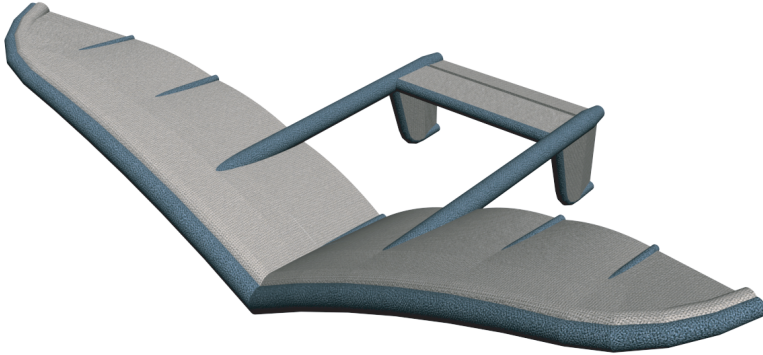


**Figure 6.24:** A 3D rendering of Kiteplane 4.

#### 6.4.5 Flight test results of the new Kiteplane 4 design

Like Kiteplane 3, the new Kiteplane 4 was built at the production facility of Hong-Kong based Lam sails. Initial tests were performed on a short, 4 meter tether to safely assess the flight characteristics of the new design. These early tests quickly showed a dramatic improvement in lateral stability behavior. Where Kiteplane 3 would oscillate and diverge, the new Kiteplane 4 showed to correct itself into the zenith position. Results from these early tests inspired confidence to fly the new kite on a longer tether.

Later flight tests saw the kite fly on a 20-meter long tether. The initial launch phase through the center of the wind window does not pose any problems. Any lateral disturbance during launch quickly converges while the kite ascends up into the zenith position. Once in this position, gusts in the wind pushes the kite into an asymmetric inverted pendulum motion. For Kiteplane 3 this would result in a diverging oscillation which quickly led to a crash. The new Kiteplane 4 shows significantly improved lateral stability. The new kite is able to correct the lateral disturbance and convert back towards the zenith position. Even when  $\theta_t$  becomes as much as 30 to 40 degrees due to a large disturbance, the new Kiteplane 4 is able to make use of the extra room the longer 20-meter tether provides and converge back to the zenith position.

Figure 6.25 shows a composite picture from the launch of the new Kiteplane 4. Notice how the initial lateral divergence during launch quickly converges as the kite flies to the zenith position.



**Figure 6.25:** *A composite representation of the new kiteplane 4 in flight.*

## 6.5 Concluding remarks

The main purpose of this chapter is to demonstrate the benefit of an engineering approach to the design of kites. The case studies done in this chapter aim to show a structured path the initial *question* to the resulting *answer*. The first question is posed in section 6.2. What are the characteristics of the effective cable length and what parameters influence it. The analysis shows a strong relation to the aerodynamic drag of the cable. The second case in section 6.3 addresses a heated issue within the kite community: What makes a kite corner. In this section, the benefit of an intuitive multi-body kite simulation is demonstrated by carefully piecing together the chain of events following a tension increase in one of the steering lines. The simulation reveals that the cornering of a surf kite is strongly related to its ability to deform. The simulation also shows to be useful in simulating kites which are impossible in real life, such as the fully rigid surf kite. Lastly, the simulation allows to make adaptations to the existing configuration and quickly simulate the kite in flight to obtain the resulting changes in performance. This loop is traditionally done in real life by cutting and stitching the real kite. The multi-body simulation allows for the same design loop within a much shorter

timeframe. Lastly, section 6.4 demonstrates the power of a rigid body model by addressing an instability mode in the Kiteplane 3 design. The model, based on lagrangian equations of motion, allows to analyse in detail the parameters which influence the unstable behavior. The analysis results in a number of design changes which are incorporated into a new Kiteplane design (Kiteplane 4) which was tested and found to be free of the unstable lateral motion. The cases presented in this chapter all lead to a greater understanding of kites. This increased understanding lies at the basis of the engineering methodology for kite design and allows for a structured design process.





---

## Conclusions and recommendations

---

This chapter presents the conclusions from the work done in this thesis and continues to give a number of recommendations to both kite designers and the scientific community.

### 7.1 Conclusions

The goal of this thesis is to develop an engineering methodology for kite design. This methodology is based on the trinity presented in figure 2.5, which is repeated below for clarity. Chapter 2 starts off by sketching the current situation in the kite industry and touches on the current state of research. chapter 3 introduces rigid body modelling for kites. Chapter 4 describes the numerical modelling of flexible kites using the principles of multi-body dynamics. Chapter 5 performs a model validation on the model presented in chapter 4. Finally, chapter 6 presents a number of case studies in order to show the benefit of an engineering methodology for kite design.

Chapter 2 shows the state of kite design. currently, kites are designed using trial-and-error approach. This chapter states that for more complex industrial applications, a more controlled design methodology is needed. Furthermore, the current kite industry stands to gain from such an approach as well.

Chapter 3 presents two rigid body models for kites, one based on conventional flight dynamics and one based on Lagrangian equations of motion. In these models, the kite is assumed to be rigid and the tether is assumed to be a stiff rod. The rigid body models show to be very useful in building understanding of basic kite dynamics. Especially the rigid body model based on conventional

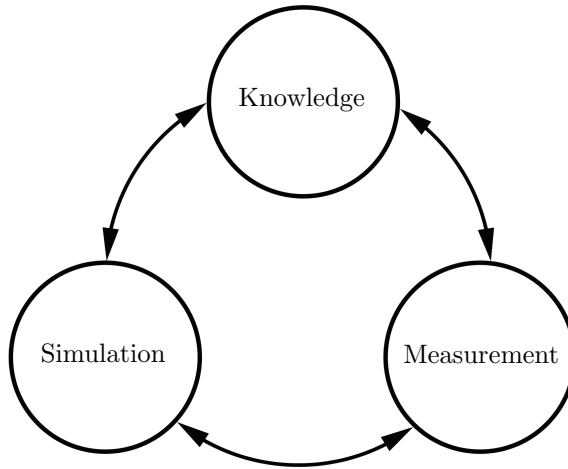


**Figure 7.1:** *The three prerequisites for an engineering approach to kite design.*

flight dynamics shows the difference between kites and airplanes. Due to the fact that a kite is tethered to the ground, eigenmodes are present which only occur with kites. Especially the pendulum eigenmode seems to be of interest due to its relation with the lateral surface of the kite and its likelihood to become unstable.

The high flexibility of a kite, which was neglected in the models of chapter 3 warranted further investigation. Chapter 4 proposes a model based on the principles of multi-body dynamics. This model has to adhere to a number of requirements such as ease of use and low resource intensity. From the literature survey and private communication it was concluded that the current state of fluid structure interaction technology, coupling a structural finite element analysis to a computational fluid dynamics analysis, is such that a full simulation of a complete kite is not feasible within the requirements for the kite simulation tool. The highly complex model would be too difficult to use and too resource intense to be funded by the current kite industry. Furthermore, the state of the industrial application of kites also does not yet warrant such a large and risky investment. The proposed kite simulation toolbox runs within MSC ADAMS and enables the designer to quickly build kite configurations from three main building blocks: Tethers, inflatable tubes and foils. The kite simulation toolbox has already seen extensive use by students who quickly picked it up. The resource friendly nature of the simulation allows it to run on a conventional laptop or desktop computer.

Chapter 5 presents the results of a validation of the model presented in chapter 4. The tether model was compared with pendulum and wave propagation experiments and showed good correlation. A model convergence study showed that for a quasi-static situation, only 10 elements were needed to approximate a 25 meter

cable. Increasing the amount of elements yielded no noticeable difference. The inflatable beams were compared to test data in a cantilever bending experiment and also showed good correlation. Furthermore, the location of wrinkling in a tapered beam was calculated as a function of taper ratio and the data was compared to tapered beam simulations. It can be concluded that the location of the wrinkles on the tapered beam coincided well with the numerical simulations. Lastly, the airfoil simulation was compared to existing data on single membrane airfoils and showed reasonable similarity. It should be noted that the simulations were based on airfoils with a thickness between 15% and 25% while the only available test data was that of an airfoil with a 10% thickness. This extrapolation of the data on which the simulation is based can give rise to inaccuracies. Lastly, the shape of the simulated two dimensional airfoil is compared to measured data and shows good agreement.

In order to validate the three dimensional canopy shape, a kite was placed in a wind tunnel and the shape was captured using photogrammetry. It was concluded that the measurement technique of photogrammetry is a particularly useful technique in kite research due to the fact that it captures the shape instantly. Furthermore, the technique is both simple to use and cheap to realize. The resulting canopy shapes showed great similarity with the simulated canopy shapes. Some details, however, cannot be obtained from the numerical simulation. For instance, wrinkling in the canopy can lead to extra turbulence and loss of lift which does not occur in the simulation. Furthermore, the structure has some measure of initial slack which can be accounted for in the simulation. However, this parameter is not easily predicted beforehand. The slack becomes especially obvious while only lightly loading the kite. In practice this is less of an issue because the more interesting cases are those where the kite is under high load. For these high load cases, the simulated canopy shape and the measured canopy shape showed good agreement. Also, the resulting load on the wing shows good correlation.

A final validation was performed by flying a number of conventional surf kites and comparing the forces on the power lines and the absolute velocity with the simulated case. The comparison showed remarkable similarity, further establishing the validity of the simulation. The kite simulation toolbox was designed to provide a kite designer with the means of virtual prototyping on a conventional computer. Model validation has shown that the kite simulation toolbox provides that capability with an acceptable measure of accuracy and the feedback from students has confirmed the ease of use of the software.

In order to establish the benefit of an engineering methodology for kite design, a number of case studies were done. First, the principle of effective cable length is introduced. Using the kite simulation toolbox, it was shown that for long tethers there is a large amount of inertia in the cable which has a damping effect on the disturbances introduced into the cable by the kite.

The second case investigates the cornering performance of a conventional surf kite, a fiercely debated issue among kite designers and kite surfers. Using the kite simulation toolbox it was concluded that the yawing motion resulting from

an increase in force on the steering line is brought about by the flexibility of the kite. By pulling on one of the steering lines, an a-symmetric tether loading is created which flexes and warps the kite such that the lift forces on the left and right tip are offset slightly. This offset creates a yawing moment. This also means that a rigid kite cannot steer, which is confirmed by running a simulation with a rigid kite. The case study continues to explore what parameters influence the cornering performance of the surf kite. By increasing the wing chord at the tip, a faster cornering performance can be obtained.

The last case study investigates the then current kiteplane design and showed that due to lack of lateral surface area, an unstable pendulum motion is created. For the kiteplane, there is a close correlation between the lateral surface area of the kite and the pendulum instability. This knowledge is used to propose a number of design changes which are incorporated into a new kiteplane design. Flight tests of this new design confirmed the predictions. The new design shows greatly improved pendulum stability

## **7.2 Recommendations to the scientific community**

The main recommendation that can be given to the scientific community is to no longer ignore the potential of kites. From a scientific point of view, a kite is an immensely interesting object. With kites, just about every complication is present, except for supersonic flow. Kites provide the means to study complex phenomena whilst keeping experiments cheap. The craftsmen of the 19th century pursuing powered flight realized the research potential of kites and benefitted greatly from it as a result. Furthermore, the research field of kites is a open field with great potential for scientists and engineers. Applications for kites are as multiple as they are diverse. Controllable kites are the enabling technology in new fields such as high altitude energy generation and can function as sensor platforms and a means of ship propulsion.

The models presented in this thesis can be refined further. The numerical model using a multi-body approach can also be applied to parachutes and paragliders, as well as to conventional aircraft. This allows these applications to benefit from the low resource intensity of this model. It is recommended to expand the aerodynamic model to include more airfoils like the double membrane airfoil in order to study its benefit. Also, the current building blocks allow the creation of complete laddermill simulation models with a flexible kite on a flexible line, attached to a ground station. This will allow for simulation of reel-in and reel-out strategies, with or without flying cross-wind patterns. Of special interest are the forces in the lines, the forces in the canopy and the resulting power output. Obtaining this data will allow for e.g. cost estimations based on the loads and duration of loads on the materials of the kite and tether.

Eventually, many years from now, a full fluid structure interaction simulation of a complete kite may become a reality. A step in that direction can be made

by using uniform pressure models for the inflated tubular structure. This method allows the designer to study wrinkling in a complex tubular frame and possibly validate the more simple multi-body model of inflated tubes. At the moment, the method of uniform pressure is being used successfully in simulation of airbags, and it holds great potential for other fields as well.

Much of what is possible today has come about with the advent of new, light-weight materials. Currently, all kites are made out of a combination of Dacron, ripstop Nylon and thermoplastic poly-urethane. These materials are relatively weak and susceptible to degradation under UV light. It comes highly recommended to invest considerable amounts of research effort into new materials for kite applications. As a matter of fact, many materials already exist which would be a tremendous improvement over the current materials. High-tensile fibers in a matrix of metallized mylar and other non-woven flexible composites are far stronger and more UV resistant. Also, the current method of building an inflated beam uses two materials: Dacron is used as the outer layer, carrying the load of the internal pressure. Thermoplastic poly-urethane is used as an inner bladder to contain the inflation gas. It is recommended to combine these two functions (structural strength and gas containment) into a single material, which has the potential to result in a lighter beam. Lastly, joining techniques deserve further attention, especially when using new materials. Currently, kites are sown together. Joining techniques such as bonding and welding allow for a less discrete transfer of load. Switching materials and joining techniques in the production process of kites is a change which has large implications. Currently, kites are mostly made in China, India and Vietnam. Switching these facilities to new materials and joining techniques is a major endeavor, but will ultimately have to be undertaken in order to advance the technology of kites. Another field which needs extensive research is that of control theory for kites. Kite control is needed to build automatically controlled kite. The field of control will benefit greatly from rigid-body models which make use of higher-order models for their stability derivatives. The field of kite control is wide open at the moment and is a great opportunity to do exciting new things.

Lastly, it is highly recommended that the scientific community engage into discussion with the kite designers. There is an enormous amount of empirical knowledge with kite designers which should be taken advantage of. In order to consolidate kite knowledge and engineering, the first kite conferences have already been held, one of which was at the Delft University in 2009. It comes highly recommended to invite the kite designers to these conferences and engage them in discussion.

### **7.3 Recommendations to kite designers**

It is remarkable to see what has been achieved by kite designers in the last decade. With limited resources and a relatively small market, they have forged a new era

for kites which has resulted in designs of incredible performance. However, in the last few years, the pace of improvement has slowed down. The trial-and-error design process has run its course and it is now time for a more structured approach.

At the basis of any structured design process lies a set of requirements. In order to quantify these requirements, measurements on riders and boards are required. Reproducible measurements are absolutely key to a structured kite design process. Not just in quantifying the set of requirements, but also in evaluating the new designs. Different designs cater to different riders. From the novice to the experienced, requirements will greatly vary. Defining these requirements will give the design a certain amount of focus. This focus is what lies at the foundation of the structured design effort.

Measurements are not necessarily complicated or expensive. In this thesis, extensive use is made of photogrammetry by using 14 cameras simultaneously. Although this allows the instantaneous capturing of the shape of the kite, such an array is not a prerequisite. Keeping a kite in a certain spot and walking around the kite while taking pictures with one camera will already result in a reasonably good wireframe model.

The shape of a kite while it lies on the beach is of far less interest than the shape of a kite while it is flying. The enormous flexibility of a kite will ensure that the loaded shape is significantly different from the unloaded shape. Again, here photogrammetry can help in determining the shape of the arc while it is loaded. It allows for evaluation of the tubular structure, as well as the bridle line system.

The airfoil shape of a kite has remained nearly unchanged in the last decade. They are all derivatives of single membrane airfoils. A double membrane airfoil will greatly increase the lift over drag of a kite. Battens can also influence the shape of the airfoil to induce certain flight characteristics. It was shown in section 6.3 that the lift in the tips is of great influence on the cornering performance of a kite. Tailoring the airfoil in the tips allows the designer to directly influence the cornering performance.

New materials will allow for higher pressures in the tubes and higher wing loadings on the canopy. Furthermore, a lighter kite will corner faster and will be able to fly in lower wind conditions. Current surf kites have greatly benefitted from earlier advances in materials science and they can do so again. Also, new joining techniques will be needed. It is highly recommended to form cooperations with the sailing industry where bonding and welding is already common practice. As a matter of fact, there are a large amount of similarities between sails and kites, such as materials, loads and weight issues. A cooperation with the sailing industry can benefit both parties.

Lastly, analogue to what was mentioned in the previous section, seek out the academic institutes and challenge them. Kites form an interesting field of study and there is a large amount of knowledge already available in the scientific community. All that needs to be done is to apply that knowledge to kites. Invite the scientists to experience the power of kites first-hand and work with them on

formulating the right questions. It is the authors strong belief that there can be no greater benefit to the development of kites than a strong cooperation between the scientific community and the kite industry.





---

## References

---

- Adler, A. L., Mikulas, M. M. & Hedgepeth, J. M. (2000). Static and dynamic analysis of partially wrinkled membrane structures. In *Proceedings of the 41st aiaa structures, structural dynamics and materials conference*. Atlanta, GA, USA: AIAA.
- Alexander, K. & Stevenson, J. (2001). Kite equilibrium and bridle length. *The aeronautical journal*, 105(1051), 535-541.
- Anderson, J. D. (1991). *Fundamentals of aerodynamics, 2nd edition*. USA: McGraw-Hill.
- Archer, C. L. & Caldeira, K. (2009). Global assessment of high-altitude wind power. *MDPI Journal of Energies*, 2, 307-319.
- Association, A. K. (2009, 25th March). *Kite history*. <http://www.gombergkites.com/nkm/hist1.html>.
- Augustino, J. (n.d.). *Augustino photos*. Available from <http://picasaweb.google.com/jason.augustino>
- Babister, A. W. (1961). *Aircraft stability and control*. Oxford, UK: Pergamon press.
- Baker, E. H., Kovalevsky, L. & Rish, F. L. (1972). *Structural analysis of shells*. USA: McGraw-Hill.
- Banerjee, S. P. & Patily, M. J. (2008, 7– 10 April). Aeroelastic analysis of membrane wings. In *The 49th structures, structural dynamics, and materials conference*. Schaumburg, Illinois, USA: AIAA.

- Bergsma, O. K. (1996). *Three-dimensional simulation of fabric draping*. Unpublished doctoral dissertation, Delft University of Technology.
- Boccard, N. (2009). Capacity factor of wind power realized values vs. estimates. *Energy Policy*, 37(7), 2679-2688.
- Boer, R. G. den. (1980). *Low speed aerodynamic characteristics of a two-dimensional sail wing with adjustable slack of the sail* (Tech. Rep. No. LR-307). Delft, the Netherlands: Delft University of Technology.
- Boer, R. G. den. (1982). *Numerical and experimental investigation of the aerodynamics of double membrane sailing airfoil sections* (Tech. Rep. No. LR-345). Delft, the Netherlands: Delft University of Technology.
- Breuer, J. C. M. (2007). *Thin walled tubes under pressure and torsion* (Tech. Rep.). Delft, the Netherlands: ASSET, Delft University of Technology (internal report).
- Breuer, J. C. M. & Ockels, W. J. (2007). An inflatable wing using the principle of tensairity. In *Proceedings of the 48th aiaa structures, structural dynamics and materials conference*. Waikiki, Hawaii, USA: AIAA.
- Breukels, J. (2003). *Design of a high altitude inflatable kite*. Delft, the Netherlands: Delft University of Technology.
- Breukels, J. (2005). *Kiteye report, wp3 to wp8* (Tech. Rep.). Delft, the Netherlands: European Space Agency.
- Breukels, J. (2006). *Kitelab progress report* (Tech. Rep.). Delft, the Netherlands: Delft University of Technology.
- Breukels, J. & Ockels, W. J. (2005). Tethered kiteplane design for the ladder-mill project. In *Proceedings of the world wind energy conference*. Melbourne, Australia: WWEC.
- Breukels, J. & Ockels, W. J. (2007a). Design of a large inflatable kiteplane. In *Proceedings of the 48th aiaa structures, structural dynamics and materials conference*. Waikiki, Hawaii, USA: AIAA.
- Breukels, J. & Ockels, W. J. (2007b). A multi-body dynamics approach to a cable simulation for kites. In *Proceedings of the asia modelling and simulation conference*. Beijing, China: IASTED.
- Breukels, J. & Ockels, W. J. (2007c). Numerical and experimental results of the airfoil in the delft university kitelab. In *Proceedings of the 37th aiaa fluid dynamics conference*. Miami, FL, USA: AIAA.

- Breukels, J. & Ockels, W. J. (2007d). Past, present and future of kites and energy generation. In *Proceedings of the iasted power and energy conference*. Clearwater, FL, USA: IASTED.
- Breukels, J. & Ockels, W. J. (2009). A multi-body system approach to simulation of inflated tubular beams. *Journal of Multi-Body System Dynamics (Submitted)*.
- Breukels, J. & Ockels, W. J. (2010a). A multi-body system approach to the simulation of flexible membrane airfoils. *Aerotecnica Missili & Spazio (Submitted)*.
- Breukels, J. & Ockels, W. J. (2010b). Simulation of a flexible arc-shaped surf kite. *AIAA Journal of Aircraft (Submitted)*.
- Breukels, J. & Ockels, W. J. (2010c). Simulation of a three dimensional flexible sail wing with an inflated tubular spar. *Aerotecnica Missili & Spazio (Submitted)*.
- Bronstein, I. N. & Semendjajew, K. A. (1991). *Taschenbuch der matematik*. Moscow, Russia: Verlag Nauka.
- Brown, G., Haggard, R. & Norton, R. (2001). Inflatable structures for deployable wings. In *Proceedings of the aiaa aerodynamic decelerator systems technology conference and seminar*. Boston, MA,USA: AIAA.
- Bryant, L. W., Brown, W. S. & Sweeting, N. E. (1942). Collected researches on the stability of kites and towed gliders. *Aeronautical Research Council, RM(2303)*.
- Bryant, L. W. & Gates, S. B. (1938). Nomenclature for stability coefficients. *Aeronautical Research Council, RM(1801)*.
- Bryja, J. (2006). Kiteboarding statistics: Worldwide participation and sales figures. *SBC Kiteboard Magazine*.
- Bulder, B. H. (1998). *Laddermill cost of energy analysis* (Tech. Rep. No. ECN-CX-98-XXX). Petten, the Netherlands: Laboratory of Technical Mechanics, Delft University of Technology.
- Cebeci, T., Platzer, M., Chen, H., Chang, K. & Shao, J. P. (2005). *Analysis of low-speed unsteady airfoil flows*. Long Beach, California, USA: Horizons Publishing.
- Chang, C., Hodges, D. H. & Patil, M. J. (2008). Flight dynamics of highly flexible aircraft. *Journal of Aircraft, 45(2)*, 538 – 545.
- Chui, H. C., Benson, R. H., Fiscella, M. D. & Burns, S. J. (1994). Mechanical and thermal wrinkling of polymer membranes. *Journal of Applied Mechanics, 67-70*.

- Co, W. B. A. (2006). *Wright brothers airplane company website*. <http://www.wright-brothers.org/TBR/History/History%20of%20Airplane/centbefore.htm>.
- Comer, R. L. & Levi, S. (1963). Deflections of an inflated circular cylindrical cantilever beam. *AIAA Journal*.
- Cook, M. V. (1997). *Flight dynamics principles*. London: Arnold.
- Corke, T. C. (2002). *Design of aircraft*. Upper Saddle River, New Jersey, USA: Prentice Hall.
- Crate, H., Batdorf, S. B. & Baab, G. W. (1944). The effect of internal pressure on the buckling stress of thin-walled circular cylinders under torsion. *NACA, WR(L-67)*.
- Damveld, H. J. & Mulder, J. A. (2005, 15– 18 August). Influence of instationary aerodynamics and trimming on the dynamics of an aeroelastic aircraft. In *Atmospheric flight mechanics conference and exhibit*. San Francisco, California, USA: AIAA.
- Dickinson, B. (1968). *Aircraft stability and control for pilots and engineers*. London, UK: sir Isaac Pitman and Sons.
- Donell, L. H. (1933). Stability of thin walled tubes under torsion. *NACA, report(3781)*.
- Ellison, D. (1969). *Usaf stability and control handbook (datcom)*. Wright-Patterson Air Force Base, Fairborn, Ohio, USA: AF Flight Dynamics Lab, AFFDL/FDCC.
- Eppler, R. (1990). *Airfoil design and data*. Berlin, Germany: Springer-verlag.
- Etkin, B. (1972). *Dynamics of atmospheric flight*. Toronto, Canada: John Wiley & Sons Inc. (University of Toronto)
- Fadul, J. A. (2009). *Kites in history, in teaching, and in therapy*. Toronto: Lulu press.
- Fichter, W. B. (1966). *a theory for inflated thin-wall cylindrical beams* (Tech. Rep. No. TN D-3466). USA: NASA.
- Fink, M. P. (1967). *Full-scale investigation of the aerodynamic characteristics of a model employing a sailwing concept* (Tech. Rep. No. TN D-4062). USA: NASA.
- Fink, M. P. (1969). *Full-scale investigation of the aerodynamic characteristics of a sailwing of aspect ratio 5.9* (Tech. Rep. No. TN D-5047). USA: NASA.

- Flugge, W. (1966). *Stresses in shells*. Berlin, Germany: Springer verlag.
- Furey, A. (2009). *Kite, airborne and high altitude wind energy blog*. <http://kiteenergy.blogspot.com>.
- Gal-Rom, Y. C. & Raveh, D. E. (2008, 7– 10 April). A simplified aero-structural model for inflated wings. In *The 49th structures, structural dynamics, and materials conference*. Schaumburg, Illinois, USA: AIAA.
- Gerard, G. & Becker, H. (1957). Handbook for structural stability part iii - buckling of curved plates and shells. *NACA, TN(3781)*.
- Gere, J. M. & Timoshenko, S. P. (1991). *Mechanics of materials, third si edition*. USA: Chapman and Hall.
- Gibbs-Smith, H. C. (1970). *Aviation, an historical survey from its origins to the end of world war ii*. London: Her majesty's stationary office.
- Glauert, M. A. (1930). The stability of a body towed by a light wire. *Aeronautical Research Council, RM(1312)*.
- Gordon, J. A. M., McFarland, M. & Gibbs-Smith, C. H. (1966). *The adventure of man's flight*. Library of Congress Catalogue Card No. 62-17517: merican Heritage Publishing Co. Inc.
- Grinspun, E., Krysl, P. & Schroder, P. (2002, 23– 26 July). Charms: a simple framework for adaptive simulation. In *The 29th annual conference on computer graphics and interactive techniques*. San Antonio, Texas, USA: ACM.
- Groeneboom, P. (2010, 8th March). *Minutes from stu p10-37 matchmaking meeting*.
- Groot, S. G. C. de. (2010). *Modelling the dynamics of an arc-shaped kite for control law design* (MSc Thesis). Delft, the Netherlands: Delft University of Technology.
- Groot, S. G. C. de, Breukels, J. & Schmehl, R. (2010). Multibody system reduction for derivation of a flight dynamics model for real-time control of kites. *Journal of Guidance, Control and Dynamics (submitted)*.
- Harvey, M. (2009, 12th November). The quest to find alternative sources of renewable energy is taking to the skies. *Times Online*. [http://business.timesonline.co.uk/tol/business/industry\\_sectors/utilities/article6913119.ece](http://business.timesonline.co.uk/tol/business/industry_sectors/utilities/article6913119.ece).
- Hoak, D. E. & Carlson, J. W. (1960). *Usaf stability and control handbook*. USA: United States air force, Wright-Patterson Airforce base.
- Hoerner, S. F. (1965a). *Fluid dynamic drag*. USA: Hoerner Fluid Dynamics.

- Hoerner, S. F. (1965b). *Fluid dynamic lift*. USA: Hoerner Fluid Dynamics.
- Houska, B. (2007). *Internal paper: a 9dof kite model* (Tech. Rep.). Leuven, Belgium: Leuven University.
- Hurwitz, A. (1964). On the conditions under which an equation has only roots with negative real parts. *Selected Papers on Mathematical Trends in Control Theory*.
- Jackson, S. B. (1942). Free-flight tests on kites in the 24ft. wind tunnel. *Aeronautical Research Council, RM(2599)*.
- Jenkins, C. H. (2001). *Gossamer spacecraft: Membrane and inflatable structures technology for space applications*. USA: AIAA.
- Jenkins, C. H. & Leonard, J. W. (1993). Dynamic wrinkling of viscoelastic membranes. *Journal of Applied Mechanics*, 575-582.
- Karamcheti, K. (1966). *Principles of ideal fluid dynamics*. USA: John Wiley and Sons, Inc.
- kites cobra. (2006, 10th Februari). *Flexifoil history*.  
<http://www.cobrakite.com/flxhstry.html>.
- KiteVes. (2009, 1st December). *Kitves project funding*.  
<http://www.kitves.com/funding.aspx>.
- Kromm, F. X., Lorriot, T., Coutand, B., Harry, R. & Quenisset, J. M. (2003). Tensile and creep properties of ultra high molecular weight pe fibres. *Polymer testing*, 22(4), 463 – 470.
- Lansdorp, B. & Ockels, W. J. (2005a). Comparison of concepts for high-altitude wind energy generation with ground based generator. In *Proceedings of the 2nd china international renewable energy equipment and technology exhibition and conference*. Beijing, China: NRE.
- Lansdorp, B. & Ockels, W. J. (2005b). Design of a 100mw laddermill for wind energy generation from 5km altitude. In *Proceedings of the 7th world congress on recovery, recycling and re-integration*. Beijing, China: UIPAC.
- Lansdorp, B. & Ockels, W. J. (2006). Design and construction of a 2 kw laddermill groundstation. In *Proceedings of the power asia conference*. Beijing, China: PennWell.
- Lansdorp, B., Remes, B. & Ockels, W. J. (2005). Design and testing of a remotely controlled surfkite for the laddermill. In *Proceedings of the world wind energy conference*. Melbourne, Australia: WVEC.

- Lansdorp, B. & Williams, P. (2006). The laddermill - innovative wind energy from high altitudes in holland and australia. In *Proceedings of the windpower 2006 conference*. Adelaide, Australia: AWEA.
- Legrand, J. (1992). *Chronicles of aviation*. United Kingdom: Chronicle communications ltd.
- Looye, G. H. N. (2008). *An integrated approach to aircraft modelling and flight control law design, control and simulation*. Unpublished doctoral dissertation, Delft University of Technology.
- Lowson, M. V. (1990). Minimum induced drag for wings with spanwise camber. *Journal of Aircraft*.
- Loyd, L. (1980). Crosswind kite power. *Journal of Energy*.
- Main, J. A. (1993). *Analysis and design of inflatable aerospace structures* (Tech. Rep.). USA: Vanderbilt University.
- Main, J. A., Peterson, S. W. & Strauss, A. M. (1995). beam-type bending of space-based inflatable structures. *Journal of aerospace engineering*.
- Maughmer, M. D. (1972). *A comparison of the aerodynamic characteristics of eight sailing airfoil sections* (Tech. Rep.). USA: Princeton University.
- McCormick, B. W. (1979). *Aerodynamics, aeronautics and flight mechanics*. USA: John Wiley and Sons.
- McLeod, A. R. (1918). On the action of wind on flexible cables, with applications to cables towed below aeroplanes, and balloon cables. *Aeronautical Research Council, RM(554)*.
- Meijaard, J. P. (1997). *Rapport over een inleidend onderzoek naar het gedrag van een laddermolen* (Tech. Rep.). Delft, the Netherlands: Laboratory of Technical Mechanics, Delft University of Technology.
- Meijaard, J. P., Ockels, W. J. & Schwab, A. L. (2004). Modelling of the dynamic behaviour of a laddermill, a novel concept to exploit wind energy. In *Proceedings third international symposium on cable dynamics* (Vol. 92, pp. 263 – 274). Trondheim, Norway: A.I.M.
- Meijaard, J. P. & Schwab, A. L. (1999). *Programma voor de simulatie van het dynamische gedrag van een laddermolen met berekeningsvoorbeelden* (Tech. Rep. No. LTM-1197). Delft, the Netherlands: Laboratory of Technical Mechanics, Delft University of Technology.
- Meirovitch, L. & Tuzcu, I. (2002, 5– 8 August). Intergated approach to flight dynamics and aeroservoelasticity of whole flexible aircraft. In *Guidance, navigation, and control conference and exhibit*. Monterey, California, USA: AIAA.

- Melkert, J. A. (1992). *Voortgangsverslag van het stratow-project*. Delft, the Netherlands: Delft University of Technology.
- Meyer, M. & Matthies, H. G. (2004). State-space representation of instationary two-dimensional airfoil aerodynamics. *Journal of Wind Engineering and Industrial Aerodynamics*, 92(3-4), 263 – 274.
- Molder, O. V. (1999). *an air inflated gangway inside the hull of a cl160 airship*. Delft, the Netherlands: Delft University of Technology.
- Mulder, J. A., Sridhar, J. K. & Breeman, J. H. (1994). *Agardograph 300, identification of dynamic systems - applications to aircraft, part 2: Nonlinear analysis and manoeuvre design* (Vol. 3). NATO: AGARD, Advisory Group for Aerospace Research and Development.
- Mulder, J. A., Staveren, W. H. J. J. van & Vaart, J. C. van der. (2007). *Flight dynamics, lecture notes* (Tech. Rep.). Delft, the Netherlands: Delft University of Technology.
- Murai, H. & Maruyama, S. (1979). Theoretical investigation of the aerodynamics of double membrane sailing airfoil sections. *Journal of Aircraft*, 17, no 5(80-4048).
- Murphey, T. W. & Mikulas, M. M. (1999). Nonlinear effects of material wrinkles on the stiffness of thin polymer films. In *proceedings of the 40th aiaa/asme/asce/ahs/asc structures, structural dynamics, and materials conference and exhibit*. St. Louis, MO, USA: AIAA.
- Nakamura, Y. (1992). Some asymptotic aspects of the nonstationary aerofoil theory. *Fluid Dynamics Research*, 10(3), 151 – 157.
- Naylor, J. L. & Ower, E. (1965). *Aviation: its historical development*. London: Peter Owen Vision Press.
- Neumark, S. (1963). Equilibrium configurations of flying cables of captive balloons, and cable derivatives for stability calculations. *Aeronautical Research Council, RM(3333)*.
- Nickel, K. & Wohlfahrt, M. (1990). *Schwanzlose flugzeuge*. Germany: Birkhauser verlag.
- Nielsen, J. N. (1963). Theory of flexible aerodynamic surfaces. *Journal of Applied Mechanics*, 435-442.
- Norris, S. R. & Andrisani, D. (2001). Longitudinal equilibrium solutions for a towed aircraft and tow cable. In *Proceedings of the aiaa atmospheric flight mechanics conference and exhibit*. Montreal, Canada: AIAA.



- Ockels, W., Breukels, J., Lansdorp, B. & Spierenburg, G. J. (2004). Laddermill, work in progress. In *Proceedings of the ewec 2004*. London, UK: EWEA.
- Ockels, W. J. (n.d.). *Private communication*.
- Ockels, W. J. (1996, 12th November). *Wind energy converter using kites* (Tech. Rep.). European Patent EP084480, Dutch Patent NL1004508, Spanish Patent SP2175268, US Patent US6072245: Ockels B.V.
- Ockels, W. J. (2001). Laddermill, a novel concept to exploit the energy in the airspace. *Journal of aircraft design*, 81-97.
- Ockels, W. J. (2007). Kite power and propulsion, the laddermill principle. *Unpublished*.
- Ockels, W. J., Lansdorp, B. & Ruitkamp, R. (2006). Ship propulsion by kites combining energy production by laddermill principle and direct kite propulsion. In *Proceedings of the kite sailing symposium*. Seattle, USA: The drachen foundation.
- Ockels, W. J., Melkert, J. A. & Roelen, A. L. C. (1994). Stratospheric towed vehicle concept. *Journal of Aircraft*.
- Onate, E. & Kroplin, B. (2005). *Textile composites and inflatable structures*. Dordrecht, the Netherlands: Springer.
- Orlandea, N., Chace, M. A. & Calahan, D. A. (1978). A sparsity-oriented approach to the dynamic analysis and design of mechanical systems - part 1. *Journal of Engineering for Industry*.
- Ormiston, R. A. (1971). Theoretical and experimental aerodynamics of the sailing. *Journal of Aircraft*.
- Pacejka, H. B. & Bakker, E. (1992). The magic formula tyre model. *Journal of Vehicle System Dynamics*.
- Parish, T. (n.d.). *A brief history of box kites*. Available from <http://www.buzzle.com/articles/box-kites-a-brief-history.html>
- Podgaets, A. R. & Ockels, W. J. (2006a). Flight control and stability of a multiple kites tethered system. In *Proceedings of the renewable energy conference*. Makuhari Messe, Chiba, Japan: Japan Council for Renewable Energy (JCRE).
- Podgaets, A. R. & Ockels, W. J. (2006b). Three-dimensional simulation of a laddermill. In *Proceedings of the windpower asia conference*. Beijing, China: WWEA.

- Podgaets, A. R. & Ockels, W. J. (2007). Flight control of the high altitude wind power system. In *Proceedings of the 7th conference on sustainable applications for tropical island states*. Havana, Cuba: UNESCO.
- Provot, X. (1995). Deformation constraints in a mass-spring model to describe rigid cloth behavior. In W. A. Davis & P. Prusinkiewicz (Eds.), *Graphics interface '95* (pp. 147–154). Qu'ebec, Canada: Canadian Human-Computer Communications Society.
- Rahnejat, H. (1998). *Multi-body dynamics. vehicles, machines and mechanisms*. London and Bury St Edmunds, UK: Professional Engineering Publishing.
- Remes, B. D. W. (2008). *Design construction and optimization of a control mechanism for the lifting surface on the laddermill* (MSc Thesis). Delft, the Netherlands: Delft University of Technology.
- Ruijgrok, G. J. J. (1970). *Gegevens van de atmosfeer*. Delft, the Netherlands: Technische Hogeschool Delft.
- Ruijgrok, G. J. J. (1994). *Elements of airplane performance*. Delft, the Netherlands: Delft University Press.
- Sanchez, G. (2006). Dynamics and control of single-line kites. *Aeronautical Journal*, 110(1111), 615 – 621.
- Shiraishi, N., Matsumoto, M., Katoh, T., Shirato, H. & Matsumura, S. (1980). A study on aerodynamic time history response characteristics of bridge cross sections due to gust. *DPRI Annuals*, 23, 29 – 41.
- Simpson, A., Rowe, J., Weaver Smith, S. & Jacob, J. (2007, 23– 26 April). Aeroelastic deformation and buckling of inflatable wings under dynamic loads. In *The 48th structures, structural dynamics, and materials conference*. Honolulu, Hawaii: AIAA.
- Software, M. (n.d.). *Msc adams*. Available from <http://www.mssoftware.com/Products/CAE-Tools/Adams.aspx>
- Spierenburg, G. J. (2005). *Continued development and experimental validation of a kite design and simulation tool* (MSc Thesis). Delft, the Netherlands: Delft University of Technology.
- Stein, M. & Hedgepeth, J. M. (1961). *Analysis of partly wrinkled membranes* (Tech. Rep. No. TN D-813). USA: NASA.
- Stevenson, A., Alexander, K. & Lynn, P. (2005). performance testing by flying in a circle. *The aeronautical journal*.
- Stockholm Sweden, K. R. institute of Technology in & Bristol, U. of. (2008). *Tornado vortex lattice method*. <http://www.redhammer.se/tornado/>.

- Struck, B. (2001). *Static geometry optimization of an undeformable kite*. Delft, the Netherlands: Delft University of Technology.
- Sweeney, T. (1961). *Exploratory sail wing research at princeton* (Tech. Rep. No. 578). USA: Princeton University.
- Synergy, R. P. (1994). *Kiting to record altitudes*. Canada: Fly Write Publications.
- Taylor, J. W. R. (n.d.). *A picture history of flight*. London: Purnell and Sons Ltd.
- Taylor, J. W. R. & Munson, K. (n.d.). *History of aviation*. London: New English Library.
- Terink, E. (2009). *Kiteplane flight dynamics* (MSc Thesis). Delft, the Netherlands: Delft University of Technology.
- Terink, E., Breukels, J., Schmehl, R. & Ockels, W. J. (2010). Flight dynamics and stability of a tethered inflatable kiteplane. *AIAA Journal of Aircraft* (accepted for publication).
- Thwaites, B. (1961). The aerodynamic theory of sails, i, two dimensional sails. In *Proceedings of the royal society* (p. 402-422). London, UK: the Royal Society.
- Torenbeek, E. (1982). *Synthesis of subsonic airplane design*. Delft, the Netherlands: Delft University of Technology.
- Török, J. S. (2000). *Analytical Mechanics*. Toronto, Canada: John Wiley & Sons, Inc.
- Vegt, A. K. van der. (1994). *Polymeren, van keten tot kunststof*. Delft, the Netherlands: Delftse Uitgevers Maatschappij.
- Veldman, S. L. (2005a). *Design and analysis methodologies for inflated beams*. Unpublished doctoral dissertation, Delft University of Technology.
- Veldman, S. L. (2005b). Wrinkling prediction of cylindrical and conical inflated beams under torsion and bending. *Thin-Walled Structures, Volume 43, Issue 3, Page 461*.
- Veldman, S. L. & Bergsma, O. K. (2002). Designing inflatable structures. In *Proceedings of the iass symposium on lightweight structures in civil engineering*. Warsaw, Poland: IASS.
- Veldman, S. L., Vermeeren, C. A. J. R. & Bergsma, O. K. (2002). Conceptual design of a high altitude kite. In *Proceedings of the 43rd aiaa/asme/asce/ahs/asc structures, structural dynamics, and materials conference*. Denver, CO, USA: AIAA.

- Veldman, S. L., Vermeeren, C. A. J. R. & Bergsma, O. K. (2003). Geometrical influences on the structural efficiency of an inflatable beam subjected to bending. In *Proceedings of the icamm conference januari 21st - 23rd 2003*. Durban, South Africa: CCSMS.
- Verheul, R. F., Breukels, J. & Ockels, W. J. (2009). Material selection and joining methods for the purpose of high-altitude inflatable kites. In *Proceedings of the 50th aiaa structures, structural dynamics and materials conference*. Palm springs, CA, USA: AIAA.
- Vlugt, R. van der. (2009). *Aero- and hydrodynamic performance analysis of a speed kiteboarder* (MSc Thesis). Delft, the Netherlands: Delft University of Technology.
- Wachter, A. de. (2008). *Deformation and aerodynamic performance of a ram-air wing* (MSc Thesis). Delft, the Netherlands: Delft University of Technology.
- Webber, J. P. H. (1982). Deflections of inflated cylindrical cantilever beams subjected to bending and torsion. *Aeronautical journal*, 306-312.
- Wielgosz, T. C. (2002). Deflections of inflatable fabric panels at high pressure. *Thin-walled structures*, 523-536.
- Williams, P., Lansdorp, B. & Ockels, W. J. (2007, 20– 23 August). Modeling and control of a kite on a variable length flexible inelastic tether. In *Aiaa modelling and simulation technologies conference and exhibit*. Hilton Head, South Carolina, USA: AIAA.
- Williams, P., Lansdorp, B. & Ockels, W. J. (2008). Optimal crosswind towing and power generation with tethered kites. *Journal of Guidance, Control and Dynamics*, 31(1), 81 – 93.
- Williams, P., Lansdorp, B., Ruitenkamp, R. & Ockels, W. J. (2008, 18– 21 August). Modeling, simulation, and testing of surf kites for power generation. In *Aiaa modelling and simulation technologies conference and exhibit*. Honolulu, Hawaii: AIAA.
- www.Airxpress.nl. (n.d.). *Onze vliegers*. Available from <http://www.airxpress.nl/Onsmateriaal/materiaal.htm>
- Yakup, A. V., Leont'ev, Y. A. & Silinskaya, E. G. (1978). Stress concentration in tube t-joints operating in the elastic region. *Strengths of materials journal*.
- Yen, J. Y. R., Chen, C. H. & Chung, S. C. (2009). Coupling behavior of wire ropes subjected to tensile impulses. *Journal of Engineering Mechanics*(8), 796-801.
- Zhang, J., Zhang, K., Grenfell, R. & Deakin, R. (2006). On the relativistic doppler effect for precise velocity determination using gps. *Journal Of Geodesy*, 80, 104-110.

---

## Kite system definitions

---

In this appendix the frames of reference will be defined. Conventional flight dynamics [Mulder et al., 2007] has defined a large array of frames of reference for aircrafts and other free flying objects. In this section we will define a set of reference frames which are specific to kites and will be used throughout this thesis.

### A.1 Frames of reference

This set of reference frames will bear a striking resemblance to the frames of reference used with conventional aircraft. The difference lies within the tether which connects the kite to the ground. This tether requires its own frame of reference. Figure A.1 shows the three basic frames of reference used.

The first frame of reference is the earth-fixed frame of reference ( $OX_EY_EZ_E$ ). It is a right-handed orthogonal axis system with its origin fixed to the earth. It is the same earth axis system used in conventional flight mechanics theory [Mulder et al., 2007].

The second frame of reference is the tether frame of reference ( $OX_tY_tZ_t$ ). This frame of reference is specific to kite applications. It is also a right-handed orthogonal axis system and its origin is connected to an arbitrary location on the tether. The  $X_t$  and  $Z_t$  axis are perpendicular to the local tether axis and the  $Z_t$  is parallel to that. In reality, a tether is able to flex and deform as a result of the forces that act on it. Therefore, for a deformable cable, the tether frame of reference has a different orientation for every location on the tether. For the purpose of this rigid body analysis, the kite is assumed to fly on a short tether, in the order of 100m. For a short tether like this, it can be assumed to be straight.

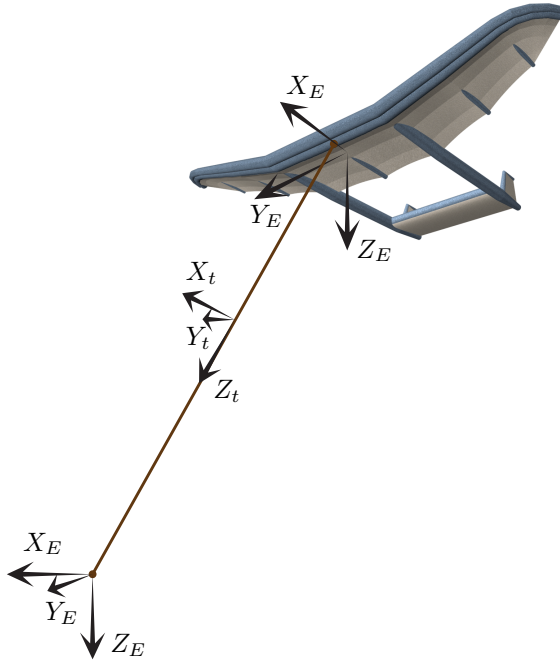


**Figure A.1:** *The three basic frames of reference for a kite.*

With this tether model, the tether frame of reference has the same orientation everywhere on the tether.

The third and last frame of reference is the body-fixed frame of reference ( $OX_B Y_B Z_B$ ). This frame of reference is also a right-handed orthogonal axis system and has its origin in the center of gravity of the kite. It is the same earth axis system used in conventional flight mechanics theory [Mulder et al., 2007] and points its  $X_B$  axis forward, its  $Y_B$  to the right and its  $Z_B$  downward with respect to the kite.

## A.2 Transformation from $E_E$ to $E_T$

The orientation of the one dimensional tether with respect to the earth axis frame of reference is defined by the two rotations  $\psi$  and  $\phi$ . The azimuth angle  $\psi$  is the angle between the wind vector and the tether projection on the surface plane. The direction of  $X_E$  is defined to coincide with the (average) wind direction (from which it originates). The zenith angle  $\phi$  is the angle between the vertical, the direction perpendicular to the surface plane, and the tether. From the rotations perspective, the tether initially coincides with  $Z_E$ . It is then rotated about this

axis with an angle  $\psi$  and subsequently rotated about  $Y_{E'}$  with an angle  $\phi$ . Figure A.2 shows the tether orientation angles.

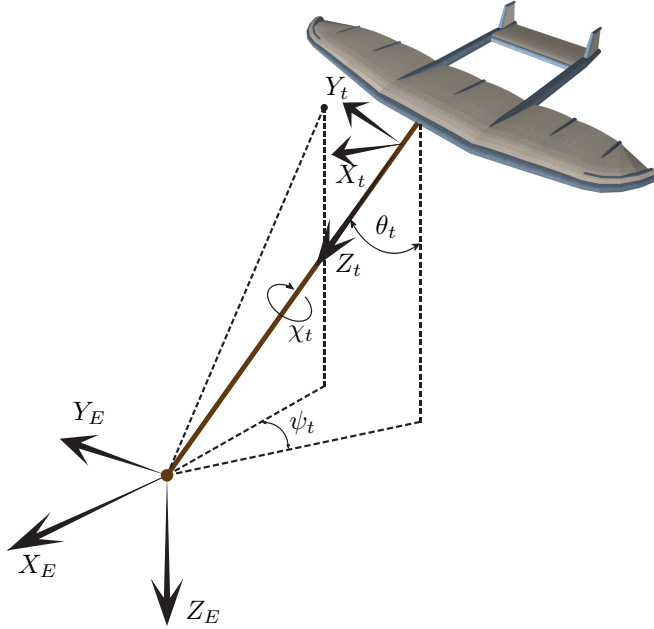


**Figure A.2:** Tether orientation angles.

The rotation matrices corresponding to these two rotations are given by equations A.1 and A.2 respectively.

$$\mathbb{T}_{E'E} = \begin{bmatrix} \cos(\psi_t) & \sin(\psi_t) & 0 \\ -\sin(\psi_t) & \cos(\psi_t) & 0 \\ 0 & 0 & 1 \end{bmatrix} \quad (\text{A.1})$$

$$\mathbb{T}_{E''E'} = \begin{bmatrix} \cos(\theta_t) & 0 & -\sin(\theta_t) \\ 0 & 1 & 0 \\ \sin(\theta_t) & 0 & \cos(\theta_t) \end{bmatrix} \quad (\text{A.2})$$

The rotation angle of the tether along its longitudinal axis is indicated with  $\chi$ . This angle gains significance once a bridle line system is included. Without a bridle, the tether is a one dimensional body. A bridle system will make it a two- or even three dimensional body, requiring an extra angle to orient it. The transformation from  $E_{E''}$  to  $E_T$  requires a single rotation about the  $Z_{E''}$ -axis with the angle  $\chi$ , the transformation matrix is given by equation (A.3).

$$\mathbb{T}_{tE''} = \begin{bmatrix} \cos(\chi_t) & \sin(\chi_t) & 0 \\ -\sin(\chi_t) & \cos(\chi_t) & 0 \\ 0 & 0 & 1 \end{bmatrix} \quad (\text{A.3})$$

The length of the tether, defined as the distance between the origin of reference frame  $E_E$  and the center of the line through the two bridle line attachment points, is again indicated by  $l_t$ .

### A.3 Transformation from $E_T$ to $E_B$

The transformation from the tether reference frame to the body axis reference frame is done by three sequential rotations:

- rotation  $\xi$ , body yaw angle w.r.t. the tether, about  $Z_t$ -axis
- rotation  $\kappa$ , body pitch angle w.r.t. the tether, about  $Y_{t'}$ -axis
- rotation  $\tau$ , body roll angle w.r.t. the tether, about  $X_B$ -axis

The rotation defines the following reference frames:

$$E_T \rightarrow E_{T'} \rightarrow E_{T''} \rightarrow E_B \quad (\text{A.4})$$

The transformation matrix for the rotation from  $E_T$  to  $E_B$  is given by:

$$\begin{aligned} \mathbb{T}_{Bt} &= \begin{bmatrix} 1 & 0 & 0 \\ 0 & \cos \tau & \sin \tau \\ 0 & -\sin \tau & \cos \tau \end{bmatrix} \begin{bmatrix} \cos \kappa & 0 & -\sin \kappa \\ 0 & 1 & 0 \\ \sin \kappa & 0 & \cos \kappa \end{bmatrix} \begin{bmatrix} \cos \xi & \sin \xi & 0 \\ -\sin \xi & \cos \xi & 0 \\ 0 & 0 & 1 \end{bmatrix} \\ &= \begin{bmatrix} \cos \kappa \cos \xi & \cos \kappa \sin \xi & -\sin \kappa \\ \begin{pmatrix} \sin \tau \sin \kappa \cos \xi \\ -\cos \tau \sin \xi \end{pmatrix} & \begin{pmatrix} \sin \tau \sin \kappa \sin \xi \\ +\cos \tau \cos \xi \end{pmatrix} & \sin \tau \cos \kappa \\ \begin{pmatrix} \cos \tau \sin \kappa \cos \xi \\ +\sin \tau \sin \xi \end{pmatrix} & \begin{pmatrix} \cos \tau \sin \kappa \sin \xi \\ -\sin \tau \cos \xi \end{pmatrix} & \cos \tau \cos \kappa \end{bmatrix} \quad (\text{A.5}) \end{aligned}$$

The angular velocity vector of the body-fixed reference frame  $F_b$  with respect to the tether-fixed reference frame  $F_t$  expressed in  $F_t$  using the rotational speed of the same rotations is given by:

$$\begin{aligned} \Omega_{bt}^b &= \mathbb{T}_{Bt'} \Omega_{t't}^{t'} + \mathbb{T}_{Bt''} \Omega_{t''t'}^{t''} + \Omega_{bt''}^b \\ &= \begin{bmatrix} \dot{\tau} - \dot{\xi} \sin \kappa \\ \dot{\kappa} \cos \tau + \dot{\xi} \sin \tau \cos \kappa \\ -\dot{\kappa} \sin \tau + \dot{\xi} \cos \tau \cos \kappa \end{bmatrix} \quad (\text{A.6}) \end{aligned}$$



Now the angular velocity of the body-fixed reference frame with respect to the earth-fixed reference frame can also be written as:

$$\boldsymbol{\Omega}_{BE}^B = \boldsymbol{\Omega}_{Bt}^B + \mathbb{T}_{Bt} \boldsymbol{\Omega}_{tE}^t \quad (\text{A.7})$$

and the transformation matrix from  $E_E$  to  $E_B$  can also be written as:

$$\mathbb{T}_{BE} = \mathbb{T}_{Bt} \mathbb{T}_{tE} \quad (\text{A.8})$$

The inverse of the transformations given in this section can be obtained by taking the inverse of the transformation matrices. Since all transformation matrices are orthogonal the inverse of the transformation matrices is equal to their transpose, i.e.  $\mathbb{T}^{-1} = \mathbb{T}^\top$ .

### **Transformation from $E_E$ to $E_B$ and derivation of $\boldsymbol{\Omega}_{BE}^B$**

In the aerospace industry the rotation sequence  $\psi \rightarrow \theta \rightarrow \phi$  is most commonly used for the rotation from  $E_E$  to  $E_b$ , where

- $\psi$  is the yaw angle, rotation about the  $Z_E$ -axis
- $\theta$  is the pitch angle, rotation about the  $Y_{E'}$ -axis
- $\phi$  is the roll angle, rotation about the  $X_B$ -axis ( $=X_{E''}$ -axis)

where the  $Y_{E'}$ -axis and  $X_{E''}$ -axis are the axes of the intermediate reference frame  $E_{E'}$  and  $E_{E''}$  respectively. The complete rotation defines the following reference frames:

$$E_E \rightarrow E_{E'} \rightarrow E_{E''} \rightarrow E_B \quad (\text{A.9})$$

The transformation matrix for the rotation from  $E_E$  to  $E_B$  is given by,

$$\begin{aligned}
\mathbb{T}_{BE} &= \mathbf{T}_{BE''} \mathbf{T}_{E''E'} \mathbf{T}_{E'E} \\
&= \begin{bmatrix} 1 & 0 & 0 \\ 0 & \cos \phi & \sin \phi \\ 0 & -\sin \phi & \cos \phi \end{bmatrix} \begin{bmatrix} \cos \theta & 0 & -\sin \theta \\ 0 & 1 & 0 \\ \sin \theta & 0 & \cos \theta \end{bmatrix} \begin{bmatrix} \cos \psi & \sin \psi & 0 \\ -\sin \psi & \cos \psi & 0 \\ 0 & 0 & 1 \end{bmatrix} \\
&= \begin{bmatrix} \cos \theta \cos \psi & \cos \theta \sin \psi & -\sin \theta \\ \begin{pmatrix} \sin \phi \sin \theta \cos \psi \\ -\cos \phi \sin \psi \end{pmatrix} & \begin{pmatrix} \sin \phi \sin \theta \sin \psi \\ +\cos \phi \cos \psi \end{pmatrix} & \sin \phi \cos \theta \\ \begin{pmatrix} \cos \phi \sin \theta \cos \psi \\ +\sin \phi \sin \psi \end{pmatrix} & \begin{pmatrix} \cos \phi \sin \theta \sin \psi \\ -\sin \phi \cos \psi \end{pmatrix} & \cos \phi \cos \theta \end{bmatrix} \quad (\text{A.10})
\end{aligned}$$

The angular velocity of the body-fixed reference frame  $E_b$  with respect to the normal earth-fixed reference frame  $E_E$  expressed in  $E_B$  is obtained using the rotational speed of the previous defined angles. This results in:

$$\boldsymbol{\Omega}_{BE}^B = \mathbb{T}_{BE'} \boldsymbol{\Omega}_{E'E}^{E'} + \mathbb{T}_{BE''} \boldsymbol{\Omega}_{E''E'}^{E''} + \boldsymbol{\Omega}_{BE''}^B = \begin{bmatrix} \dot{\phi} - \dot{\psi} \sin \theta \\ \dot{\theta} \cos \phi + \dot{\psi} \sin \phi \cos \theta \\ -\dot{\theta} \sin \phi + \dot{\psi} \cos \phi \cos \theta \end{bmatrix} \quad (\text{A.11})$$

---

## Bridle line model

---

This appendix gives the bridle line model used in the rigid body model of section 3.2. The bridle lines constrain the kite in a mix of roll ( $p$ ) and yaw ( $r$ ) motion depending on the body pitch angle with respect to the tether  $\kappa$ . See figures B.1, B.2 and B.3.

For simplicity of implementation the bridle lines are not explicitly modelled by two spring-dampers, but rather by a moment caused by the main tether force in  $Y_B$ -direction:  $G$ . The tether force in body components is shown in figure B.2.

When the tether has a tether force  $T$  and the tether is in the symmetric plane of the kite, that is  $\tau$  and  $\xi$  are zero, the vertical components of the forces in the bridle lines are equal to  $\frac{1}{2}T$ . Furthermore the tether force in  $Y_b$ -direction  $G$  is zero, so  $\frac{1}{2}T$  is equal to  $\frac{1}{2}\sqrt{F^2 + H^2}$ .

Two assumptions are made for modelling the forces in the bridle lines:

1. The forces act in the  $Y_tZ_t$ -plane or parallel to this plane
2. The bridle angle  $\vartheta$  is invariant

From the first assumption follows that the angle between the bridle line and the main line in the  $X_tZ_t$ -plane stays small. From the second assumption follows that the elastic elongation of the bridle lines stays small.

The absolute value of the tether forces in the bridle lines are given by the parameters  $T_L$  and  $T_R$  for the left and right bridle line respectively. The vertical components in the  $Y_tZ_t$ -plane are given by the parameters  $T_L^v$  and  $T_R^v$ . The horizontal components in the  $Y_tZ_t$ -plane are given by the parameters  $T_L^h$  and  $T_R^h$ . See figure B.1. Furthermore the bridle angle is specified by  $\vartheta$  as shown in figure

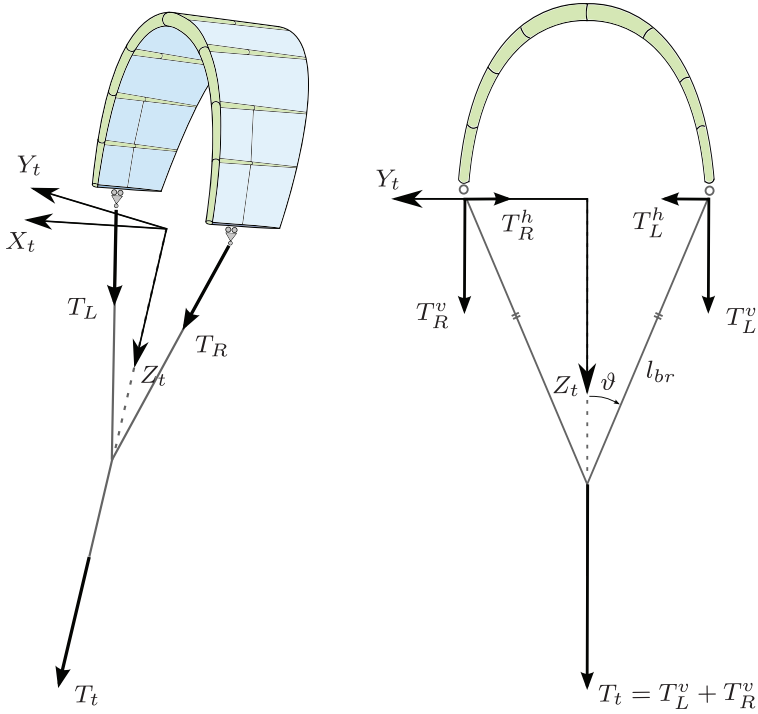


**Figure B.1:** Bridle line forces,  $G = 0$ .

B.1. The absolute value of the forces in the bridle lines can be written as:

$$\begin{aligned}
 T_L &= \sqrt{T_L^{v2} + T_L^{h2}} \\
 T_R &= \sqrt{T_R^{v2} + T_R^{h2}}
 \end{aligned}
 \tag{B.1}$$

Now when the tether force component  $G$  has a nonzero value the forces in the bridle lines will not be equal anymore. A moment acting in the  $X_t Z_t$ -plane will result to counteract this asymmetric condition.

This moment, given by  $\mathcal{M}_{bridle}$ , is simply equal to:

$$\mathcal{M}_{bridle} = -G \cdot l_{br} \cos \vartheta
 \tag{B.2}$$

where  $l_{br}$  is the length of one of the bridle lines. See figure B.3.

As this moment is actually caused by a difference in the bridle line forces, this moment is transferred by the bridle line forces  $T_L$  and  $T_R$  to the body. Only the change in the vertical components of the bridle lines will transfer this moment, as the horizontal components do not act about the arm  $l_{br}$ , because they act about

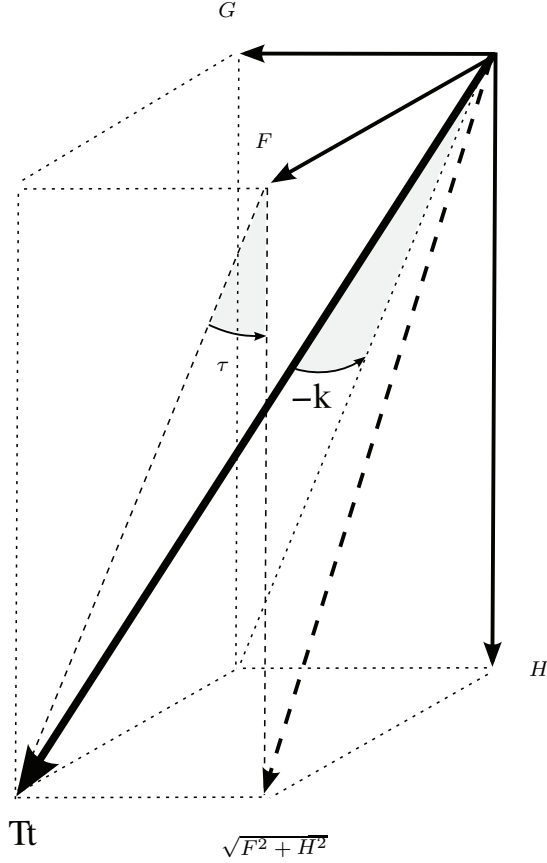


**Figure B.2:** Tether force  $T_t$  in body components  $F$ ,  $G$  and  $H$ .

$\langle x_{taL}, z_{taL} \rangle$  and  $\langle x_{taR}, z_{taR} \rangle$ . The change in the vertical components will cause a moment given by:

$$\mathcal{M}_{bridle} = (\Delta T_R^v - \Delta T_L^v) \cdot l_{br} \sin \vartheta$$

Because it is assumed that  $\vartheta$  is constant, it means that  $\Delta T_R^v$  is equal to  $-\Delta T_L^v$ . From this follows that:

$$\Delta T_L^v = -\Delta T_R^v = \frac{1}{2} \frac{\cos \vartheta}{\sin \vartheta} \cdot G = \frac{G}{2 \tan \vartheta}$$

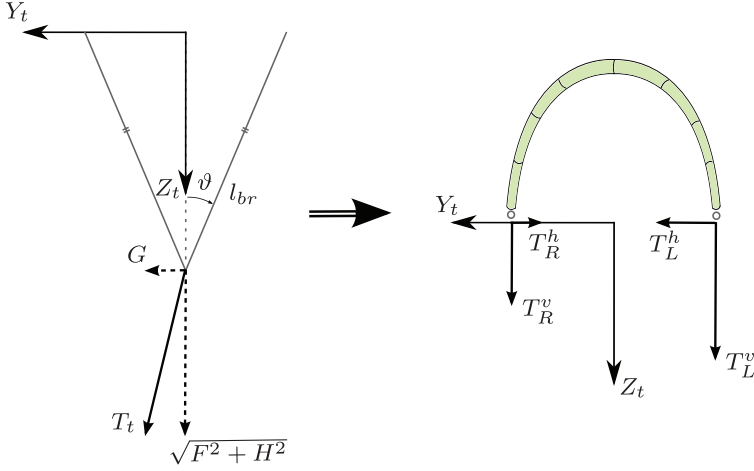


**Figure B.3:** Bridle line forces,  $G \neq 0$ .

Now the vertical components of the bridle forces are given by equations (B.3):

$$\begin{aligned}
 T_L^v &= \frac{1}{2}T_{G=0} + \Delta T_L^v \\
 &= \frac{1}{2} \left( \sqrt{F^2 + H^2} + \frac{G}{\tan \vartheta} \right) \\
 T_R^v &= \frac{1}{2}T_{G=0} + \Delta T_R^v \\
 &= \frac{1}{2} \left( \sqrt{F^2 + H^2} - \frac{G}{\tan \vartheta} \right)
 \end{aligned} \tag{B.3}$$

The horizontal components of the bridle  $T_L^h$  and  $T_R^h$  follow from force equilibrium and the fact that  $\vartheta$  is constant:

$$\begin{aligned}
 T_L^h &= T_{L,G=0}^h + \frac{1}{2}G \\
 &= \frac{1}{2}T_{G=0} \tan \vartheta + \frac{1}{2}G \\
 T_R^h &= T_{R,G=0}^h - \frac{1}{2}G \\
 &= \frac{1}{2}T_{G=0} \tan \vartheta - \frac{1}{2}G
 \end{aligned} \tag{B.4}$$

If the bridle line forces are given in components of the body-fixed reference frame  $\langle F_L, G_L, H_L \rangle$  and  $\langle F_R, G_R, H_R \rangle$  than the bridle line moments  $\mathcal{M}_{tL}$  and

$\mathcal{M}_{tR}$  are obtained by equations (B.5):

$$\begin{aligned}\mathcal{M}_{tL} &= \begin{bmatrix} P_L \\ Q_L \\ R_L \end{bmatrix} = \mathbf{r}_{taL} \times \begin{bmatrix} F_L \\ G_L \\ H_L \end{bmatrix} \\ \mathcal{M}_{tR} &= \begin{bmatrix} P_R \\ Q_R \\ R_R \end{bmatrix} = \mathbf{r}_{taR} \times \begin{bmatrix} F_R \\ G_R \\ H_R \end{bmatrix}\end{aligned}\tag{B.5}$$

where  $\mathbf{r}_{taL}$  and  $\mathbf{r}_{taR}$  are the left and right position vectors of the tether attachment point with respect to the center of gravity in the body-fixed reference frame. They are given by equations (B.6):

$$\begin{aligned}\mathbf{r}_{taL} &= \begin{bmatrix} x_{taL} \\ -l_{br} \sin \vartheta \\ z_{taL} \end{bmatrix} \\ \mathbf{r}_{taR} &= \begin{bmatrix} x_{taR} \\ l_{br} \sin \vartheta \\ z_{taR} \end{bmatrix}\end{aligned}\tag{B.6}$$

where it is assumed that  $y_{taL}$  is equal to  $-y_{taR}$  by the fact that  $\vartheta$  is invariable.

The total tether moment  $\mathcal{M}_t$  is obtained by adding the moments of the bridle lines  $\mathcal{M}_{t,L}$  and  $\mathcal{M}_{t,R}$ , so:

$$\mathcal{M}_t = \begin{bmatrix} P \\ Q \\ R \end{bmatrix} = \begin{bmatrix} P_L \\ Q_L \\ R_L \end{bmatrix} + \begin{bmatrix} P_R \\ Q_R \\ R_R \end{bmatrix}\tag{B.7}$$

Writing the bridle forces  $T_L$  and  $T_R$  in body components is done by:

$$\begin{aligned}\begin{bmatrix} F_L \\ G_L \\ H_L \end{bmatrix} &= \mathbf{e}_L^b \cdot T_L \\ \begin{bmatrix} F_R \\ G_R \\ H_R \end{bmatrix} &= \mathbf{e}_R^b \cdot T_R\end{aligned}\tag{B.8}$$

where  $\mathbf{e}_L^b$  and  $\mathbf{e}_R^b$  are the unit vectors of the left and right bridle line respectively.

The direction of the bridle lines are determined by the angles  $\kappa$  and  $\vartheta$  and their unit vectors are computed by:

$$\begin{aligned}\mathbf{e}_L^b &= \begin{bmatrix} -\sin \kappa \cos \vartheta \\ \sin \vartheta \\ \cos \kappa \cos \vartheta \end{bmatrix} \\ \mathbf{e}_R^b &= \begin{bmatrix} -\sin \kappa \cos \vartheta \\ -\sin \vartheta \\ \cos \kappa \cos \vartheta \end{bmatrix}\end{aligned}\tag{B.9}$$

where  $\kappa$  is a rotation about  $Y_{t'}$ -axis and is given by (see figure B.2):

$$\kappa = \arctan\left(-\frac{F}{\sqrt{G^2 + H^2}}\right) \quad \text{for} \quad -\frac{1}{2}\pi < \kappa < \frac{1}{2}\pi \quad (\text{B.10})$$

The body roll angle with respect to the tether  $\tau$  can be obtained by:

$$\tau = \arctan\left(\frac{G}{H}\right) \quad \text{for} \quad -\frac{1}{2}\pi < \kappa < \frac{1}{2}\pi \quad (\text{B.11})$$

$\tau$  is a rotation about  $X_b$ -axis. Since the tether force  $T_t$  is directed in the  $Z_t$ -axis, the body yaw angle with respect to the tether  $\xi$  has no influence on the body components of the tether force.



---

## Linearization of the symmetric equations of motion

---

This section outlines the linearization of the symmetric equations of motion of section 3.2 Figure C.1 shows a graphical representation of this system with the definition of the angles  $\kappa$ ,  $\theta_t$  and  $\theta$ .

### Accelerations

The linearized acceleration terms are given by:

$$\begin{aligned}
 F_x(\Delta \mathbf{X}) &= m \cdot \Delta \dot{u}_k \\
 F_z(\Delta \mathbf{X}) &= m \cdot \Delta \dot{w}_k \\
 \mathcal{M}_y(\Delta \mathbf{X}) &= I_y \cdot \Delta \dot{q}
 \end{aligned} \tag{C.1}$$

### Forces and moments

The forces and moments for the symmetric case are a function of:

$$\begin{aligned}
 W &\rightarrow f(\theta) \\
 X, Z, M &\rightarrow f(u_a, w_a, \dot{w}_a, q) \\
 F, H, Q &\rightarrow f(x_t a, l_t, \dot{l}_t, \kappa)
 \end{aligned}$$

where the left and right bridle attachment positions have been replaced by one parameter  $x_t a$ , because they move synchronously for the symmetric case.

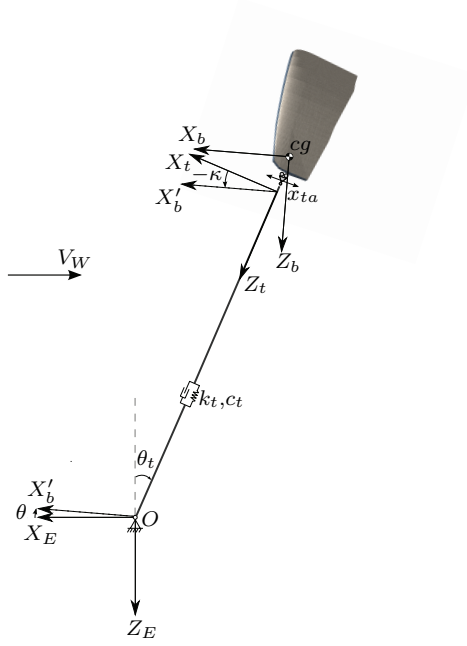


**Figure C.1:** *Symmetric state-space kite system.*

The linearized symmetric forces and moment become:

$$\begin{aligned}
 F_x(\Delta \mathbf{X}) &= -W \cos \theta_0 \cdot \Delta \theta + X_{u_a} \cdot \Delta u_a + X_{w_a} \cdot \Delta w_a + X_q \cdot \Delta q \\
 &\quad + F_{x_{ta}} \cdot \Delta x_{ta} + F_{l_t} \cdot \Delta l_t + F_{\dot{l}_t} \cdot \Delta \dot{l}_t + F_{\kappa} \cdot \Delta \kappa \\
 F_z(\Delta \mathbf{X}) &= -W \sin \theta_0 \cdot \Delta \theta + Z_{u_a} \cdot \Delta u_a + Z_{w_a} \cdot \Delta w_a + Z_{\dot{w}_a} \cdot \Delta \dot{w}_a + Z_q \cdot \Delta q \\
 &\quad + H_{x_{ta}} \cdot \Delta x_{ta} + H_{l_t} \cdot \Delta l_t + H_{\dot{l}_t} \cdot \Delta \dot{l}_t + H_{\kappa} \cdot \Delta \kappa \\
 M_y(\Delta \mathbf{X}) &= M_{u_a} \cdot \Delta u_a + M_{w_a} \cdot \Delta w_a + M_{\dot{w}_a} \cdot \Delta \dot{w}_a + M_q \cdot \Delta q \\
 &\quad + Q_{x_{ta}} \cdot \Delta x_{ta} + Q_{l_t} \cdot \Delta l_t + Q_{\dot{l}_t} \cdot \Delta \dot{l}_t + Q_{\kappa} \cdot \Delta \kappa
 \end{aligned} \tag{C.2}$$

The derivatives of the tether forces and moment are derived from the tether model.

### Tether forces and moments

Expressions for the tether forces and moments with respect to a change in  $\kappa$ ,  $l_t$ ,  $\dot{l}_t$  and  $\delta$  can be derived. The tether is modelled as a spring-damper given by the values  $k_t$  and  $c_t$  for the spring and damping constant respectively. The tether

force is given by, see equation 3.33:

$$T_t = k_t \cdot \delta l_t + c_t \cdot \dot{l}_t$$

where  $\delta l_t$  is the elastic elongation at  $t = 0$  s.

Writing this in the body axes by the transformation  $\mathbb{T}_{Bt}$  gives:

$$\begin{aligned} F &= -k_t \sin \kappa \cdot \delta l_t - c_t \sin \kappa \cdot \dot{l}_t \\ H &= k_t \cos \kappa \cdot \delta l_t + c_t \cos \kappa \cdot \dot{l}_t \end{aligned} \quad (\text{C.3})$$

These forces give the tether moment by:

$$Q = F \cdot z_{ta} - H \cdot x_{ta} \quad (\text{C.4})$$

Linearizing the previous expressions, (C.3) and (C.4), gives:

$$\begin{aligned} F(\mathbf{X}_0) &= -k_t \sin \kappa_0 \cdot \delta l_{t0} - c_t \sin \kappa_0 \cdot \dot{l}_{t0} \\ H(\mathbf{X}_0) &= k_t \cos \kappa_0 \cdot \delta l_{t0} + c_t \cos \kappa_0 \cdot \dot{l}_{t0} \\ Q(\mathbf{X}_0) &= F_0 \cdot z_{ta} - H_0 \cdot x_{ta0} \end{aligned} \quad (\text{C.5})$$

and

$$\begin{aligned} F(\Delta \mathbf{X}) &= -H_0 \cdot \Delta \kappa - k_t \sin \kappa_0 \cdot \Delta l_t - c_t \sin \kappa_0 \cdot \Delta \dot{l}_t \\ H(\Delta \mathbf{X}) &= F_0 \cdot \Delta \kappa + k_t \cos \kappa_0 \cdot \Delta l_t + c_t \cos \kappa_0 \cdot \Delta \dot{l}_t \\ Q(\Delta \mathbf{X}) &= z_{ta} F_\kappa \cdot \Delta \kappa - z_{ta} k_t \sin \kappa_0 \cdot \Delta l_t \\ &\quad - z_{ta} c_t \sin \kappa_0 \cdot \Delta \dot{l}_t - x_{ta0} H_\kappa \cdot \Delta \kappa \\ &\quad - x_{ta0} k_t \cos \kappa_0 \cdot \Delta l_t - x_{ta0} c_t \cos \kappa_0 \cdot \Delta \dot{l}_t \\ &\quad - H_0 \cdot \Delta x_{ta} \end{aligned} \quad (\text{C.6})$$

where  $F_\kappa = -H_0$  and  $H_\kappa = F_0$ .

### Kinematic relations

Applying the initial conditions to the body related kinematic relations yields:

$$\dot{\theta}(\Delta \mathbf{X}) = \Delta q \quad (\text{C.7})$$

The linearization of the first of the kinematic relations of the tether, equation (3.21), is done by first writing equation (3.21) as a function of the symmetric

parameters.

$$\begin{aligned}
\begin{bmatrix} \dot{x}_t^t \\ \dot{y}_t^t \\ \dot{z}_t^t \end{bmatrix} &= \mathbb{T}_{tB} \left( \begin{bmatrix} u_k^b \\ v_k^b \\ w_k^b \end{bmatrix} + \boldsymbol{\Omega}_{bE}^b \times \mathbf{r}_{ta}^b \right) \\
&= \mathbb{T}_{tB} \left( \begin{bmatrix} \dot{x}_k^b \\ 0 \\ \dot{z}_k^b \end{bmatrix} + \begin{bmatrix} q \cdot z_{ta} \\ 0 \\ -q \cdot x_{ta} \end{bmatrix} \right) \\
&= \mathbb{T}_{Bt}^\top \begin{bmatrix} u_t^b \\ 0 \\ w_t^b \end{bmatrix} \\
&= \begin{bmatrix} \cos \kappa \cdot \dot{x}_t^b + \sin \kappa \cdot \dot{z}_t^b \\ 0 \\ -\sin \kappa \cdot \dot{x}_t^b + \cos \kappa \cdot \dot{z}_t^b \end{bmatrix}
\end{aligned}$$

This gives:

$$\begin{aligned}
\dot{x}_t^t &= \cos \kappa (u_k + q \cdot z_{ta}) + \sin \kappa (w_k - q \cdot x_{ta}) \\
\dot{z}_t^t &= -\sin \kappa (u_k + q \cdot z_{ta}) + \cos \kappa (w_k - q \cdot x_{ta})
\end{aligned}$$

Linearizing this equation gives for  $\mathbf{X}_0$  and  $\Delta \mathbf{X}$ :

$$\begin{aligned}
\dot{x}_t^t(\mathbf{X}_0) &= \cos \kappa_0 (u_{k0} + q_0 \cdot z_{ta}) + \sin \kappa_0 (w_{k0} - q_0 \cdot x_{ta0}) \\
\dot{z}_t^t(\mathbf{X}_0) &= -\sin \kappa_0 (u_{k0} + q_0 \cdot z_{ta}) + \cos \kappa_0 (w_{k0} - q_0 \cdot x_{ta0})
\end{aligned} \tag{C.8}$$

$$\begin{aligned}
\dot{x}_t^t(\Delta \mathbf{X}) &= \cos \kappa_0 \cdot \Delta u_k + z_{ta} \cos \kappa_0 \cdot \Delta q \\
&\quad + \sin \kappa_0 \cdot \Delta w_k - x_{ta0} \sin \kappa_0 \cdot \Delta q \\
\dot{z}_t^t(\Delta \mathbf{X}) &= -\sin \kappa_0 \cdot \Delta u_k - z_{ta} \sin \kappa_0 \cdot \Delta q \\
&\quad + \cos \kappa_0 \cdot \Delta w_k - x_{ta0} \cos \kappa_0 \cdot \Delta q
\end{aligned} \tag{C.9}$$

where the initial condition has been applied and  $z_{ta}$  is assumed constant as defined in section 3.2.3

Linearization after applying the initial conditions to the second tether kinematic relation (3.22) yields:

$$\begin{aligned}
\dot{l}_t(\Delta \mathbf{X}) &= -\Delta \dot{z}_t^t \\
\dot{\theta}_t(\Delta \mathbf{X}) &= -\frac{1}{l_{t0}} \Delta \dot{x}_t^t
\end{aligned} \tag{C.10}$$

From relations (A.6) and (A.7) one can obtain a relation between the rotational velocities of the body and the tether, which is used to remove the state  $\kappa$  and to be replaced by  $\theta$  and  $\theta_t$ . Linearization for the symmetric case with the initial conditions gives:

$$q(\Delta \mathbf{X}) = \Delta \dot{\kappa} + \Delta \dot{\theta}_t \tag{C.11}$$

## Wind kinematics

Applying the initial conditions to the wind kinematic relations (3.29) yields:

$$\begin{aligned}u_a^b &= u_k^b + W_x \cos \theta \\w_a^b &= w_k^b + W_x \sin \theta\end{aligned}\tag{C.12}$$

Applying linearization on equation (C.12) results in:

$$\begin{aligned}u_a(\mathbf{X}_0) &= u_{k,0} + W_{x0} \cos \theta_0 \\w_a(\mathbf{X}_0) &= w_{k,0} + W_{x0} \sin \theta_0\end{aligned}\tag{C.13}$$

and

$$\begin{aligned}u_a(\Delta \mathbf{X}) &= \Delta u_k + \cos \theta_0 \cdot \Delta W_x - W_{x0} \sin \theta_0 \cdot \Delta \theta \\w_a(\Delta \mathbf{X}) &= \Delta w_k + \sin \theta_0 \cdot \Delta W_x + W_{x0} \cos \theta_0 \cdot \Delta \theta\end{aligned}\tag{C.14}$$

Furthermore for the linearization of the wind acceleration, equation (3.30), holds:

$$\begin{aligned}\dot{u}_a^b(\mathbf{X}_0) &= \dot{u}_{k,0} - q_0 \sin \theta_0 W_{x,0} \\ \dot{w}_a^b(\mathbf{X}_0) &= \dot{w}_{k,0} + q_0 \cos \theta_0 W_{x,0}\end{aligned}\tag{C.15}$$

and

$$\begin{aligned}\dot{u}_a^b(\Delta \mathbf{X}) &= \Delta \dot{u}_k - W_{x0} \sin \theta_0 \Delta q \\ \dot{w}_a^b(\Delta \mathbf{X}) &= \Delta \dot{w}_k + W_{x0} \cos \theta_0 \Delta q\end{aligned}\tag{C.16}$$

Where  $\dot{u}_{k,0} = \dot{w}_{k,0} = q_0 = 0$  as stated by the initial conditions of section 3.2.5.



## APPENDIX D

---

### Linearization of the asymmetric equations of motion

---

The linearized equations of motion for the asymmetric case are [Groot, 2010]

$$\begin{aligned} F_y(\Delta \mathbf{X}) &= m \cdot \Delta \dot{v}_k \\ \mathcal{M}_x(\Delta \mathbf{X}) &= I_x \cdot \Delta \dot{p} - J_{xz} \cdot \Delta \dot{r} \\ \mathcal{M}_z(\Delta \mathbf{X}) &= I_z \cdot \Delta \dot{r} - J_{xz} \cdot \Delta \dot{p} \end{aligned} \tag{D.1}$$

#### Forces and moments

The forces and moments for the asymmetric case are a function of:

$$\begin{aligned} W &\rightarrow f(\phi) \\ Y, L, N &\rightarrow f(v_a, \dot{v}_a, p, r) \\ G, P, R &\rightarrow f(x_{ta}^L, x_{ta}^R, \tau) \end{aligned}$$

where  $x_{ta}^L$  and  $x_{ta}^R$  are the displacements of the left and right bridle attachment points to the kite. The linearized asymmetric forces and moments become [Groot,

2010]:

$$\begin{aligned}
F_y(\Delta \mathbf{X}) &= W \cos \theta_0 \cdot \Delta \phi \\
&\quad + Y_{v_a} \cdot \Delta v_a + Y_{\dot{v}_a} \cdot \Delta \dot{v}_a + Y_p \cdot \Delta p + Y_r \cdot \Delta r \\
&\quad + G_{x_{taL}} \cdot \Delta x_{taL} + G_{x_{taR}} \cdot \Delta x_{taR} + G_\tau \cdot \Delta \tau \\
\mathcal{M}_x(\Delta \mathbf{X}) &= L_{v_a} \cdot \Delta v_a + L_p \cdot \Delta p + L_r \cdot \Delta r \\
&\quad + P_{x_{taL}} \cdot \Delta x_{taL} + P_{x_{taR}} \cdot \Delta x_{taR} + P_\tau \cdot \Delta \tau \\
\mathcal{M}_z(\Delta \mathbf{X}) &= N_{v_a} \cdot \Delta v_a + N_{\dot{v}_a} \cdot \Delta \dot{v}_a + N_p \cdot \Delta p + N_r \cdot \Delta r \\
&\quad + R_{x_{taL}} \cdot \Delta x_{taL} + R_{x_{taR}} \cdot \Delta x_{taR} + R_\tau \cdot \Delta \tau
\end{aligned} \tag{D.2}$$

### Tether forces and moments

Expressions for derivatives of the tether forces and moments can be found by linearizing the equations for the bridle lines given in appendix B. The tether unit vector  $\mathbf{e}_t$  expressed in the body-fixed reference frame is defined by three angles  $\tau$ ,  $\kappa$  and  $\xi$  as defined by the transformation from  $F_t$  to  $F_b$ . The transformation of the tether force in the tether-fixed reference frame to the body-fixed reference frame is given by:

$$\begin{aligned}
\mathbf{T}^b &= \mathbb{T}_{Bt} \mathbf{T}^t \\
\begin{bmatrix} F \\ G \\ H \end{bmatrix} &= \mathbb{T}_{Bt} \begin{bmatrix} 0 \\ 0 \\ T_t \end{bmatrix} \\
\begin{bmatrix} F \\ G \\ H \end{bmatrix} &= T_t \begin{bmatrix} -\sin \kappa \\ \sin \tau \cos \kappa \\ \cos \tau \cos \kappa \end{bmatrix}
\end{aligned} \tag{D.3}$$

From equation (D.3) can be obtained by applying the initial conditions  $\tau_0 = 0$  and  $\kappa_0 \neq 0$ :

$$\begin{aligned}
\Delta F &= -\sin \kappa_0 \cdot \Delta T_t - T_{t0} \cos \kappa_0 \cdot \Delta \kappa \\
\Delta G &= T_{t0} \cos \kappa_0 \cdot \Delta \tau \\
\Delta H &= \cos \kappa_0 \cdot \Delta T_t - T_{t0} \sin \kappa_0 \cdot \Delta \kappa
\end{aligned} \tag{D.4}$$

Since  $T_t$  and  $\kappa$  are symmetric quantities  $\Delta T_t$  and  $\Delta \kappa$  are zero for the asymmetric motions, so only  $\Delta G$  is not zero.

Linearizing equations (B.8) the derivative of the bridle force components in body-fixed reference is obtained:

$$\begin{aligned}
F_L(\Delta \mathbf{X}) &= -\sin \kappa_0 \cos \vartheta \cdot \Delta T_L & F_R(\Delta \mathbf{X}) &= -\sin \kappa_0 \cos \vartheta \cdot \Delta T_R \\
G_L(\Delta \mathbf{X}) &= \sin \vartheta \cdot \Delta T_L & G_R(\Delta \mathbf{X}) &= -\sin \vartheta \cdot \Delta T_R \\
H_L(\Delta \mathbf{X}) &= \cos \kappa_0 \cos \vartheta \cdot \Delta T_L & H_R(\Delta \mathbf{X}) &= \cos \kappa_0 \cos \vartheta \cdot \Delta T_R
\end{aligned}$$



(D.5)

Linearizing the equations for  $T_L$  and  $T_R$  gives:

$$\begin{aligned} T_L(\Delta \mathbf{X}) &= \frac{T_{br0}^v}{\sqrt{T_{br0}^{v2} + T_{br0}^{h2}}} \cdot \Delta T_L^v + \frac{T_{br0}^h}{\sqrt{T_{br0}^{v2} + T_{br0}^{h2}}} \cdot \Delta T_L^h \\ T_R(\Delta \mathbf{X}) &= \frac{T_{br0}^v}{\sqrt{T_{br0}^{v2} + T_{br0}^{h2}}} \cdot \Delta T_R^v + \frac{T_{br0}^h}{\sqrt{T_{br0}^{v2} + T_{br0}^{h2}}} \cdot \Delta T_R^h \end{aligned} \quad (\text{D.6})$$

where  $br$  stands for the left and right bridle line and where is used that  $T_{L0}^v = T_{R0}^v = T_{br0}^v$  and  $T_{L0}^h = T_{R0}^h = T_{br0}^h$  for the initial condition where  $G$  is zero.

Linearizing the vertical and horizontal components of  $T_L$  and  $T_R$  gives:

$$\begin{aligned} T_L^v(\Delta \mathbf{X}) &= \frac{1}{2 \tan \vartheta} \cdot \Delta G & T_R^v(\Delta \mathbf{X}) &= -\frac{1}{2 \tan \vartheta} \cdot \Delta G \\ T_L^h(\Delta \mathbf{X}) &= \frac{1}{2} \cdot \Delta G & T_R^h(\Delta \mathbf{X}) &= -\frac{1}{2} \cdot \Delta G \end{aligned} \quad (\text{D.7})$$

Linearizing equations (B.5) for the asymmetric left and right bridle moments  $P_L$ ,  $P_R$ ,  $R_L$  and  $R_R$  results in:

$$\begin{aligned} P_L(\Delta \mathbf{X}) &= y_{taL} \cdot \Delta H_L - z_{taL} \cdot \Delta G_L \\ P_R(\Delta \mathbf{X}) &= y_{taR} \cdot \Delta H_R - z_{taR} \cdot \Delta G_R \\ R_L(\Delta \mathbf{X}) &= x_{taL0} \cdot \Delta G_L + G_{L0} \cdot \Delta x_{taL} - y_{taL} \cdot \Delta F_L \\ R_R(\Delta \mathbf{X}) &= x_{taR0} \cdot \Delta G_R + G_{R0} \cdot \Delta x_{taR} - y_{taR} \cdot \Delta F_R \end{aligned} \quad (\text{D.8})$$

Finally the resulting moments on the body  $P$  and  $R$  are than given by:

$$\begin{aligned} P(\Delta \mathbf{X}) &= \Delta P_L + \Delta P_R \\ R(\Delta \mathbf{X}) &= \Delta R_L + \Delta R_R \end{aligned} \quad (\text{D.9})$$

Finally condensing the previously obtained equations will give the first derivatives of  $G$ ,  $P$  and  $R$  as a function of  $\tau$ ,  $x_{taL}$  and  $x_{taR}$ :

$$\begin{aligned} G_\tau &= T_{t0} \cos \kappa_0 \\ P_\tau &= -\frac{z_{ta} \sin \vartheta \cos \kappa_0 \sqrt{T_{t0}^2 (1 + \tan^2 \vartheta)}}{\tan \vartheta} + \frac{y_{taL} \cos \vartheta \cos^2 \kappa_0 \sqrt{T_{t0}^2 (1 + \tan^2 \vartheta)}}{\tan \vartheta} \\ R_\tau &= \frac{y_{taL} \cos \vartheta \sin \kappa_0 \cos \kappa_0 \sqrt{T_{t0}^2 (1 + \tan^2 \vartheta)}}{\tan \vartheta} + \frac{x_{ta0} \sin \vartheta \cos \kappa_0 \sqrt{T_{t0}^2 (1 + \tan^2 \vartheta)}}{\tan \vartheta} \end{aligned} \quad (\text{D.10})$$

where the fact is used that  $y_{taL} = -y_{taR}$  and  $z_{taL} = z_{taR} = z_{ta}$ .

## Kinematic relations

Applying the initial conditions to the body related kinematic relations [Mulder et al., 2007] yields:

$$\begin{aligned}\dot{\phi}(\Delta \mathbf{X}) &= \Delta p + \tan \theta_0 \cdot \Delta r \\ \dot{\psi}(\Delta \mathbf{X}) &= \frac{1}{\cos \theta_0} \cdot \Delta r\end{aligned}\tag{D.11}$$

The kinematic relations relating to the tether, equations (3.21) for the asymmetric motion are linearized as follows.

Equation (3.21) is written as a function of only the asymmetric degree of freedom,  $\dot{y}_t^t$ :

$$\begin{aligned}\begin{bmatrix} \dot{x}_t^t \\ \dot{y}_t^t \\ \dot{z}_t^t \end{bmatrix} &= \mathbb{T}_{tB} \left( \begin{bmatrix} u_k^b \\ v_k^b \\ w_k^b \end{bmatrix} + \boldsymbol{\Omega}_{bE}^b \times \mathbf{r}_{ta}^b \right) \\ &= \mathbb{T}_{tB} \left( \begin{bmatrix} 0 \\ v_k \\ 0 \end{bmatrix} + \begin{bmatrix} 0 \\ r \cdot x_{ta} - p \cdot z_{ta} \\ 0 \end{bmatrix} \right) \\ &= \mathbb{T}_{Bt}^\top \begin{bmatrix} 0 \\ \dot{y}_t^b \\ 0 \end{bmatrix} \\ &= \begin{bmatrix} 0 \\ \cos \tau \cdot \dot{y}_t^b \\ 0 \end{bmatrix}\end{aligned}$$

This gives:

$$\dot{y}_t^t = \cos \tau \cdot (v_k + r \cdot x_{ta} - p \cdot z_{ta})$$

Linearizing this equation gives for  $\mathbf{X}_0$  and  $\Delta \mathbf{X}$ :

$$\dot{y}_t^t(\mathbf{X}_0) = -p_0 \cdot z_{ta} + r_0 \cdot x_{ta0}\tag{D.12}$$

where  $x_{ta0}$  is the initial cart position and  $z_{ta}$  is invariant.

$$\dot{y}_t^t(\Delta \mathbf{X}) = \Delta v_k - z_{ta} \cdot \Delta p + x_{ta0} \cdot \Delta r\tag{D.13}$$

The linearization of the second of the kinematic relations relating to the tether, equation (3.21), for the asymmetric variable results in:

$$\dot{\psi}_t(\Delta \mathbf{X}) = -\frac{1}{l_{t0} \sin \theta_{t0}} \Delta \dot{y}_t^t\tag{D.14}$$

Taking equations (D.13) and (D.14) together results in:

$$\Delta \dot{\psi}_t = -\frac{1}{l_{t0} \sin \theta_{t0}} \cdot \Delta v_k + \frac{z_{ta}}{l_{t0} \sin \theta_{t0}} \cdot \Delta p - \frac{x_{ta0}}{l_{t0} \sin \theta_{t0}} \cdot \Delta r\tag{D.15}$$

Another equation can be obtained from the kinematic relation (A.6) for a relation between the rotational velocities of the body and the tether, which is used to remove the state  $\tau$  and to be replaced by  $\theta$  and  $\theta_t$ . The asymmetric body rotations  $p$  and  $r$  are given by:

$$\begin{aligned} p &= \dot{\tau} - \dot{\xi} \cdot \sin \kappa - \dot{\psi}_t \cdot (\sin \theta_t \cos \kappa \cos \xi + \cos \theta_t \sin \kappa) \\ r &= -\dot{\kappa} \cdot \sin \tau + \dot{\xi} \cdot \cos \tau \cos \kappa - \dot{\psi}_t \cdot \sin \theta_t (\cos \tau \sin \kappa \cos \xi + \sin \tau \sin \xi) \\ &\quad + \dot{\psi}_t \cos \theta_t \cos \tau \cos \kappa \end{aligned} \quad (\text{D.16})$$

Linearizing these equations with the initial condition gives for  $\Delta \mathbf{X}$ :

$$\begin{aligned} p(\Delta \mathbf{X}) &= \Delta \dot{\tau} - \sin \kappa_0 \cdot \Delta \dot{\xi} - (\sin \theta_{t0} \cos \kappa_0 + \cos \theta_{t0} \sin \kappa_0) \cdot \Delta \dot{\psi}_t \\ r(\Delta \mathbf{X}) &= \cos \kappa_0 \cdot \Delta \dot{\xi} - (\sin \theta_{t0} \sin \kappa_0 - \cos \theta_{t0} \cos \kappa_0) \cdot \Delta \dot{\psi}_t \end{aligned} \quad (\text{D.17})$$

### Wind kinematics

The wind kinematics equation (3.29) can be written as:

$$\begin{aligned} \mathbf{V}_a^b &= \mathbf{V}_k^b + \mathbf{V}_w^b \\ \begin{bmatrix} u_a \\ v_a \\ w_a \end{bmatrix} &= \begin{bmatrix} u_k \\ v_k \\ w_k \end{bmatrix} + \mathbb{T}_{BE} \begin{bmatrix} W_x \\ W_y \\ 0 \end{bmatrix} \end{aligned} \quad (\text{D.18})$$

Evaluating the previous for  $v_a$  results in:

$$\begin{aligned} v_a &= v_k + (\sin \phi \sin \theta \cos \psi - \cos \phi \sin \psi) \cdot W_x \\ &\quad + (\sin \phi \sin \theta \sin \psi + \cos \phi \cos \psi) \cdot W_y \end{aligned} \quad (\text{D.19})$$

Linearization of (D.19) with the initial conditions gives:

$$v_a(\mathbf{X}_0) = 0 \quad (\text{D.20})$$

and

$$v_a(\Delta \mathbf{X}) = \Delta v_k + \Delta W_y + W_{x0} \sin \theta_0 \cdot \Delta \phi - W_{x0} \cdot \Delta \psi \quad (\text{D.21})$$

For the wind acceleration, equation (3.30), with the initial conditions holds:

$$\dot{v}_a(\Delta \mathbf{X}) = \Delta \dot{v}_k + W_{x0} \sin \theta_0 \cdot \Delta \dot{p} - W_{x0} \cdot \Delta \dot{r} \quad (\text{D.22})$$



---

## Asymmetric control authority using shifting tow points

---

Section 3.2.7 derives the linearized asymmetric equations of motion and writes them in dimensionless matrix notation. This derivation yields the coefficients  $C_{G_{x_{taL}}}$ ,  $C_{G_{x_{taR}}}$ ,  $C_{P_{x_{taL}}}$ ,  $C_{P_{x_{taR}}}$ ,  $C_{R_{x_{taL}}}$  and  $C_{R_{x_{taR}}}$ . These coefficients describe the control authority of the shifting tow point control system outlined in section 3.2. The discussion in this section focusses on these coefficients and their effect on the kite. The shifting tow point control system is a derivative from the conventional control system found on most surf kites (see figure 5.23). By pulling on the steering lines, the resultant force on the tip, consisting of the sum of the power and steering line on that tip, shifts aft. The tow point shifting control system introduced in section 3.2 replaces the power and steering line with a single line which is physically shifted along the surf kite tip. Figure E.1 shows a schematic representation of a kite with a sliding tow point control system.

In the analysis of this section, the following assumptions are made:

- $\lambda_L$  and  $\lambda_R$  are small
- Controls move anti-symmetric ( $x_{taL} = -x_{taR}$ )
- Controls move instantly

When the kite flies in its zenith position, as indicated by the initial conditions of section 3.2.5, the angle between the tether and the mean aerodynamic chord will be close to 90 degrees (in the  $X_B$ - $Z_B$  plane). In this situation we can also assume  $\lambda_L = -\lambda_R$ . For the position of the controls we can write:



Figure E.2 shows a schematic representation of the same kite, but from the front.

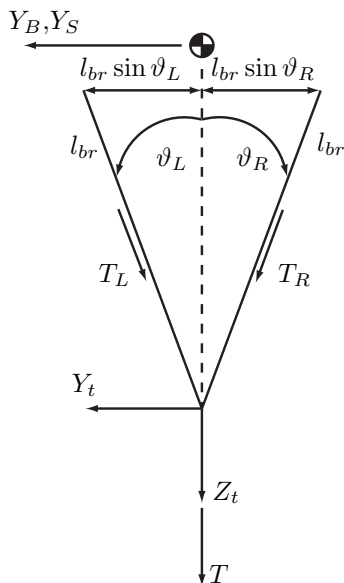


**Figure E.2:** A schematic representation of a kite with a towpoint sliding control mechanism (front view).

A new set of assumptions regarding figure E.2 are added to the previous assumptions:

- $\vartheta_L = -\vartheta_R$
- $\vartheta_L$  and  $\vartheta_R$  are assumed invariant
- $\vartheta_L$  and  $\vartheta_R$  are small

With these assumptions, it is now possible to state:

$$T_L = T_R = T_{br} \tag{E.5}$$

Which is an assumption in itself. It is deemed acceptable due to the fact that the bridle lines are generally long (in the order of 20-25 meters) and the displacement of the tow points is relatively small (in the order of 20cm). Of interest here is not so much the magnitude of the bridle line forces but the moments

they introduce when the tow points shift. For the bridle line forces  $\mathbf{T}_L$  and  $\mathbf{T}_R$  we can write:

$$\mathbf{T}_L^t = \begin{bmatrix} T_{xL} \\ T_{yL} \\ T_{zL} \end{bmatrix}^t = \begin{bmatrix} T_L \cos \vartheta_L \sin \lambda_L \\ T_L \sin \vartheta_L \\ T_L \cos \vartheta_L \cos \lambda_L \end{bmatrix}^t \quad (\text{E.6})$$

$$\mathbf{T}_R^t = \begin{bmatrix} T_{xR} \\ T_{yR} \\ T_{zR} \end{bmatrix}^t = \begin{bmatrix} T_R \cos \vartheta_R \sin \lambda_R \\ T_R \sin \vartheta_R \\ T_R \cos \vartheta_R \cos \lambda_R \end{bmatrix}^t \quad (\text{E.7})$$

We can transform the vectors of equations (E.6) and (E.7) from the tether axis system to the stability axis system:

$$\mathbf{T}_L^S = \mathbb{T}_{SB} \cdot \mathbb{T}_{Bt} \cdot \mathbf{T}_L^t \quad (\text{E.8})$$

$$\mathbf{T}_R^S = \mathbb{T}_{SB} \cdot \mathbb{T}_{Bt} \cdot \mathbf{T}_R^t \quad (\text{E.9})$$

The components of the bridle line forces are now expressed in the stability frame of reference. This is schematically represented in figure E.3

### Tether force component $G$ in $Y_S$ direction

For tether force component  $G$  we can write:

$$G = T_{yL}^S + T_{yR}^S = T_{yL}^B + T_{yR}^B \quad (\text{E.10})$$

Using the transformation matrices of appendix A, we can write:

$$\begin{aligned} G = & \mathbb{T}_{Bt}(1, 2) \cdot (\cos \vartheta_L \sin \lambda_L) \cdot T_{br} + \mathbb{T}_{Bt}(2, 2) \cdot \sin \vartheta_L \cdot T_{br} \\ & + \mathbb{T}_{Bt}(3, 2) \cdot (\cos \vartheta_L \cos \lambda_L) \cdot T_{br} + \mathbb{T}_{Bt}(1, 2) \cdot (\cos \vartheta_R \sin \lambda_R) \cdot T_{br} \\ & + \mathbb{T}_{Bt}(2, 2) \cdot \sin \vartheta_R \cdot T_{br} + \mathbb{T}_{Bt}(3, 2) \cdot (\cos \vartheta_R \cos \lambda_R) \cdot T_{br} \end{aligned} \quad (\text{E.11})$$

Because of the assumptions  $\vartheta_L = -\vartheta_R$  and  $\lambda_L = -\lambda_R$  we can rewrite equation (E.11):



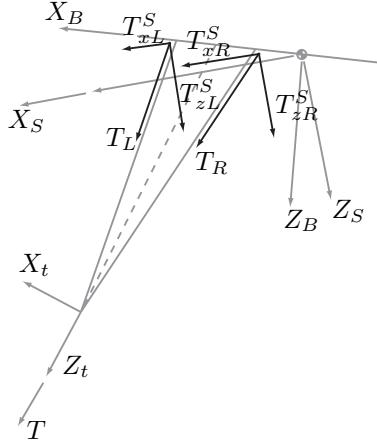


**Figure E.3:** A schematic representation of the bridle line forces in the stability frame of reference.

$$G = [(\sin \tau \cos \kappa) \cdot (\cos \vartheta_L \cos \lambda_L) + (\sin \tau \cos \kappa) \cdot (\cos \vartheta_R \cos \lambda_R)] \cdot T_{br} \quad (\text{E.12})$$

Due to the presence of the bridle lines, the body roll angle with regard to the tether  $\tau$  will most likely be very small. This means that the sine of this small angle will also be very small. As such, equation (E.12) leads to the conclusion that  $G$  will be small as well. And thus will have only a marginal effect on the control of the kite.

### Tether moment component $P$ around $X_S$

For the tether moment component  $P$  around  $X_S$  we can write:

$$\begin{aligned} P = & (x_{cg} - (x_{taL0} + \Delta x_{taL})) \cdot \sin \alpha_e \cdot T_{yL}^B \\ & + (x_{cg} - (x_{taR0} - \Delta x_{taR})) \cdot \sin \alpha_e \cdot T_{yR}^B \\ & + l_{br} \sin \vartheta_L \cdot T_{zL}^S + l_{br} \sin \vartheta_R \cdot T_{zR}^S \quad (\text{E.13}) \end{aligned}$$

With the assumptions  $\vartheta_L = -\vartheta_R$ ,  $\Delta x_{taL} = \Delta x_{taR}$ ,  $T_L = T_R$ ,  $x_{taL0} = x_{taR0}$ , and the rotation matrix:

$$\mathbb{T}_{SB} = \begin{bmatrix} \cos \alpha_e & 0 & -\sin \alpha_e \\ 0 & 1 & 0 \\ \sin \alpha_e & 0 & \cos \alpha_e \end{bmatrix} \quad (\text{E.14})$$

We can now write:

$$l_{br} \sin \vartheta_L \cdot T_{zL}^S + l_{br} \sin \vartheta_R \cdot T_{zR}^S = l_{br} \sin \vartheta_L (T_{zL}^S - T_{zR}^S) \quad (\text{E.15})$$

and:

$$\mathbf{T}_L^S - \mathbf{T}_R^S = \mathbb{T}_{SB} \cdot \mathbb{T}_{Bt} \cdot T_L \cdot \begin{bmatrix} \cos \vartheta_L \sin \lambda_L - \cos \vartheta_R \sin \lambda_R \\ \sin \vartheta_L - \sin \vartheta_R \\ \cos \vartheta_L \cos \lambda_L - \cos \vartheta_R \cos \lambda_R \end{bmatrix} \quad (\text{E.16})$$

Evaluation of the previous equations yields:

$$\begin{aligned} T_{zL}^S - T_{zR}^S = & \\ & [(\sin \alpha_e \cos \kappa \cos \chi + \cos \alpha_e (\cos \tau \sin \kappa \cos \chi + \sin \tau \sin \chi)) \\ & \cdot (\cos \vartheta_L \sin \lambda_L - \cos \vartheta_R \sin \lambda_R) \\ & + (\sin \alpha_e \cos \kappa \sin \chi + \cos \alpha_e (\cos \tau \sin \kappa \sin \chi - \sin \tau \cos \chi)) \\ & \cdot (\sin \vartheta_L - \sin \vartheta_R) \\ & + (-\sin \alpha_e \sin \kappa + \cos \alpha_e \cos \tau \cos \kappa) \\ & \cdot (\cos \vartheta_L \cos \lambda_L - \cos \vartheta_R \cos \lambda_R)] \cdot T_L \quad (\text{E.17}) \end{aligned}$$

With  $\vartheta_L = -\vartheta_R$  and  $\lambda_L = -\lambda_R$ :

$$\cos \vartheta_L \cos \lambda_L - \cos \vartheta_R \cos \lambda_R = 0 \quad (\text{E.18})$$

For the tether moment component  $P$  around  $X_S$  we can now write:

$$\begin{aligned}
P = & (x_{cg} - (x_{taL0} + \Delta x_{taL})) \cdot \sin \alpha_e \cdot T_{yL}^B \\
& + (x_{cg} - (x_{taR0} - \Delta x_{taR})) \cdot \sin \alpha_e \cdot T_{yR}^B \\
& + l_{br} \sin \vartheta_L [(\sin \alpha_e \cos \kappa \cos \chi + \cos \alpha_e (\cos \tau \sin \kappa \cos \chi + \sin \tau \sin \chi)) \\
& \cdot (\cos \vartheta_L \sin \lambda_L - \cos \vartheta_R \sin \lambda_R) \\
& + (\sin \alpha_e \cos \kappa \sin \chi + \cos \alpha_e (\cos \tau \sin \kappa \sin \chi - \sin \tau \cos \chi)) \\
& \cdot (\sin \vartheta_L - \sin \vartheta_R)] \cdot T_L \quad (\text{E.19})
\end{aligned}$$

In the previous subsection we have established that  $G$  is small. This means that  $T_{yL}^B + T_{yR}^B$  must also be small. Furthermore, considering that for the simulation presented in section 3.2 the initial position of the cable is in the center of gravity, the quantities  $(x_{cg} - (x_{taL0} + \Delta x_{taL}))$  and  $(x_{cg} - (x_{taR0} - \Delta x_{taR}))$  are of equal magnitude and opposed in sign. Coupled with the multiplication by the sine of the small angle  $\alpha_e$ , this results in the first half of equation (E.19) being small.

Furthermore, it was established earlier that  $\vartheta_L$  and  $\lambda_L$  are small angles. Therefore, the sine of these angles is also small. This renders the second part of equation (E.19) small as well. The conclusion is thus, that the contribution of  $P$  during an anti-symmetric control input is small, if not close to zero.

### Tether moment component $R$ around $Z_S$

For the tether moment component  $R$  around  $Z_S$  we can write:

$$\begin{aligned}
R = & (x_{cg} - (x_{taL0} + \Delta x_{taL})) \cdot \cos \alpha_e \cdot T_{yL}^B \\
& + (x_{cg} - (x_{taR0} - \Delta x_{taR})) \cdot \cos \alpha_e \cdot T_{yR}^B \\
& + l_{br} \sin \vartheta_L \cdot T_{xL}^S + l_{br} \sin \vartheta_R \cdot T_{xR}^S \quad (\text{E.20})
\end{aligned}$$

Analogue to the component  $P$ , we can write equations for  $T_{xL}^S - T_{xR}^S$ :

$$\begin{aligned}
T_{xL}^S - T_{xR}^S = & [(\cos \alpha_e \cos \kappa \cos \chi + \sin \alpha_e (\cos \tau \sin \kappa \cos \chi + \sin \tau \sin \chi)) \\
& \cdot (\cos \vartheta_L \sin \lambda_L - \cos \vartheta_R \sin \lambda_R)] \cdot T_L \\
& + [(\cos \alpha_e \cos \kappa \sin \chi - \sin \alpha_e (\cos \tau \sin \kappa \sin \chi - \sin \tau \cos \chi)) \\
& \cdot (\sin \vartheta_L - \sin \vartheta_R)] \cdot T_L \\
& + [(-\cos \alpha_e \sin \kappa - \sin \alpha_e \cos \tau \cos \kappa) \\
& \cdot (\cos \vartheta_L \cos \lambda_L - \cos \vartheta_R \cos \lambda_R)] \cdot T_L \quad (\text{E.21})
\end{aligned}$$

Which leads to the following expression for  $R$ :

$$\begin{aligned}
R = & (x_{cg} - (x_{taL0} + \Delta x_{taL})) \cdot \cos \alpha_e \cdot T_{yL}^B \\
& + (x_{cg} - (x_{taR0} - \Delta x_{taR})) \cdot \cos \alpha_e \cdot T_{yR}^B \\
& + l_{br} \sin \vartheta_L [(\cos \alpha_e \cos \kappa \cos \chi - \sin \alpha_e (\cos \tau \sin \kappa \cos \chi + \sin \tau \sin \chi)) \\
& \cdot (\cos \vartheta_L \sin \lambda_L - \cos \vartheta_R \sin \lambda_R) \\
& + (\cos \alpha_e \cos \kappa \sin \chi - \sin \alpha_e (\cos \tau \sin \kappa \sin \chi - \sin \tau \cos \chi)) \\
& \cdot (\sin \vartheta_L - \sin \vartheta_R)] \cdot T_L \quad (\text{E.22})
\end{aligned}$$

For the same reasons as in equation (E.19), the second half of equation (E.22) can be considered small. The difference with equation (E.19) is mostly in the first half where the terms are now multiplied by the cosine of the small angle  $\alpha_e$  instead of the sine. This leads to the conclusion that, for the initial conditions and the assumptions made in this appendix, the contribution of  $R$  as a result of an anti-symmetric control input will be small, but larger than the contributions of  $P$  and  $G$ .

These findings seem to agree with the findings of section 6.3.3 where a multi-body model of a rigid kite is simulated. The effects of a asymmetric control input result in a slight increase in yaw angle. No direct result of  $G$  and  $P$  are found. The yaw increase as a result of a changing  $R$  is only small compared to actual surf kites. Section 6.3.3 continues to state the role of flexibility on the yaw rate of such a kite.

---

## Comparison of rigid body models

---

Basic verification Of both the Newtonian and Lagrangian equations of motion is done by insertion of a proven aerodynamic model in order to find out if the equations and implementation of the generalized forces and aerodynamic states are correct. For this purpose, an aerodynamics model of the Cessna CE500 Citation is used. An accurate model for this aircraft is available Mulder et al. [2007], because this particular aircraft is partly owned by the faculty of Aerospace Engineering and used as a flying laboratory. In order to make this model suitable for flying as a kite, a small change needs to be made. The mass of the Citation is far to large to allow it to fly as a kite in conventional wind speeds. Therefore, the mass of the Citation was reduced by 96%. Since the stability derivatives are dimensionless, they remain the same for this adapted Citation model.

Further details on the aerodynamics model are interesting, but irrelevant since the purpose is to validate the models it is inserted to. For this purpose a comparison is made between two different simulation models using both the same aerodynamics model, the Newtonian model of section 3.2 and the Lagrangian model of 3.3. The two test cases that have been selected are:

- Symmetric motion disturbed by an elevator step input at  $t = 1$  s starting from equilibrium conditions
- Asymmetric motion disturbed by a constant wind gust of  $10 \text{ ms}^{-1}$  in  $Y_E$  direction

The results of the symmetric motion simulation are displayed in Fig. F.1. In general the results are similar, they converge to the same point and the overall

behavior is the same. The oscillation amplitude and damping however, are slightly different. Both models should produce exactly the same result, but the difference in method and implementation apparently causes minor differences. Nevertheless, the differences are small enough to provide additional confidence in both models.

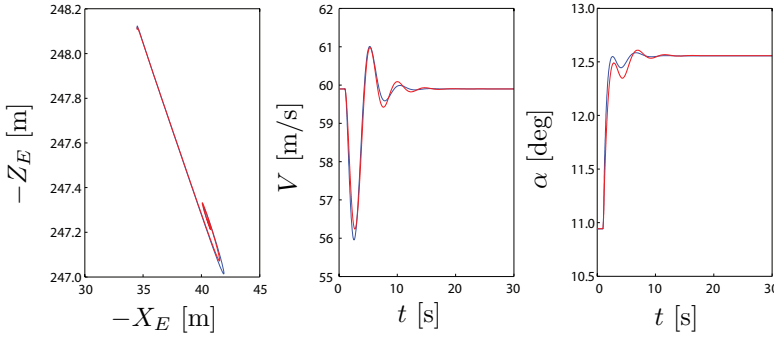


**Figure F.1:** *Symmetric motion comparison of the Lagrangian model — with the Newtonian model —.*

For the asymmetric motion simulation the results are displayed in Fig. F.2. As with the symmetric motion results, the general behavior of both models is similar, but there are differences as well. Due to the fact that the motion does not converge to an equilibrium state, the end point of the simulations is not the same in this case. The Lagrangian model is falling faster compared to the Newtonian model, which can be observed from Fig. F.2 by the lower  $-Z_E$  value for the black line. This is in accordance with the overall greater apparent velocity. The oscillation in the apparent velocity of the Lagrangian model is again of higher amplitude and damping compared to the Newtonian model. As for the asymmetric case, the differences in the results are small enough for a gain in confidence in the models.

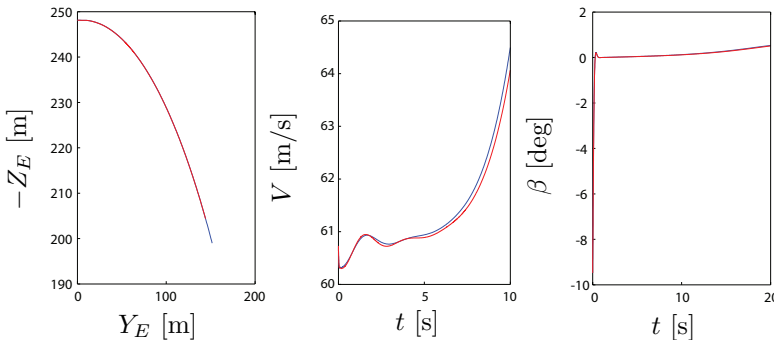


**Figure F.2:** *Asymmetric motion comparison of the Lagrangian model — with the Newtonian model —.*

# APPENDIX G

---

## Fitted constants

---

In this section, the numerical values are given of the coefficients which are used in the kite simulation toolbox. The numerical values of coefficients are obtained using a fitting procedure on experimental or numerical data.

### G.1 Inflated tube constants

This section contains the coefficients which govern the behavior of the inflatable tubes in the numerical model presented in chapter 4

**Table G.1:** *Coefficients which govern the behavior of the inflatable tubes.*

Component	Coefficient	Value	Coefficient	Value
Beam bending	$C_1$	6582.82	$C_5$	271865251.42
	$C_2$	-272.43	$C_6$	215.93
	$C_3$	40852.38	$C_7$	14021.79
	$C_4$	14.31	$C_8$	-589.05
Beam collapse	$C_9$	322.55	$C_{11}$	5.3833
	$C_{10}$	0.0239	$C_{12}$	0.0461
Beam torsion	$C_{13}$	1467	$C_{17}$	-17703
	$C_{14}$	40.908	$C_{18}$	358.05
	$C_{15}$	-191.8	$C_{19}$	0.0918
	$C_{16}$	47.406		

## G.2 Aerodynamic constants

This section contains the coefficients which govern the aerodynamic forces in the numerical model presented in chapter 4

**Table G.2:** *Coefficients which govern the behavior of the aerodynamic forces.*

Component	Coefficient	Value	Coefficient	Value
Lift	$C_{20}$	-0.008011	$C_{32}$	0
	$C_{21}$	-0.000336	$C_{33}$	0
	$C_{22}$	0.000992	$C_{34}$	0
	$C_{23}$	0.013936	$C_{35}$	-3.371000
	$C_{24}$	-0.003838	$C_{36}$	0.858039
	$C_{25}$	-0.000161	$C_{37}$	0.141600
	$C_{26}$	0.001243	$C_{38}$	7.201140
	$C_{27}$	-0.009288	$C_{39}$	-0.676007
	$C_{28}$	-0.002124	$C_{40}$	0.806629
	$C_{29}$	0.012267	$C_{41}$	0.170454
	$C_{30}$	-0.002398	$C_{42}$	-0.390563
Drag	$C_{31}$	-0.000274	$C_{43}$	0.101966
	$C_{44}$	0.546094	$C_{50}$	0.123685
	$C_{45}$	0.022247	$C_{51}$	0.143755
	$C_{46}$	-0.071462	$C_{52}$	0.495159
	$C_{47}$	-0.006527	$C_{53}$	-0.105362
	$C_{48}$	0.002733	$C_{54}$	0.033468
	$C_{49}$	0.000686		
Moment	$C_{55}$	-0.284793	$C_{59}$	-1.787703
	$C_{56}$	-0.026199	$C_{60}$	0.352443
	$C_{57}$	-0.024060	$C_{61}$	-0.839323
	$C_{58}$	0.000559	$C_{61}$	0.137932



---

## Kiteplane properties

---

In this appendix the specifications and technical details are presented starting with the geometry in Section H.1, followed by Section H.2 on the structure and inertia of the Kiteplane, the chapter concludes with a separate discussion on the flexibility issue.

### H.1 Kiteplane geometry

The shape of the Kiteplane and the major dimensions are displayed in figure H.1. It features an approximate elliptic wing with positive dihedral from the tail boom section to the tips and is in size comparable to a small surfkite. The twin tail booms support the horizontal tail plane that is located in between and two vertical tail planes on top. The only control surface included in the design is an elevator. However, as the need arises, additional surfaces can be attached with modest effort.

The main geometrical properties are listed in Table H.1, where the mean aerodynamic cord and its location are calculated using the definitions from [Torenbeek, 1982]. The definitions are repeated in equations (H.1) and (H.2) respectively.

$$\bar{c} = \frac{2}{S} \int_0^{\frac{b}{2}} c^2 dy \quad (\text{H.1})$$

$$\bar{y} = \frac{2}{S} \int_0^{\frac{b}{2}} cy dy \quad (\text{H.2})$$

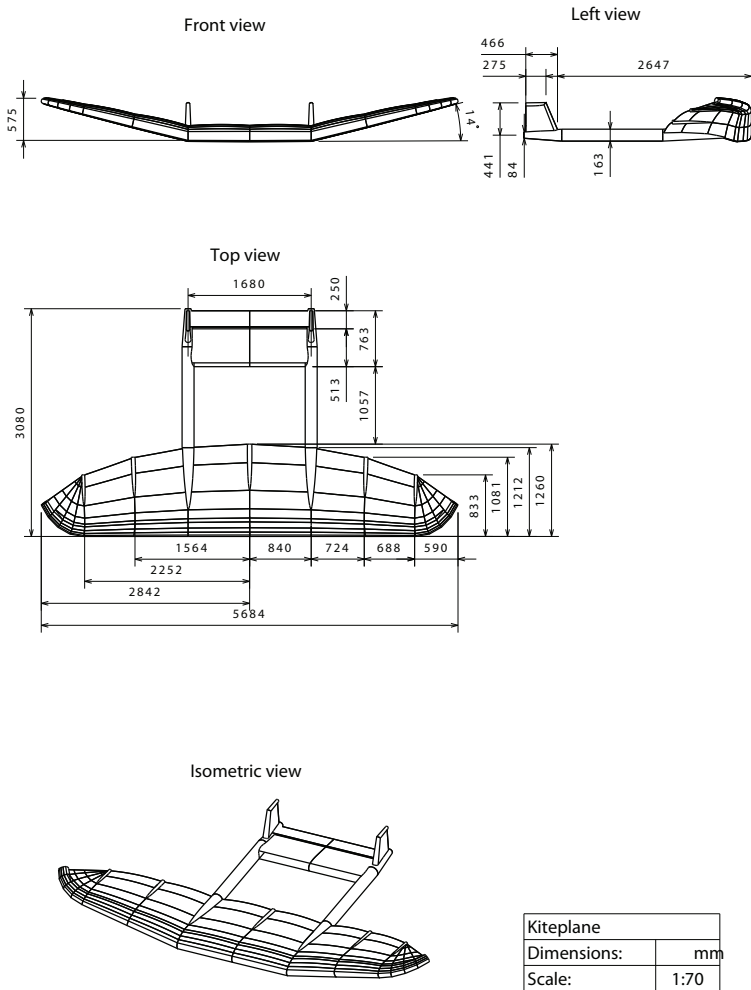


**Figure H.1:** *Kiteplane geometry.*

All geometrical properties are merely design values, because the flexible nature of the structure tends to deform significantly under load. Section H.3 discusses this matter and its implications in more detail.

**Table H.1:** *Geometric properties of the undeformed Kiteplane.*

Component	Parameter	Symbol	Value	Unit
Wing	Surface area	$S_w$	5.67	m <sup>2</sup>
	Span	$b_w$	5.68	m
	Aspect ratio	$AR_w$	5.65	
	Taper ratio	$\lambda$	0.66	
	Leading edge sweep	$\Lambda_{LE}$	0	Deg
	Dihedral angle outer wing <sup>1</sup>	$\Gamma$	14	Deg
	Center cord	$c_c$	1.26	m
	Root cord	$c_r$	1.21	m
	Tip cord	$c_t$	0.83	m
	Mean aerodynamic cord	$\bar{c}_w$	1.08	m
	MAC spanwise location	$\bar{y}_w$	1.21	m
Airframe	Total length	$l$	3.08	m
	Horizontal tail distance	$l_{HT}$	2.24	m
	Vertical tail distance	$l_{VT}$	2.56	m
Horizontal tail	Surface area	$S_{HT}$	1.28	m <sup>2</sup>
	Span	$b_{HT}$	1.68	m
	Aspect ratio	$AR_{HT}$	2.2	
	Taper ratio	$\lambda_{HT}$	1.0	
	Cord	$c_{HT}$	0.76	m
Vertical tail	2 × surface area	$S_{VT}$	0.33	m <sup>2</sup>
	Span	$b_{VT}$	0.44	m
	Aspect ratio	$AR_{VT}$	1.2	
	Taper ratio	$\lambda_{VT}$	0.59	
	Leading edge sweep	$\Lambda_{LE,VT}$	23	Deg
	Root cord	$c_{r,VT}$	0.47	m
	Tip cord	$c_{t,VT}$	0.28	m
	Mean aerodynamic cord	$\bar{c}_{VT}$	0.38	m
MAC spanwise location	$\bar{y}_{VT}$	0.20	m	

<sup>1</sup> The center wing has a zero dihedral angle.

## H.2 Kiteplane structure and inertia

The structure of the Kiteplane consists of inflatable beams and canopy surfaces that are stitched together. The beams carry the aerodynamic loads that are generated by the canopy surfaces. Figure H.2 displays the Kiteplane beam structure, the diameters of the tubes can be found in Table H.2.

Because the beams need to be both strong and airtight they are made of two layers, one for strength and one to keep the air inside. Besides, a single airtight layer would hardly be airtight after all the stitches to join the parts. The materials

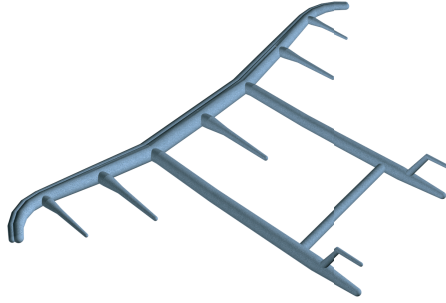


**Figure H.2:** *Drawing of the Kiteplane beam structure.*

**Table H.2:** *Inflatable beam specifications.*

Parameter	Value	Unit
Nominal pressure	0.400	Bar
LE front beam root diameter	0.151	m
LE front beam tip diameter	0.100	m
LE rear beam root diameter	0.214	m
LE rear beam tip diameter	0.142	m
Tail beam main diameter	0.163	m
Tail beam end diameter	0.084	m
Tail beam length (wing TE to end)	1.868	m
Horizontal tail front beam diameter	0.126	m
Horizontal tail rear beam diameter	0.062	m
Vertical tail root beam diameter	0.084	m
Vertical tail tip beam diameter	0.042	m

used for both layers of the beams and the canopy surfaces are listed in Table H.3.

**Table H.3:** *Basic structural weight break down.*

Part	Material	Density [ $\text{gm}^{-2}$ ]
Beam outer layer	Dimension Polyant Dacron	170
Beam inner bladder	100 micron thermoplastic polyurethane	100
Canopy surfaces	Teijin polyester	50

By combining the density of the materials and the geometry, the weight and inertia can be estimated. The total inertia of the Kiteplane consists of three parts, the pressurized beam structure, the canopy surfaces and the air confined in the

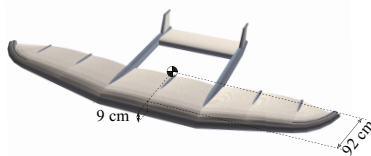
tubes and airfoils.

To obtain the inertial information of the first two parts, the CAD model is analyzed using CATIA V5. The model is split up in two assemblies, the canopy surfaces and the beam structure. By applying a surface density the inertia of both assemblies are calculated. For the canopy assembly a surface density of  $50 \text{ gm}^{-2}$  is used and for the beam structure  $300 \text{ gm}^{-2}$ . The latter consists of  $170 \text{ gm}^{-2}$  for the Dacron layer,  $100 \text{ gm}^{-2}$  for the bladder and an additional 10% for the sum of the stitches, bladder valves, velcro etc.

To calculate the contribution of the air volume to the inertia, the air is assumed to be concentrated at lines and points throughout the Kiteplane structure. The wing is, for example, modeled as a constant density rod located at the quarter cord. The inertia of the tree parts combined is calculated by applying Steiner's parallel axis theorem. The results of the calculations are shown in Table H.4.

**Table H.4:** Kiteplane inertia and center of gravity with respect to the leading edge.

Parameter	Value	Unit
Mass	4.21	kg
$x_{cg}$	0.916	m
$y_{cg}$	0	m
$z_{cg}$	0.089	m
$I_{xx}$	7.38	$\text{kgm}^2$
$I_{yy}$	4.20	$\text{kgm}^2$
$I_{zz}$	11.43	$\text{kgm}^2$
$I_{xy}$	0	$\text{kgm}^2$
$I_{xz}$	0.18	$\text{kgm}^2$
$I_{yz}$	0	$\text{kgm}^2$



Apparently the center of gravity is located at about 92 cm behind the leading edge of the wing, this is at approximately 85% of the MAC. The vertical location of the center of gravity is 9 cm above the leading edge in the center section of the wing, this coincides approximately with the top of the airfoil at the wing center section. For an aircraft this outcome would be unsatisfactory, because the aerodynamic center of the Kiteplane is located at approximately  $l_{HT} \frac{S_{HT}}{S} = 0.51$  m behind the wing ac or 15 cm in front of the cg. However, for a kite with a tether that is attached at a location much in front of the center of gravity, the system is stabilized because  $\alpha$  and tether tension are positively related in the normal operating domain.

The moments of inertia in Table H.4 are important as well, for they determine the control power to meet the required turning rates. For aerodynamic controls, the surface areas are proportional to the required turn rate and the moment of inertia divided by the available moment arm. Since lift based control forces are more efficient compared to drag forces, control surfaces should not be placed normal to the airflow. Keeping this in mind, the ideal locations that maximize

the moment arm of the control surfaces are easily deduced from the geometry:

- For rolling about the  $x$ -axis the surfaces should be placed at the wingtips.
- For pitching about the  $y$ -axis the surface should be placed at the horizontal tail.
- For yawing about the  $z$ -axis the surface should be placed at the vertical tails.

Just like a regular airplane. The resulting moment arms (to the hinge locations) and forces required for a unit angular acceleration are displayed in Table H.5, with the right column calculated using equation (H.3).

**Table H.5:** *Preliminary control power requirements.*

Axis	Motion	Moment arm [m]	Force for unit angular acceleration [Ns <sup>-2</sup> ]
$x$	Rolling	2.25	3.3
$y$	Pitching	1.89	2.2
$z$	Yawing	2.14	5.3

$$\frac{F}{\ddot{\alpha}} = \frac{I}{r} \tag{H.3}$$

Since the moment arms do not differ a lot, the force required for angular acceleration is ordered in the same way as the moments of inertia. Pitching is relatively easy achieved and yawing requires most effort.

### H.3 Kiteplane flexibility

Up to now this chapter has discussed both geometry and inertia as if it were a static property, but due to the flexible nature of the Kiteplane these are simplifications that require investigation. The first question to be answered here is how flexible is the Kiteplane? This is in fact a twofold question because if flexibility is something as the amount of deformation occurring in normal operation, it is determined by both stiffness and loads. For aircraft, stiffness is a structural property and loads are probably best represented by wing loading if a single figure is to be used.

If the Kiteplane is compared with a surfkite that has about the same wing loading, the inflatable structure makes the Kiteplane much more rigid. On the other hand, a Cessna 172 Skyhawk has about a ten times higher wing loading, but the relative wing deformation in normal operation is significantly less. Still

the global shape of the the Kiteplane, i.e. the relative position and orientation of its major components, can be considered fairly constant in its normal operating domain.

From the test flights is concluded that the only global parameter from Table H.1 that changes significantly is the wing dihedral. However, if the wing is bridled at more points this deformation becomes insignificant at global scale as well. For these reasons the inertia of the Kiteplane as displayed in Table H.4 and the geometric properties of Table H.1 are considered constant in the remainder of this text. For the focus of this text, small variations in these properties are not important. Besides, the inaccuracies in the measured values are in size similar to the variations.

Although the deformation of the Kiteplane does not affect its properties globally, locally the fluid structure interaction can be considerable. Deformation at airfoil level has a large impact on the aerodynamic forces and vice versa. This can affect controllability in a negative way, but may also be an opportunity for sophisticated controls. However, due to a lack of experimental data, incorporating aerodynamic effects of local deformation modes is beyond the scope of this appendix.





### **Een Systematische Methodologie voor Vlieger Ontwerp**

Vliegers bestaan al zo'n 3000 jaar [Fadul, 2009], en toch hebben ze weinig aandacht genoten van de wetenschap. En dit terwijl vliegers een belangrijke rol hebben gespeeld bij de ontwikkeling van het vliegtuig in de negentiende eeuw. In de eerste helft van de twintigste eeuw heeft de aandacht van de wetenschappelijke gemeenschap er voor gezorgd dat de luchtvaart kunde en techniek is uitgegroeid tot een bloeiende tak van wetenschap. De systematische en wetenschappelijke aanpak van het ontwerp van het vliegtuig heeft er toe geleid dat het vliegtuig een geavanceerd en ver doorontwikkeld product is geworden en die de maatschappij als geheel gevormd heeft.

Het ontwerp van vliegers is nog steeds een voornamelijk proefondervindelijk proces. Voor hedendaagse applicaties zoals kite surfing en andere sport-gerelateerde activiteiten heeft een dergelijk proces laten zien dat het mogelijk is om tot goede resultaten te komen. Dit is mogelijk gemaakt door verbeterde materialen en het feit dat het relatief goedkoop is om prototypes te maken. Deze fase van prototype ontwerp en evaluatie is aanzienlijk goedkoper van voor conventionele vliegtuigen.

In het laatste decennium heeft er een toename plaatsgevonden van aandacht voor nieuwe industriële toepassingen van vliegers. Meer dan 40 instituten wereldwijd houden zich momenteel bezig met energieopwekking en transport met behulp van vliegers [Furey, 2009]. Deze nieuwe industriële toepassingen van vliegers introduceren een eisenpakket wat veel strikter en complexer is. De eisen met betrekking tot prestaties en veiligheid zijn aanzienlijk complexer dan voor conventionele surf kites.

Het gebruik van een proefondervindelijk ontwerp proces bij het ontwerp van deze complexe industriële vliegers leidt ertoe dat het aantal benodigde prototypes drastisch zal toenemen. Ook loopt men het gevaar dat de evaluatie van al die prototypes oncontroleerbaar wordt. Om grip te houden op het ontwerp van deze complexe vlieger systemen is er een systematische ontwerp methodologie nodig. Een proces wat lijkt op het proces van vliegtuig ontwerp.

De methodologie die in deze dissertatie gepresenteerd wordt is gestoeld op drie pijlers:

- Kennis over de dynamica, constructie en ontwerp van vliegers en vliegergerelateerde technologie.
- Ontwerp programma's die intuïtief en rekenvriendelijk zijn.
- Reproduceerbare metingen om kennis te ontwikkelen en modellen te valideren.

Om de basiskennis van vliegers neer te zetten is er eerst gekeken naar een zo simpel mogelijke modelvorming. In deze modelvorming wordt de vlieger gezien als een rigide lichaam. Twee rigide lichaam modellen worden ontwikkeld en met elkaar vergeleken. Deze vergelijking toont aan dat de twee modellen vergelijkbaar zijn in de resultaten die ze produceren. Elementaire vragen met betrekking tot stabiliteit kunnen met deze modellen beantwoord worden. Voorts maakt de analogie met de modelvorming van conventionele vliegtuigen het mogelijk om een eenvoudige vergelijking te maken tussen vliegtuigen en vliegers. Deze vergelijking is gebaseerd op de eigenwaarden en eigenbewegingen van een vlieger en een vliegtuig.

De flexibiliteit is een van de voornaamste verschillen tussen vliegers en vliegtuigen. Deze flexibiliteit is iets wat moet worden verwelkomd. Het stelt de vlieger in staat om op een uiterst elegante wijze te reageren op verstoringen door te vervormen en de verstoring te absorberen. Voor een flexibele vlieger speelt de flexibiliteit een belangrijke rol in de stabiliteit en vliegprestaties. Daarintegen presenteert de flexibiliteit wel een extra complexiteit voor de ontwerper. Om de flexibiliteit te simuleren is gekozen voor een "Multi-body dynamics" aanpak.

De "Kite Simulation Toolbox" is een numeriek simulatie software pakket voor flexibele vlieger constructies en is opgezet als een "toolbox" binnen *MSCADAMS* om zo een intuïtieve interactie met de gebruiker te bewerkstelligen. De goede toegankelijkheid van de software is een belangrijke eis omdat de huidige vlieger industrie niet de financiële middelen heeft om een complexe software infrastructuur op te zetten.

De "Kite Simulation Toolbox" gebruikt drie basis blokken om vliegers te bouwen. Deze blokken zijn (1) "kabels", (2) "opblaasbare buizen" en (3) "doekvleugel profielen". Deze blokken kunnen worden gebruikt om een groot aantal vlieger configuraties te bouwen.

De kabels bestaan uit een ketting van rigide cilindrische elementen die verbonden zijn met kardanscharnieren. Op elk van deze elementen werkt een aerodynamische weerstandskracht.

De opblaasbare buizen worden beschreven door een ketting van korte cilindrische elementen die verbonden zijn met bolscharnieren. Deze bolscharnieren maken rotaties om alle drie de assen mogelijk. Twee van deze rotaties zijn voor buiging, de derde voor torsie. Over deze bolscharnieren staan drie-dimensionale

rotatieveren. De stijfheden van deze rotatieveren bepalen het buig- en torsiegedrag van de buis. Een algoritme wordt gedefinieerd voor deze stijfheden, als functie van interne druk, lokale buisstraal en lokale deflectie, om het juiste buiggedrag te bewerkstelligen. Deze algoritmen zijn gebaseerd om een serie buigproeven op opblaasbare buizen.

De doek-vleugel profielen worden gemodelleerd door een verbinding te maken tussen de voorzijde en achterzijde van de vleugel. De voorzijde bestaat uit de eerder beschreven opblaasbare buis, de achterzijde wordt gevormd door een kabel. De verbinding bestaat uit een ketting van rigide cilindrische elementen. Op de kruispunten van deze elementen staan de krachtscomponenten die de aerodynamische belasting op de vleugel introduceren. Een algoritme is gedefinieerd die aan de hand van invalshoek, profielwelling en profieldikte de juiste aerodynamische coëfficiënten geeft. Dit algoritme is gebaseerd op een CFD analyse van een groot aantal profielen met verschillende diktes en welvingen bij verschillende invalshoeken.

De thesis presenteert tevens een validatie van dit model. Eerst is er gekeken naar een vergelijking op het niveau van de basis blokken. Daarna is er een evaluatie gedaan aan de hand van de drie dimensionale zeilvorm van de vleugel. Deze vorm is eerst gemeten in de windtunnel van de Universiteit van Stuttgart door middel van fotogrammetrie en vervolgens vergeleken met de gesimuleerde vorm. Deze vergelijking toont aan dat er een sterke overeenkomst is tussen gemeten en gesimuleerde waarden. Ten slotte zijn er metingen gedaan aan surf kites tijdens de vlucht. De krachten op de lijnen zijn gemeten, alsmede de absolute snelheid van de vlieger ten opzichte van de aarde, en deze zijn vergeleken met de gesimuleerde waarden. Wederom toonde de vergelijking een sterke overeenkomst.

Met de toegenomen kennis en ontwikkelde gereedschappen zijn er een aantal casussen aangepakt. De eerste casus berteft het fenomeen van effectieve kabel lengte. De tweede casus was bedoeld op de discussie die er bestaat binnen de vliegerwereld omtrent het sturen van een surf kite. De reden waarom een surf kite een stampend stuur gedrag vertoont was niet duidelijk. De ontwikkelde numerieke simulatie presenteert een nieuwe, onderbouwde hypothese. Voorts toont de simulatie aan hoe het stuurgedrag beïnvloed kan worden. De derde casus betreft de stabiliteit van de "kiteplane", een vlieger met een vliegtuig-achtige configuratie. Tijdens de vliegtests was gebleken dat de kiteplane een instabiel asymmetrisch geïnverteerde slingerbeweging vertoont. Door middel van een analyse van de bewegingsvergelijkingen wordt de oorzaak van dit gedrag bloot gelegd. Een aanpassing in het ontwerp wordt geformuleerd en een vliegtest van het nieuwe ontwerp toont een sterk verbeterde asymmetrische stabiliteit.

Deze dissertatie concludeert uiteindelijk dat een wetenschappelijke aanpak van het ontwerp van vliegers leidt tot een sterk verbeterd begrip en een meer gestructureerd ontwerp proces. De modellen hebben aangetoont een significante bijdrage te kunnen leveren aan de toekomstige ontwikkelingen van vliegers en vlieger-gerelateerde technologie.



---

## Curriculum Vitae

---

Jeroen Breukels was born in Elst, the Netherlands on April 22nd 1975. From 1987 to 1995 he attended the Lorenz college in Arnhem where he went through the Mavo, Havo and VWO.

In 1995 Jeroen started his studies at the Faculty of Aerospace Engineering at the Delft University of technology. During his studies, Jeroen moved abroad to the United States for 6 months to do an internship at Lightspeed Engineering in Santa Paula, California where he worked on a new design of a wing for a Rutan LongEZE which was to take part in the Reno Air Races. After completion of his internship, Jeroen returned to Delft and continued his studies. Due to personal interest, Jeroen took some time away from engineering to follow philosophy courses at the Faculty of Philosophy and Technical Social Sciences. For his master's degree, Jeroen enrolled at the chair for Production Technology under Prof. Ir. Adriaan Beukers where he researched the mechanical behavior of inflated tubular structures. In 2003, Jeroen obtained his Master's degree in Aerospace Engineering.

After graduation, Jeroen started working at the newly formed chair called ASSET (AeroSpace for Sustainable Engineering and Technology) under Prof. Dr. Wubbo Ockels. In 2004, Jeroen worked on a joint project with the European Space Agency called the KitEye project. This project was aimed at breaking the high altitude record for a single kite on a single line. In 2005, Jeroen started his PhD work. Initial efforts were aimed at building KiteLab, a kite testing facility on the roof of the faculty building. After completion, Jeroen moved into the modelling of kites and kite-related structures which eventually culminated into this thesis.

